Autonomous Collision Avoidance by Lane Change Maneuvers using Integrated Chassis Control for Road Vehicles

Amrik Singh Phuman Singh

Autonomous Collision Avoidance by Lane Change Maneuvers using Integrated Chassis Control for Road Vehicles

Amrik Singh Phuman Singh

Department of Systems Science
Graduate School of Informatics
Kyoto University
Kyoto, Japan

March 2019

Doctoral dissertation
submitted to the Graduate School of Informatics, Kyoto University
in partial fulfillment of the requirement for the degree of
DOCTOR OF INFORMATICS
(Systems Science)

This dissertation is dedicated to my family.

Abstract

Although road vehicles are an essential means of transportation, a significant number of lives have been claimed by road accidents. Vehicle control systems, such as electronic stability control systems, have been effective in avoiding collisions by stabilizing the vehicle and thereby preventing understeering and oversteering. However, in these systems, the human driver is still required to perform the steering and braking actions to avoid a collision. In emergency situations, the human driver may fail to react to a threat, and even if the driver does react, he or she may saturate the steering and braking inputs in performing an avoidance maneuver. In such situations, the vehicle is expected to autonomously perform an avoidance maneuver. One such emergency situation occurs when a vehicle encounters an obstacle in its current lane. This dissertation focused on the incorporation of autonomous lane change maneuvers with the friction constraint to avoid an obstacle encountered in the current lane.

In a friction-limiting situation, it is important to determine the best combination of steering and braking inputs that can achieve the shortest longitudinal distance to the obstacle during an avoidance maneuver. To achieve the minimum longitudinal avoidance distance, the obstacle avoidance problem is formulated as an optimal control problem. A single dimensionless equation with one unknown is then derived to provide a solution to this problem. This equation characterizes the optimal state feedback control. Because this equation can be solved using a one-dimensional root finding method, such as the bisection method, a fast computation of the control inputs is expected. The nondimensionalized equations for the braking, steering, and steering with braking avoidance maneuvers provide useful insights into the collision avoidance problem. The benefit of braking in addition to steering during the changing of lanes was made clearer by the two-dimensional decision-making diagram presented in this dissertation.

Based on the optimal control theory, another dimensionless equation with one unknown was derived to provide a solution to the minimum resultant vehicle force problem with a specified longitudinal distance to the obstacle. Once this equation is solved using the bisection method, the desired longitudinal and lateral vehicle forces could be readily calculated. These desired forces were allocated to the longitudinal and lateral tire forces using the minimax optimization of the tire workload for a four-wheel steering (4WS) and four-wheel independent driving/braking distribution. The simulation results demonstrated the effectiveness of the controller in achieving collision avoidance, including those cases in

which there was a change in the situation after the avoidance maneuver had been initiated. These results also demonstrated the capability of the obstacle avoidance controller together with the tire force distributor in achieving near optimal paths.

The lane change maneuver for the emergency obstacle avoidance can result in a high jerk, which may be harmful to the driver and passengers. A trajectory generation method was developed that considered the friction constraint and minimized the time integral of the squared resultant vehicle jerk during the maneuver. The desired lateral accelerations at the centres of percussion and the desired longitudinal force to track the desired trajectory were obtained by using the sliding mode control method. These desired lateral accelerations and longitudinal force were then translated into the front and rear wheel steering angles and direct yaw moment. Numerical simulations demonstrated the effectiveness of the integration of the 4WS control and direct yaw moment control in simultaneously achieving trajectory tracking and vehicle stabilization.

The optimal allocation of tire forces by maintaining equal usage of force by the tires has received considerable attention. The purpose of maintaining an equal usage of force by the tires is to avoid a situation where a tire is under a higher force usage condition than the remaining tires. An algebraic solution was derived and investigated for the allocation of tire force with a workload equalization for a 4WS and four-wheel independent driving/braking distribution. The limit performance of a vehicle with a minimum common tire workload was evaluated and discussed. The regions on a longitudinal-lateral acceleration plane in which there were no solutions to the workload equalization were identified. This study found that when the total yaw moment is zero, the tire force allocation with the minimum common tire workload among the four tires is always achievable and the limit performance is similar to that obtained using the minimax optimization of the tire workload.

The collision avoidance methods proposed in this dissertation were effective in avoiding collisions and in keeping the vehicle stable while operating near its limit of friction.

Acknowledgements

First of all, I would like to express my sincere gratitude to my academic advisor, Associate Professor Dr. Osamu Nishihara. This dissertation could not have been completed without his guidance and advice. Over the years, I have learned a great deal from him. Dr. Nishihara has interesting approaches to solve engineering problems, especially in his works on the design of dynamic vibration absorbers, which he loves to talk about. But it was his paper on the optimal tire force allocation that caught my attention and made me decide to pursue my studies under his supervision. I am grateful that I had Dr. Nishihara as my academic advisor and I very much appreciate the time and effort he has put in for me. I wish him all the best in his career.

I would also like to say a big thank you to Professor Dr. Manabu Kano for accepting me as a student at the Human Systems Laboratory. I would like to thank Assistant Professor Dr. Koichi Fujiwara, who made the arrangements for my workstation when I joined the laboratory. I am thankful to Mr. Naoki Ishimatsu for helping me to translate documents from Japanese to English. I would also like to express my gratitude to the staff and students of the Human System Laboratory for their help and for making my academic life an interesting one. Special thanks to Dr. Ryouhei Hayama from JTEKT Corporation for the fruitful discussions and for providing me with an opportunity to use the driving simulator at JTEKT. I would like to thank Professor Dr. Hidetoshi Shimodaira and Professor Dr. Toshiyuki Ohtsuka for providing valuable advice and suggestions towards the end of my study.

I would like to express my appreciation to the Ministry of Higher Education Malaysia and Universiti Teknikal Malaysia Melaka for providing me with a scholarship for my study at Kyoto University. With the scholarship, I was able to focus on my study without having to worry about finding financial support for my tuition fees and daily expenses. I would also like to thank my friends, Xinmin, Azly, Habibah, Fary, and all those who have been a part of my life while studying at Kyoto University.

Finally, and most importantly, I would like to thank my family for their love and support. To my mum, thank you for everything that you have done for me, especially for all the sacrifices that you made. To my masi Rina, thank you for always motivating and supporting me in every way possible. To all my brothers and sister, especially Navin, Kavin, Sonam, and Neelam, thank you for making the arrangements for me while I was in Japan. To my bapu, who calls me Nicky, I truly miss you, and knowing that I will not

have a chance to meet you again, the moments we spent together are now memories for life.

Contents

List of Figures

List of Tables

Chapter 1

Introduction

1.1 Motivation

Road vehicles are an essential means of mobility and they provide the convenience of commuting from one place to another. On the other hand, accidents involving vehicles contribute to a significant loss of lives. In the United States, 37,461 people were killed and 3,144,000 people were injured in road accidents in 2016 [77]. In the same year in Germany, 3,206 people lost their lives and 396,666 people were injured in road accidents [15]. Fig. 1.1 shows the number of accidents, the number of people injured, and the number of people killed in road accidents in Japan from the year 1991 to 2016. Even though these numbers have been decreasing in recent years, the number of people who have been injured and killed is still at a serious level. In Japan, 3,904 people were killed and 618,853 people were injured in road accidents in 2016 [2].

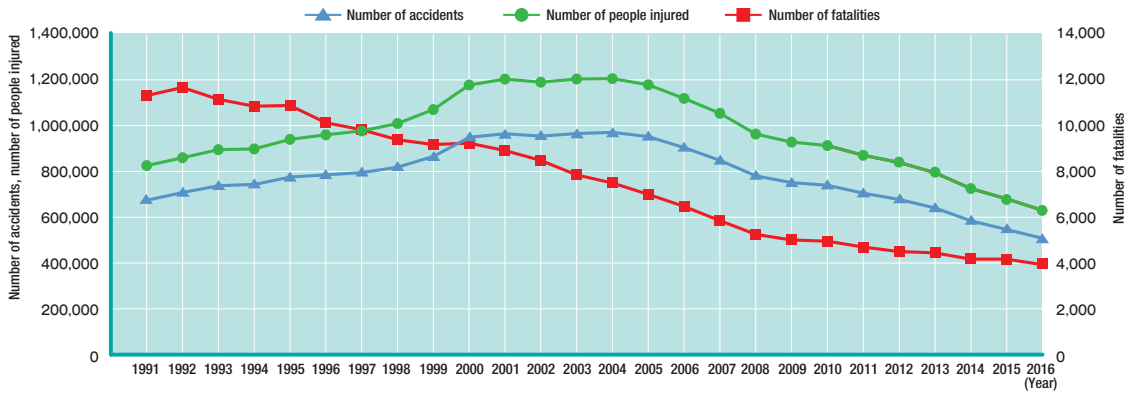

Figure 1.1: The number of accidents, the number of people injured, and the number of people killed in road accidents in Japan from the year 1991 to 2016 [2].

The introduction of safety systems, such as the anti-lock braking system (ABS) and

the electronic stability control (ESC), have contributed to a reduction in the number of accidents. The ABS prevents the wheels from locking up when the driver applies hard braking. This reduces the stopping distance and enables the driver to maintain the steerability of the vehicle. The ESC system controls the lateral and yaw motions of the vehicle in critical situations to prevent the vehicle from unstable conditions such as spin and drift-out. These driver assistance systems are less effective in cases where the driver is inattentive or distracted and is slow to recognize an obstacle. In such cases, the vehicle is expected to autonomously perform an avoidance maneuver.

Autonomous vehicles have attracted the interest of not only the academia and automakers but also other key players such as Google as well as government agencies. By leveraging on advancements in sensing, actuation and control technologies, autonomous vehicles can be capable of performing driving operations that are as good as a human driver or even up to the level of a race car driver [61]. The introduction of autonomous vehicles on the road will eliminate the accidents caused by human errors as the human driver is no longer performing the driving operations. More than 90% of the accidents on highways are said to be caused by human driver-related errors [98]. The fact that autonomous vehicles are able to perform maneuvers near or at the limits of friction is highly relevant to collision avoidance as the autonomous vehicles can safely avoid collisions in emergency situations where a human driver may saturate the steering and braking inputs.

Although autonomous vehicles are not yet ready for the road, autonomous driving features, such autonomous collision avoidance systems, are already available in the cars that are being produced. One such collision avoidance system is the autonomous emergency braking (AEB) system. The AEB is able to detect an imminent collision and it then brakes to avoid a collision or to reduce the relative velocity on impact, without the intervention of the human driver. In some emergency situations, the automatic control of both the steering and braking inputs is necessary to avoid a collision. This dissertation studied the avoidance maneuvers whereby the steering and braking actions were performed by a controller that operated the vehicle up to the limit of friction. The collision avoidance system is a key technology for autonomous driving systems and has a high potential to be implemented on autonomous vehicles in the future. According to the J3016 driving automation taxonomy [101], for vehicles equipped with an automated driving system (ADS) that describes levels 3 to 5 and has the capability of performing the entire dynamic driving task on a sustained basis, collision avoidance is a function of ADS. Also, the collision avoidance system can be included at any level for a vehicle equipped with driving automation systems. With the collision avoidance system, safer vehicles can be expected in the future.

1.2 Background

There are many situations in which a human driver/controller has to perform a maneuver to avoid a collision. These avoidance maneuvers include those that are required to avoid an obstacle that suddenly appears in the current lane [10], avoid an unintended roadway departure [9], avoid a collision at an intersection [11], avoid a collision with an oncoming vehicle in an overtaking maneuver [12], and to avoid a secondary collision after a light impact [129].

The approaches adopted in driver assistance systems for the avoidance of collisions may be divided into two types; one is a shared control approach and the other is an autonomous control approach. In the shared control approach, the human driver and the control system work together to avoid a collision [33]. In [14], a predictive haptic feedback steering torque is generated to assist the human driver in avoiding an obstacle. In the shared control approach, the torque provided by the controller is given by the product of a gain, known as the level of haptic authority (LoHA) [4], and the difference in the steering angles of the human driver and the controller. The controller gives the desired steering angle to follow a given path. Inoue *et al.* [57] combined the haptic steering torque control and the direct yaw-moment control (DYC) to achieve an improved path tracking performance and good cooperative characteristics between the driver and the control system. These shared control approaches are outside the scope of this dissertation as here the focus was on autonomous collision avoidance maneuvers that are performed independently of the human driver.

Lane change is an important collision avoidance maneuver and it is useful in cases where it is impossible to avoid a collision in the current lane by braking. The avoidance maneuver considered in this dissertation was limited to a lane change maneuver, whereby a vehicle underwent a transition from the current lane to the adjacent lane on the assumption that it was safe to move to the adjacent lane. The lane change maneuver that was considered here was one that required the integrated control of the steering and braking, and where the vehicle was operated up to the limit of friction.

1.2.1 Control Architecture for Obstacle Avoidance Control System

One approach to address the obstacle avoidance problem is by adopting a hierarchical structure for the control system design [41]. The hierarchical structure has been used in numerous studies previously, where the dynamic control systems of the vehicle are designed to be hierarchical [71, 87, 81]. Similarly, an obstacle avoidance system with three levels, as shown in Fig. 1.2, can be designed. The higher-level controller or the obstacle avoidance controller determines the desired longitudinal and lateral forces of the vehicle and the yaw moment that is required to avoid an obstacle, based on the preview information provided

by the sensors such as the camera, radar, and lidar. The middle-level controller or the tire force distributor calculates the desired longitudinal and lateral tire forces to achieve the desired forces and moment of the vehicle. The lower-level controller or the steering and braking controller layer converts the desired longitudinal and lateral tire forces to the steering angle and braking torque commands.

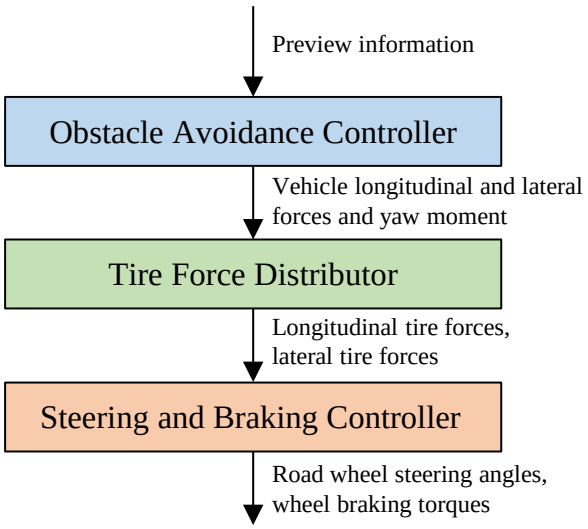

Figure 1.2: Structure of obstacle avoidance control system.

In another approach, the obstacle avoidance problem is formulated as an optimal control problem, which provides the optimal steering and braking inputs to achieve the obstacle avoidance [52]. In this approach, the optimal control problem is converted to a nonlinear programming problem. While this approach gives an accurate solution of the control inputs and the resultant trajectory as it considers a nonlinear vehicle model, including a nonlinear tire model, the computational effort required to solve the nonlinear programming problem is large and therefore, makes it less suitable for real-time implementation. In contrast to this approach, the hierarchical structure approach separates the obstacle avoidance problem into three different sub-problems that can be solved more easily. Therefore, this dissertation adopted the hierarchical structure approach to address the obstacle avoidance problem.

1.2.2 Decision-making

The making of the decision as to when a controller, such as the one shown in Fig. 1.2, should be activated is important in designing a collision avoidance system. When presented with an obstacle in the current lane, it is important to decide whether the braking avoidance or steering avoidance will be effective in avoiding the obstacle and whether the obstacle can be avoided by these maneuvers. Braking avoidance here refers to the application of

full braking to stop the vehicle in the current lane, while steering avoidance refers to a lane change maneuver by pure steering. Two typical indices to decide if a collision is avoidable are the longitudinal distance to the obstacle and the time to collision (ttc). The longitudinal distances required to avoid the obstacle by the braking avoidance and steering avoidance are denoted by x_b and x_s, respectively and are given as

$$x_b = \frac{m_t}{2F_{\max}} v_{x0}^2 \tag{1.1}$$

$$x_s = \sqrt{\frac{2m_t y_f}{F_{\max}}} v_{x0} \tag{1.2}$$

where m_t is the total vehicle mass, v_{x0} is the initial longitudinal velocity, $F_{\max}$ is the maximum available vehicle force, and y_f is the distance between the centers of adjacent lanes.

Fig. 1.3 shows the plots of the longitudinal distances required to avoid the obstacle as a function of the initial longitudinal velocity for the braking avoidance and steering avoidance. The following parameters were assumed: $m_t = 1830$ kg, $y_f = 3.5$ m, and $F_{\max} = 8.967$ kN. The blue solid line indicates the steering avoidance and the red dashed line indicates the braking avoidance. Each of these curves divides the region into the region where the obstacle is avoidable and the region where a collision is unavoidable using the avoidance maneuver. The region above the curve is where the obstacle is avoidable and the region below the curve is where the obstacle is unavoidable. The region in light grey is where the obstacle is unavoidable by either of these maneuvers. Region I, in light blue, is where the obstacle is unavoidable by the steering avoidance but can be avoided by the braking avoidance. In region II (light purple), the obstacle becomes unavoidable by the braking avoidance and can only be avoided by the steering avoidance. Region III, in light green, is where there is no necessity to perform an avoidance maneuver.

The ttc at which the braking avoidance must be initiated is denoted as ttc_b and the ttc at which the steering avoidance must be initiated is denoted as ttc_s, and these times to collision are given as

$$ttc_b = \frac{x_b}{v_{x0}} = \frac{m_t}{2F_{\max}} v_{x0} \tag{1.3}$$

$$ttc_s = \frac{x_s}{v_{x0}} = \sqrt{\frac{2m_t y_f}{F_{\max}}} \tag{1.4}$$

Fig. 1.4 shows the ttc at which the avoidance maneuver must be initiated. The diagram in Fig. 1.4 can be explained in a similar way as Fig. 1.3. Similar diagrams can be found in [31, 42, 52, 106, 130]. Although these diagrams are commonly used for decision-making, they have some limitations. As can be seen in these diagrams, only a single variable effect (in this case, the initial longitudinal velocity) can be studied on a two-dimensional plot. Besides, the switching point moves if the fixed parameters (in this case, the total

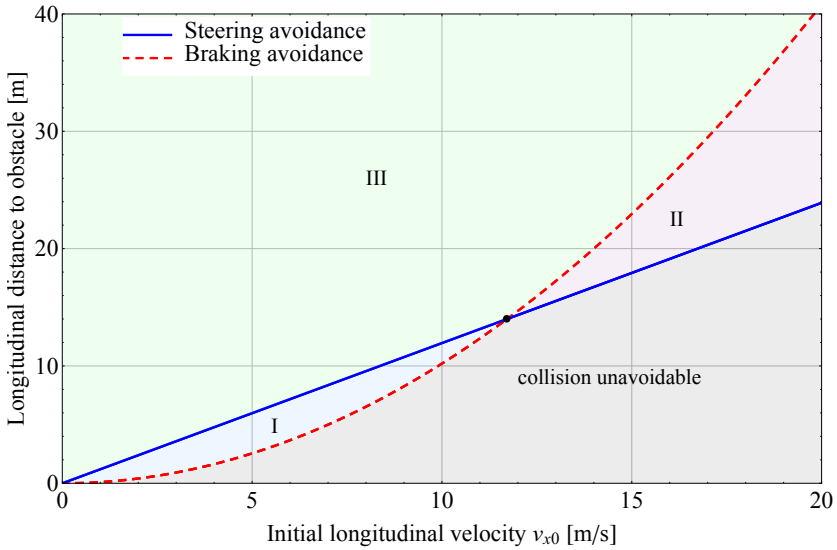

Figure 1.3: Longitudinal distance to obstacle.

vehicle mass, the maximum available vehicle force, and the distance between the centres of adjacent lanes) are changed. This means that there is no general switching condition. This dissertation sought to find a more compact representation of the essential variables for decision-making on a two-dimensional plot and to determine a unique switching condition.

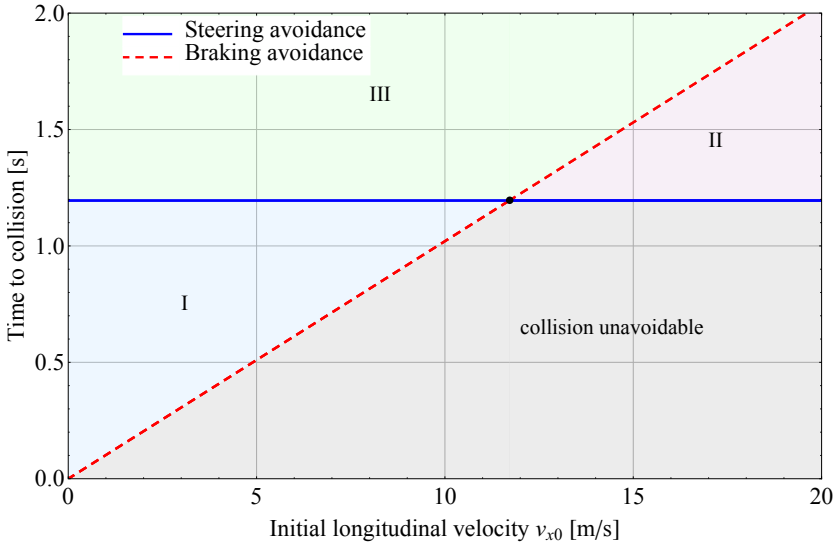

Figure 1.4: Time to collision.

1.2.3 Friction Circle

According to the tire friction circle concept, the longitudinal and lateral tire forces are limited by the maximum available tire force, which is given as the product of the tire-

road friction coefficient and the vertical tire load. Fig. 1.5 shows a tire friction circle, where X and Y are the longitudinal and lateral tire forces, respectively. The radius of the circle is equal to the product of the friction coefficient μ and the vertical tire force Z. At any instant, the operating point is inside the circle, and if the operating point is on the boundary of the circle, then the tire is said to be operating at its friction limit. The limiting friction force at the tires limits the longitudinal and lateral acceleration of the vehicle; the resultant acceleration cannot exceed the product of the friction coefficient and the gravitational acceleration. The limit on the resultant acceleration should be incorporated in the obstacle avoidance controller, which is the higher-level controller shown in Fig. 1.2.

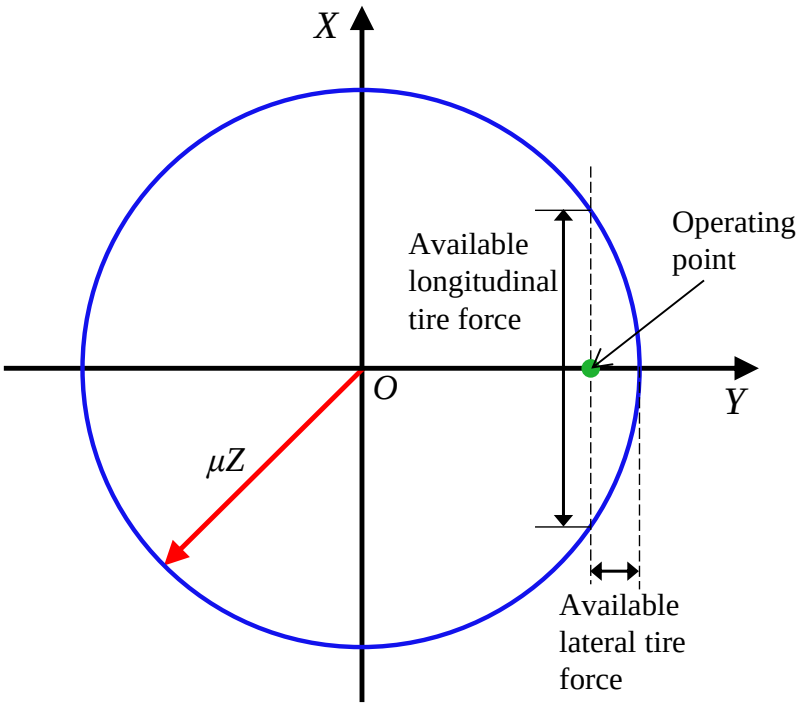

Figure 1.5: Tire friction circle.

1.2.4 Trajectory Generation

The trajectory generation is an important stage in collision avoidance, where the desired trajectory for the obstacle avoidance is generated. The desired trajectory defines the desired path and desired velocity profile that a vehicle should follow. With respect to lane change, various approaches, including simple functions and optimal control with different complexities of vehicle models have been considered for the generation of the desired trajectory.

The desired trajectory is generated to satisfy some criteria such as comfort and safety.

Chee and Tomizuka [23] generated the lane change path using the trapezoidal acceleration profile (TAP) by incorporating the lateral acceleration and jerk limits for ride comfort. Soudbakhsh *et al.* [116] used the TAP to generate a lane change path for obstacle avoidance. To generate a lane change path that considers the constraints on the maximum lateral acceleration and maximum jerk, Isermann *et al.* [58] used a sigmoid, and showed that the sigmoid was able to achieve a lane change with a shorter longitudinal distance to the obstacle compared to that of a clothoid for different initial longitudinal velocities and maneuver widths. Funke and Gerdes [38] proposed the use of a simple clothoid to generate the lane change trajectory that considers the constraint imposed by the friction between the tires and road, and discussed the benefit of braking during the lane change maneuver to achieve a shorter longitudinal avoidance distance. These simple heuristic approaches enable fast computations but they do not yield an optimal trajectory for obstacle avoidance.

Shiller and Sundar [106] proposed a lane change trajectory with a minimum longitudinal avoidance distance by considering the constraints due to the tire friction ellipse, the maximum traction force, and the maximum absolute steering angle. Horiuchi *et al.* [52] also formulated the obstacle avoidance problem as an optimal control problem. They minimized the time integral of the weighted sum of the squared steering rate and the squared sum of the tire force usage of each tire for a given longitudinal distance to the obstacle. These methods yield the optimal trajectory but they are computationally less efficient. Instead of using a rigid body vehicle model coupled with a nonlinear tire model as in [52, 106], a point mass model can be used for the formulation of the optimal control problem, as in [42]. In [42], where the authors used the optimal control theory to generate a minimum longitudinal avoidance distance lane change trajectory. The optimal control inputs are represented by numerical mapping and therefore, a precise solution cannot be expected.

1.2.5 Trajectory Tracking

Numerous studies have proposed methods to control the steering and driving/braking inputs in order to track the desired trajectory. Park and Gerdes [91] developed a combined feedforward-feedback controller that calculates the desired longitudinal and lateral vehicle forces and yaw moment to track the desired trajectory and then, these desired forces and moment are allocated to the longitudinal and lateral tire forces. To track the desired path, a four-wheel steering (4WS) sliding mode controller based on the centres of percussion relative to the rear and front wheels was first proposed in [65] and then, further studied in [49]. Since in obstacle avoidance, braking contributes to a shorter longitudinal avoidance distance, the integration of the 4WS and direct yaw-moment control (DYC) is able to achieve both trajectory tracking and vehicle stabilization.

1.2.6 Direct Yaw-moment Control

A direct yaw moment is defined as the yaw moment generated by the difference between the longitudinal tire forces at the left and right sides of a vehicle body. To better understand the benefit of using the DYC in controlling the motion of a vehicle near its friction limits, let us consider the operating point, which is represented by a green point in Fig. 1.5. Fig. 1.5 was prepared based on an example presented in [6]. Detailed explanations of these benefits can be found in [6] and a summary of the benefits is given here. As shown in Fig. 1.5, the operating point is near the saturation of the lateral tire force and, in such a case, the DYC is often necessary. The range of the available longitudinal tire force is larger than that of the available lateral tire force and therefore, it is reasonable to use the longitudinal tire force rather than the lateral tire force to control the motion of the vehicle. Another advantage of the DYC over the steering control is that the driving/braking torque command can accurately generate the longitudinal tire force. In the steering control, the generation of the lateral tire force is controlled by the steering angle. The application of the DYC and its effects on the improvement of the performance of the vehicle dynamics have been reported in previous studies [5, 76, 105].

1.2.7 Optimal Tire Force Allocation

The integration of the steering control and the DYC can solve this problem by optimally allocating the tire forces so that the tires are prevented from saturation. In a typical tire force allocator, the inputs are the desired longitudinal and lateral vehicle forces and the desired yaw moment, while the outputs are the desired longitudinal and lateral tire forces. The desired vehicle forces and yaw moment are given by an upper-level controller such as a vehicle dynamics controller [87] or a collision avoidance controller [41], and the desired tire forces are converted to the steering angle and driving/braking torque commands.

To avoid tire force saturation, Mokhiamar and Abe [71] suggested the minimization of the weighted sum of the squared tire workloads for a vehicle with four-wheel independent steering (4WIS) and four-wheel independent driving/braking force distribution systems. The tire workload is defined as the ratio of the resultant longitudinal and lateral tire forces to the vertical tire load [71]. Assuming that the friction coefficients at the four tires are the same, the tire workload is a reasonable performance index for measuring how far the tire forces are from saturation. However, in cases such as in a μ-split maneuver, the friction coefficients of the left and right tires are not equal and the minimization using the tire workload-based objective function is not effective. In such cases, the tire force usage, which is defined as the ratio of the resultant longitudinal and lateral tire forces to the product of the friction coefficient and the vertical tire load, is more appropriate because the friction coefficient at each tire is considered. Ono *et al.* [87] minimized the

common tire force usage among the four tires for the 4WIS and four-wheel independent driving/braking force distribution.

Nishihara and Higashino [81] studied the minimax optimization of the tire workload or, more specifically, the minimization of the maximum squared tire workload for the 4WS and four-wheel independent driving/braking force distribution. Later, Nishihara [79] compared the limit performance of the vehicle for the minimax optimization and square sum minimization of the tire workload based on the contour plots of the maximum tire workload. For the 4WS/4WIS and four-wheel independent driving/braking force distribution, the minimax optimization gave a better limit performance compared to the square sum minimization, where the benefit of using the minimax optimization became more significant for the 4WIS and four-wheel independent driving/braking force distribution. In [79], a heuristic approach, whereby a two-stage square sum minimization was performed in which in the second stage, the vertical tire load was divided by the square root of the tire workload obtained in the first stage, was shown to provide considerable improvement compared to the ordinary square sum minimization approach. This heuristic modification requires about twice the computational effort that is required for the ordinary square sum minimization approach [79].

To further extend the limit performance of the vehicle, Ono *et al.* [86] proposed the minimization of the common tire force usage problem by optimizing the longitudinal and lateral tire forces as well as the vertical tire loads. In [86], the vertical tire loads were controlled by using a roll stiffness distribution. The study by Luo *et al.* [68] also focused on optimizing the three forces of the tires by keeping the tire force usage of the tires near each other. In their study, the vertical tire loads were controlled by using an active suspension. Nishihara and Sono [83] studied the minimax optimization of the tire workload on the assumption that the vertical tire load control uses the roll stiffness distribution or active suspension, and demonstrated that the tire force distribution with an active suspension achieved the best limit performance. This achievement with the limit performance was at the expense of the computational burden. For example, in [83], in addition to the direct yaw moment, the load transfer for an active suspension or the distribution ratio for the roll stiffness distribution was treated as a variable to be optimized. To find the optimal variables in [83], a two-dimensional golden section search method was used. This method is computationally less efficient than the one-dimensional golden section search method that is used for problems without a vertical load distribution control, as in [81]. In this dissertation, reasonably fast tire force distribution methods were considered for realization of the avoidance maneuvers.

1.3 Dissertation Objectives

This dissertation sought to develop a simple and reasonably fast autonomous obstacle avoidance methods that incorporate the friction constraint and explore the effects of the integrated chassis control while simultaneously achieving obstacle avoidance and vehicle stabilization. The specific objectives of this dissertation are as follows:

(i) To develop a simple and precise solution to the optimal feedback control of steering and braking for the problem of the minimum longitudinal distance to the obstacle on the assumption that the maximum available vehicle force is given.

(ii) To develop a simple and precise solution to the optimal feedback control of steering and braking for the problem of the minimum resultant vehicle force with a given longitudinal distance to the obstacle.

(iii) To develop a simple and fast lane change trajectory generation method for obstacle avoidance with a minimum resultant vehicle jerk and with consideration given to the friction limit.

(iv) To design a control system for the integrated control of a 4WS and direct yaw moment to simultaneously achieve trajectory tracking while maintaining vehicle stability.

(v) To derive an algebraic solution for the tire force allocation with a tire workload equalization for a vehicle with 4WS and four-wheel independent driving/braking distribution systems.

1.4 Dissertation Contributions

The contributions of this dissertation are as follows:

(i) A dimensionless equation with an unknown that characterizes the optimal state feedback control for obstacle avoidance with the minimum longitudinal distance to the obstacle.

(ii) A decision-making diagram, which is a two-dimensional plot that captures the important parameters required to determine the minimum longitudinal distance to the obstacle.

(iii) A dimensionless equation with an unknown that characterizes the optimal state feedback control for obstacle avoidance with the minimum resultant vehicle force.

(iv) A fast trajectory generation method for a lane change with minimum jerk and with consideration given to the friction limits for obstacle avoidance.

(v) A trajectory tracking controller using a combination of a 4WS control based on the centers of percussion with respect to the front and rear wheels and DYC.

(vi) An algebraic solution to the optimization of the direct yaw moment with a tire workload equalization for a 4WS and four-wheel independent driving/braking distribution.

1.5 Dissertation Outline

Chapter 2: Minimum Longitudinal Avoidance Distance Optimal State Feedback Control

In Chapter 2, integration of steering and braking is studied for a collision avoidance from the standpoint of optimal control theory. First, the collision avoidance by braking, steering, and steering with braking maneuvers are theoretically investigated. By some assumptions such as the point mass vehicle model and constant resultant vehicle force in all directions, the selection of the best maneuver for collision avoidance is represented by the regions on a two-dimensional diagram. The nondimensionalized axes of this diagram stand for all required vehicle state and geometrical conditions, more specifically, the remaining distance, longitudinal vehicle velocity, lane width, and friction coefficient. Secondly, a two-point boundary value problem derived for the integrated control is reduced to a single equation with an unknown via algebraic simplifications, and the bisection method turns out to be the most appropriate among the algorithms that have been tested. It turned out that the efficient and precise solution of the optimal control problem is guaranteed, including the cases in which the intervention has been initiated. Consequently, this study realizes the efficient identification of the theoretically reliable reference maneuver of single lane change with the minimum collision avoidance distance in the framework of feedback control.

Chapter 3: Minimum Resultant Vehicle Force Optimal State Feedback Control

In Chapter 3, an optimal feedback control with minimum resultant vehicle force for obstacle avoidance is investigated. In Chapter 2, four equations were derived for the two-point boundary value problem that determines the optimal feedback control for the minimum longitudinal avoidance distance problem in which the maximum vehicle force is given. In Chapter 3, these equations are fully nondimensionalized, and the dimensionless equations are simplified by successive algebraic manipulations; until the control parameters are identified as functions of one unknown that is readily determined by an equation defined in an implicit form. The stable solution of this equation is expectable by the application of the bisection method. The two dimensionless inputs to this equation are: the ratio of the lateral to longitudinal velocity and the ratio of the remaining lateral to longitudinal distance. The optimal control is therefore described in the form of a state feedback controller. In the numerical simulations, the longitudinal and lateral vehicle

forces required to realize the optimal control are distributed to the tires using a minimax optimization scheme that assumes a four-wheel steering vehicle. In each case, the maximum tire workload is minimized, and the vehicle center of gravity closely traced the paths expected by the point-mass model assumed in the controller design. Additional examples are provided to demonstrate the effectiveness of online optimization in accommodating the lateral movement of the obstacle or the appearance of another object, after the initiation of the avoidance maneuver.

Chapter 4: Minimum Jerk Trajectory for Obstacle Avoidance

Intelligent vehicles are expected to perform emergency lane change maneuver to avoid a collision. During this aggressive maneuver, a high jerk may occur and this reduces the comfort level and may be harmful to the vehicle occupants. Chapter 4 addresses the autonomous collision avoidance, in the context of minimum jerk. First, the desired trajectory described by the desired path and desired velocity profile is generated using quintic polynomials. These quintic polynomials are derived using the Euler-Lagrange equations for the functional defined as the time integral of the squared resultant jerk. The generation of the trajectory depends on the essential parameters that are the initial longitudinal vehicle velocity, the desired final lateral position, and the tire-road friction coefficient. As a result of nondimensionalization and algebraic manipulations, the collision avoidance problem reduces to a nondimensionalized equation that is an implicit equation in one unknown that is the aspect ratio of lane change and an input capturing the essential parameters. The plot of the aspect ratio for lane change against the input gives a curve that indicates the last point to avoid a collision. The sliding mode control method is used to translate the trajectory tracking errors into the reference values of the total longitudinal force and centers of percussion lateral accelerations that are the inputs to the tire force distributor. This distributor allocates these reference values to the tires by reducing the tire force usage. Numerical simulations at different initial longitudinal vehicle velocities demonstrate the effectiveness of controller in avoiding the obstacle and keeping the vehicle motion stable.

Chapter 5: Optimal Tire Force Allocation with Workload Equalization

The optimal tire force allocation for achieving stable vehicle motion has been actively studied in the past. Various objective functions have been considered for reducing the tire workload for vehicles with a four-wheel independent driving/braking force distribution and either two-wheel steering (2WS), four-wheel steering (4WS), or four-wheel independent steering (4WIS) systems. In Chapter 5, the tire force allocation by equalizing the tire workload of the four tires for a vehicle with 4WS and a four-wheel independent driving/braking force distribution system is studied. First, algebraic manipulations are performed to derive two quadratic equations with respect to the direct yaw moment. The

solution of these quadratic equations that gives the minimum common tire workload among four tires is the optimal direct yaw moment. Once the optimal direct yaw moment has been determined, the optimal longitudinal and lateral tire forces can be readily evaluated. Next, the limit performance of a vehicle with optimal tire force allocation is investigated and clarified. Workload equalization is found not to be possible in some cases, and the regions in which there are no feasible solutions to the optimal tire force allocation with workload equalization are identified.

Chapter 6: Conclusion and Future Work

This chapter summarizes the findings of the previous chapters and provides suggestions for future work.

Chapter 2

Minimum Longitudinal Avoidance Distance Optimal State Feedback Control

2.1 Introduction

Collision avoidance has become an important topic in the field of the intelligent transportation system as a vehicle should perform an avoidance maneuver in the case of emergency. Many types of research have been conducted to study different aspects of collision avoidance [41, 124, 37, 59, 78, 102]. Two key questions for collision avoidance are if a collision can be avoided for a given situation and what kind of maneuver is the best. For a straight lane, an appropriate index to determine if a collision is avoidable is the avoidance distance, defined as the traveling distance along the lane required to complete the avoidance maneuver. The maneuver that requires the shortest avoidance distance is considered to be the best maneuver. In the cases where braking to stop the vehicle is not possible, a lane change maneuver should be performed.

Because of the shorter avoidance distance, a combination of steering and braking for lane change maneuver to avoid an obstacle has gained much interest. Various approaches have been put forward to solve the design problems related to the in-lane collision avoidance by combining the steering and braking actions. Hayashi *et al.* proposed the use of a combination of two equal radius arcs to represent the avoidance path with constant deceleration [44]. This method is less suitable when the vehicle is forced to operate at its limits because the combined effect of cornering and braking forces with respect to the friction circle was not taken into account. Furthermore, at the intersection of the two arcs, the curvature becomes discontinuous, and therefore, poses a challenge for the steering controller. Funke and Gerdes [38] generated a lane change path that has a continuous curvature using a combination of straights, clothoids, and arcs. The longitudinal velocity profile was determined by the path curvature and tire-road friction coefficient. However,

the paths generated using this heuristic method are not optimal. More specifically, if the distance to the obstacle is shorter than the distance required by the method in [38], there is a possibility that the avoidance is still feasible.

To yield a trajectory that has a minimum avoidance distance with combined steering and braking inputs taking into account the friction constraint, the obstacle avoidance problem must be formulated as an optimal control problem. In a study of the minimum obstacle avoidance distance, integrated steering and braking actions by utilizing the optimal control theory and satisfying the constraint imposed by the tire friction ellipse were proposed [106]. Hattori and co-workers used a simplified vehicle model capturing the longitudinal, lateral, and yaw motions to solve the shortest avoidance distance problem based on the second-order cone programming [41]. In the case of the zero initial yaw angle and the zero initial yaw velocity, the optimal lane change maneuver was accomplished by vehicle longitudinal and lateral motions without any yaw motion. Thus, a point mass is sufficient to represent the vehicle [41]. The methods in [106, 41] do not consider the situation where there is a disturbance after the avoidance maneuver is initiated. In such situation, an optimal state feedback controller is desirable. The complex solution methods used in [106, 41] do not facilitate the implementation of the controller in a feedback form.

Assuming point mass representation of the vehicle, Hattori *et al.* [42] proposed a feedback controller for the minimum avoidance distance problem with optimal steering and braking control. A set of nonlinear equations containing the solutions of the control problem was derived. Because the solution process of these equations is not stable enough for on-line implementation, an approximation solution was proposed instead [42]. The solution for optimal control was found by off-line computation and represented by a two-dimensional map. This seems to be a less precise solution method. Moreover, other essential information such as the avoidance distance, avoidance time or final vehicle velocity is not retrievable from this map. In their study, dedicated maps would be required to acquire this information.

To best of our knowledge, a closed-form solution for the optimal state feedback control to the minimum avoidance distance problem with combined steering and braking is not known. The aim of the present work is to derive a simple solution method to this problem. In this chapter, instead of directly solving the simultaneous nonlinear equations for the two-point boundary value problem (TPBVP) resulting from the necessary conditions for optimality, we reduce the problem to a one-variable root finding problem. As a result, we have a dimensionless equation that characterizes the optimal state feedback control. The root finding problem can be efficiently solved using appropriate root finding techniques for one unknown. This unknown, the dimensionless final time, which is the dimensionless form of the time taken for the avoidance maneuver, is an essential control parameter.

The main contribution of this chapter is the determination of the state feedback optimal control to the minimum avoidance distance problem by a single nondimensional equation with one unknown. Since this unknown can be determined numerically using bisection method, fast computation is expectable, and this allows reliable real-time implementation. In addition, the avoidance distance, avoidance time or final vehicle velocity can be readily calculated by the efficient solution of the nondimensional equation. Therefore, the proposed feedback controller is more attractive than the controller proposed in [10]. The present study is not limited to implementation. Since the problem is formulated precisely and the optimality of the solution is guaranteed, our results serve as a reference for the obstacle avoidance study.

The implementation of the obstacle avoidance controller requires an effective tire force distributor. A tire force distributor determines the reference longitudinal and lateral tire forces, according to the longitudinal and lateral vehicle forces and yaw moment demands. The reference values of longitudinal and lateral vehicle forces are determined by the obstacle avoidance controller. The minimax tire force distributor that minimizes the maximum tire workload [81] is the most effective to avoid saturation of tire forces on the assumption of the uniform friction coefficient of all tires. The tire workload is defined as the ratio between the resultant tire force and vertical tire load. For the minimax optimization of the tire force distribution to four tires, it turns out that the vehicle performance envelopes for both four-wheel steering (4WS) and four-wheel independent steering (4WIS) are almost identical when the yaw moment demand is zero. In this case, it follows that the shape of these envelopes for various workloads resembles concentric circles and that a lane change without yaw motion is considered to be the best strategy. From a practical viewpoint, 4WS is much preferable over 4WIS. Therefore, 4WS configuration with the minimax tire force distributor can be used to realize the avoidance maneuver.

The organization of this chapter is as follows. Section 2.2 describes the obstacle avoidance maneuvers. Section 2.3 provides the mathematical formulation of the obstacle avoidance maneuvers. In Section 2.4, the nondimensionalization technique and collision avoidance index are introduced. The design of the state feedback controller for the optimal trajectory is presented in Section 2.5. Numerical examples are presented in Section 2.6. Section 2.7 concludes the findings of this study.

2.2 Obstacle Avoidance Maneuvers

It is known that an in-lane obstacle can be avoided by braking, steering, and steering with braking maneuvers. In this section, these maneuvers are described.

2.2.1 Automatic Obstacle Avoidance Scenario

In this chapter, braking, steering, and steering with braking maneuvers are considered as emergency obstacle avoidance maneuvers. These maneuvers are to be performed when an obstacle suddenly appears in the traveling lane. The minimum longitudinal distance and time required to avoid the obstacle are derived for each of these cases.

2.2.2 Braking Maneuver

In this chapter, the braking maneuver is defined as the obstacle avoidance method that applies the maximum braking force on the vehicle so that a minimum stopping distance is achieved. Assuming the tire-road friction condition for all the wheels is the same, the braking forces are applied equally on the left and right tires. Therefore, the vehicle moves in a straight line. Fig. 2.1 shows the schematic diagram for obstacle avoidance using the braking maneuver.

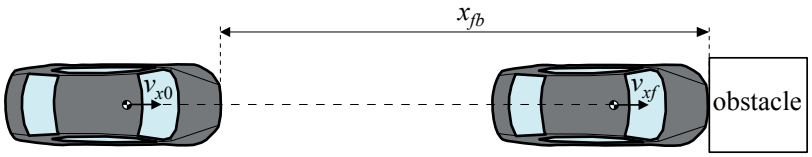

Figure 2.1: Obstacle avoidance using the braking maneuver.

2.2.3 Lane Change Maneuver

The steering and steering with braking maneuvers can be generalized into the lane change maneuver. For the lane change maneuver as depicted in Fig. 2.2, a vehicle moving with initial longitudinal and lateral velocities, denoted as v_{x0} and v_{y0}, respectively, encounters an obstacle in the current lane, and the vehicle automatically performs a lane change maneuver such that the longitudinal distance required for the complete lane change is minimized. At the same time, the trajectory generation is subjected to initial and final state conditions of the vehicle as well as the road surface conditions. In this problem, the lateral center point of the obstacle is assumed to be coinciding with the current lane center line. The final lateral distance depends on the width of the obstacle taking into consideration the safety margin or width of the lane. At the final time, the lateral velocity of the vehicle must be zero, indicating that there is no lateral motion at this instant. Zero final lateral velocity is desirable because, at the final time, the human driver should take over the control of the vehicle.

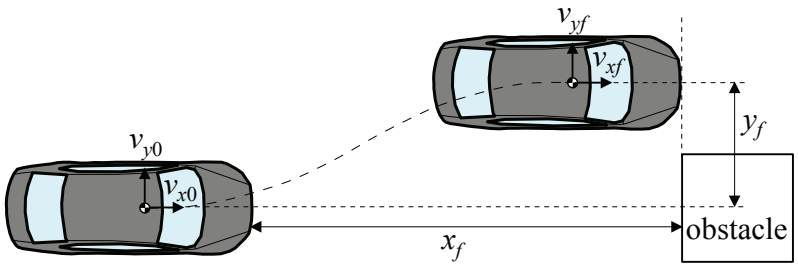

Figure 2.2: Obstacle avoidance using the lane change maneuver.

2.3 Formulation of Optimal Control Problems

This section formulates the obstacle avoidance problems as optimal control problems. For the braking, steering, and steering with braking maneuvers, the shortest longitudinal avoidance distances are assumed to be achieved by fully using the maximum available vehicle force $F_{\max}$.

2.3.1 Braking Maneuver

To bring a vehicle to a complete stop with the minimum longitudinal distance, maximum braking force should be applied. The minimum longitudinal distance required to avoid the obstacle by full braking is given by

$$x_{fb} = \frac{m_t v_{x0}^2}{2F_{\max}} \tag{2.1}$$

where m_t is the mass of the vehicle, v_{x0} is the initial longitudinal velocity of the vehicle, and $F_{\max}$ is the maximum available vehicle force that is given by the product of tire-road friction coefficient and vehicle weight. For this maneuver, we assume $F_{\max}$ is positive corresponding to the constant deceleration. Note that v_{x0} is positive for a vehicle moving in the forward direction. The braking time t_{fb} is defined as the time required to bring the vehicle to a stop by applying the full braking force:

$$t_{fb} = \frac{m_t v_{x0}}{F_{\max}} \tag{2.2}$$

The avoidance distance (2.1) and braking time (2.2) are the same as given in [41].

2.3.2 Steering Maneuver

The steering maneuver is defined as the obstacle avoidance method in which the maximum available vehicle force $F_{\max}$ is fully used to move the vehicle by a given lateral distance y_f. Obstacle avoidance with steering at a constant vehicle longitudinal velocity takes the form of bang-bang control. The lateral acceleration u_s required for the lane change maneuver

can be written as

$$u_s(t) = \begin{cases} \dfrac{F_{\max}}{m_t}, & t_0 \leq t < t_s \\ -\dfrac{F_{\max}}{m_t}, & t_s < t \leq t_{fs} \end{cases} \tag{2.3}$$

where t_s is the switching time and t_{fs} is the final time. A detailed discussion on the steering maneuver can be found in [42]. We will refer to the positive lateral acceleration phase as Phase A and the negative acceleration phase as Phase B.

The lateral velocity v_{yA} for Phase A is obtained by integrating $u_s(t) = F_{\max}/m_t$ with respect to time, and then, applying the initial lateral velocity condition $v_{yA}(0) = v_{y0}$:

$$v_{yA}(t) = v_{y0} + \frac{F_{\max}}{m_t} t \tag{2.4}$$

In Phase A, the lateral distance is determined by integrating (2.4) with respect to time, and then, applying the initial lateral distance condition $y_A(0) = 0$:

$$y_A(t) = v_{y0} t + \frac{F_{\max}}{2m_t} t^2 \tag{2.5}$$

The lateral velocity v_{yB} for Phase B is obtained by integrating $u_s(t) = -F_{\max}/m_t$ with respect to time, and then, applying the final lateral velocity condition $v_{yB}(t_{fs}) = 0$:

$$v_{yB}(t) = \frac{F_{\max}}{m_t}(t_{fs} - t) \tag{2.6}$$

The lateral distance for Phase B is determined by integrating (2.6), and then, applying the final lateral distance condition $y_B(t_{fs}) = y_f$:

$$y_B(t) = y_f - \frac{F_{\max}}{2m_t}(t - t_{fs})^2 \tag{2.7}$$

Both the lateral velocity and the lateral distance are continuous at t_s. Simultaneously solving $v_{yA}(t_s) = v_{yB}(t_s)$ and $y_A(t_s) = y_B(t_s)$ with respect to t_s and t_{fs} yields:

$$t_s = \frac{-2m_t v_{y0} + \sqrt{2}\sqrt{m_t^2 v_{y0}^2 + 2m_t y_f F_{\max}}}{2F_{\max}} \tag{2.8}$$

$$t_{fs} = \frac{-m_t v_{y0} + \sqrt{2}\sqrt{m_t^2 v_{y0}^2 + 2m_t y_f F_{\max}}}{F_{\max}} \tag{2.9}$$

The minimum longitudinal avoidance distance for the steering maneuver is simply the product of t_{fs} and v_{x0}:

$$x_{fs} = \frac{-m_t v_{y0} + \sqrt{2}\sqrt{m_t^2 v_{y0}^2 + 2m_t y_f F_{\max}}}{F_{\max}} v_{x0} \tag{2.10}$$

2.3.3 Steering with Braking Maneuver

The steering with braking maneuver is the obstacle avoidance method that uses an optimal combination of steering and braking to minimize the longitudinal avoidance distance. Pontryagin's minimum principle, which gives the necessary conditions for optimality, is used to derive the optimal control law. The general form of the dynamic system model can be described by the differential equation

$$\dot{\boldsymbol{s}}(t) = \boldsymbol{f}(\boldsymbol{s}(t), u(t), t), \quad \boldsymbol{s}(t_0) = \boldsymbol{s_0} \tag{2.11}$$

where $\boldsymbol{s}(t)$, a n-dimensional state vector, is determined by the control input $u(t)$. Note that the initial time t_0 is assumed to be zero.

The dynamics of the point mass for the longitudinal and lateral directions are expressed as

$$m_t \ddot{x}\,(t) = X_t\,(t) \tag{2.12}$$

$$m_t \ddot{y}\,(t) = Y_t\,(t) \tag{2.13}$$

where X_t is the total longitudinal force and Y_t is the total lateral force. At any instant, X_t and Y_t that can be applied to a vehicle are limited by the vehicle friction circle. The radius of the friction circle is equal to $F_{\max}$. The friction circle can be realized using optimal tire force distribution methods such as the minimization of the maximum tire workload [81] and the minimization of the equalized tire force usage [87].

The accelerations in (2.12) and (2.13) can be expressed as

$$\ddot{x}\,(t) = -\frac{F_{\max}}{m_t}\sin\varphi\,(t) \tag{2.14}$$

$$\ddot{y}\,(t) = -\frac{F_{\max}}{m_t}\cos\varphi\,(t) \tag{2.15}$$

where φ is the force direction angle. The force direction angle is defined as the angle between the vector of $F_{\max}$ and the negative direction of the pure lateral force. It should be noted that for the derivation of the optimal control, $F_{\max}$ is assumed to be constant. The control input u in this problem is

$$u(t) = \varphi(t) \tag{2.16}$$

The states of the dynamical system are

$$\boldsymbol{s}(t) = \begin{bmatrix} s_1(t) & s_2(t) & s_3(t) & s_4(t) \end{bmatrix}^T = \begin{bmatrix} x(t) & \dot{x}(t) & y(t) & \dot{y}(t) \end{bmatrix}^T \tag{2.17}$$

Now, the system differential equation as given in (2.11) can be written as

$$\boldsymbol{f}(\boldsymbol{s}(t), \varphi(t), t) = \begin{bmatrix} s_2(t) & -\frac{F_{\max}}{m_t}\sin\varphi(t) & s_4(t) & -\frac{F_{\max}}{m_t}\cos\varphi(t) \end{bmatrix}^T \tag{2.18}$$

The initial and final conditions on the states (2.17) are given as

$$\boldsymbol{s}(t_0) = \begin{bmatrix} 0 & v_{x0} & 0 & v_{y0} \end{bmatrix}^T \tag{2.19}$$

$$\boldsymbol{s}(t_f) = \begin{bmatrix} x_{fc} & v_{xf} & y_f & 0 \end{bmatrix}^T \tag{2.20}$$

where x_{fc} is the longitudinal distance at the end of the maneuver and this distance is to be minimized. v_{xf} is the final longitudinal velocity, and it is assumed to be free.

The state equality constraint can be imposed at any specific time:

$$\boldsymbol{\psi}(\boldsymbol{s}(t), t) = \begin{bmatrix} y(t) - y_f & \dot{y}(t) \end{bmatrix}^T \tag{2.21}$$

At the final time t_f, the state constraint becomes

$$\boldsymbol{\psi}(\boldsymbol{s}(t_f), t_f) = \mathbf{0} \tag{2.22}$$

The performance function J for the optimal control problem can be defined as

$$J = \phi(\boldsymbol{s}(t_f), t_f) + \int_{t_0}^{t_f} f_0(\boldsymbol{s}(t), \varphi(t), t)\, dt \tag{2.23}$$

where the first term is the final state penalty, and the second term is the running performance function. For the obstacle avoidance problem, the aim is to minimize the longitudinal distance required to complete the lane change. The performance function is written as

$$J = x(t_f) = x_{fc} \tag{2.24}$$

Comparing (2.24) with (2.23), we have the following:

$$\phi(\boldsymbol{s}(t_f), t_f) = x(t_f) = x_{fc} \tag{2.25}$$

$$f_0(\boldsymbol{s}(t), \varphi(t), t) = 0 \tag{2.26}$$

Therefore, the relation with the performance function takes the linear Mayer form [117].

Pontryagin's minimum principle states that the Hamiltonian function must be minimized over all admissible control u [66]. This Hamiltonian function is expressed as

$$H(\boldsymbol{s}(t), \varphi(t), \boldsymbol{\lambda}(t), t) = f_0(\boldsymbol{s}(t), \varphi(t), t) + \boldsymbol{\lambda}^T(t)\boldsymbol{f}(\boldsymbol{s}(t), \varphi(t), t) \tag{2.27}$$

where $\boldsymbol{\lambda}(t)$ is known as the adjoint vector with n dimensions

$$\boldsymbol{\lambda}(t) = \begin{bmatrix} \lambda_x(t) & \lambda_u(t) & \lambda_y(t) & \lambda_v(t) \end{bmatrix}^T \tag{2.28}$$

Substituting (2.18) and (2.28) into (2.27), the Hamiltonian function becomes

$$H(\boldsymbol{s}(t), \varphi(t), \boldsymbol{\lambda}(t), t) = \lambda_x(t)\dot{x}(t) - \lambda_u(t)\frac{F_{\max}}{m_t}\sin\varphi(t) + \lambda_y(t)\dot{y}(t) - \lambda_v(t)\frac{F_{\max}}{m_t}\cos\varphi(t) \tag{2.29}$$

The following differential equation, known as the adjoint equation, is satisfied by the adjoint vector:

$$\dot{\boldsymbol{\lambda}}(t) = -H_{\boldsymbol{s}}^T(\boldsymbol{s}(t), \varphi(t), \boldsymbol{\lambda}(t), t) \tag{2.30}$$

where $H_{\boldsymbol{s}}$ denotes the partial derivative of H with respect to $\boldsymbol{s}$. The optimal control equation is given as

$$H_\varphi(\boldsymbol{s}(t), \varphi(t), \boldsymbol{\lambda}(t), t) = 0 \tag{2.31}$$

where H_φ denotes the partial derivative of H with respect to φ.

The necessary conditions for the control φ and for the corresponding trajectory to be optimal solutions are that there exist $\boldsymbol{\lambda}(t)$ that satisfies (2.30) and (2.31). Taking the partial derivative of the Hamiltonian in (2.29) with respect to the state vector $\boldsymbol{s}$, we have the following:

$$H_{\boldsymbol{s}}^T(\boldsymbol{s}(t), \varphi(t), \boldsymbol{\lambda}(t), t) = \begin{bmatrix} 0 & \lambda_x(t) & 0 & \lambda_y(t) \end{bmatrix}^T \tag{2.32}$$

Now, the adjoint equation (2.30) can be written as

$$\dot{\boldsymbol{\lambda}}(t) = \begin{bmatrix} \dot{\lambda}_x(t) & \dot{\lambda}_u(t) & \dot{\lambda}_y(t) & \dot{\lambda}_v(t) \end{bmatrix}^T = \begin{bmatrix} 0 & -\lambda_x(t) & 0 & -\lambda_y(t) \end{bmatrix}^T \tag{2.33}$$

The partial derivative of the Hamiltonian with respect to the control input φ gives the following form:

$$H_\varphi = H_\varphi(\boldsymbol{s}(t), \varphi(t), \boldsymbol{\lambda}(t), t) = -\lambda_u(t)\frac{F_{\max}}{m_t}\cos\varphi(t) + \lambda_v(t)\frac{F_{\max}}{m_t}\sin\varphi(t) \tag{2.34}$$

It is convenient to define an augmented performance function

$$\Phi(\boldsymbol{s}(t), t) = \phi(\boldsymbol{s}(t), t) + \boldsymbol{\nu}^T\boldsymbol{\psi}(\boldsymbol{s}(t), t) \tag{2.35}$$

with the terminal Lagrange multiplier given by

$$\boldsymbol{\nu} = \begin{bmatrix} \nu_y & \nu_v \end{bmatrix}^T \tag{2.36}$$

In addition, the following condition must be satisfied:

$$\boldsymbol{\lambda}(t_f) = \Phi_{\boldsymbol{s}}^T(\boldsymbol{s}(t), t)\big|_{t=t_f} \tag{2.37}$$

where $\Phi_{\boldsymbol{s}}$ is the partial derivative of Φ with respect to $\boldsymbol{s}$. Because in this problem t_f is free, another condition must be satisfied:

$$H(\boldsymbol{s}(t_f), \varphi(t_f), \boldsymbol{\lambda}(t_f), t_f) = -\Phi_t(\boldsymbol{s}(t), t)|_{t=t_f} \tag{2.38}$$

where Φ_t is the partial derivative of Φ with respect to t. The conditions (2.37) and (2.38) are called transversality conditions [66].

The partial derivative of Φ with respect to $\boldsymbol{s}$ is obtained as

$$\Phi_{\boldsymbol{s}}^T(\boldsymbol{s}(t), t)|_{t=t_f} = \begin{bmatrix} 1 & 0 & \nu_y & \nu_v \end{bmatrix}^T \tag{2.39}$$

and the partial derivative of Φ with respect to t is expressed as

$$\Phi_t(\boldsymbol{s}(t), t)|_{t=t_f} = 0 \tag{2.40}$$

The transversality condition in (2.37) can then be written as

$$\boldsymbol{\lambda}(t_f) = \begin{bmatrix} 1 & 0 & \nu_y & \nu_v \end{bmatrix}^T \tag{2.41}$$

and the transversality condition as in (2.38) becomes

$$\lambda_x(t_f)\dot{x}(t_f) - \lambda_u(t_f)\frac{F_{\max}}{m_t}\sin\varphi(t_f) + \lambda_y(t_f)\dot{y}(t_f) - \lambda_v(t_f)\frac{F_{\max}}{m_t}\cos\varphi(t_f) = 0 \tag{2.42}$$

Integrating the optimality equation (2.33) and applying the final conditions (2.41), we have

$$\boldsymbol{\lambda}(t) = \begin{bmatrix} \lambda_x(t) \\ \lambda_u(t) \\ \lambda_y(t) \\ \lambda_v(t) \end{bmatrix} = \begin{bmatrix} 1 \\ -t + t_f \\ \nu_y \\ -\nu_y t + \nu_y t_f + \nu_v \end{bmatrix} \tag{2.43}$$

By substituting (2.43) into (2.34), the optimal control can be obtained as

$$\tan\varphi(t) = \frac{\lambda_u(t)}{\lambda_v(t)} = \frac{-t + t_f}{-\nu_y t + \nu_y t_f + \nu_v} \tag{2.44}$$

This form of the control law can be referred to as the bilinear tangent law [22]. A control triangle diagram showing the relation is illustrated in Fig. 2.3.

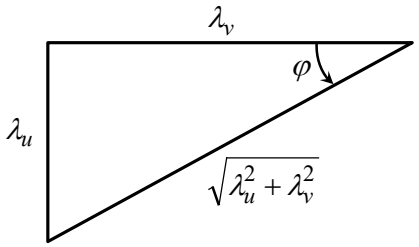

Figure 2.3: Control triangle diagram illustrating the bilinear tangent law.

From the control triangle, $\sin\varphi(t)$ and $\cos\varphi(t)$ are

$$\sin\varphi(t) = \frac{\lambda_u(t)}{\sqrt{\lambda_u^2(t) + \lambda_v^2(t)}} \tag{2.45}$$

$$\cos\varphi(t) = \frac{\lambda_v(t)}{\sqrt{\lambda_u^2(t) + \lambda_v^2(t)}} \tag{2.46}$$

The optimal longitudinal acceleration u_x and optimal lateral acceleration u_y that are functions of φ are expressed as

$$u_x(t) = -\frac{F_{\max}}{m_t}\sin\varphi(t) = -\frac{F_{\max}}{m_t}\frac{-t + t_f}{\sqrt{(-t + t_f)^2 + (-\nu_y t + \nu_y t_f + \nu_v)^2}} \tag{2.47}$$

$$u_y(t) = -\frac{F_{\max}}{m_t}\cos\varphi(t) = -\frac{F_{\max}}{m_t}\frac{-\nu_y t + \nu_y t_f + \nu_v}{\sqrt{(-t+t_f)^2 + (-\nu_y t + \nu_y t_f + \nu_v)^2}} \tag{2.48}$$

It is worth noting that the expressions of the optimal control (2.47) and (2.48) are the same as those reported in [42]. In [42], the authors considered an inequality constraint such that the vector sum of the total longitudinal force and the total lateral force must not exceed $F_{\max}$. In the present study, we assume that the resultant of the vehicle forces is equal to $F_{\max}$. Despite the difference in the constraint, the optimal control solutions of these two studies are identical. This also proves the correctness of the equality constraint considered in this study.

At $t = t_f$, $u_x = 0$ and $u_y = -F_{\max}/m_t$, indicating that at this instant, there is no braking, and all the available force is used for steering.

From (2.42), the final vehicle longitudinal velocity is expressed as

$$\dot{x}(t_f) = \frac{F_{\max}}{m_t}\nu_v = v_{xf} \tag{2.49}$$

in which ν_v must be positive, recognizing that vehicle should not be moving in the reverse direction ($v_{xf} < 0$).

For $\varphi(t)$ to be a minimum, the Weierstrass condition

$$H(\boldsymbol{s}(t), \varphi_*(t), \boldsymbol{\lambda}(t), t) - H(\boldsymbol{s}(t), \varphi(t), \boldsymbol{\lambda}(t), t) > 0 \tag{2.50}$$

for all $\varphi_* \neq \varphi$, must hold over the interval $[t_0, t_f]$ [56]. In (2.50), $\varphi_*(t)$ is an admissible comparison control. In addition, the Legendre-Clebsch condition, which is a necessary condition for the local minimum, must be obeyed over the interval $[t_0, t_f]$ [56].

$$H_{\varphi\varphi} \geq 0 \tag{2.51}$$

Applying the Weierstrass condition gives

$$\lambda_u(t)\frac{F_{\max}}{m_t}\left(\sin\varphi(t) - \sin\varphi_*(t)\right) + \lambda_v(t)\frac{F_{\max}}{m_t}\left(\cos\varphi(t) - \cos\varphi_*(t)\right) > 0 \tag{2.52}$$

Because $F_{\max}/m_t \neq 0$, (2.52) becomes

$$\lambda_u(t)\left(\sin\varphi(t) - \sin\varphi_*(t)\right) + \lambda_v(t)\left(\cos\varphi(t) - \cos\varphi_*(t)\right) > 0 \tag{2.53}$$

Eliminating $\lambda_v(t)$ by using $\lambda_v(t) = \lambda_u(t)/\tan\varphi(t)$ from the control law (2.44) and performing algebraic manipulations, (2.53) takes the form

$$\frac{\lambda_u(t)\left(1 - \cos(\varphi(t) - \varphi_*(t))\right)}{\sin\varphi(t)} > 0 \tag{2.54}$$

For $t < t_f$, $\lambda_u(t) > 0$ and $\sin\varphi(t) > 0$. Because $\varphi(t) \neq \varphi_*(t)$, $-1 \leq \cos(\varphi(t) - \varphi_*(t)) < 1$. Therefore, the Weierstrass condition holds except at $t = t_f$.

The second partial derivative of the Hamiltonian function with respect to φ is

$$H_{\varphi\varphi} = \lambda_u(t)\frac{F_{\max}}{m_t}\sin\varphi(t) + \lambda_v(t)\frac{F_{\max}}{m_t}\cos\varphi(t) \tag{2.55}$$

Substituting (2.45) and (2.46) into (2.55) and simplifying this by removing the radical $\sqrt{\lambda_u^2(t)+\lambda_v^2(t)}$ from the denominator leads to

$$H_{\varphi\varphi} = \frac{F_{\max}}{m_t}\sqrt{\lambda_u^2(t)+\lambda_v^2(t)} \tag{2.56}$$

which is positive. Hence, the Legendre-Clebsch condition as in (2.51) is obeyed. Because both of these conditions hold, the control solution is a minimum.

Using (2.18), (2.47), and (2.48), (2.11) is rewritten as

$$\begin{bmatrix}\dot{s}_1(t)\\ \dot{s}_2(t)\\ \dot{s}_3(t)\\ \dot{s}_4(t)\end{bmatrix} = \begin{bmatrix} s_2 \\ -\dfrac{F_{\max}}{m_t}\dfrac{-t+t_f}{\sqrt{(-t+t_f)^2+(-\nu_y t+\nu_y t_f+\nu_v)^2}} \\ s_4 \\ -\dfrac{F_{\max}}{m_t}\dfrac{-\nu_y t+\nu_y t_f+\nu_v}{\sqrt{(-t+t_f)^2+(-\nu_y t+\nu_y t_f+\nu_v)^2}}\end{bmatrix} \tag{2.57}$$

Integrating $\dot{s}_2(t)$ with respect to time and using the initial longitudinal velocity condition $\dot{x}(0) = v_{x0}$ and the final longitudinal velocity condition (2.49), we get

$$\frac{m_t v_{x0}}{F_{\max}} - \frac{\nu_y\nu_v W}{\left(1+\nu_y^2\right)^{3/2}} - \frac{\nu_y^2\nu_v + \sqrt{(\nu_y t_f+\nu_v)^2+t_f^2}}{1+\nu_y^2} = 0 \tag{2.58}$$

where

$$W = \ln\left(\frac{\sqrt{1+\nu_y^2}\sqrt{(\nu_y t_f+\nu_v)^2+t_f^2} - \nu_y\nu_v - \left(1+\nu_y^2\right)t_f}{\nu_v\sqrt{1+\nu_y^2} - \nu_y\nu_v}\right) \tag{2.59}$$

Similarly, integrating $\dot{s}_4(t)$ and applying the initial lateral velocity condition $\dot{y}(0) = v_{y0}$ and the final lateral velocity condition $\dot{y}(t_f) = 0$, we obtain

$$\frac{m_t v_{y0}}{F_{\max}} + \frac{\nu_v W}{\left(1+\nu_y^2\right)^{3/2}} + \frac{\nu_y\nu_v - \nu_y\sqrt{(\nu_y t_f+\nu_v)^2+t_f^2}}{1+\nu_y^2} = 0 \tag{2.60}$$

Next, integrating $\dot{s}_4(t)$ and using the initial lateral velocity condition $\dot{y}(0) = v_{y0}$, and then, integrating the resulting equation and applying the initial lateral position condition $y(0) = 0$ and the final lateral position condition $y(t_f) = y_f$, we get

$$\begin{aligned}&\frac{m_t v_{y0} t_f}{F_{\max}} - \frac{m_t y_f}{F_{\max}} - \frac{3\nu_y\nu_v^2 W}{2\left(1+\nu_y^2\right)^{5/2}} - \frac{\left(\nu_y^2-2\right)\nu_v^2}{2\left(1+\nu_y^2\right)^2} \\ &- \frac{\left[\left(1+\nu_y^2\right)\nu_y t_f - \left(\nu_y^2-2\right)\nu_v\right]\sqrt{(\nu_y t_f+\nu_v)^2+t_f^2}}{2\left(1+\nu_y^2\right)^2} = 0\end{aligned} \tag{2.61}$$

The minimum distance required to avoid the obstacle is obtained by integrating $\dot{s}_2(t)$ and using the initial longitudinal velocity condition $\dot{x}(0) = v_{x0}$, followed by, integrating the resulting equation and applying the initial longitudinal position condition $x(0) = 0$ and the final longitudinal position condition $x(t_f) = x_{fc}$

$$x_{fc} = \frac{F_{\max}}{m_t}\left(- \frac{\left[\left(1+\nu_y^2\right)t_f - 3\nu_y\nu_v\right]\sqrt{\left(\nu_y t_f + \nu_v\right)^2 + t_f^2}}{2\left(1+\nu_y^2\right)^2} + \frac{m_t v_{x0} t_f}{F_{\max}} - \frac{3\nu_v^2 W}{2\left(1+\nu_y^2\right)^{5/2}} - \frac{3\nu_y\nu_v^2}{2\left(1+\nu_y^2\right)^2} + \frac{\nu_v^2 W}{\left(1+\nu_y^2\right)^{3/2}}\right) \tag{2.62}$$

To evaluate the optimal control or the respective optimal trajectory, the control parameters (ν_y, ν_v, and t_f) need to be determined first. These values are the solutions of the simultaneous equations (2.58), (2.60), and (2.61). These equations are highly nonlinear. Thus, it is not likely that closed-form solutions to this problem can be obtained. Local numerical methods such as the Newton-Raphson method or Broyden's method can be used for solving these equations if a good initial guess of the control parameters is available. Among the three control parameters, only t_f is a physical variable, for which a good initial guess can be found intuitively.

The homotopy method, a global numerical method, can be utilized to obtain the solutions of these highly nonlinear equations [88]. The advantages of the homotopy method over the Newton-Raphson method are that it does not require an accurate initial guess, and convergence is possible if the step size is sufficiently small. However, the homotopy method may not be computationally efficient because three highly nonlinear equations are to be solved simultaneously.

Alternatively, this TPBVP can be solved using the indirect shooting method. The success of this straightforward method depends on the initial approximation quality of $\boldsymbol{\lambda}(t_0)$, $\boldsymbol{\nu}$, and t_f. Among other similar methods, the shooting method is very sensitive to small changes in the boundary conditions [22].

Therefore, it is preferable to reduce the problem of solving these equations simultaneously to a single-variable root finding problem with t_f as the variable to be solved because we can expect a good initial guess for t_f. In the next sections, we prove that this is possible. Two different cases will be considered. In the first case, a feedforward control where v_{y0} is zero is derived. A state feedback controller is then developed.

2.4 Nondimensionalization and Collision Avoidance Index

This section first introduces the nondimensionalization method and then, develops a dimensionless collision avoidance index.

Table 2.1: Dimensionless Variables

Original variables	Dimension	Dimensionless variable
$(F_{\max}, m_t, v_{x0}, y_f)$	$[\mathrm{MLT}^{-2}]^{-\frac{1}{2}}[\mathrm{M}]^{\frac{1}{2}}[\mathrm{LT}^{-1}]^1[\mathrm{L}]^{-\frac{1}{2}}$	$V_{x0} = \sqrt{\frac{m_t}{F_{\max} y_f}} v_{x0}$
$(F_{\max}, m_t, v_{y0}, y_f)$	$[\mathrm{MLT}^{-2}]^{-\frac{1}{2}}[\mathrm{M}]^{\frac{1}{2}}[\mathrm{LT}^{-1}]^1[\mathrm{L}]^{-\frac{1}{2}}$	$V_{y0} = \sqrt{\frac{m_t}{F_{\max} y_f}} v_{y0}$
(ν_y)	–	$N_y = \nu_y$
(ν_v, t_f)	$[\mathrm{T}]^1[\mathrm{T}]^{-1}$	$N_v = \frac{\nu_v}{t_f}$
$(F_{\max}, m_t, y_f, t_f)$	$[\mathrm{MLT}^{-2}]^{\frac{1}{2}}[\mathrm{M}]^{-\frac{1}{2}}[\mathrm{L}]^{-\frac{1}{2}}[\mathrm{T}]^1$	$\tau_f = \sqrt{\frac{F_{\max}}{m_t y_f}} t_f$

2.4.1 Nondimensionalization

Nondimensionalization removes the units in the equations by substituting appropriate dimensionless variables to represent the system input and output variables. Reduction in the number of variables through nondimensionalization facilitates easy handling of equations [121].

The first step to nondimensionalizing a set of equations is to identify the input and output variables. In these equations, the input variables are m_t, $F_{\max}$, v_{x0}, v_{y0}, and y_f, and the output variables are ν_y, ν_v, and t_f. From Buckingham's π theorem, the equations with eight original variables and three physical dimensions, mass M, length L, and time T, can be expressed by five dimensionless variables. These dimensionless variables are expressed as the combination of the original variables as shown in Table 2.1. The input variables are the dimensionless initial longitudinal velocity V_{x0} and the dimensionless initial lateral velocity V_{y0}. The output variables are the dimensionless control parameters N_y and N_v as well as the dimensionless final time τ_f.

Using the definitions for the dimensionless variables provided in Table 2.1, (2.58), (2.60), and (2.61) can be expressed in dimensionless form as given by (2.63) to (2.65), respectively:

$$\frac{V_{x0}}{\tau_f} - \frac{N_y^2 N_v}{1+N_y^2} - \frac{N_y N_v \Omega}{(1+N_y^2)^{3/2}} - \frac{\sqrt{1+(N_y+N_v)^2}}{1+N_y^2} = 0 \tag{2.63}$$

$$\frac{V_{y0}}{\tau_f} + \frac{N_y N_v}{1+N_y^2} + \frac{N_v \Omega}{(1+N_y^2)^{3/2}} - \frac{N_y \sqrt{1+(N_y+N_v)^2}}{1+N_y^2} = 0 \tag{2.64}$$

$$\begin{aligned} &- \frac{\sqrt{1+N_y^2}\sqrt{1+(N_y+N_v)^2}\left[N_y^3 + N_y - N_v(N_y^2-2)\right]}{2(1+N_y^2)^{5/2}} \\ &+ \frac{V_{y0}\tau_f - 1}{\tau_f^2} - \frac{3N_y N_v^2 \Omega}{2(1+N_y^2)^{5/2}} - \frac{\sqrt{1+N_y^2} N_v^2 (N_y^2-2)}{2(1+N_y^2)^{5/2}} = 0 \end{aligned} \tag{2.65}$$

where

$$\Omega = \ln\left(\frac{\Omega_n}{N_v}\right) \tag{2.66}$$

with

$$\Omega_n = \left[\sqrt{1+N_y^2}\sqrt{1+(N_y+N_v)^2} - N_y\left(N_y+N_v\right) - 1\right]\left(N_y + \sqrt{1+N_y^2}\right)$$

By setting $v_{y0} = 0$ and hence $V_{y0} = 0$, and performing algebraic manipulations on (2.63) to (2.65), we obtain

$$N_v = -N_y - \frac{\sqrt{V_{x0}^2 - \tau_f^2}}{\tau_f} \tag{2.67}$$

$$N_y = -\frac{V_{x0}\tau_f + 4\tau_f\sqrt{V_{x0}^2 - \tau_f^2}}{4(\tau_f^2 - 1)} - \frac{\sqrt{V_{x0}^2(\tau_f^2+16) - 8V_{x0}(\tau_f^2-2)\sqrt{V_{x0}^2-\tau_f^2} - 16}}{4(\tau_f^2-1)} \tag{2.68}$$

(2.65) can be rewritten as $f_3(N_y, N_v, \tau_f) = 0$. Substituting (2.68) into (2.67), we obtained $N_v(N_y(\tau_f), \tau_f)$. Now, substituting this and (2.68) into $f_3(N_y, N_v, \tau_f) = 0$ yields $f_3(N_y(\tau_f), N_v(N_y(\tau_f), \tau_f), \tau_f) = 0$. The resulting equation is equivalent to the simultaneous equations (2.63) to (2.65). Note that the only unknown left in $f_3(N_y(\tau_f), N_v(N_y(\tau_f), \tau_f), \tau_f) = 0$ is τ_f, and this implicit equation can be solved using one of root finding methods that will be explained in the next section.

2.4.2 Dimensionless Final Time

Assuming that $t_0 = 0$, the final time corresponds to the maneuver time. From (2.9), when v_{y0} is set to zero, the final time for the steering maneuver is reduced to

$$t_{fs} = 2\sqrt{\frac{m_t y_f}{F_{\max}}} \tag{2.69}$$

Using the definition $\tau_{fs} = \sqrt{F_{\max}/(m_t y_f)}t_{fs}$, the dimensionless final time for steering maneuver $\tau_{fs} = 2$. For braking, the dimensionless final time τ_{fb} turns out to be equal to V_{x0}.

$$\tau_{fb} = \sqrt{\frac{F_{\max}}{m_t y_f}}t_{fb} = V_{x0} \tag{2.70}$$

Fig. 2.4 shows the dimensionless final time for braking, steering, and steering with braking maneuvers. Among these maneuvers, the steering maneuver requires the shortest time, whereas the braking maneuver requires the longest time. The final time for the steering with braking maneuver is between the times for the steering and braking maneuvers. As V_{x0} increases, the dimensionless time for the steering with braking maneuver reduces

and is bounded by that for the steering maneuver. This figure clarifies the bounds on the final time for the steering with braking maneuver.

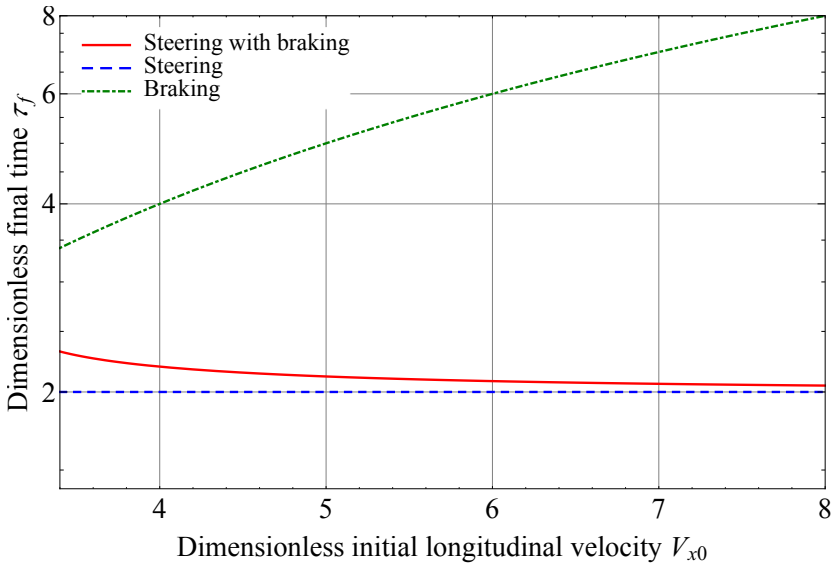

Figure 2.4: Dimensionless final time as a function of dimensionless initial longitudinal velocity.

2.4.3 Dimensionless Collision Avoidance Distance

For collision warning and automatic avoidance maneuver timing, it is essential to evaluate the minimum longitudinal distance required to avoid the obstacle. For the given conditions, by comparing the minimum distances for the braking, steering, and steering with braking maneuvers, the decision on the most effective avoidance maneuver should be made. The conventional plots show the relation between the minimum avoidance distance and the longitudinal velocity assuming the conditional parameters are fixed [103, 42, 52]. Yoshida *et al.* [130] presented the effect of the longitudinal vehicle velocity and the friction coefficient on the avoidance distance by using a three-dimensional plot. If the final lateral distance is included as the input variable, the comparison would require a four-dimensional plot, which is not practical for choosing the optimal maneuver.

In this study, a unified nondimensionalized collision avoidance index is presented. This index represents the dimensionless avoidance distance called the aspect ratio as a function of V_{x0} that is a combination of the initial longitudinal velocity, final lateral distance, vehicle mass, and maximum available vehicle force. The aspect ratio is the ratio of the longitudinal avoidance distance to the final lateral distance. The aspect ratio for the braking maneuver AR_b is

$$AR_b = \frac{x_{fb}}{y_f} = \frac{1}{2}V_{x0}^2 \tag{2.71}$$

For the steering maneuver, the aspect ratio AR_s takes the following form:

$$AR_s = \frac{x_{fs}}{y_f} = 2V_{x0} \tag{2.72}$$

The final longitudinal distance for the steering with braking maneuver can be translated to the aspect ratio AR_c:

$$\begin{aligned} AR_c &= \frac{x_{fc}}{y_f} \\ &= V_{x0}\tau_f + \frac{3N_yN_vV_{x0}\tau_f}{2(1+N_y^2)^2} - \frac{3N_v^2\tau_f^2\Omega}{2(1+N_y^2)^{5/2}} - \frac{V_{x0}\tau_f}{2(1+N_y^2)} - \frac{3N_yN_v^2\tau_f^2}{2(1+N_y^2)^2} + \frac{N_v^2\tau_f^2\Omega}{(1+N_y^2)^{3/2}} \end{aligned} \tag{2.73}$$

Once $f_3\left(N_y(\tau_f), N_v\left(N_y(\tau_f), \tau_f\right), \tau_f\right) = 0$ is solved for τ_f, AR_c can be readily evaluated.

An analytical approach to find the minimum distance steering with braking maneuver was studied by Shiller and Sundar [106]. In their study, the longitudinal and lateral motions of the point mass were treated separately, and these problems were only coupled by the boundary conditions. The first problem deals with minimizing the longitudinal distance on the basis of braking maneuver, and the latter problem evaluates the final time on the basis of steering maneuver. They assumed that the longitudinal and lateral forces that can be applied to the vehicle are bounded by individual maximum longitudinal and lateral forces. Unlike the assumption of the friction circle, this will lead to less accurate solutions.

For these three maneuvers, by comparing the values of the aspect ratio at any given V_{x0}, the optimal maneuver can be decided. The optimal maneuver is the one with the lowest aspect ratio. For convenience, the plot of the aspect ratio against V_{x0} is shown in Fig. 2.5 so that the optimal maneuver can be clearly seen. As shown in Fig. 2.5, at a lower V_{x0}, the braking maneuver gives a shorter avoidance distance until just before the switching point A, which occurs at $V_{x0} = 3.413631$ and $AR = 5.826440$. Beyond this point, the minimum avoidance distance is provided by the steering with braking maneuver. By equating (2.71) and (2.72), and solving this equation with respect to V_{x0}, we obtain $V_{x0} = 4$. Point B at $V_{x0} = 4$ and $AR = 8$ represents the switching between the braking and steering maneuvers. If $V_{x0} < 4$, the braking maneuver requires a shorter avoidance distance compared to the steering maneuver, and if $V_{x0} > 4$, the steering maneuver is better than the braking maneuver.

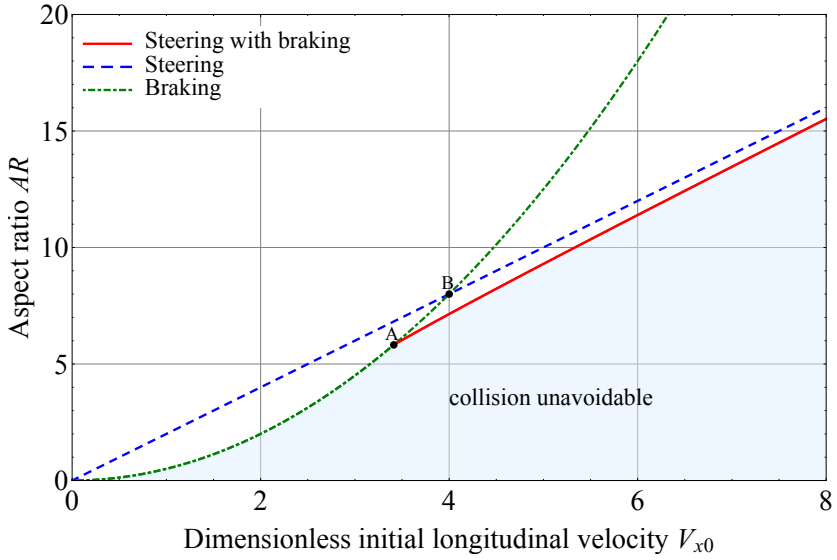

Figure 2.5: Aspect ratio as a function of dimensionless initial longitudinal velocity.

Interestingly, for fixed m_t and y_f, both can be assumed to be time invariant; the effect of a change in v_{x0} or $F_{\max}$ on x_f can be seen in the same figure. This plot also shows the inverse relation between $F_{\max}$ and x_f. An increase in $F_{\max}$ corresponds to a decrease in x_f. Similarly, a diagram for another collision avoidance index termed as the dimensionless time to collision can be produced, and the details on this are given in [111].

Another use of Fig. 2.5 is to show how the safety margin for the estimation error of the tire-road friction coefficient μ can be incorporated. Because the weight of the vehicle is a constant, a change in μ directly reflects a change in $F_{\max}$. It can be assumed that the friction coefficient can be estimated prior to initiation of the intervention using available estimation methods [96]. A safety margin can be considered by setting the estimated value to a slightly lower value. For all the three maneuvers as indicated in Fig. 2.5, the aspect ratio increases as V_{x0} increases. Since $F_{\max} = \mu m_t g$ appears in the denominator of the radicand in $V_{x0} = \sqrt{m_t/(F_{\max} y_f)} v_{x0}$ and the parameters m_t, v_{x0}, and y_f are constant for a given situation, a lower μ results in a longer x_f, and this is evident from Fig. 2.5.

2.5 On-line Solution for State Feedback Control

2.5.1 Derivation of State Feedback Controller

According to the principle of optimality, any point on the optimal trajectory can be taken as a possible input for that trajectory. Without disturbances, the closed-loop trajectories coincide with the open-loop trajectories.

In the previous section, the case with $v_{y0} = 0$ was considered. By redefining $t = 0$ as

the current time, v_{x0} as the current vehicle longitudinal velocity, v_{y0} as the current vehicle lateral velocity, x_{fc} as the longitudinal distance-to-go, y_f as the lateral distance-to-go, and t_f as the time-to-go, the optimal control becomes a state feedback control. By computing the control parameters at each time, one can obtain the optimal control inputs u_x and u_y. Setting $t = 0$ in (2.47) and (2.48), the optimal control inputs u_x and u_y can now be represented as

$$u_x = -\frac{F_{\max}}{m_t} \frac{t_f}{\sqrt{(\nu_y t_f + \nu_v)^2 + t_f^2}} \tag{2.74}$$

$$u_y = -\frac{F_{\max}}{m_t} \frac{\nu_y t_f + \nu_v}{\sqrt{(\nu_y t_f + \nu_v)^2 + t_f^2}} \tag{2.75}$$

A feedback controller in the form of a numerical map was previously proposed [42]. The construction of an accurate map requires computation of the map output variable using a smaller step size, especially when the output is sensitive to the inputs. For this reason, a large amount of data is required to be stored to produce reasonably accurate maps. In this section, an on-line feedback optimal control based exact numerical solution of τ_f is developed. This feedback controller yields a fast iterative solution for τ_f, which in turn will be used to calculate ν_y, ν_v, and t_f, and then substituting these results into (2.74) and (2.75) gives the optimal control. Algebraic manipulations are performed on (2.63) to (2.65) to eliminate Ω. After some simplifications, we obtain

$$2 + 2N_v V_{x0}\tau_f - 2V_{y0}\tau_f + N_y\tau_f\left(V_{x0} - N_v V_{y0}\right) - 2N_v^2\tau_f^2 + N_y^2\left(2 - V_{y0}\tau_f\right) = 0 \tag{2.76}$$

$$V_{x0}^2 + 2N_y V_{x0} V_{y0} + N_y^2 V_{y0}^2 - \tau_f^2 - N_y^2\tau_f^2 - 2N_y N_v\tau_f^2 - N_v^2\tau_f^2 = 0 \tag{2.77}$$

These equations can be seen as a system of polynomial equations in N_y. Given two polynomials with coefficients k and l, say

$$f(N_y) = \sum_{i=0}^{n} k_i N_y^i = k_n \prod_{i=1}^{n} \left(N_y - \alpha_i\right) \tag{2.78}$$

$$g(N_y) = \sum_{j=0}^{m} l_j N_y^j = l_m \prod_{j=1}^{m} \left(N_y - \beta_j\right) \tag{2.79}$$

where the roots of $f(N_y)$ are $\alpha_i, i = 1, ..., n$ and the roots of $g(N_y)$ are $\beta_j, j = 1, ..., m$, the resultant [26] of these polynomials is defined as

$$\rho\left(f, g\right) = k_n^m l_m^n \prod_{i=1}^{n}\prod_{j=1}^{m}\left(\alpha_i - \beta_j\right) \tag{2.80}$$

The computation of the resultant (2.80) can be performed using symbolic manipulation software such as Mathematica [123]. By taking the resultant of (2.76) and (2.77) with respect to N_y, N_y is eliminated, and we obtain a quartic equation in N_v:

$$a_4 N_v^4 + a_3 N_v^3 + a_2 N_v^2 + a_1 N_v + a_0 = 0 \tag{2.81}$$

where the coefficients are given as

$$a_4 = \tau_f^4 \left[3V_{y0}^4 + 8V_{y0}^3\tau_f + 4(\tau_f^2-1)^2 - 8V_{y0}^2(\tau_f^2+1)\right] \tag{2.82a}$$

$$a_3 = -4V_{x0}\tau_f^3(3V_{y0}^4 + V_{y0}^3\tau_f - V_{y0}^2 - 8V_{y0}\tau_f + \tau_f^4 - \tau_f^2) \tag{2.82b}$$

$$\begin{aligned} a_2 =& \tau_f^2\big\{8V_{y0}^5\tau_f + 16\tau_f^2 + 4V_{y0}\tau_f^3(\tau_f^2-3) + V_{y0}^4(7\tau_f^2-8) \\ &- 4V_{y0}^3\tau_f(3\tau_f^2+4) + V_{y0}^2(\tau_f^4+8\tau_f^2+8) + V_{x0}^2\big[\tau_f^4 - 8 \\ &- 8V_{y0}^2 + 9V_{y0}^4 + 8V_{y0}\tau_f(V_{y0}^2-3) + 4\tau_f^2(V_{y0}^2-2)\big]\big\} \end{aligned} \tag{2.82c}$$

$$a_1 = 4V_{x0}\tau_f\left[3V_{x0}^2(V_{y0}^2 - V_{y0}^3\tau_f + \tau_f^2) + 3V_{y0}^4 - 8V_{y0}\tau_f - 3V_{y0}^5\tau_f + 9V_{y0}^2\tau_f^2 - 2\tau_f^4\right] \tag{2.82d}$$

$$a_0 = (V_{x0}^2 + V_{y0}^2)\big\{V_{x0}^2[4 - \tau_f(8V_{y0} - 4V_{y0}^2\tau_f + \tau_f^3)] + (2V_{y0} - 2V_{y0}^2\tau_f + \tau_f^3)^2\big\} \tag{2.82e}$$

The quartic (2.81) in a monic form is given as

$$N_v^4 + b_3N_v^3 + b_2N_v^2 + b_1N_v + b_0 = 0 \tag{2.83}$$

Equation (2.83) can be factorized into a product of two quadratics:

$$\begin{aligned} \left(N_v^2 + c_1N_v + d_1\right)\left(N_v^2 + c_2N_v + d_2\right) &= N_v^4 + (c_1+c_2)\,N_v^3 \\ + (c_1c_2 + d_1 + d_2)\,N_v^2 &+ (c_1d_2 + c_2d_1)\,N_v + d_1d_2 = 0 \end{aligned} \tag{2.84}$$

Equating the coefficients in (2.83) and (2.84), we have

$$c_1 + c_2 = b_3 \tag{2.85a}$$

$$c_1c_2 + d_1 + d_2 = b_2 \tag{2.85b}$$

$$c_1d_2 + c_2d_1 = b_1 \tag{2.85c}$$

$$d_1d_2 = b_0 \tag{2.85d}$$

Applying Vieta's formulas, two quadratic equations that contain the solution of the coefficients in (2.84) are obtained:

$$c^2 - b_3c + b_2 - z_1 = 0 \tag{2.86a}$$

$$d^2 - z_1d + b_0 = 0 \tag{2.86b}$$

where z_1 is the real root of (2.87), which is the cubic resolvent [109] of (2.83):

$$z^3 - b_2z^2 + (b_3b_1 - 4b_0)\,z + \left(4b_2b_0 - b_1^2 - b_3^2b_0\right) = 0 \tag{2.87}$$

The coefficients c_1 and c_2 in (2.84) are obtained by solving (2.86a) and the coefficients d_1 and d_2 are obtained by solving (2.85b) and (2.85c):

$$\left.\begin{matrix} c_1 \\ c_2 \end{matrix}\right\} = \frac{1}{2}\left(b_3 \pm \sqrt{b_3^2 - 4b_2 + 4z_1}\right) \tag{2.88a}$$

$$\left.\begin{matrix} d_1 \\ d_2 \end{matrix}\right\} = \frac{1}{2}\left(z_1 \pm \frac{b_3z_1 - 2b_1}{\sqrt{b_3^2 - 4b_2 + 4z_1}}\right) \tag{2.88b}$$

The discriminant [19] of the cubic in (2.87) is

$$D_3 = Q^3 + R^2 \tag{2.89}$$

where

$$Q = -\frac{1}{9}\left(b_2^2 - 3b_3b_1 + 12b_0\right) \tag{2.90a}$$

$$R = \frac{1}{54}\left(2b_2^3 + 27b_3^2b_0 + 27b_1^2 - 9b_3b_2b_1 - 72b_2b_0\right) \tag{2.90b}$$

If $D_3 > 0$, there is one real root and a pair of complex conjugates. The real root of the cubic takes the form

$$z_1 = \frac{b_2}{3} + S + T \tag{2.91}$$

where

$$\left.\begin{matrix} S \\ T \end{matrix}\right\} = \sqrt[3]{R \pm \sqrt{D_3}} \tag{2.92}$$

If $D_3 \leq 0$, all the roots of the cubic are real and these roots can be expressed as

$$z_1 = \frac{b_2}{3} + 2\sqrt{-Q}\cos\left(\frac{\theta}{3}\right) \tag{2.93a}$$

$$z_2 = \frac{b_2}{3} + 2\sqrt{-Q}\cos\left(\frac{\theta + 2\pi}{3}\right) \tag{2.93b}$$

$$z_3 = \frac{b_2}{3} + 2\sqrt{-Q}\cos\left(\frac{\theta + 4\pi}{3}\right) \tag{2.93c}$$

where

$$\theta = \arccos\left(\frac{R}{\sqrt{-Q^3}}\right) \tag{2.94}$$

The root (2.93a) is chosen if $D_3 < 0$. The four roots of (2.83) are

$$\left.\begin{matrix} N_{v1} \\ N_{v2} \end{matrix}\right\} = -\frac{c_1}{2} \pm \sqrt{\frac{c_1^2}{4} - d_1} \tag{2.95a}$$

$$\left.\begin{matrix} N_{v3} \\ N_{v4} \end{matrix}\right\} = -\frac{c_2}{2} \pm \sqrt{\frac{c_2^2}{4} - d_2} \tag{2.95b}$$

The expressions of these roots are the same as in [13]. Because there are four roots, and only one root represents the correct solution, we identified that $N_v = N_{v1}$ if $c_1 < 0$ and $N_v = N_{v4}$ if $c_1 > 0$. More specifically, the minimum longitudinal avoidance distance is achieved using $N_v = N_{v1}$ if $c_1 < 0$ and $N_v = N_{v4}$ if $c_1 > 0$. Now, we express N_v as a function of only one unknown τ_f.

After performing algebraic manipulations, N_y can be expressed as a function of two unknowns, N_v and τ_f, as follows:

$$N_y = \frac{N_{yn}}{N_{yd}} \tag{2.96}$$

where

$$N_{yn} = 2N_v^2\tau_f^4 - 2V_{x0}^2 + 2V_{y0}^2 - 2N_v^2\tau_f^2(V_{y0}^2 - 1) + \tau_f^3\left[V_{y0} - N_v(2V_{x0} + N_vV_{y0})\right] + V_{y0}\tau_f(V_{x0}^2 + 2N_vV_{x0}V_{y0} - 2V_{y0}^2)$$

$$N_{yd} = N_v\tau_f(V_{y0}^3 - 4\tau_f + V_{y0}\tau_f^2) + V_{x0}(4V_{y0} - 3V_{y0}^2\tau_f + \tau_f^3)$$

Substituting N_v into (2.96) and then substituting this and N_v into (2.65), we have an implicit equation for τ_f. The closed-form solution to (2.65) is not expectable, and therefore, an iterative method should be used. Once the solution of τ_f is obtained, N_v and N_y can be evaluated from (2.95) and (2.96), respectively. It is important to note that the reduction of the three dimensionless simultaneous equations to a single equation in τ_f is deliberate, because among the control parameters, τ_f is the only physical parameter for which an initial guess can be obtained with relative ease.

2.5.2 Numerical Methods for Solving Scalar Nonlinear Equations

The numerical methods to solve a nonlinear equation with one unknown can be divided on the basis of the type of the initial guess into bracketing methods and open methods. Bracketing methods require an initial guess for the interval containing the root. Examples of bracketing methods are the bisection method and the false position method. Open methods require one or more initial guesses, but it is not mandatory for the root to lie within these guesses. Among the open methods are the Newton-Raphson method, secant method, and inverse quadratic method. Open methods are fast but less reliable. On the other hand, bracketing methods are numerically more robust but may converge more slowly. Because in the obstacle avoidance problem, we need a method that guarantees convergence, we limit our study to the application of bracketing and hybridization of bracketing and open methods.

Bisection method

In this method, the search interval is always divided into halves until the termination criterion is met.

Illinois method

The Illinois method is a modification of the standard false position method to prevent retention of the end point [29].

Pegasus method

This is also a modified false position method with the motivation same as the Illinois method [30].

Ridders' method

Ridders' method is an intelligent modification of the false position method in which the false position method is applied to the linearized original function [62]. The drawback of this method is that it requires two function evaluations for each iteration.

Brent's method

Among the one-dimensional root solving methods, Brent's method is the most popular. Brent's method combines the robust bisection method with the fast secant and inverse quadratic interpolation methods. Details on Brent's method can be found in [73].

2.5.3 Search Interval Bounds for Dimensionless Final Time

To implement the root finding methods described in the previous subsection, knowledge of the initial interval bounds is required. One of the promising methods is to use the Chebyshev approximation on the numerical solutions of τ_f. The approximation given by the Chebyshev polynomial is very close to that of the minimax polynomial, which has the minimum value of the maximum error [95]. Because of the difficulty in finding the minimax polynomial, the Chebyshev polynomial is preferred for function approximation.

The Chebyshev polynomials that are orthogonal polynomials can be expressed in a three-term recurrence relation as given in [95]

$$T_{n+1}(x) = 2xT_n(x) - T_{n-1}(x) \quad n \geq 1 \tag{2.98}$$

with starting values of $T_0 = 1, T_1 = x$. The subscript n in the polynomial $T_n(x)$ denotes the degree of the polynomial. Therefore, there are n zeros within the interval $[-1, 1]$, and these zeros are given by

$$x_k = \cos\left(\frac{\pi(k - 1/2)}{n}\right) \quad k = 1, 2, ..., n \tag{2.99}$$

Within the same interval, $T_n(x)$ has $n + 1$ extrema at

$$x'_k = \cos\left(\frac{\pi k}{n}\right) \quad k = 0, 1, ..., n \tag{2.100}$$

The property that $T_n(x) = -1$ at all minima and $T_n(x) = 1$ at all maxima is the reason why Chebyshev polynomials are used for function approximation [95].

The Chebyshev polynomials satisfy the discrete orthogonality condition

$$\sum_{k=1}^{m} T_i(x_k)T_j(x_k) = \begin{cases} 0, & i \neq j \\ m/2, & i = j \neq 0 \\ m, & i = j = 0 \end{cases} \tag{2.101}$$

The Chebyshev approximation for a function $f(x)$ in the interval $[-1, 1]$ is given by

$$f(x) \approx -\frac{1}{2}c_0 + \sum_{j=0}^{N-1} c_j T_j(x) \tag{2.102}$$

where the coefficients c_j are computed by evaluating $f(x)$ at the zeros.

$$c_j = \frac{2}{N}\sum_{k=1}^{N} f(x_k)T_j(x_k) \tag{2.103}$$

In (2.103), $T_j(x_k)$ is expressed as

$$T_j(x_k) = \cos\left(\frac{\pi j(k - 1/2)}{N}\right) \tag{2.104}$$

This approximation can be done for an arbitrary interval $[x_0, x_1]$ by using the linear variable transformation

$$\tilde{x} = \frac{x - \frac{1}{2}(x_1 + x_0)}{\frac{1}{2}(x_1 - x_0)} \tag{2.105}$$

The Chebyshev polynomial approximation of a univariate function can be extended to a bivariate function [16, 1]. A bivariate function $f(x, y)$ can be approximated as

$$f(x, y) \approx \sum_{i=0}^{M-1}\sum_{j=0}^{N-1} c_{ij}T_i(x)T_j(y) \tag{2.106}$$

Again, by evaluating $f(x, y)$ at the zeros, the coefficients c_{ij} are determined.

$$c_{ij} = \frac{\alpha}{MN}\sum_{k=1}^{M}\sum_{l=1}^{N} f(x_k, y_l)T_i(x_k)T_j(y_l) \tag{2.107}$$

If $ij = 00$, then $\alpha = 1$; if $ij = 0j$ or $ij = i0$, then $\alpha = 2$, otherwise $\alpha = 4$ [1].

To use lower-order Chebyshev polynomials, the original objective region ($3.413 \leq V_{x0} \leq 60; 0 \leq V_{y0} \leq 1.4$) is divided into four regions: $f_A(3.413 \leq V_{x0} \leq 7.4; 0 \leq V_{y0} \leq 0.3)$, $f_B(3.413 \leq V_{x0} \leq 7.4; 0.3 \leq V_{y0} \leq 1.4)$, $f_C(7.4 \leq V_{x0} \leq 60; 0 \leq V_{y0} \leq 0.3)$, and $f_D(7.4 \leq V_{x0} \leq 60; 0.3 \leq V_{y0} \leq 1.4)$. By setting $M = 5$ and $N = 5$, the approximation

Table 2.2: Bivariate Chebyshev Approximation

$$
\begin{aligned}
f_A(\tilde{V}_{x0},\tilde{V}_{y0}) =& 1.94821 - 0.0562331\tilde{V}_{x0} + 0.0332002\tilde{V}_{x0}^2 - 0.0373777\tilde{V}_{x0}^3 + 0.0230394\tilde{V}_{x0}^4 - 0.138877\tilde{V}_{y0} + 0.00866585\tilde{V}_{x0}\tilde{V}_{y0} \\
& - 0.00711002\tilde{V}_{x0}^2\tilde{V}_{y0} + 0.0166899\tilde{V}_{x0}^3\tilde{V}_{y0} - 0.0123105\tilde{V}_{x0}^4\tilde{V}_{y0} + 0.0126551\tilde{V}_{y0}^2 - 0.000532515\tilde{V}_{x0}\tilde{V}_{y0}^2 \\
& + 0.000638897\tilde{V}_{x0}^2\tilde{V}_{y0}^2 - 0.00528182\tilde{V}_{x0}^3\tilde{V}_{y0}^2 + 0.00444426\tilde{V}_{x0}^4\tilde{V}_{y0}^2 - 0.000336932\tilde{V}_{y0}^3 - 0.000206299\tilde{V}_{x0}\tilde{V}_{y0}^3 \\
& + 0.000142076\tilde{V}_{x0}^2\tilde{V}_{y0}^3 + 0.0018055\tilde{V}_{x0}^3\tilde{V}_{y0}^3 - 0.00166347\tilde{V}_{x0}^4\tilde{V}_{y0}^3 - 0.0000152033\tilde{V}_{y0}^4 + 0.000128026\tilde{V}_{x0}\tilde{V}_{y0}^4 \\
& - 0.000108053\tilde{V}_{x0}^2\tilde{V}_{y0}^4 - 0.000535944\tilde{V}_{x0}^3\tilde{V}_{y0}^4 + 0.000521177\tilde{V}_{x0}^4\tilde{V}_{y0}^4 \\
f_B(\tilde{V}_{x0},\tilde{V}_{y0}) =& 1.5352 - 0.025534\tilde{V}_{x0} + 0.010956\tilde{V}_{x0}^2 - 0.0061491\tilde{V}_{x0}^3 + 0.0026964\tilde{V}_{x0}^4 - 0.174164\tilde{V}_{y0} + 0.0210704\tilde{V}_{x0}\tilde{V}_{y0} \\
& - 0.0124986\tilde{V}_{x0}^2\tilde{V}_{y0} + 0.00959777\tilde{V}_{x0}^3\tilde{V}_{y0} - 0.00484117\tilde{V}_{x0}^4\tilde{V}_{y0} + 0.0890867\tilde{V}_{y0}^2 + 0.00111418\tilde{V}_{x0}\tilde{V}_{y0}^2 \\
& + 0.00190296\tilde{V}_{x0}^2\tilde{V}_{y0}^2 - 0.00465382\tilde{V}_{x0}^3\tilde{V}_{y0}^2 + 0.00314188\tilde{V}_{x0}^4\tilde{V}_{y0}^2 - 0.0264461\tilde{V}_{y0}^3 + 0.00249658\tilde{V}_{x0}\tilde{V}_{y0}^3 \\
& - 0.000783937\tilde{V}_{x0}^2\tilde{V}_{y0}^3 + 0.0026695\tilde{V}_{x0}^3\tilde{V}_{y0}^3 - 0.0021175\tilde{V}_{x0}^4\tilde{V}_{y0}^3 - 0.00334432\tilde{V}_{y0}^4 - 0.000184375\tilde{V}_{x0}\tilde{V}_{y0}^4 \\
& + 0.000619981\tilde{V}_{x0}^2\tilde{V}_{y0}^4 - 0.0015415\tilde{V}_{x0}^3\tilde{V}_{y0}^4 + 0.00115671\tilde{V}_{x0}^4\tilde{V}_{y0}^4 \\
f_C(\tilde{V}_{x0},\tilde{V}_{y0}) =& 1.86474 - 0.0000231567\tilde{V}_{x0} + 0.00106648\tilde{V}_{x0}^2 - 0.0207124\tilde{V}_{x0}^3 + 0.0179382\tilde{V}_{x0}^4 - 0.127787\tilde{V}_{y0} \\
& - 0.000321286\tilde{V}_{x0}\tilde{V}_{y0} + 0.000189436\tilde{V}_{x0}^2\tilde{V}_{y0} + 0.00229768\tilde{V}_{x0}^3\tilde{V}_{y0} - 0.00211287\tilde{V}_{x0}^4\tilde{V}_{y0} + 0.0111111\tilde{V}_{y0}^2 \\
& + 9.86683\times10^{-6}\tilde{V}_{x0}\tilde{V}_{y0}^2 + 2.79252\times10^{-6}\tilde{V}_{x0}^2\tilde{V}_{y0}^2 - 0.000306642\tilde{V}_{x0}^3\tilde{V}_{y0}^2 + 0.000271447\tilde{V}_{x0}^4\tilde{V}_{y0}^2 \\
& - 0.000125154\tilde{V}_{y0}^3 - 4.76106\times10^{-6}\tilde{V}_{x0}\tilde{V}_{y0}^3 + 2.63862\times10^{-6}\tilde{V}_{x0}^2\tilde{V}_{y0}^3 + 0.0000391657\tilde{V}_{x0}^3\tilde{V}_{y0}^3 \\
& - 0.000035801\tilde{V}_{x0}^4\tilde{V}_{y0}^3 - 0.000028847\tilde{V}_{y0}^4 + 3.50092\times10^{-7}\tilde{V}_{x0}\tilde{V}_{y0}^4 - 3.41033\times10^{-7}\tilde{V}_{x0}^2\tilde{V}_{y0}^4 \\
& - 1.20585\times10^{-6}\tilde{V}_{x0}^3\tilde{V}_{y0}^4 + 1.21968\times10^{-6}\tilde{V}_{x0}^4\tilde{V}_{y0}^4 \\
f_D(\tilde{V}_{x0},\tilde{V}_{y0}) =& 1.48691 - 0.00161949\tilde{V}_{x0} + 0.00210173\tilde{V}_{x0}^2 - 0.0130434\tilde{V}_{x0}^3 + 0.0107441\tilde{V}_{x0}^4 - 0.149118\tilde{V}_{y0} - 0.00164537\tilde{V}_{x0}\tilde{V}_{y0} \\
& + 0.00102431\tilde{V}_{x0}^2\tilde{V}_{y0} + 0.00619187\tilde{V}_{x0}^3\tilde{V}_{y0} - 0.00585262\tilde{V}_{x0}^4\tilde{V}_{y0} + 0.0952055\tilde{V}_{y0}^2 - 0.000163\tilde{V}_{x0}\tilde{V}_{y0}^2 \\
& - 0.000152997\tilde{V}_{x0}^2\tilde{V}_{y0}^2 + 0.00239862\tilde{V}_{x0}^3\tilde{V}_{y0}^2 - 0.00202893\tilde{V}_{x0}^4\tilde{V}_{y0}^2 - 0.0169275\tilde{V}_{y0}^3 + 0.0011962\tilde{V}_{x0}\tilde{V}_{y0}^3 \\
& - 0.0012417\tilde{V}_{x0}^2\tilde{V}_{y0}^3 + 0.00266543\tilde{V}_{x0}^3\tilde{V}_{y0}^3 - 0.00188132\tilde{V}_{x0}^4\tilde{V}_{y0}^3 - 0.000232886\tilde{V}_{y0}^4 + 0.00102134\tilde{V}_{x0}\tilde{V}_{y0}^4 \\
& - 0.000928762\tilde{V}_{x0}^2\tilde{V}_{y0}^4 + 0.000841642\tilde{V}_{x0}^3\tilde{V}_{y0}^4 - 0.000398731\tilde{V}_{x0}^4\tilde{V}_{y0}^4
\end{aligned}
$$

polynomials are formed as given in Table 2.2. These polynomials are offset appropriately to form the lower and upper bounds.

For the region outside these four regions, the lower bound can be approximated by using the pure steering case. From (2.9) and the definition of v_{y0}, in Table 2.1, the dimensionless final time for the steering maneuver τ_{fs} is given by

$$\tau_{fs} = -V_{y0} + \sqrt{2}\sqrt{2 + V_{y0}^2} \tag{2.108}$$

For the four regions, if (2.108) gives a higher value compared to that of the lower bound obtained by offsetting the polynomial, it is used for the lower bound.

For the region outside the region $(3.413 \leq V_{x0} \leq 60; 0 \leq V_{y0} \leq 1.4)$, the upper bound for τ_f is set using the dimensionless final time required for the steering with constant braking avoidance maneuver. For example, by allocating 20% of $F_{\max}/m_t$ for braking, the dimensionless final time for steering with constant braking τ_{fu} is

$$\tau_{fu} = \frac{1}{12}\left(-5\sqrt{6}V_{y0} + 2\sqrt{60\sqrt{6} + 75V_{y0}^2}\right) \tag{2.109}$$

2.5.4 Implementation

In this subsection, the procedures for the implementation of the feedback controller are summarized. It is assumed that for a given situation, the collision can be avoided by only steering with braking maneuver. Once the intervention is initiated, the following procedures determine the optimal control:

1. Measure/estimate v_{x0}, v_{y0}, y_f, and μ. The vehicle velocities v_{x0}, v_{y0}, and the position y can be estimated using integration of Inertial Navigation System (INS) and Global Positioning System (GPS). Details on the integration of INS and GPS can be found in [18]. y_f is obtained by subtracting y from the value of y_f at the beginning of the maneuver. The friction coefficient μ can be estimated prior to the avoidance maneuver using the methods that are suitable for real-time implementation such as in [96].

2. Using the values of v_{x0}, v_{y0}, y_f, and μ, compute the dimensionless variables V_{x0} and V_{y0} as
$$V_{x0} = \sqrt{\frac{m_t}{F_{\max} y_f}} v_{x0}, \quad V_{y0} = \sqrt{\frac{m_t}{F_{\max} y_f}} v_{y0} \tag{2.110}$$
where $F_{\max} = m_t \mu g$. Note that g is the gravitational acceleration.

3. Using bisection method, solve (2.65) respect to τ_f, with N_y given by (2.96) and N_v given as $N_v = N_{v1}$ if $c_1 < 0$ and $N_v = N_{v4}$ otherwise. The lower and upper bounds are determined according to the method described in the previous subsection.

4. The solution of τ_f that is the midpoint of the last search interval is converted to t_f according to
$$t_f = \sqrt{\frac{m_t y_f}{F_{\max}}} \tau_f \tag{2.111}$$
Using the solution of τ_f, N_v is determined as following: $N_v = N_{v1}$ if $c_1 < 0$ and $N_v = N_{v4}$ otherwise. Substitute τ_f and N_v into (2.96) to yield N_y. Then, ν_y and ν_v are computed as $\nu_y = N_y$ and $\nu_v = N_v t_f$, respectively.

5. Substitute ν_y, ν_v, t_f, and $F_{\max}$ into (2.74) and (2.75) to yield u_x and u_y, respectivley. The total longitudinal force X_t and the total lateral force Y_t that are the inputs to the tire force distributor are given as $X_t = m_t u_x$ and $Y_t = m_t u_y$, respectively.

2.5.5 Hamiltonian

The Hamiltonian (2.29) by setting $t = t_0 = 0$ can be written as
$$H(\boldsymbol{s}(t_0), \varphi(t_0), \boldsymbol{\lambda}(t_0), t_0) = -\frac{F_{\max}}{m_t} \frac{t_f^2 + (\nu_y t_f + \nu_v)^2}{\sqrt{t_f^2 + (\nu_y t_f + \nu_v)^2}} + v_{x0} + v_{y0}\nu_y \tag{2.112}$$

The Hamiltonian has a dimension of LT^{-1}; therefore, dividing (2.112) by v_{x0} and then using the definitions in Table 2.1, the dimensionless Hamiltonion π_H is expressed as

$$\pi_H = \frac{H}{v_{x0}} = \frac{V_{x0} + N_y V_{y0} - \tau_f \sqrt{1 + (N_y + N_v)^2}}{V_{x0}} \tag{2.113}$$

The optimality of the computed solution can be verified by computing the Hamiltonian. The Hamiltonian (2.29) is not expressed explicitly as a function of time, and hence this Hamiltonian is a constant. Furthermore, this is a free final time problem. Therefore, the Hamiltonian must be zero. Note that the numerator of (2.113) is directly proved to be zero by elimination of Ω from (2.63) and (2.64), followed by simplifications.

2.6 Numerical Examples

2.6.1 State Feedback Controller Verification

A simulation is performed using a point mass vehicle model to verify the feedback controller. The simulation parameters are $m_t = 1707$ kg, $F_{\max} = 8.373$ kN, $v_{x0} = 30$ m/s, $v_{y0} = 0$ m/s, and $y_f = 3$ m. Fig. 2.6 shows the solutions of τ_f together with the search interval bounds. It can be seen that the solutions of τ_f are within the search interval bounds. Numerical instabilities were encountered near 1.4 s, and the control was switched to that of the steering maneuver, where $F_{\max}$ is fully used as the total lateral force. This switching is triggered by the value of y_f. More specifically, if $y_f < 0.1$ m, the controller switches to pure steering control.

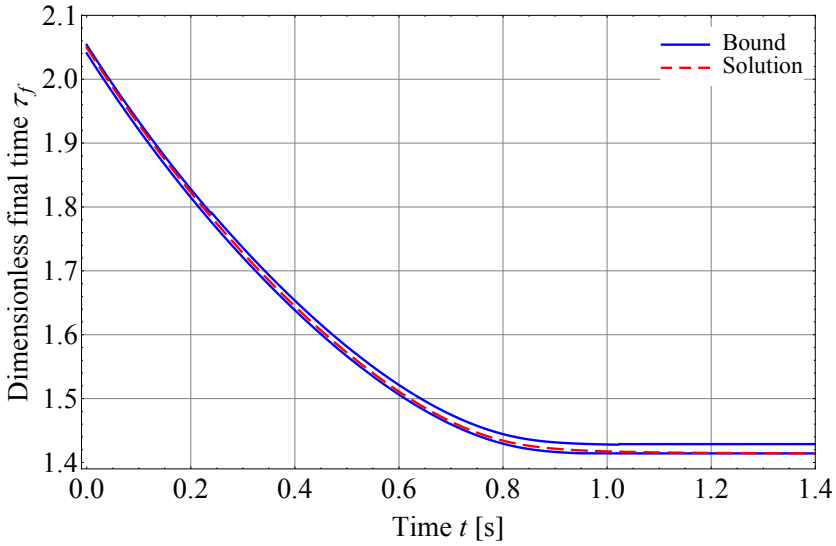

Figure 2.6: Dimensionless final time along the lane change maneuver.

Table 2.3 indicates the maximum number of function evaluations of the five root finding methods for different termination criteria. These methods except Ridders' method require

one function evaluation per iteration. Ridders' method requires two function evaluations per iteration. Because of the different number of function evaluation per iteration for these methods, the performance comparison is done on the basis of the number of function evaluations instead of the number of iterations. For each termination criteria, the bisection method requires the lowest maximum number of function evaluations.

Table 2.3: Comparison of Maximum Number of Function Evaluations with Termination Criteria $|\tau_{fu} - \tau_{fl}| < \epsilon$ or $f(\tau_{fu}) = 0$ for Various Root Finding Methods

Method	$\epsilon = 10^{-6}$	$\epsilon = 10^{-9}$	$\epsilon = 10^{-12}$	$\epsilon = 10^{-15}$
Brent	27	40	47	58
Bisection	16	26	36	46
Pegasus	28	31	49	49
Illinois	21	32	36	50
Ridders'	26	34	46	54

Fig. 2.7 shows the number of function evaluations required for $\epsilon = 10^{-6}$ at each time instant with a sampling time of 0.001 s. For all the methods except the bisection method, the number of function evaluations is low during the first half of the maneuver and then increases with the simulation time. The increase in the number of function evaluations in the second half of the maneuver implies an increase in the difficulty of solving the nonlinear equation. From a practical viewpoint, the bisection method is recommended because it has the lowest maximum number of function evaluations. Furthermore, the bisection method is the simplest algorithm available for one-variable root finding problem.

Figs. 2.8a and 2.8b show the total longitudinal forces and total lateral forces along the lane change maneuver for both feedforward control and feedback control. The total longitudinal force and total lateral force for the feedback control coincide with the respective forces for the feedforward control. In Fig. 2.8a, it is shown that the total longitudinal force for the feedback control was switched to zero at $t = 1.4$ s. At this time instant, the total lateral force for the feedback control was switched to $-F_{\max}$.

The vehicle position trajectories for both the feedforward control and feedback control are shown in Fig. 2.8c. The position trajectory of the feedback control overlaps with that of the feedforward control. Although the control was switched to the steering controller near the end of the maneuver, the effect on the position trajectory was minimal. The longitudinal velocity of the vehicle along the maneuver can be seen in Fig. 2.9. There is a small deviation starting at approximately $t = 1.4$ s because of the maneuver switching.

The total longitudinal force and the total lateral force generated at each time instant

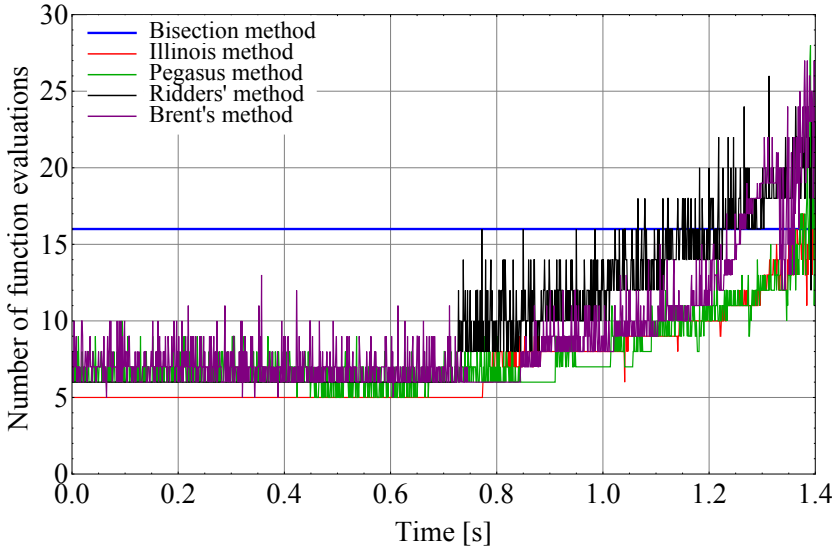

Figure 2.7: Number of function evaluations along the lane change maneuver with $\epsilon = 10^{-6}$ for different root finding methods.

with a sampling of 0.01 s are shown in Fig. 2.10. The filled blue circle indicates the total vehicle force for the feedforward control, the red circle indicates the total vehicle force for the feedback control, and the green circle indicates the vehicle friction circle. It can be clearly seen that the total vehicle force for feedback control coincides with that of the feedforward control. In addition, the total vehicle forces for both feedforward and feedback controls coincide with the vehicle friction circle.

2.6.2 Crosswind Disturbance Scenario

In the previous subsection, disturbance during the lane change maneuver was not considered. In this subsection, the effectiveness of the feedback controller under crosswind disturbance is investigated. For crosswind disturbance, the scenario outlined in JASO Z108-76 [3] is adopted. As illustrated in Fig. 2.11, a vehicle performing an evasive lane change maneuver with an initial velocity of 30 m/s encounters a crosswind force at a wind velocity v_w of 20 m/s for a length of 15 m. The original scenario as described in this standard assumes the vehicle is traveling at a constant velocity of 27.78 m/s. Because the velocity of the vehicle is reducing owing to the braking effect, 30 m/s was chosen as the initial velocity.

The crosswind force is expressed as

$$Y_s = C_y \frac{\varrho}{2} A_f [v_x^2 + (v_y + v_w)^2] \tag{2.114}$$

where C_y is the lateral force coefficient, which is expressed as a function of the aerodynamic sideslip angle ψ_a [55]; ϱ is the air density; A_f is the vehicle frontal area; v_x is

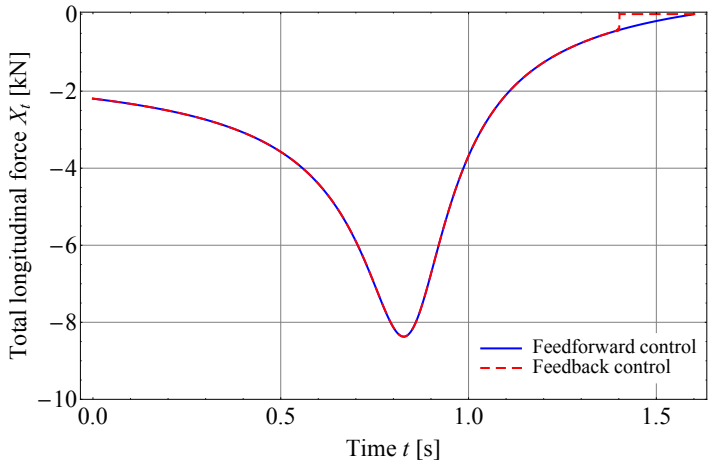

(a)

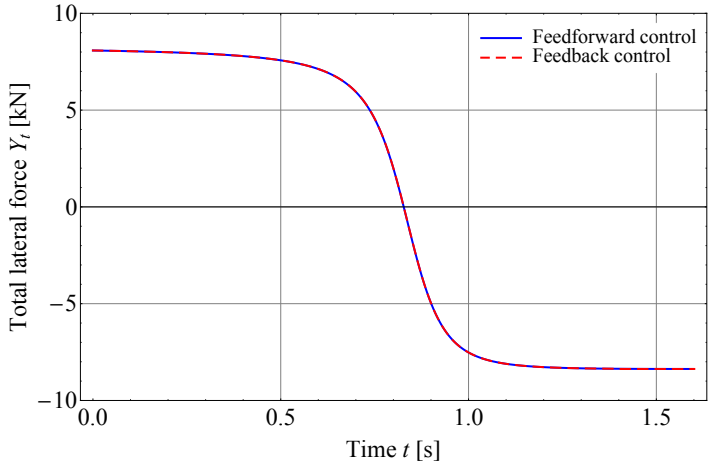

(b)

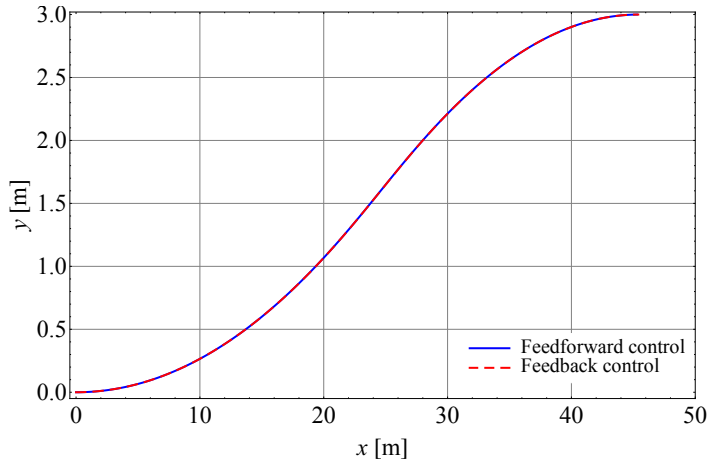

(c)

Figure 2.8: Optimal control and vehicle position trajectory. (a) Total longitudinal forces along the lane change maneuver for feedforward control and feedback control. (b) Total lateral forces along the lane change maneuver for feedforward control and feedback control. (c) Vehicle position trajectories for feedforward control and feedback control.

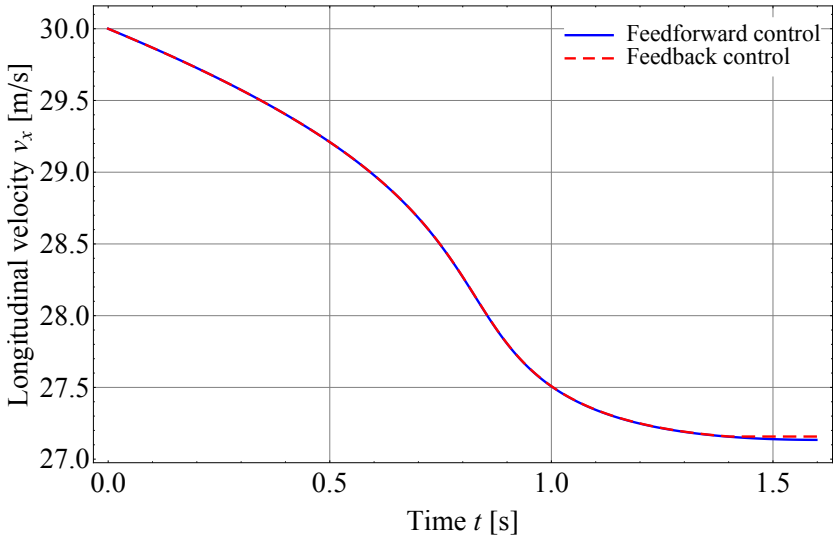

Figure 2.9: Longitudinal velocity profiles along the lane change maneuver for feedforward control and feedback control.

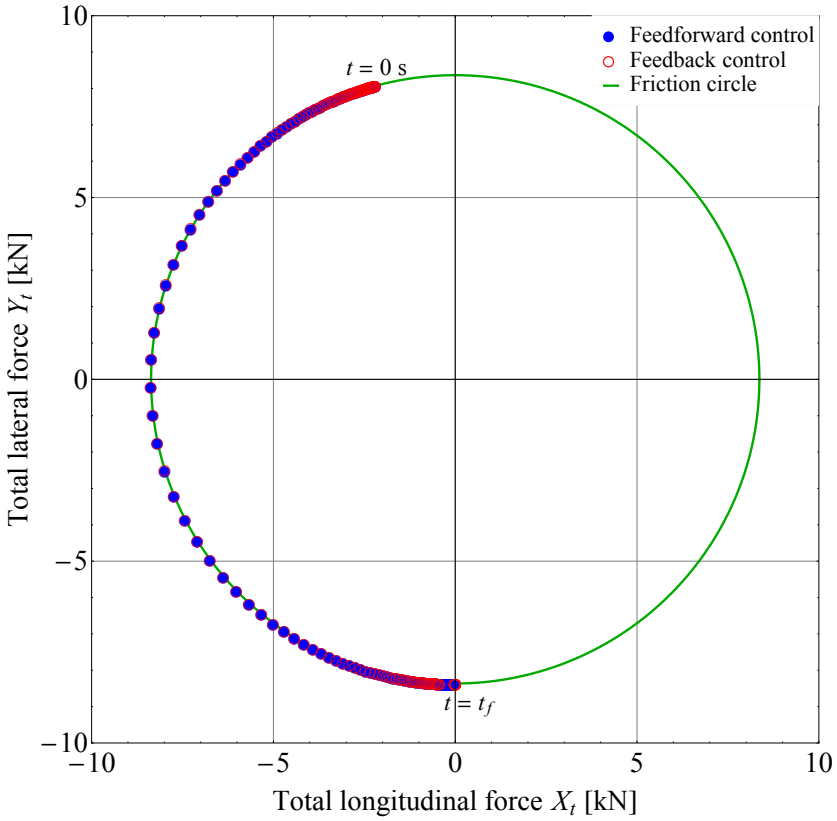

Figure 2.10: Total vehicle force and vehicle friction circle.

the longitudinal vehicle velocity; and v_y is the lateral vehicle velocity. The aerodynamic sideslip angle is defined as

$$\psi_a = \arctan\left(\frac{v_y + v_w}{v_x}\right) \tag{2.115}$$

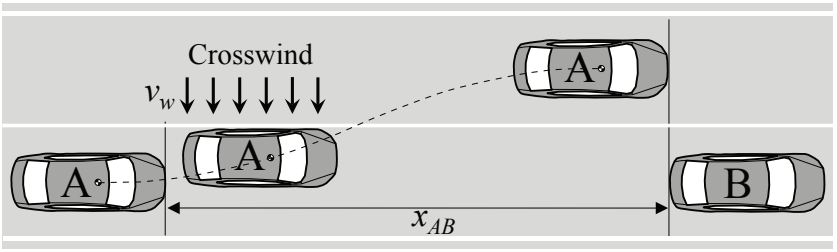

Figure 2.11: Simulation scenario for crosswind disturbance. Vehicle A performs a lane change maneuver with a longitudinal distance x_{AB} to avoid static vehicle B.

The frontal area is estimated on the basis of the vehicle mass [128] by using

$$A_f = 1.6 + 0.00056\,(m_t - 765) \tag{2.116}$$

The simulation results for the feedforward and feedback controls are presented in Fig. 2.12. The feedforward control is incapable of compensating for the wind disturbance, and therefore the desired final lateral distance is not achieved. On the other hand, the feedback control yields a successful lane change maneuver.

2.7 Conclusion

In this chapter, a collision avoidance problem was studied from the standpoint of optimal control theory. The benefit of the nondimensionalization technique in reducing the number of givens from five to two and unknowns from three to one has been demonstrated. This algebraic simplification allows derivation of the dimensionless collision avoidance index, which is essential for determining if a collision is avoidable and for choosing the optimal maneuver. Another advantage of the simplification is the reduction of the original problem of finding the feedback control law applicable to the one-dimensional root finding problem. For this one-dimensional root finding problem, bracketing and hybrid methods were tested together with search intervals determined using the Chebyshev polynomial that guarantee convergence. For the region outside the polynomial approximation region, simpler maneuvers are used for the search interval. The bisection method is the simplest among the methods considered and requires the lowest maximum number of function evaluations. The verification results show that if there are no disturbances, the feedback control responses coincide with that of the feedforward control. Simulation results of lane change obstacle avoidance with crosswind disturbance confirm the robustness of the feedback controller.

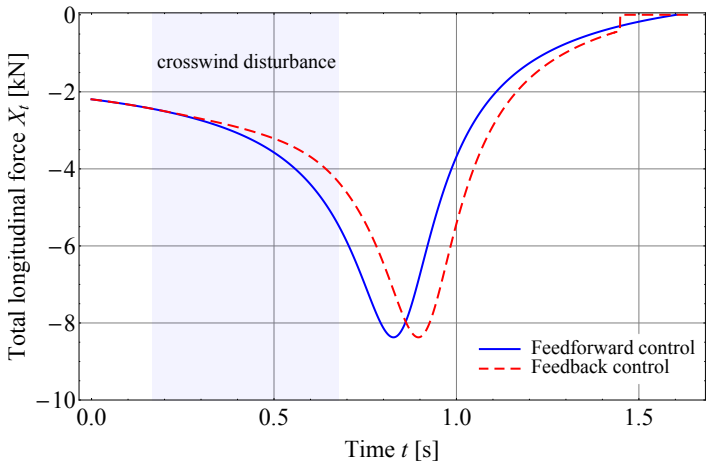

(a)

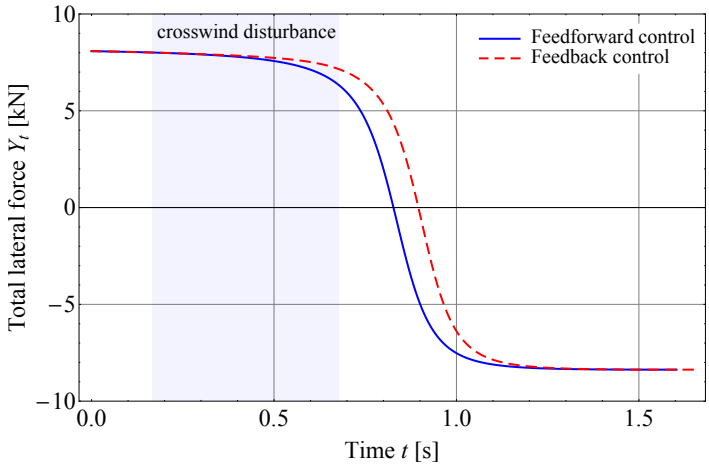

(b)

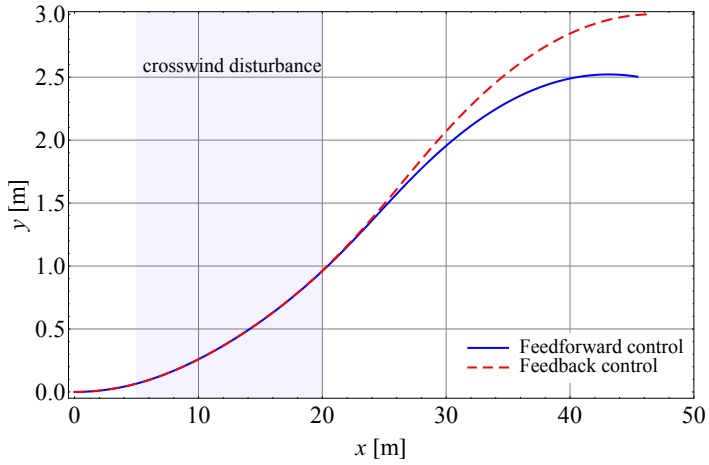

(c)

Figure 2.12: Simulation results for crosswind disturbance. (a) Total longitudinal force along the lane change maneuver. (b) Total lateral force along the lane change maneuver. (c) Vehicle position trajectory along the lane change maneuver.

Chapter 3

Minimum Resultant Vehicle Force Optimal State Feedback Control

3.1 Introduction

A key aspect of an autonomous vehicle is an automatic collision avoidance system. A collision avoidance system generates the best path to avoid one or more obstacles. Obstacle avoidance may require a single lane change [106, 118], a double lane change [53, 107], or a curve maneuver [20, 63]. In some situations, maneuvering with pure obstacle avoidance, barrier avoidance, and recovery maneuver phases, in this order, should be performed [28]. In this chapter, we consider the single lane change maneuver for obstacle avoidance as the basic case. This maneuver has been discussed in numerous previous papers [130, 52, 17, 84, 43].

To generate a single lane change path to avoid an obstacle, various simple functions are used. These functions include arctangent [10], sigmoids [58], polynomials [103], and clothoids [38]. To track the path, a controller that controls the steering with or without braking inputs, is designed. These path generation methods are computationally efficient. However, the paths generated are not optimal and may require longer longitudinal distance to avoid obstacle or employ a higher usage of vehicle force.

In a study of minimum longitudinal avoidance distance, integrated steering and braking actions, utilizing optimal control theory and satisfying the constraints imposed by the friction ellipse, are proposed [106]. In another study, also using optimal control theory for the given longitudinal avoidance distance to the obstacle, Horiuchi *et al.* [52] minimized an objective function that is defined as the time integral of the weighted sum of the squared steering angular speed and the sum of the squared tire force usage of each tire. Tire force usage is defined as the ratio between the resultant of the longitudinal and lateral tire

forces and the radius of the tire friction circle [9]. Best [17] investigated the optimal combinations of steering and driving/braking inputs for different objective functions. These studies made use of bicycle and eight-degree-of-freedom models, coupled with nonlinear tire models. The higher-degree-of-freedom model gave more realistic simulations but made the optimal control problem more complex. This complexity means the solution method is computationally inefficient, and therefore, the implementation of optimal control in a feedback form becomes a challenging task. Consequently, these studies were limited to open-loop optimal control, in which the trajectory and the control are calculated only once.

In order to simplify the collision avoidance problem, the collision avoidance system can be designed to be hierarchical. The hierarchical structure consists of an upper level controller and a lower level controller. The upper level controller determines the desired vehicle forces and moment required to avoid the obstacle. Meanwhile, the lower level controller simultaneously determines the steering and driving/braking commands required to achieve the desired vehicle forces and moment, and minimize the maximum tire force usage. The force usage of the tire under the worst force usage condition is minimized to avoid the saturation of tire forces. If the tire forces are saturated, the vehicle motion may become unstable and collision avoidance may not be realized. The lower level controller is referred to as the tire force distributor. For problem simplification, an optimal state feedback controller that is capable of responding to situation changes (such as lateral movement of the obstacle during the maneuver) can be designed.

In order to cope with the situation changes, Ohmuro and Hattori [84] proposed a feedback optimal control method that gave the resultant vehicle force and force direction angle based on the relative distance and velocity between the vehicle and the obstacle. In their paper, the collision avoidance problem was formulated as a minimum resultant vehicle force optimal control problem. Using Pontryagin's Minimum Principle, which gives the necessary conditions for optimality, a two-point boundary value problem (TPBVP) was obtained. The solution of this TPBVP is given by simultaneous nonlinear equations. Because of the difficulty expected in solving these equations for online implementation, a pair of two-dimensional maps for the resultant vehicle force and the force direction angle was proposed.

In this chapter, we derived a dimensionless equation that gives the state feedback optimal control for the minimum resultant vehicle force problem. This equation is an implicit equation in an unknown that is a control parameter. Since only one implicit equation in one unknown is to be solved, one-dimensional robust root finding methods with a reliable search bound can provide a stable solution to the control problem. For the same objective function, a more precise solution can be expected from the proposed method than that given by the lookup table approach (as shown in [84]).

In Chapter 2, we proposed a dimensionless equation that gave the optimal state feedback control for the minimum longitudinal avoidance distance based on the maximum available vehicle force; which was limited by the tire-road friction coefficient. The drawback of the minimum longitudinal avoidance distance problem, from a feedback control viewpoint, is that a fixed maximum available force will cause a change in the longitudinal distance; which is undesirable, as collision avoidance may not be achieved in a case where there is a situation change after the initiation of the avoidance maneuver. In this chapter, since the longitudinal distance to the obstacle is an input, and the resultant vehicle force is minimized, the longitudinal distance can be updated according to the situation change and the resultant vehicle force is reduced to a minimum value. Furthermore, in Chapter 2, detailed simulations using a tire force distributor and high-fidelity vehicle model were not included. In this chapter, simulations are performed using a tire force distributor and a vehicle model coupled with a nonlinear tire model.

The total longitudinal force and the total lateral force, given by the optimal controller, should be distributed to the tires using a distributor that minimizes tire force usage. If the friction coefficients at the four tires are assumed to be equal, then the maximum tire workload is a reasonable objective function to be minimized. Tire workload is defined as the ratio between the resultant tire force and the vertical tire force [70]. Assuming the integration of steering and driving/braking, Mokhiamar and Abe proposed a minimization of the squared sum of the workload of each tire for four-wheel independent steering (4WIS) [70]. The minimization of the squared sum of the workload of each tire does not effectively describe the problem of a tire experiencing a severe load condition [79]. For 4WIS, Ono *et al.* developed an optimal tire force distribution with tire force usage equalization criteria [87]. Nishihara and Higashino investigated and clarified the performance limits of the minimax optimization that considers the worst workload condition [81]. This optimization problem was investigated for both 4WIS and four-wheel steering (4WS).

In this chapter, a more practical 4WS configuration is considered instead of the 4WIS. In the minimax optimization for 4WS, the optimization of tire force distribution is reduced to a one-dimensional optimization problem; for which the robust and reasonably fast golden section search method becomes applicable [81]. However, in the minimax optimization for 4WIS, three key variables need to be optimized numerically. Therefore, the minimax optimization for 4WS is computationally more efficient than that of the 4WIS.

The remainder of this chapter is organized as follows. In Section 3.2, the optimal control for obstacle avoidance is derived. Section 3.3 describes the development of the yaw motion controller. Section 3.4 describes the minimax optimization and square sum minimization of tire workload for 4WS. Section 3.5 presents numerical examples on the obstacle avoidance scenarios. Finally, conclusions are presented in Section 3.6.

3.2 Optimal Obstacle Avoidance Control

3.2.1 Emergency Lane Change Maneuver

Fig. 3.1 shows a schematic diagram of an emergency lane change maneuver. An obstacle suddenly appears in the traveling lane of the vehicle. The vehicle will perform an automatic lane change maneuver to avoid a collision if pure braking in the current lane is infeasible. The initial longitudinal and lateral velocities of the vehicle are denoted as v_{x0} and v_{y0}, respectively. The final longitudinal and lateral velocities of the vehicle are represented by v_{xf} and v_{yf}, respectively. At the end of the maneuver, v_{yf} should be zero because, at this time instant, the control authority will be switched from the controller to the human driver. The longitudinal and lateral distances that the vehicle must travel during the avoidance maneuver are denoted as x_f and y_f, respectively. The resultant vehicle force F_t is minimized to avoid tire force saturation. In Fig. 3.1, φ is the force direction angle.

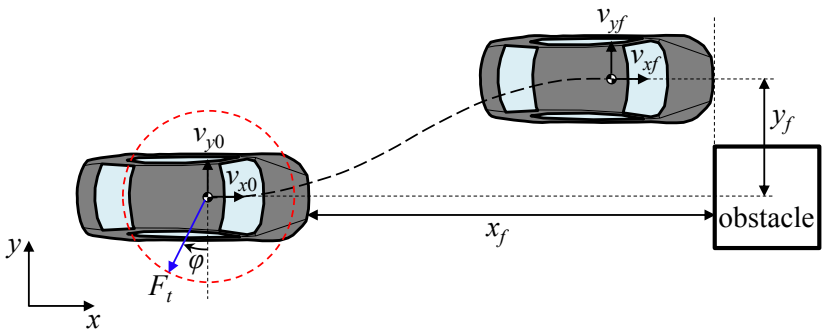

Figure 3.1: Obstacle avoidance lane change maneuver.

3.2.2 Problem Formulation

The problem definition for the minimum resultant vehicle force given here is based on a previous study [40]. A detailed description of this problem can be found in [84]. The minimum resultant vehicle force problem seeks to identify the control input $\boldsymbol{u}(t)$ that minimizes the objective function

$$J = F_t \tag{3.1}$$

subject to the differential constraint

$$\dot{\boldsymbol{x}}(t) = \boldsymbol{f}(\boldsymbol{x}(t), \boldsymbol{u}(t), t), \tag{3.2}$$

the prescribed boundary conditions, and the constraint on the control. The state $\boldsymbol{x}(t)$ and the control input $\boldsymbol{u}(t)$ are written as

$$\boldsymbol{x}(t) = \begin{bmatrix} x_1(t) & x_2(t) & x_3(t) & x_4(t) \end{bmatrix}^T = \begin{bmatrix} x(t) & \dot{x}(t) & y(t) & \dot{y}(t) \end{bmatrix}^T \tag{3.3a}$$

$$\boldsymbol{u}(t) = \begin{bmatrix} u_1(t) & u_2(t) \end{bmatrix}^T = \begin{bmatrix} \dfrac{X_t(t)}{m_t} & \dfrac{Y_t(t)}{m_t} \end{bmatrix}^T \tag{3.3b}$$

where $X_t = m_t\ddot{x}$ is the longitudinal vehicle force, $Y_t = m_t\ddot{y}$ is the lateral vehicle force, and m_t is the total vehicle mass. The following equality constraint on the control must hold:

$$u_1^2(t) + u_2^2(t) = \left(\frac{F_t}{m_t}\right)^2 \tag{3.4}$$

The initial conditions of the states are

$$\boldsymbol{x}(t_0) = \begin{bmatrix} x(t_0) & \dot{x}(t_0) & y(t_0) & \dot{y}(t_0) \end{bmatrix}^T = \begin{bmatrix} 0 & v_{x0} & 0 & v_{y0} \end{bmatrix}^T \tag{3.5}$$

where t_0 is the initial time and is equal to zero. The final conditions are represented as

$$\boldsymbol{\psi}(\boldsymbol{x}(t), t) = \begin{bmatrix} x(t) - x_f & y(t) - y_f & \dot{y}(t) \end{bmatrix}^T \tag{3.6a}$$

$$\boldsymbol{\psi}(\boldsymbol{x}(t_f), t_f) = 0 \tag{3.6b}$$

where t_f is the final time, which is set to be free in order to obtain a better result than that expected under the assumption of an intuitive fixed final time.

3.2.3 Solution of the Optimal Control Problem

Hattori and Ohmuro have shown that the minimum resultant vehicle force problem is strongly related to the minimum longitudinal avoidance distance problem [40]. These two problems have different sets of given and unknown. In the minimum longitudinal avoidance distance problem, F_t is given and x_f is determined, whereas in the minimum resultant vehicle force problem, x_f is given and F_t is determined. This relation is clearly understood in the light of the bi-objective optimization problem. Fig. 3.2 shows the trade-off curve for $m_t = 1830$ kg, $v_{x0} = 30$ m/s, $v_{y0} = 0$ m/s, and $y_f = 3.5$ m. The value of x_f is specified, and the corresponding F_t is to be determined in this chapter. The trade-off curve is recognizable as the Pareto front to the bi-objective optimization problem that minimizes the longitudinal avoidance distance and the resultant vehicle force.

In Chapter 2, the solution of the optimal control problem for the minimum longitudinal avoidance distance is given by four equations. First, three equations are solved simultaneously, and the remaining equation is then used to determine the longitudinal avoidance distance based on this solution. Since these two optimal control problems are related to the same bi-objective optimization, the four equations derived for the minimum longitudinal avoidance distance are used for the determination of the minimum resultant

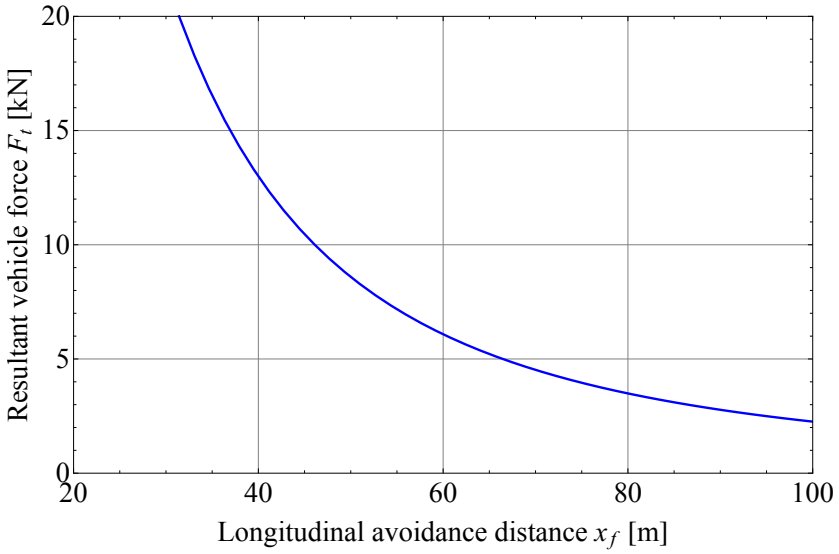

Figure 3.2: Trade-off curve. This plot is an example for $m_t = 1830$ kg, $v_{x0} = 30$ m/s, $v_{y0} = 0$ m/s, and $y_f = 3.5$ m.

vehicle force.

$$\frac{m_t v_{x0}}{F_t} - \frac{\nu_1 \nu_2 \eta}{\left(1+\nu_1^2\right)^{3/2}} - \frac{\nu_1^2 \nu_2 + \sqrt{\left(\nu_1 t_f + \nu_2\right)^2 + t_f^2}}{1+\nu_1^2} = 0 \tag{3.7a}$$

$$\begin{aligned}&\frac{m_t v_{x0} t_f}{F_t} - \frac{3\nu_2^2 \eta}{2\left(1+\nu_1^2\right)^{5/2}} - \frac{3\nu_1 \nu_2^2}{2\left(1+\nu_1^2\right)^2} + \frac{\nu_2^2 \eta}{\left(1+\nu_1^2\right)^{3/2}} \\ &- \frac{\left[\left(1+\nu_1^2\right) t_f - 3\nu_1 \nu_2\right] \sqrt{\left(\nu_1 t_f + \nu_2\right)^2 + t_f^2}}{2\left(1+\nu_1^2\right)^2} - \frac{m_t x_f}{F_t} = 0\end{aligned} \tag{3.7b}$$

$$\frac{m_t v_{y0}}{F_t} + \frac{\nu_2 \eta}{\left(1+\nu_1^2\right)^{3/2}} + \frac{\nu_1 \nu_2 - \nu_1 \sqrt{\left(\nu_1 t_f + \nu_2\right)^2 + t_f^2}}{1+\nu_1^2} = 0 \tag{3.7c}$$

$$\begin{aligned}&\frac{m_t v_{y0} t_f}{F_t} - \frac{m_t y_f}{F_t} - \frac{3\nu_1 \nu_2^2 \eta}{2\left(1+\nu_1^2\right)^{5/2}} - \frac{\left(\nu_1^2 - 2\right)\nu_2^2}{2\left(1+\nu_1^2\right)^2} \\ &- \frac{\left[\left(1+\nu_1^2\right)\nu_1 t_f - \left(\nu_1^2 - 2\right)\nu_2\right] \sqrt{\left(\nu_1 t_f + \nu_2\right)^2 + t_f^2}}{2\left(1+\nu_1^2\right)^2} = 0\end{aligned} \tag{3.7d}$$

where

$$\eta = \ln\left(\frac{\sqrt{1+\nu_1^2}\sqrt{\left(\nu_1 t_f + \nu_2\right)^2 + t_f^2} - \nu_1 \nu_2 - \left(1+\nu_1^2\right) t_f}{\nu_2 \sqrt{1+\nu_1^2} - \nu_1 \nu_2}\right)$$

In (3.7a) to (3.7d), ν_1 and ν_2 are the terminal Lagrange multipliers. In this problem, these multipliers, t_f, and F_t are the unknowns. Solving (3.7a) with respect to F_t/m_t

and substituting the solution into (3.7b) to (3.7d) eliminates F_t/m_t. The resulting three equations are solved simultaneously for ν_1, ν_2, and t_f. These simultaneous equations are highly nonlinear and are not easily solved. The complexity of this problem is considerably reduced by nondimensionalization and algebraic manipulations.

The optimal control (3.3b) can be expressed in the following form [42]:

$$u_1(t) = -\frac{F_t}{m_t}\frac{-t+t_f}{\sqrt{(-t+t_f)^2+(-\nu_1 t+\nu_1 t_f+\nu_2)^2}} \tag{3.8a}$$

$$u_2(t) = -\frac{F_t}{m_t}\frac{-\nu_1 t+\nu_1 t_f+\nu_2}{\sqrt{(-t+t_f)^2+(-\nu_1 t+\nu_1 t_f+\nu_2)^2}} \tag{3.8b}$$

3.2.4 Nondimensionalization

By introducing the following dimensionless variables, the three simultaneous equations can be converted into dimensionless form:

$$L_y = \frac{y_f}{x_f}, V_y = \frac{v_{y0}}{v_{x0}}, N_1 = \nu_1, N_2 = \frac{\nu_2}{t_f}, \tau_f = \frac{v_{x0}t_f}{x_f} \tag{3.9}$$

Using the definitions given in (3.9), after some manipulation, we obtain three dimensionless equations:

$$\begin{aligned} &N_1N_2\eta\left[\tau_f\left(2V_yP_1-3N_2\right)-2L_yP_1\right]-\sqrt{P_1}\left\{N_2^2\tau_fP_2\right. \\ &\quad +P_1P_3\left[2L_y+\tau_f\left(N_1-2V_y\right)\right] \\ &\quad \left.+N_2\left[2N_1^2P_1\left(L_y-V_y\tau_f\right)-\tau_fP_2P_3\right]\right\}=0 \end{aligned} \tag{3.10a}$$

$$\begin{aligned} &N_2^2\eta\left[L_y+3P_4-V_y\tau_f-2N_1^2\left(L_y-V_y\tau_f\right)\right] \\ &\quad +\sqrt{P_1}\left(N_2^2\left\{2-2\tau_f+N_1\left[3L_y+P_4-3V_y\tau_f\right]\right\}\right. \\ &\quad +P_1P_3\left[L_y+P_4-V_y\tau_f\right] \\ &\quad \left.+N_2\left\{2\left(\tau_f-1\right)-N_1\left[3L_y+P_4-3V_y\tau_f\right]\right\}P_3\right)=0 \end{aligned} \tag{3.10b}$$

$$\begin{aligned} &N_2\eta\left[2L_yP_1-V_y\tau_f\left(2P_1+3N_1N_2\right)\right] \\ &\quad +\sqrt{P_1}\left\{N_2\left[V_y\tau_fP_2P_3+2\left(N_1+N_1^3\right)\left(L_y-V_y\tau_f\right)\right]\right. \\ &\quad \left.-N_2^2V_y\tau_fP_2-N_1P_1P_3\left(2L_y-V_y\tau_f\right)\right\}=0 \end{aligned} \tag{3.10c}$$

where

$$\eta = \ln\left(\frac{\left(N_1+\sqrt{P_1}\right)\left[P_3\sqrt{P_1}-N_1\left(N_1+N_2\right)-1\right]}{N_2}\right)$$

with

$$
\begin{aligned}
P_1 &= 1 + N_1^2 \\
P_2 &= N_1^2 - 2 \\
P_3 &= \sqrt{1 + (N_1 + N_2)^2} \\
P_4 &= N_1 (\tau_f - 1)
\end{aligned}
$$

3.2.5 Derivation of Optimal Feedback Control

In this subsection, we derive the solution for the feedback optimal control. The principle of optimality [21] states that all points on the optimal trajectory can be treated as the initial points for that trajectory. This concept is useful in deriving the optimal feedback control law. For simplicity, the point mass model of the vehicle is assumed as in the previous studies [84, 40]. Even with this assumption, the solution for the feedback optimal control is not easy, especially in the case of online optimization.

If $t = 0$ is regarded as the current time, the optimal control given in (3.8a) and (3.8b) reduces to

$$
u_1(0) = -\frac{F_t}{m_t} \frac{t_f}{\sqrt{t_f^2 + (\nu_1 t_f + \nu_2)^2}} \tag{3.11a}
$$

$$
u_2(0) = -\frac{F_t}{m_t} \frac{\nu_1 t_f + \nu_2}{\sqrt{t_f^2 + (\nu_1 t_f + \nu_2)^2}} \tag{3.11b}
$$

(3.11a) and (3.11b) are the current optimal control inputs. Now, v_{x0} is the current longitudinal velocity, v_{y0} is the current lateral velocity, x_f is the longitudinal distance-to-go, y_f is the lateral distance-to-go, and t_f is the time-to-go. Note that (3.10a) to (3.10c) constitute a nonlinear feedback law since they are representations of N_1, N_2, and τ_f determined as implicit functions of L_y and V_y.

In the previous studies [84, 40], numerical mapping tables from $\{L_y, V_y\}$ to the dimensionless form of the resultant vehicle force and the force direction angle were developed in order to represent the optimal feedback control. Fairly good approximation using these lookup tables could be obtained at the expense of a large amount of storage memory. Moreover, individual mappings are also required to compute other quantities, e.g., the final time and final longitudinal velocity.

In order to overcome these problems, we reduce the solution of simultaneous equations (3.10a) to (3.10c) to a one-dimensional root finding problem. In the general case, $V_y \neq 0$, the solution process is more involved than the special case $V_y = 0$ that is discussed in the next subsection.

Equations (3.10a) to (3.10c) contain the natural logarithmic function η. The key idea here is to remove η so that we can obtain polynomial equations. By eliminating η, after some manipulation, (3.10a) and (3.10b) are reduced to a single equation:

$$\begin{aligned} &N_2^3\tau_f + N_2^2\left[2N_1\left(1+L_yN_1\right) - \tau_f P_3 - 2N_1\tau_f\left(1+N_1V_y\right)\right] \\ &+ P_3\left[L_y\left(N_1-N_2\right) + N_1P_4 + N_2V_y\tau_f + N_1\left(N_2 - V_y\tau_f\right)\right] = 0 \end{aligned} \tag{3.12}$$

Similarly, (3.10a) and (3.10c) give

$$2L_yP_1P_3 - 2N_2^2\tau_f\left(1+N_1V_y\right) - \tau_fP_3\left\{V_y\left[2+N_1\left(N_1+N_2\right)\right] - N_1 - 2N_2\right\} = 0 \tag{3.13}$$

and (3.10b) and (3.10c) give

$$\begin{aligned} &N_2^3V_y\tau_f + P_3\left[N_1+2N_2+L_y\left(2N_1N_2-1\right)\right] - \tau_fP_3\left[N_1+2N_2+V_y\left(N_1N_2-1\right)\right] \\ &- N_2^2\left[2-2\tau_f+V_y\tau_fP_3+2N_1\left(L_y-V_y\tau_f\right)\right] = 0 \end{aligned} \tag{3.14}$$

Eliminating P_3 from (3.12) to (3.14), we obtain another three equations. These new equations have a common factor that is given in the left-hand side of (3.15). This factor corresponds to the common root of (3.12) to (3.14).

$$2 + 2L_yN_1 - \tau_f\left[1+V_y\left(N_1+N_2\right)\right] = 0 \tag{3.15}$$

By isolating the radical P_3 in (3.14) and then taking the square of both sides of the equation and rearranging the result, we obtain

$$\begin{aligned} &N_2^4\left\{2+2L_yN_1-\tau_f\left[2+V_y\left(2N_1+N_2\right)\right]\right\}^2 \\ &-\left[1+\left(N_1+N_2\right)^2\right]\left(L_y-N_1-2N_2\left(1+L_yN_1\right)\right. \\ &\left.+\tau_f\left\{N_1+2N_2+V_y\left[N_2\left(N_1+N_2\right)-1\right]\right\}\right)^2 = 0 \end{aligned} \tag{3.16}$$

Both (3.15) and (3.16) are polynomial equations with respect to τ_f. One of the elimination methods that can be used to remove τ_f is taking the resultant of (3.15) and (3.16) with respect to τ_f. Equation (3.15) can be rewritten as

$$f\left(\tau_f\right) = a_1\tau_f + a_0 = 0 \tag{3.17}$$

and (3.16) can be rewritten as

$$g\left(\tau_f\right) = b_2\tau_f^2 + b_1\tau_f + b_0 = 0 \tag{3.18}$$

where a_1, a_0, b_2, b_1, and b_0 are the coefficients of the respective polynomials.

By taking the resultant of (3.17) and (3.18) with respect to τ_f, we obtain an equation that is a sixth-order polynomial with respect to N_1 and a fourth-order polynomial with respect to N_2. We focus on the fourth-order polynomial, because a closed-form solution

is obtainable for a quartic equation [13], as shown in this section. This quartic equation is written as

$$f_4(N_2) = c_4 N_2^4 + c_3 N_2^3 + c_2 N_2^2 + c_1 N_2 + c_0 = 0 \tag{3.19}$$

where

$$\begin{aligned}
c_4 =& V_y \left[N_1 \left(3 + 2L_y N_1\right) - L_y\right] \left\{4 + N_1 V_y + L_y \left[V_y + 2N_1 \left(2 + N_1 V_y\right)\right]\right\} \\
c_3 =& -2 \left[L_y + N_1 \left(3 + 4L_y N_1\right) - 2V_y P_1\right] \left[2 - N_1 V_y + L_y \left(2N_1 + V_y\right)\right] \\
c_2 =& 18N_1^3 \left(V_y - 2L_y\right) - 6N_1^4 \left(V_y - 2L_y\right)^2 - \left(4 + L_y^2\right)\left(1 + V_y^2\right) \\
&+ N_1^2 \left[36L_y V_y + 2L_y^2 \left(V_y^2 - 8\right) - 13\left(1 + V_y^2\right)\right] + 6N_1 \left\{V_y \left[4 + L_y \left(V_y - L_y\right)\right] - 3L_y\right\} \\
c_1 =& -2 \left\{2V_y - L_y + N_1 \left[V_y \left(L_y + N_1\right) - 2L_y N_1 - 1\right]\right\} \\
&\left\{N_1 \left[3V_y + N_1 \left(2N_1 V_y - 3\right)\right] - L_y \left[3N_1 + 4N_1^3 + V_y\right] - 2\right\} \\
c_0 =& -P_1 \left\{N_1 + L_y \left(1 + 2N_1^2\right) - V_y \left[2 + N_1 \left(L_y + N_1\right)\right]\right\}^2
\end{aligned}$$

Let $d_3 = c_3/c_4$, $d_2 = c_2/c_4$, $d_1 = c_1/c_4$, and $d_0 = c_0/c_4$. Then, (3.19) is rewritten as

$$N_2^4 + d_3 N_2^3 + d_2 N_2^2 + d_1 N_2 + d_0 = 0 \tag{3.20}$$

Assuming that the coefficients d_3, d_2, d_1, and d_0 are real, (3.20) is factorized as

$$\left(N_2^2 + e_1 N_2 + k_1\right)\left(N_2^2 + e_2 N_2 + k_2\right) = 0 \tag{3.21}$$

where the two quadratics in (3.21) can have real roots or complex conjugate roots depending on the discriminants which are defined as functions of the coefficients e_1, k_1, e_2, and k_2. We are interested in finding the real root that gives the minimum resultant vehicle force.

Expanding (3.21) gives

$$N_2^4 + \left(e_1 + e_2\right) N_2^3 + \left(e_1 e_2 + k_1 + k_2\right) N_2^2 + \left(e_1 k_2 + e_2 k_1\right) N_2 + k_1 k_2 = 0 \tag{3.22}$$

By equating the coefficients in (3.20) and (3.22), the following system of equations is obtained:

$$e_1 + e_2 = d_3 \tag{3.23a}$$

$$e_1 e_2 + k_1 + k_2 = d_2 \tag{3.23b}$$

$$e_1 k_2 + e_2 k_1 = d_1 \tag{3.23c}$$

$$k_1 k_2 = d_0 \tag{3.23d}$$

The application of the Vieta's theorem using (3.23) leads to two quadratic equations [109] which when solved separately give the coefficients e_1, e_2, k_1, and k_2.

$$e^2 - d_3 e + d_2 - z_c = 0 \tag{3.24a}$$

$$k^2 - z_c k + d_0 = 0 \tag{3.24b}$$

z_c can be derived from (3.23c), and a cubic resolvent of (3.20) is obtained.

$$z_c^3 - d_2 z_c^2 + (d_3 d_1 - 4d_0)\, z_c + 4d_2 d_0 - d_1^2 - d_3^2 d_0 = 0 \tag{3.25}$$

The discriminant of the cubic (3.25) is given by

$$D_3 = Q^3 + R^2 \tag{3.26}$$

where

$$\begin{aligned} Q =& -\frac{1}{9}\left(d_2^2 - 3d_3 d_1 + 12 d_0\right) \\ R =& \frac{1}{54}\left(2d_2^3 + 27 d_3^2 d_0 + 27 d_1^2 - 9 d_3 d_2 d_1 - 72 d_2 d_0\right) \end{aligned}$$

If D_3 is positive, there is only one real root

$$z_{c1} = \frac{d_2}{3} + S + T \tag{3.27}$$

where

$$\left.\begin{matrix} S \\ T \end{matrix}\right\} = \sqrt[3]{R \pm \sqrt{D_3}}$$

and if D_3 is negative, there are three real roots

$$z_{c1} = \frac{d_2}{3} + 2\sqrt{-Q}\cos\left(\frac{\theta}{3}\right) \tag{3.28a}$$

$$z_{c2} = \frac{d_2}{3} + 2\sqrt{-Q}\cos\left(\frac{\theta + 2\pi}{3}\right) \tag{3.28b}$$

$$z_{c3} = \frac{d_2}{3} + 2\sqrt{-Q}\cos\left(\frac{\theta + 4\pi}{3}\right) \tag{3.28c}$$

where

$$\theta = \arccos\left(\frac{R}{\sqrt{-Q^3}}\right)$$

Let z_{c1} be the real root of (3.25). Then, solving (3.24a) with respect to e yields

$$\left.\begin{matrix} e_1 \\ e_2 \end{matrix}\right\} = \frac{1}{2}\left(d_3 \pm \sqrt{d_3^2 - 4d_2 + 4z_{c1}}\right) \tag{3.29}$$

Instead of solving (3.24b) with respect to k, simultaneous equations (3.23b) and (3.23c) are solved with respect to k_1 and k_2.

$$\left.\begin{matrix} k_1 \\ k_2 \end{matrix}\right\} = \frac{1}{2}\left(z_{c1} \pm \frac{d_3 z_{c1} - 2d_1}{\sqrt{d_3^2 - 4d_2 + 4z_{c1}}}\right) \tag{3.30}$$

The expressions of the coefficients in (3.29) and (3.30) are the same as they appear in [13]. Then, the roots of the quartic equation can be computed by separately solving the two quadratics in (3.21).

$$\left.\begin{matrix} N_{2a} \\ N_{2b} \end{matrix}\right\} = -\frac{e_1}{2} \pm \sqrt{\frac{e_1^2}{4} - k_1} \tag{3.31a}$$

$$\left.\begin{matrix} N_{2c} \\ N_{2d} \end{matrix}\right\} = -\frac{e_2}{2} \pm \sqrt{\frac{e_2^2}{4} - k_2} \tag{3.31b}$$

From the roots given in (3.31), the two roots N_{2c} and N_{2d} provide the appropriate solution to the minimum resultant vehicle force problem, depending on the combination of L_y and V_y. We have identified the switching condition between these two roots as the zero radicand of the second term in (3.31b). Fig. 3.3 shows the curve that corresponds to the zero radicand. For the region above the switching curve, N_{2c} is the appropriate root, and for the region below the curve, N_{2d} is the appropriate root.

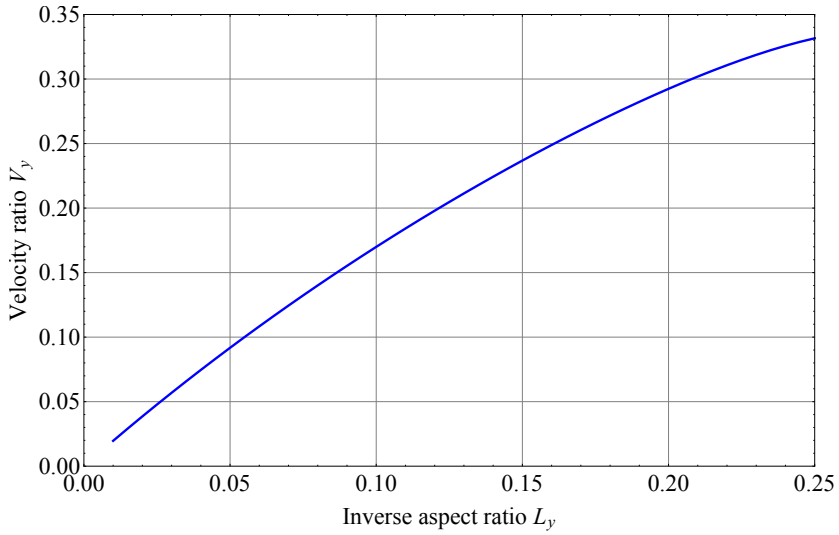

Figure 3.3: Switching curve for the selection of appropriate quartic roots. For the region above the curve, N_{2c} is selected, and for the region below the curve, N_{2d} is selected.

We have obtained the solution of N_2 as a function of N_1. Next, we will find τ_f as a function of N_1 and N_2. This is done by solving (3.15) with respect to τ_f.

$$\tau_f = \frac{2(1 + L_y N_1)}{1 + V_y (N_1 + N_2)} \tag{3.32}$$

Now, we have the closed-form solutions $N_2(N_1)$ and $\tau_f(N_1, N_2)$. Substituting $N_2(N_1)$ into $\tau_f(N_1, N_2)$ gives $\tau_f(N_1, N_2(N_1))$. Then, substituting the resulting equation and $N_2(N_1)$ into (3.10a) yields $f_1(N_1, N_2(N_1), \tau_f(N_1, N_2(N_1))) = 0$. The resulting equation is equivalent to the simultaneous equations (3.10a) to (3.10c) with only one unknown N_1. Note that the closed-form solution of this nonlinear equation is not expectable. In order to solve $f_1(N_1, N_2(N_1), \tau_f(N_1, N_2(N_1))) = 0$ with respect to N_1, the bisection method is chosen because of its robustness.

Unlike other root solving methods, such as Newton's method, that require only an initial guess, or the secant method, which requires two initial guesses near the root, the

bisection method requires a starting interval containing the root. In order to set up the lower and upper bounds of this interval, a numerical mapping table from $\{L_y, V_y\}$ to N_1 must first be built. However, a relatively large amount of data is required due to the shape of the surface. This is why function approximation using lower-order polynomials is not considered here. Instead of building a numerical mapping from $\{L_y, V_y\}$ to N_1, we choose to build the table from $\{\tilde{L}_y, \tilde{V}_y\}$ to N_1, where

$$\tilde{L}_y = \frac{L_y - \frac{1}{2}(L_{yu} + L_{yl})}{\frac{1}{2}(L_{yu} - L_{yl})} \tag{3.33a}$$

$$\tilde{V}_y = \frac{V_y - \frac{1}{2}(V_{yu} + V_{yl})}{\frac{1}{2}(V_{yu} - V_{yl})} \tag{3.33b}$$

with $L_{yl} = 0.01$, $L_{yu} = 0.1716314$, $V_{yl} = 0$, and V_{yu} varying with L_y as indicated by the blue solid curve in Fig. 3.4a. This curve corresponds to $N_1 = -1.5$. By performing the change of variables as in (3.33), the non-rectangular domain in Fig. 3.4a is transformed into a rectangular domain as in Fig. 3.4b. A lookup table is built for this domain, and the search interval is set based on the resulting lookup table. The advantage of building a lookup table using the change of variables (3.33) over the original variables is that fewer data are required to obtain a reasonably accurate approximation of N_1.

3.2.6 Special Case in which $V_y = 0$

If the lateral velocity at the beginning of the maneuver is equal to zero ($V_y = 0$), then c_4 becomes zero. Therefore, N_2 cannot be computed using (3.31). In this case, the quartic in (3.19) reduces to a cubic given as

$$f_3(N_2) = p_3 N_2^3 + p_2 N_2^2 + p_1 N_2 + p_0 = 0 \tag{3.34}$$

where

$$\begin{aligned}
p_3 &= -4(1 + L_y N_1)(L_y + 3N_1 + 4L_y N_1^2) \\
p_2 &= -4 - 13N_1^2 - 18L_y(N_1 + 2N_1^3) - L_y^2(1 + 16N_1^2 + 24N_1^4) \\
p_1 &= -2(L_y + N_1 + 2L_y N_1^2)[2 + 3N_1^2 + L_y N_1(3 + 4N_1^2)] \\
p_0 &= -P_1(L_y + N_1 + 2L_y N_1^2)^2
\end{aligned}$$

Equation (3.34) is transformed into the monic form by setting $q_2 = p_2/p_3$, $q_1 = p_1/p_3$, and $q_0 = p_0/p_3$.

$$N_2^3 + q_2 N_2^2 + q_1 N_2 + q_0 = 0 \tag{3.35}$$

The appropriate solution to the cubic equation (3.35) is

$$N_2 = -\frac{q_2}{3} + 2\sqrt{-Q_0}\cos\left(\frac{\theta_0}{3}\right) \tag{3.36}$$

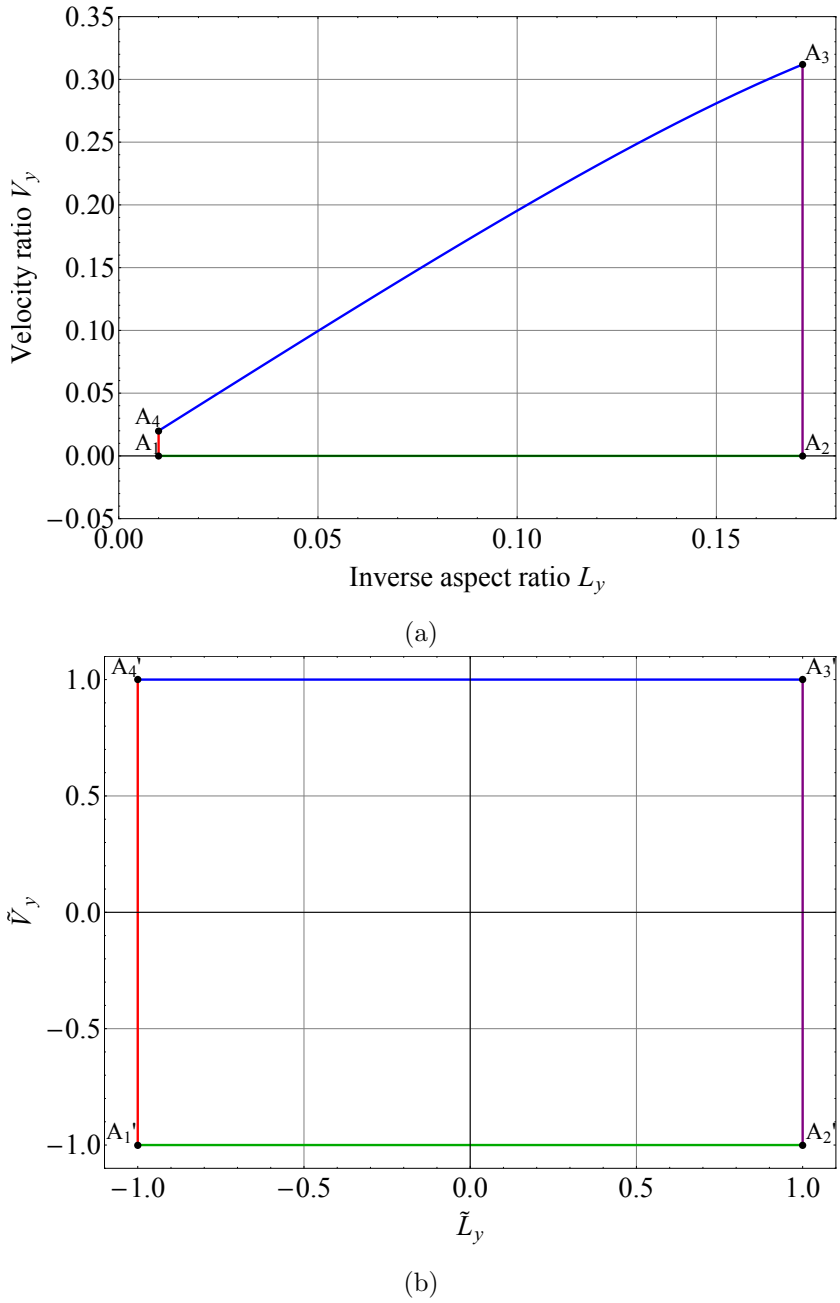

Figure 3.4: Mapping of a (a) non-rectangular shape to a (b) rectangle.

where

$$\theta_0 = \arccos\left(\frac{R_0}{\sqrt{-Q_0^3}}\right)$$
$$Q_0 = \frac{3q_1 - q_2^2}{9}$$
$$R_0 = \frac{9q_2q_1 - 27q_0 - 2q_2^3}{54}$$

Substituting $V_y = 0$ into (3.32) gives

$$\tau_f = 2(1 + L_y N_1) \tag{3.37}$$

Next, we substitute (3.36) and (3.37) into (3.10a). The resulting equation is a function of a single unknown N_1, but a closed-form solution for N_1 is not expected. For given L_y, N_1 is determined iteratively using the bisection method. In order to set up the initial search interval, a degree-four Chebyshev polynomial is prepared to approximate the inverse of N_1, which is denoted as $1/N_1(L_y)$. For the interval $0.01 \leq L_y \leq 0.17$, the approximation is

$$\frac{1}{N_1(L_y)} \approx A = -496.64L_y^4 + 100.489L_y^3 - 10.7973L_y^2 - 1.67289L_y - 0.00281681 \quad (3.38)$$

Fig. 3.5 shows the exact solutions of N_1. The approximation on $1/N_1(L_y)$ turned out to be more accurate than that of N_1, as implied by the shape of the curve in Fig. 3.5. The lower and upper bounds of the initial search interval are set as $1.03/A$ and $0.97/A$, respectively, and are shown in Fig. 3.5. Efficient evaluation of the polynomial in (3.38) is performed using Horner's method [45].

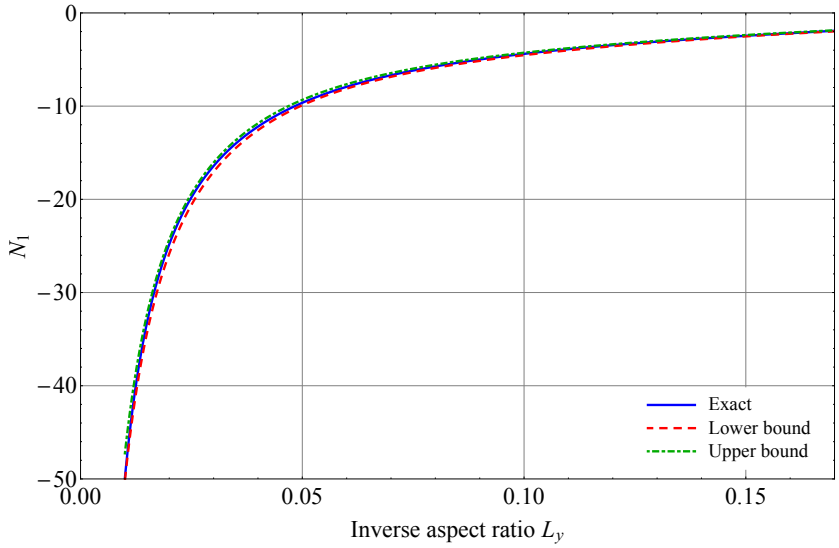

Figure 3.5: Exact solutions together with the bounds for the dimensionless terminal Lagrange multiplier.

3.2.7 Decision Making for Collision Avoidance

The vehicle force F, either resultant, longitudinal, or lateral, can be defined in a dimensionless form and is then referred to as the dimensionless vehicle force [111]

$$\pi_F = \frac{y_f}{m_t v_{x0}^2} F \quad (3.39)$$

For steering with braking avoidance, the vehicle force required to avoid a collision is F_t, and the dimensionless form is denoted as π_{Ft}. We consider two additional avoidance

maneuvers: steering avoidance and braking avoidance. In steering avoidance, the vehicle moves in a purely lateral direction, satisfying the final lateral distance y_f and zero final lateral velocity constraints. In braking avoidance, the vehicle makes a full stop in the traveling lane with zero longitudinal distance between the front of the vehicle and the rear of the obstacle. The vehicle forces required to avoid collision for steering avoidance and braking avoidance maneuvers are denoted as F_s and F_b, respectively, and are given by

$$F_s = \frac{4m_t v_{x0}^2 y_f}{x_f^2} \tag{3.40a}$$

$$F_b = \frac{m_t v_{x0}^2}{2x_f} \tag{3.40b}$$

These equations are based on the equations for steering and braking avoidances as given in [42].

Using (3.39), the dimensionless vehicle forces for the three avoidance maneuvers are defined as

$$\pi_{Ft} = \frac{y_f}{m_t v_{x0}^2} F_t \tag{3.41a}$$

$$\pi_{Fs} = \frac{y_f}{m_t v_{x0}^2} F_s \tag{3.41b}$$

$$\pi_{Fb} = \frac{y_f}{m_t v_{x0}^2} F_b \tag{3.41c}$$

Let us first consider the case of steering with braking. We solve (3.7a) with respect to F_t. Then, the resulting equation is substituted into (3.41a), and using the definitions in (3.9), we have

$$\pi_{Ft} = \frac{L_y P_1^{3/2}}{\tau_f [N_1 N_2 \eta + \sqrt{P_1}(N_1^2 N_2 + P_3)]} \tag{3.42}$$

Similarly, the dimensionless vehicle forces for steering avoidance π_{Fs} and braking avoidance π_{Fb} are obtained as $4L_y^2$ and $L_y/2$, respectively.

Fig. 3.6 shows a plot of the dimensionless vehicle force with respect to the inverse aspect ratio L_y. Each curve in this plot indicates the dimensionless force required for the collision avoidance maneuver. The minimum dimensionless vehicle force is equal to $\min(\pi_{Ft}, \pi_{Fs}, \pi_{Fb})$, and the maneuver with the minimum dimensionless vehicle force is assumed to be the best maneuver. Point A at $L_y = 1/8$ and $\pi_F = 1/16$ is the switching point between the steering avoidance and braking avoidance maneuvers. Similarly, point B at $L_y = 0.171631$ and $\pi_F = 0.085816$ is the switching point between the steering with braking avoidance and braking avoidance maneuvers.

A collision is only avoidable if $\pi_F \leq \pi_{F\max}$ with $\pi_{F\max}$ as the dimensionless vehicle maximum force

$$\pi_{F\max} = \frac{y_f}{m_t v_{x0}^2} F_{\max} \tag{3.43}$$

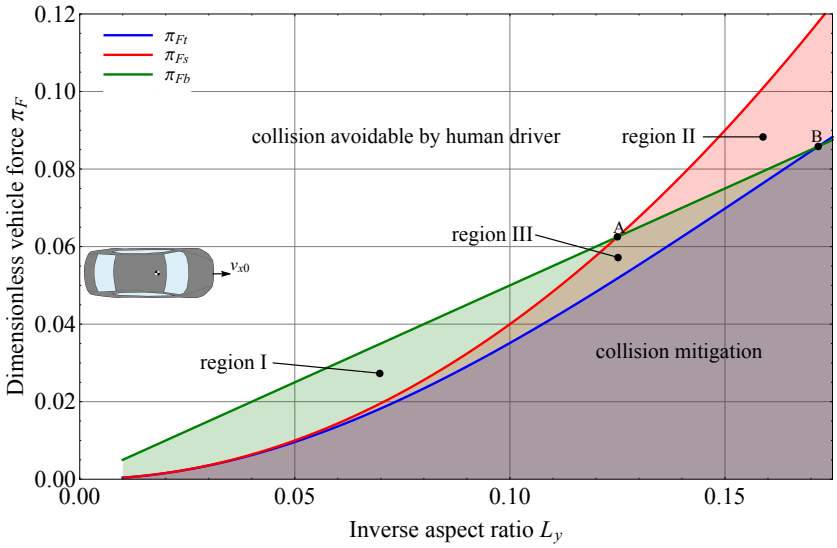

Figure 3.6: Decision making diagram for the most effective maneuver.

where $F_{\max}$ is the maximum available vehicle force, which depends on the vehicle weight and road surface conditions. The case in which $\pi_F > \pi_{F\max}$ simply indicates that the vehicle force required for avoidance is not possible and the collision is not avoidable. Real-time estimation of the tire-road friction coefficient is possible [96], and the maximum force can therefore be estimated.

In Fig. 3.6, the region above $\max(\pi_{Ft}, \pi_{Fs}, \pi_{Fb})$ is the region in which there is no need for an intervention, and the collision can be avoided by a human driver. In region I, the collision can no longer be avoided by the braking avoidance maneuver, and there are two options for the lane change maneuver: steering avoidance and steering with braking avoidance. In region II, the collision can be avoided by either the braking or the steering with braking maneuver. The benefit of using the steering with braking avoidance maneuver is represented by region III, where the collision can only be avoided by the steering with braking maneuver. For the region below $\min(\pi_{Ft}, \pi_{Fs}, \pi_{Fb})$, the collision can no longer be avoided, and full braking in the traveling lane to reduce the vehicle longitudinal velocity would be the best option.

To avoid a vehicle operating at its friction limit, the avoidance maneuver using steering and braking can be initiated at a longitudinal distance to an obstacle longer than the distance that is given if the vehicle is operated at $F_{\max}$. If the intervention is initiated at a vehicle force lower than $F_{\max}$, the reserve force can be used to handle situation change after the intervention has been initiated. For example, in the scenario described in [40], the desired final lateral position increases after the intervention has been initiated. This causes an increase in the resultant vehicle force during the avoidance maneuver. In such a case, if there is sufficient reserve force, the obstacle avoidance is still achievable.

3.2.8 Dimensionless Vehicle CG Path

Let us introduce a dimensionless longitudinal distance traveled, which is the ratio of the longitudinal distance traveled x to the final longitudinal distance x_f. The ratio is derived as

$$\frac{x}{x_f} = \frac{\tau_f \Delta_x}{2L_y P_1^{5/2}} \tag{3.44}$$

where

$$\begin{aligned}\Delta_x =& N_2\tau_f\pi_{Ft}\eta_0[N_2(2N_1^2-1) - 2N_1P_1P_6] + \sqrt{P_1}\{3N_1N_2\tau_f\pi_{Ft}(P_3-P_5) \\ &+ P_1[2L_yP_1\tau + \tau_f\pi_{Ft}(P_3 - 2P_3\tau + P_5P_6)]\}\end{aligned}$$

$$\begin{aligned}P_5 &= \sqrt{1+(N_1+N_2)^2 - 2\tau - 2N_1\tau(N_1+N_2) + P_1\tau^2} \\ P_6 &= \tau - 1\end{aligned}$$

$$\eta_0 = \ln\left(\frac{1+N_1(N_1+N_2) - P_3\sqrt{P_1}}{1+N_1(N_1+N_2) - P_5\sqrt{P_1} - P_1\tau}\right)$$

Note that $\tau = t/t_f$ is the dimensionless time. Next, we define dimensionless lateral distance traveled as the ratio of the lateral distance traveled y to the final lateral distance y_f, given by

$$\frac{y}{y_f} = \frac{\tau_f^2\pi_{Ft}\Delta_y}{2L_y^2P_1^{5/2}} \tag{3.45}$$

where

$$\begin{aligned}\Delta_y =& N_2\eta_0(2P_1P_6 - 3N_1N_2) + \sqrt{P_1}\{P_5(N_1P_1P_6 - N_2P_2) \\ &+ P_3[N_1(N_1N_2 + P_1 - 2P_1\tau) - 2N_2]\}\end{aligned}$$

Equations (3.44) and (3.45) can be seen as parametric equations with τ as the independent variable. Fig. 3.7 shows a parametric plot obtained using (3.44) and (3.45) by varying τ from 0 to 1 for given L_y. The purpose of this plot is to show that the shape of the path of vehicle center of gravity (CG) depends only on L_y. There are many combinations of x_f and y_f that give the same value of L_y. Fig. 3.8 shows the trajectories for three example cases corresponding to $L_y = 0.10$.

3.3 Yaw Motion Control

In this section, a yaw motion controller is developed that determines the desired total yaw moment for the vehicle. In a study using optimal control theory, for the obstacle avoidance problem that assumes a rigid body representation of the vehicle, with initial

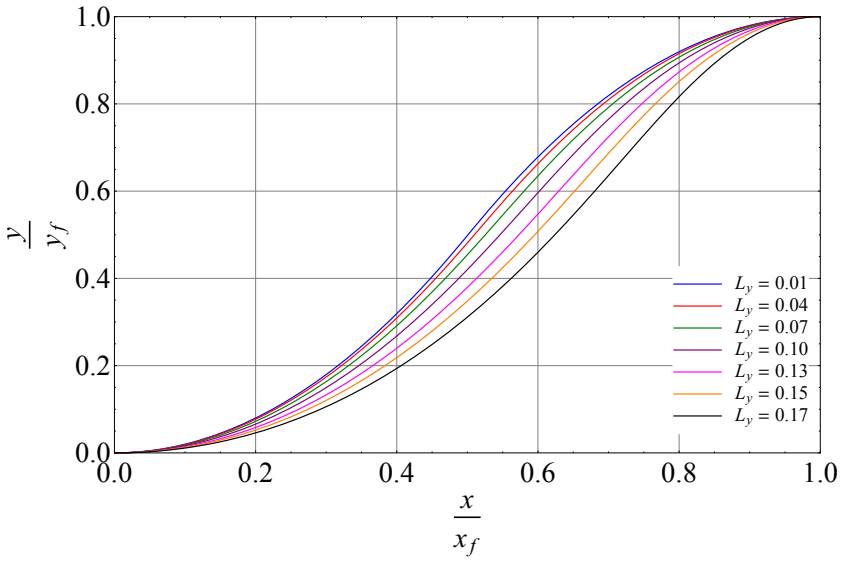

Figure 3.7: Dimensionless vehicle CG paths for various L_y. The shape of the path depends on only L_y.

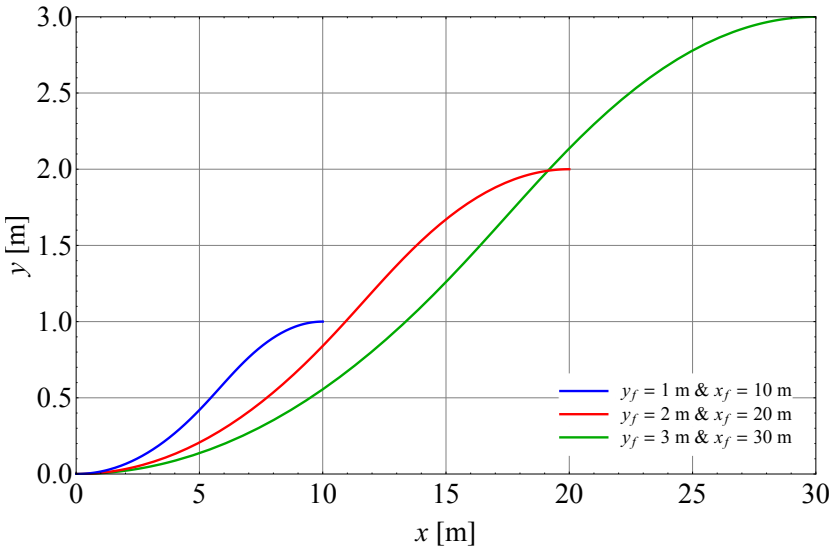

Figure 3.8: Vehicle CG paths for three cases corresponding to $L_y = 0.1$. All three of the curves shown here are simply magnifications of the curve corresponding to $L_y = 0.1$ in Fig. 3.7.

and final conditions of yaw angle and yaw rate at zero, the shortest longitudinal avoidance distance for the given vehicle force is achieved without any yaw motion [41]. To reduce yaw angle and yaw rate, a sliding mode control technique is used in this chapter. The sliding mode control is chosen because of its robustness with respect to the modeling and parametric uncertainties and its successful applications for various nonlinear systems including automotive systems [113]. The sliding surface can be defined as a combination

of yaw angle and yaw rate errors [125]

$$\sigma_z = \lambda_\psi(\psi - \psi_d) + (\gamma - \gamma_d) \tag{3.46}$$

where λ_ψ is a strictly positive constant, ψ is the yaw angle, ψ_d is the desired yaw angle, γ is the yaw rate, and γ_d is the desired yaw rate. The time derivative of (3.46) is

$$\dot{\sigma}_z = \lambda_\psi(\gamma - \gamma_d) + (\dot{\gamma} - \dot{\gamma}_d) \tag{3.47}$$

The yaw dynamics can be written as

$$M_t = I_z\dot{\gamma} \tag{3.48}$$

Substituting $\dot{\gamma} = M_t/I_z$ into (3.47) gives

$$\dot{\sigma}_z = \lambda_\psi(\gamma - \gamma_d) + \left(\frac{M_t}{I_z} - \dot{\gamma}_d\right) \tag{3.49}$$

The equivalent control input is obtained by solving $\dot{\sigma}_z = 0$ with respect to M_t

$$M_{t,eq} = I_z[\dot{\gamma}_d - \lambda_\psi(\gamma - \gamma_d)] \tag{3.50}$$

The control input total yaw moment M_t is written as

$$M_t = M_{t,eq} - k_z \operatorname{sgn}(\sigma_z) \tag{3.51}$$

In order to prevent chattering, the sign function can be approximated as a continuous function [110]

$$\operatorname{sgn}(\sigma_z) \approx \frac{\sigma_z}{|\sigma_z| + \lambda_1} \tag{3.52}$$

where λ_1 is a small positive parameter, and the approximation tends to the sign function as λ_1 tends to zero. Substituting (3.50) and (3.52) into (3.51) gives

$$M_t = I_z[\dot{\gamma}_d - \lambda_\psi(\gamma - \gamma_d)] - k_z\frac{\sigma_z}{|\sigma_z| + \lambda_1} \tag{3.53}$$

Note that $\dot{\gamma}_d = 0$, $\gamma_d = 0$, and $\psi_d = 0$. The gain k_z can be determined from the sliding condition [113] which is defined as

$$\frac{1}{2}\frac{d}{dt}\sigma_z^2 = \sigma_z\dot{\sigma}_z \leq -\eta_z|\sigma_z| \tag{3.54}$$

where η_z is a strictly positive constant. From (3.49), (3.50), (3.51), and (3.54), k_z is obtained as

$$k_z \geq \eta_z I_z \tag{3.55}$$

3.4 Tire Force Distribution

In the previous subsections, the desired longitudinal and lateral vehicle forces and yaw moment are derived. The vehicle is assumed to have full control over the driving, braking, and steering actuators. In this section, we provide a brief formulation of two tire force distribution methods that distribute the longitudinal and lateral vehicle forces, and the yaw moment to the tires in such a way that the workloads of the tires are reduced. Workload is defined as the resultant tire force divided by the vertical tire force [6]. The workload of tire i is given as

$$W_i = \frac{\sqrt{X_i^2 + Y_i^2}}{Z_i} \tag{3.56}$$

where X_i and Y_i are the tire forces in the directions of the longitudinal and lateral vehicle axes, respectively, as shown in Fig. 3.9, and for the purpose of tire force distribution, these forces are treated as the longitudinal and lateral tire forces, respectively. Moreover, Z_i is the estimated vertical tire force of tire i. If the workload of any tire reaches the value of the tire-road friction coefficient, then the tire can no longer generate additional longitudinal and/or lateral force to stabilize the vehicle motion. In order to prevent unstable vehicle motion, the workload should be reduced.

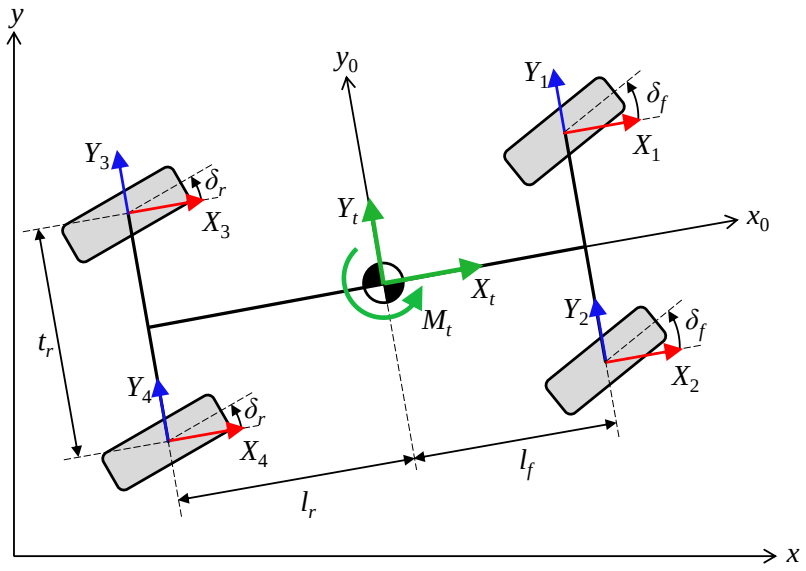

Figure 3.9: Two-track vehicle model.

The longitudinal tire forces must satisfy the following equality constraints for the reference value of total longitudinal force X_t and the direct yaw moment M [81]:

$$X_1 + X_2 + X_3 + X_4 = X_t \tag{3.57a}$$

$$\frac{t_r}{2}(X_2 - X_1 + X_4 - X_3) = M \tag{3.57b}$$

Let $X_1 + X_3 = X_L$ and $X_2 + X_4 = X_R$, and then simultaneously solve (3.57a) and (3.57b) for X_L and X_R to obtain

$$\left.\begin{matrix} X_L \\ X_R \end{matrix}\right\} = \frac{X_t}{2} \mp \frac{M}{t_r} \tag{3.58}$$

Since the left and right wheels on the same axle are assumed to have the same steering angle, the lateral tire force of each tire can be estimated as in [81]

$$Y_1 = \frac{Z_1}{Z_1 + Z_2} \frac{m_t a_p l_r - M}{l_f + l_r} \tag{3.59a}$$

$$Y_2 = \frac{Z_2}{Z_1 + Z_2} \frac{m_t a_p l_r - M}{l_f + l_r} \tag{3.59b}$$

$$Y_3 = \frac{Z_3}{Z_3 + Z_4} \frac{m_t a_q l_f + M}{l_f + l_r} \tag{3.59c}$$

$$Y_4 = \frac{Z_4}{Z_3 + Z_4} \frac{m_t a_q l_f + M}{l_f + l_r} \tag{3.59d}$$

where a_p and a_q are the lateral accelerations of the centers of percussion [81] and are given by

$$a_p = \frac{Y_t}{m_t} + \frac{M_t}{m_t l_r} \tag{3.60a}$$

$$a_q = \frac{Y_t}{m_t} - \frac{M_t}{m_t l_f} \tag{3.60b}$$

Note that Y_t is the total lateral force, and M_t is the total yaw moment. The vertical tire forces can be estimated by taking into account the load transfers due to the pitching and rolling motions [108]

$$Z_1 = \frac{1}{2}\frac{m_s g l_r}{l_f + l_r} + \frac{m_{uf} g}{2} - \frac{1}{2}\frac{m_t a_x h_s}{l_f + l_r} - \frac{m_s a_y h_{sr}}{t_r}\frac{k_{\phi f}}{k_{\phi f} + k_{\phi r}} - \frac{m_s a_y h_f l_r}{t_r (l_f + l_r)} - \frac{m_{uf} a_y h_{uf}}{t_r} \tag{3.61a}$$

$$Z_2 = \frac{1}{2}\frac{m_s g l_r}{l_f + l_r} + \frac{m_{uf} g}{2} - \frac{1}{2}\frac{m_t a_x h_s}{l_f + l_r} + \frac{m_s a_y h_{sr}}{t_r}\frac{k_{\phi f}}{k_{\phi f} + k_{\phi r}} + \frac{m_s a_y h_f l_r}{t_r (l_f + l_r)} + \frac{m_{uf} a_y h_{uf}}{t_r} \tag{3.61b}$$

$$Z_3 = \frac{1}{2}\frac{m_s g l_f}{l_f + l_r} + \frac{m_{ur} g}{2} + \frac{1}{2}\frac{m_t a_x h_s}{l_f + l_r} - \frac{m_s a_y h_{sr}}{t_r}\frac{k_{\phi r}}{k_{\phi f} + k_{\phi r}} - \frac{m_s a_y h_r l_f}{t_r (l_f + l_r)} - \frac{m_{ur} a_y h_{ur}}{t_r} \tag{3.61c}$$

$$Z_4 = \frac{1}{2}\frac{m_s g l_f}{l_f + l_r} + \frac{m_{ur} g}{2} + \frac{1}{2}\frac{m_t a_x h_s}{l_f + l_r} + \frac{m_s a_y h_{sr}}{t_r}\frac{k_{\phi r}}{k_{\phi f} + k_{\phi r}} + \frac{m_s a_y h_r l_f}{t_r (l_f + l_r)} + \frac{m_{ur} a_y h_{ur}}{t_r} \tag{3.61d}$$

where m_s is the sprung mass, l_f is the distance from the vehicle CG to the front axle, l_r is the distance from the vehicle CG to the rear axle, t_r is the track width, and h_s is the height of the sprung mass CG. Note that m_{uf} and m_{ur} are the front and rear unsprung masses, respectively, h_{sr} is the height of the sprung mass CG from the roll center of the sprung mass, h_f and h_r are the heights of the front and rear roll centers, respectively, and h_{uf} and h_{ur} are the heights of the CGs of the front and rear unsprung masses, respectively. Moreover, k_{ϕ_f} and k_{ϕ_r} represent the front and rear roll stiffnesses, respectively.

3.4.1 Minimax Optimization

The first tire force distribution considered here is the minimax optimization method. The details on the derivation and a discussion of this method are presented in [81]. In [81], the vehicle-limited performance was evaluated on the basis of the envelopes on the acceleration plane for different values of total yaw moment. For a smaller total yaw moment, the envelopes for 4WS are almost concentric circles, which is very similar to the case of 4WIS. The longitudinal and lateral tire forces are mainly used to move in longitudinal and lateral directions. This is why the 4WS configuration is adopted here.

For the minimax optimization method, the objective is to minimize the maximum value of the squared tire workload W_i, which is given as

$$J_\infty = \max_i W_i^2 = \max_i \frac{X_i^2 + Y_i^2}{Z_i^2} = \max(J_L, J_R) \tag{3.62}$$

The longitudinal force for the left half of the body is distributed to the front and rear wheels according to

$$J_L = \max\left(W_1^2, W_3^2\right) = \max\left(\frac{X_1^2 + Y_1^2}{Z_1^2}, \frac{(X_L - X_1)^2 + Y_3^2}{Z_3^2}\right) \tag{3.63}$$

and the longitudinal force for the right half of the body is distributed to the wheels according to

$$J_R = \max\left(W_2^2, W_4^2\right) = \max\left(\frac{X_2^2 + Y_2^2}{Z_2^2}, \frac{(X_R - X_2)^2 + Y_4^2}{Z_4^2}\right) \tag{3.64}$$

Because the minimization problems (3.63) and (3.64) have identical structures, only (3.63) is described here. The difference in the squared tire workload between the front and rear wheels is given by $F_L(X_1)$

$$F_L(X_1) = W_1^2 - W_3^2 = aX_1^2 + bX_1 + c \tag{3.65}$$

where

$$a = \frac{1}{Z_1^2} - \frac{1}{Z_3^2}, b = \frac{2X_L}{Z_3^2}, c = \frac{Y_1^2}{Z_1^2} - \frac{Y_3^2 + X_L^2}{Z_3^2}$$

Using (3.65), three modes for optimum distribution are identified [81].

Mode F

$X_1 = X_L$, $X_3 = 0$. This mode is active when the following inequality is satisfied:

$$F_L(X_L) \leq 0 \tag{3.66}$$

Mode R

$X_1 = 0$, $X_3 = X_L$. This mode is active when the following inequality is satisfied:

$$F_L(0) \geq 0 \tag{3.67}$$

Mode C

$X_1 = X_c$, $X_3 = X_L - X_c$. This mode is active when neither (3.66) nor (3.67) is satisfied. In this chapter, a new solution expression is derived for the quadratic equation $F_L(X_1) = 0$. This derivation is based on the formula for the solution of a quadratic equation [95]. This solution yields

$$X_c = \frac{\left(X_L^2 + Y_3^2\right) Z_1^2 - Y_1^2 Z_3^2}{Z_1^2 \left(X_L + \dfrac{Z_3}{Z_1} \operatorname{sgn}(X_L) \sqrt{A}\right)} \tag{3.68}$$

where

$$A = X_L^2 + \left(1 - \frac{Z_3^2}{Z_1^2}\right) Y_1^2 + \left(1 - \frac{Z_1^2}{Z_3^2}\right) Y_3^2$$

In the previous study [81], when $Z_1 \simeq Z_3$, the function for X_c becomes singular, and therefore an approximate formula was used to avoid numerical instabilities. Consequently, the solution in the neighborhood of $Z_1 = Z_3$ becomes less accurate. Using the new formulation (4.88), it is obvious that when $Z_1 = Z_3$, the denominator of (4.88) is not equal to zero, and, therefore, the singularity condition is not encountered. Hence, accurate solutions can be expected.

The tire force distribution problem was reduced to the one-dimensional minimization problem for which the convexity is readily verified. Since the derivative of the objective function with respect to M may become discontinuous, a golden section search was used in the previous study [81]. The lower and upper bounds for the search interval of the optimal direct yaw moment M_{opt} are as given in [81].

3.4.2 Square Sum Minimization

For square sum minimization, which is a well-known optimization method [70, 6], the objective is to minimize the square sum of the tire workloads.

$$J_2 = \sum_{i=1}^{4} W_i^2 = \sum_{i=1}^{4} \frac{X_i^2 + Y_i^2}{Z_i^2} \tag{3.69}$$

The front left longitudinal tire force X_1 and the front right longitudinal tire force X_2 are obtained by solving $\partial J_2 / \partial X_1 = 0$ and $\partial J_2 / \partial X_2 = 0$ with respect to X_1 and X_2,

respectively

$$X_1 = -\frac{(2M - t_r X_t)\, Z_1^2}{2t_r \left(Z_1^2 + Z_3^2\right)} \tag{3.70}$$

$$X_2 = \frac{(2M + t_r X_t)\, Z_2^2}{2t_r \left(Z_2^2 + Z_4^2\right)} \tag{3.71}$$

The rear left and rear right longitudinal tire forces are evaluated as

$$X_3 = X_L - X_1 \tag{3.72}$$

$$X_4 = X_R - X_2 \tag{3.73}$$

By substituting (3.70) through (3.73) and (3.59) into (3.69), and then solving $\partial J_2/\partial M = 0$ with respect to M gives

$$M_{\text{opt}} = \frac{\dfrac{4a_p l_r m_t}{(Z_1 + Z_2)^2} - \dfrac{4a_q l_f m_t}{(Z_3 + Z_4)^2} + \dfrac{(l_f + l_r)^2 X_t B_1}{t_r}}{2(l_f + l_r)^2 \left(\dfrac{B_3}{(l_f + l_r)^2} + \dfrac{B_2}{t_r^2}\right)} \tag{3.74}$$

where

$$\left.\begin{matrix} B_1 \\ B_2 \end{matrix}\right\} = \frac{1}{Z_1^2 + Z_3^2} \mp \frac{1}{Z_2^2 + Z_4^2}$$

$$B_3 = \frac{2}{(Z_1 + Z_2)^2} + \frac{2}{(Z_3 + Z_4)^2}$$

The formulation for this problem was used to generate the maximum tire workload contour plots but was not explicitly shown in [79]. Unlike in [70], which does not provide an explicit expression for optimal direct yaw moment M_{opt}, in this chapter, we provide the explicit expression for M_{opt}.

3.4.3 Wheel Torque and Steering Angle Commands

The wheel torque and steering angle commands are determined from the tire forces. The wheel torque command of each wheel is expressed as

$$T_i = r_w X_i \tag{3.75}$$

where r_w is the wheel radius.

The lateral tire force f_{ty} given by the modified brush tire model [47] is

$$f_{ty} = \begin{cases} -C_\alpha \bar{\alpha} + \dfrac{C_\alpha^2}{3\xi\mu F_z}|\bar{\alpha}|\bar{\alpha} - \dfrac{C_\alpha^3}{27\xi^2\mu^2 F_z^2}\bar{\alpha}^3, & \text{if } |\alpha| \le \alpha_{sl} \\ -\xi\mu F_z \operatorname{sgn}(\alpha), & \text{otherwise.} \end{cases} \tag{3.76}$$

where C_α is the tire cornering stiffness, α is the tire slip angle, μ is the tire-road friction coefficient, F_z is the vertical tire force, $\bar{\alpha} = \tan\alpha$, and $\alpha_{sl} = \arctan(3\xi\mu F_z/C_\alpha)$. Note that α_{sl} is the angle at which total sliding starts, and a further increase in the slip angle would not increase the cornering force. In (3.76), ξ is the derating factor, which limits the maximum lateral tire force in the presence of the driving/braking force F_x [47]. More specifically,

$$\xi = \frac{\sqrt{\mu^2 F_z^2 - F_x^2}}{\mu F_z}$$

The desired tire slip angle can be obtained by taking the inverse function of (3.76)

$$f_{ty}^{-1} = \begin{cases} \arctan\Big(\dfrac{\sqrt[3]{\omega}}{3} - \dfrac{3\xi\mu F_z \operatorname{sgn}(f_{ty})}{C_\alpha}\Big), & \text{if } |f_{ty}| \le \xi\mu F_z \\ \arctan\Big(-\dfrac{3\xi\mu F_z \operatorname{sgn}(f_{ty})}{C_\alpha}\Big), & \text{otherwise.} \end{cases} \tag{3.77}$$

where

$$\omega = \frac{729\xi^2\mu^2 F_z^2(\xi\mu F_z \operatorname{sgn}(f_{ty}) - f_{ty})}{C_\alpha^3}$$

The inverse tire model (3.77) can be used for axle with the assumption that both tires at an axle are considered as a single tire located at the center of the axle. Then, C_α is the sum of the cornering stiffnesses of the tires at each axle. Similarly, F_z is regarded as the sum of the vertical tire forces at each axle. The sum of the vertical tire forces at the front axle and that at the rear axle are given as $Z_1 + Z_2$ and $Z_3 + Z_4$, respectively. The lateral tire forces can be converted to the front steering angle δ_f and the rear steering angle δ_r, respectively, as given in [36]

$$\delta_f = \beta + \frac{l_f\gamma}{v_x} - f_{ty}^{-1}(Y_f) \tag{3.78a}$$

$$\delta_r = \beta - \frac{l_r\gamma}{v_x} - f_{ty}^{-1}(Y_r) \tag{3.78b}$$

where v_x is the longitudinal vehicle velocity. The sum of the lateral tire forces at the front axle Y_f and that at the rear axle Y_r are given as $Y_1 + Y_2$ and $Y_3 + Y_4$, respectively.

3.5 Numerical Examples

The simulations are performed using a 14-degree-of-freedom (14DOF) vehicle model with a combined slip nonlinear tire model. The 14DOF vehicle model includes the longitudinal, lateral, vertical, pitch, roll, and yaw motions of the vehicle body, the vertical motions of the four unsprung masses, and the spin of each wheel [69]. The vehicle parameters corresponding to the E-segment sedan as indicated in Table 3.1 are used for the numerical simulations.

Table 3.1: Vehicle Parameters

Parameter	Symbol	Value
Total vehicle mass	m_t	1830 kg
Sprung mass	m_s	1650 kg
Yaw moment of inertia	I_z	3234 kgm^2
Distance from vehicle CG to front axle	l_f	1.40 m
Distance from vehicle CG to rear axle	l_r	1.65 m
Track width	t_r	1.60 m
Height of sprung mass CG	h_s	0.53 m
Front suspension roll stiffness	$k_{\phi f}$	1144 Nm/deg
Rear suspension roll stiffness	$k_{\phi r}$	1372 Nm/deg
Height of front roll center	h_f	0.062 m
Height of rear roll center	h_r	0.405 m
Front unsprung mass	m_{uf}	90 kg
Rear unsprung mass	m_{ur}	90 kg
Height of front unsprung mass CG	h_{uf}	0.32 m
Height of rear unsprung mass CG	h_{ur}	0.30 m
Wheel radius	r_w	0.353 m

In order to verify the effectiveness of the controller, we consider three emergency cases: a static obstacle, movement of the obstacle in the lateral direction after the intervention has been initiated, and the appearance of a second obstacle between the vehicle and first obstacle after the intervention has been initiated.

3.5.1 Static Obstacle

In the first case, the scenario shown in Fig. 3.1 is considered. A vehicle traveling at a longitudinal velocity of 26 m/s performs a lane change maneuver with $y_f = 3.5$ m and $x_f = 50$ m. In this case, a tire-road friction coefficient of 0.5 is assumed.

Fig. 3.10 shows the vehicle CG paths for a point mass model, 14DOF model with the minimax tire force distributor, and 14DOF model with the square sum tire force distributor. The path using either of the tire force distributors is very similar to that of the point mass model. This indicates the ability of the online controller with the tire force distributor to successfully avoid the obstacle.

In order to compare the performances of the two types of tire force distributor, we consider the maximum tire workload as a performance index. Previous studies [9, 52] have used the maximum tire force usage as a performance index. Tire force usage is the

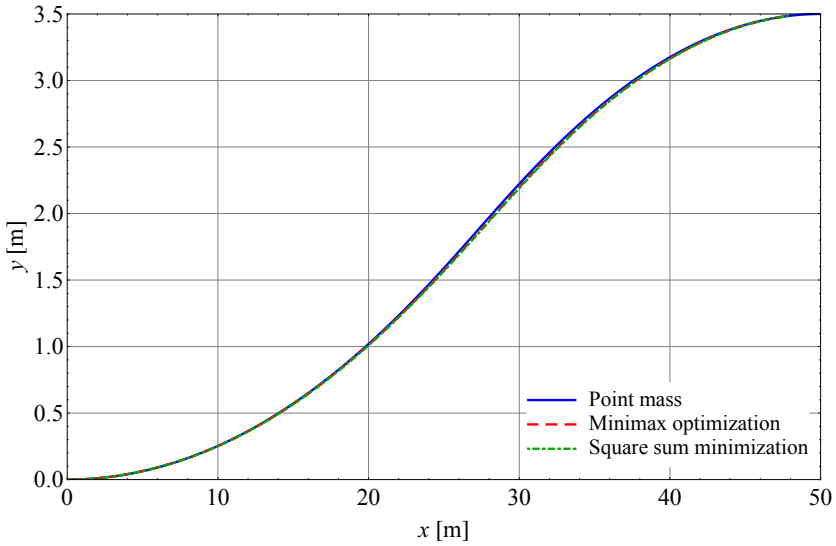

Figure 3.10: Vehicle CG paths for the point mass model and the 14DOF model with two types of tire force distributors.

workload divided by the tire-road friction coefficient. Since the four tires are assumed to have the same friction conditions, the tire workload is used in this chapter.

Fig. 3.11 shows the maximum tire workload for each tire during the avoidance maneuver. For all the tires, except for the rear left tire, the minimax tire force distributor yields lower maximum tire workloads compared to those obtained using the square sum tire force distributor. For the minimax tire force distributor, among the four tires, the rear left tire has the highest maximum tire workload, which is equal to 0.4438. For the square sum tire force distributor, the front left tire has the highest maximum tire workload, which is equal to 0.4469. The ratio between the maximum resultant vehicle force and the vehicle weight for the point mass model is 0.3599.

Comparing the highest maximum tire workloads between these tire force distributors reveals that the minimax tire force distributor is better than the square sum tire force distributor because the minimax tire force distributor provides a larger margin to the friction limit (in this case, 0.5). Thus, only the minimax tire force distributor is considered for the remaining scenarios.

In the subsection 3.2.5, we have already explained that the optimal control is computable once a nondimensionalized equation is solved with respect to N_1 by using the bisection method. Fig. 3.12 shows the number of function evaluations required by the bisection method during the avoidance maneuver for three different termination criteria. Three absolute errors $\varepsilon = 10^{-6}, 10^{-10}, 10^{-14}$ for stopping the computation are considered. In Fig. 3.12, the blue, red, and green solid lines indicate the number of function evaluations for $\varepsilon = 10^{-6}, 10^{-10}, 10^{-14}$, respectively. The computation terminates when the width of

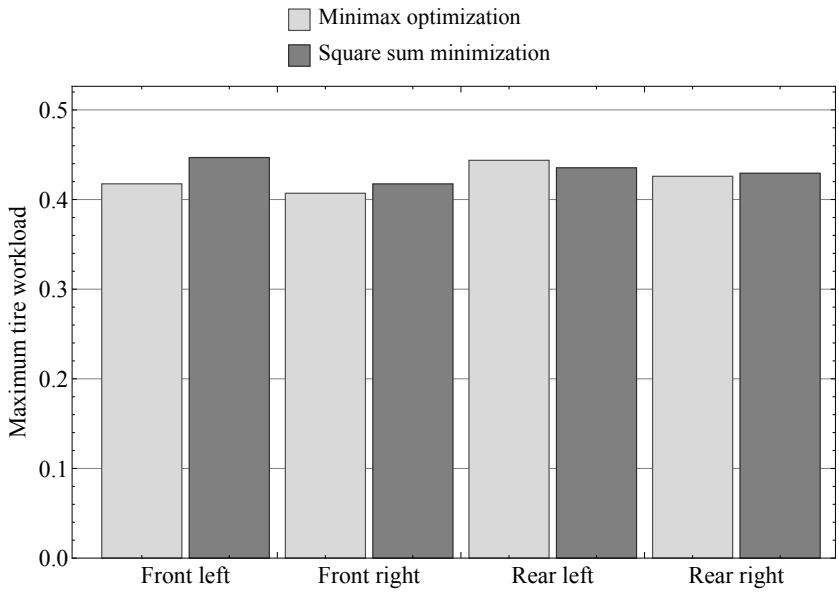

Figure 3.11: Maximum tire workloads for the two types of tire force distributors: minimax optimization and square sum minimization.

the search interval falls below ε. As expected, among the three absolute errors, the lowest maximum number of function evaluations along the maneuver is achieved when $\varepsilon = 10^{-6}$ and this number is equal to 24. This reasonably small number suggests that the proposed optimal control method can be considered for real-time implementation.

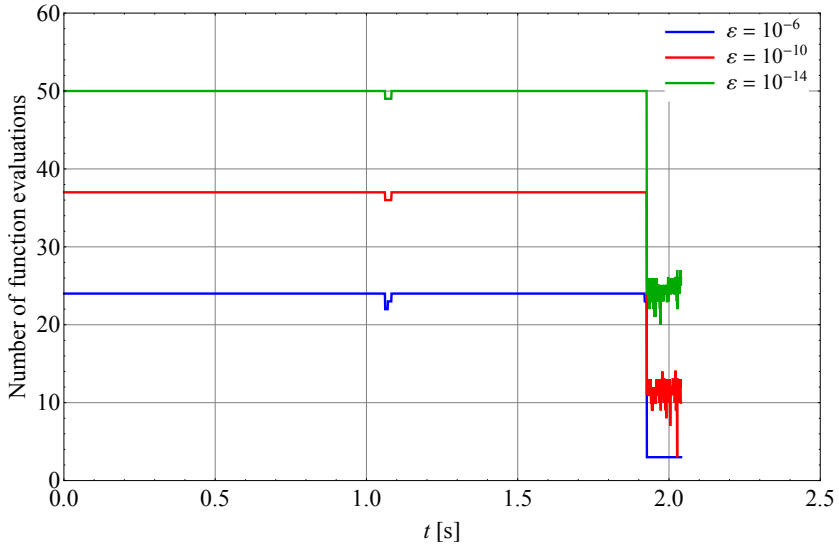

Figure 3.12: Number of function evaluations along the avoidance maneuver for three different termination criteria.

3.5.2 Movement of the Obstacle in the Lateral Direction after the Intervention Has Been Initiated

In the second case, as shown in Fig. 3.13, the vehicle with initial longitudinal velocity $v_{x0} = 27$ m/s performs the lane change maneuver with $y_f = 2.5$ m and $x_f = 50$ m, and at $x = 15$ m, the final lateral distance y_f changes to 3.5 m. The change in the final lateral distance corresponds to the movement of the obstacle in the lateral direction. The increase in the final lateral distance indicates that additional resultant vehicle force is required for the remainder of the maneuver. The optimal controller estimates the minimum resultant vehicle force required during the maneuver. The friction coefficient is assumed to be 0.7.

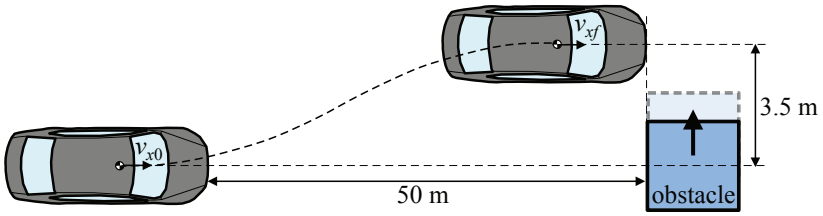

Figure 3.13: Obstacle avoidance lane change maneuver for an obstacle moving in the lateral direction after the intervention has been initiated. At $t = 0$ s, $y_f = 2.5$ m, and at $x = 15$ m, y_f changes to 3.5 m as the obstacle starts to move in the lateral direction.

Fig. 3.14 shows the vehicle CG paths for two conditions in which 1) the controller takes into account the lateral movement of the obstacle and 2) the controller does not take into account the lateral movement of the obstacle. The blue solid line represents the optimal path using a point mass model, and the red dashed line represents the optimal path using the 14DOF model with the minimax tire force distributor, both for the case in which the lateral movement of the obstacle is considered. The case in which the controller does not consider the lateral movement of the obstacle is represented by the green solid line for the point mass model and the orange dashed line for the 14DOF model with the minimax tire force distributor. The effectiveness of the controller in adapting to the lateral movement of the obstacle is clearly shown in Fig. 3.14. Moreover, the path generated using the 14DOF model is in good agreement with that of the point mass model.

Fig. 3.15 shows the maximum tire workload for each tire before and after the change in y_f. The increase in the maximum tire workload for all of the tires after the change in y_f indicates the increase in the force used in the maneuver. Interestingly, when $y_f = 3.5$ m, there is not much difference in the maximum tire workload between the tires. All of the maximum tire workloads are below the friction limit, which is equal to 0.7, and this indicates that there are available tire forces. For the point mass model in the case in which the lateral movement of the obstacle is considered, the ratios between the maximum resultant vehicle force and the vehicle weight are 0.2860 for $x < 15$ m and 0.4715 for $x > 15$

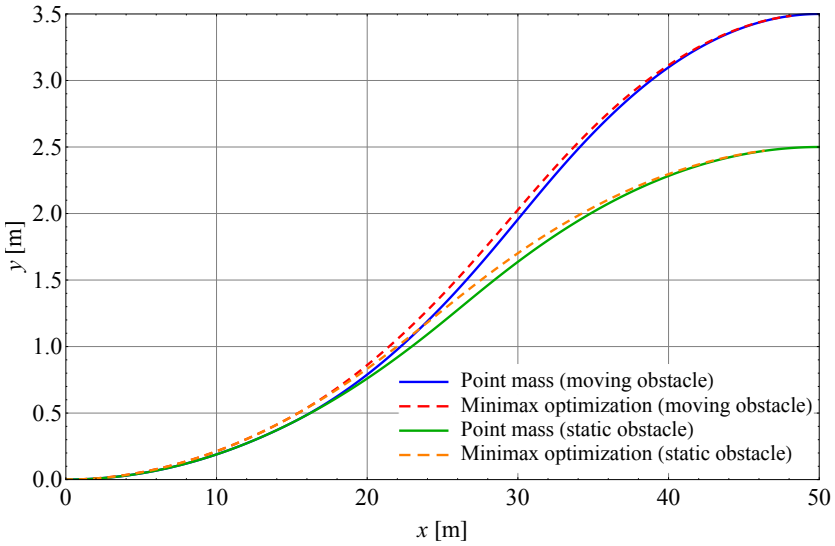

Figure 3.14: Vehicle CG paths of the point mass model and the 14DOF model with the minimax tire force distributor for Scenario B.

m.

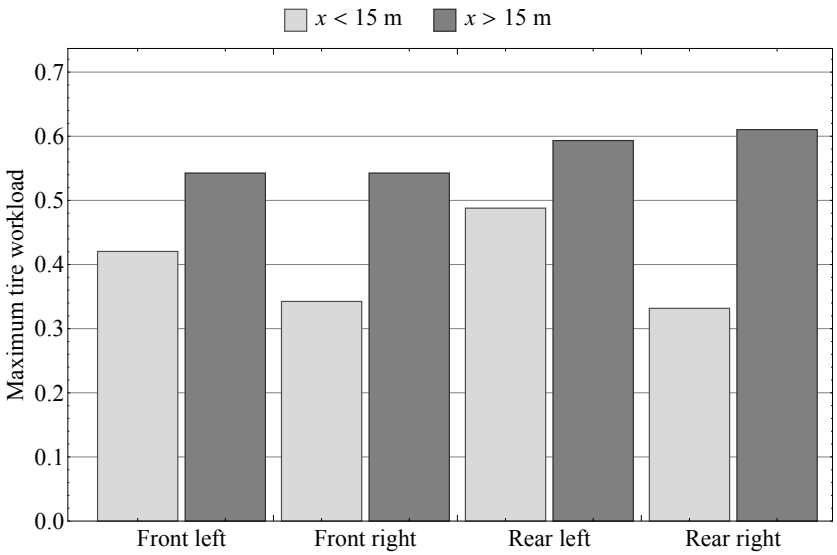

Figure 3.15: Comparison of the maximum tire workloads before and after the change in y_f.

The simulation results demonstrate the effectiveness of the online controller in handling the lateral movement of the obstacle after the intervention has been initiated.

3.5.3 Appearance of a Second Obstacle Between the Vehicle and First Obstacle after the Intervention Has Been Initiated

Fig. 3.16 shows the third case, in which a vehicle moving at $v_{x0} = 27$ m/s executes a lane change maneuver with $y_f = 3.5$ m and $x_f = 60$ m, and, at $x = 10$ m, the final longitudinal distance x_f changes to 50 m. A friction coefficient of 0.7 is assumed. The reduction in the final longitudinal distance corresponds to the appearance of another obstacle, which imposes a stricter constraint on the maneuver.

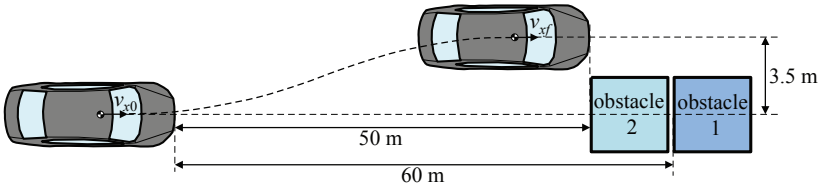

Figure 3.16: Obstacle avoidance lane change maneuver with a second obstacle appearing between the vehicle and the first obstacle after the intervention has been initiated. At $t = 0$ s, $x_f = 60$ m, and at $x = 10$ m, x_f changes to 50 m.

Similar to the previous scenario, Fig. 3.17 shows the vehicle CG paths for two conditions in which 1) the controller takes into account the appearance of an obstacle after the initiation of the intervention and 2) the controller does not take into account the appearance of an obstacle after the initiation of the intervention. The blue solid line and the red dashed line represent the paths of the point mass and 14DOF models, respectively, for the case in which the change in x_f is taken into account by the controller. These paths demonstrate the ability of the controller to successfully avoid the second obstacle. The green solid line and the orange dashed line are the vehicle CG paths for the case in which the change in x_f is not taken into account for the point mass model and the 14DOF model, respectively.

Fig. 3.18 shows the maximum tire workloads before and after the change in x_f. Although the longitudinal distance for the collision-free path decreases from 60 m to 50 m, the maximum tire workload of the tires remain below its limit of 0.7. Note that, for the point mass model in the case in which the change in x_f is taken into account, the ratios between the maximum resultant vehicle force and the vehicle weight are 0.2747 for $x < 10$ m and 0.4425 for $x > 10$ m.

This scenario highlights the ability of the online controller to avoid an obstacle that is introduced after intervention initiation.

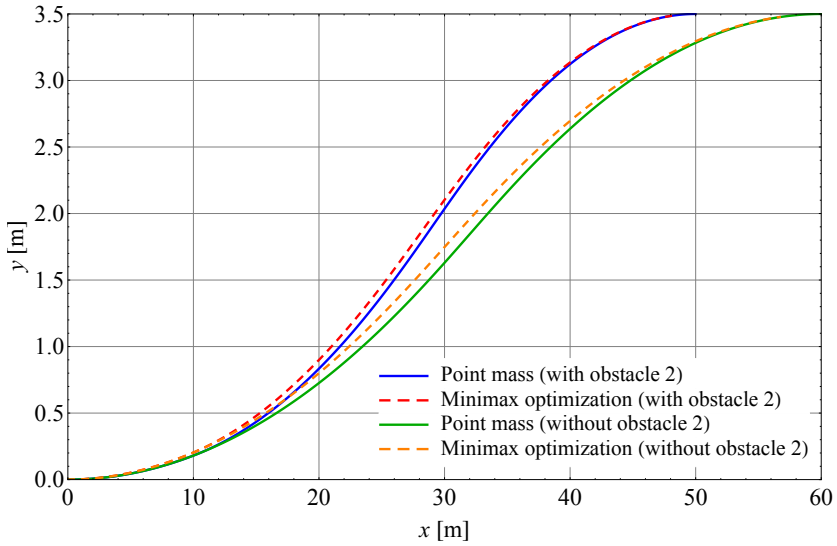

Figure 3.17: Vehicle CG paths of the point mass model and the 14DOF model with the minimax tire force distributor for Scenario C.

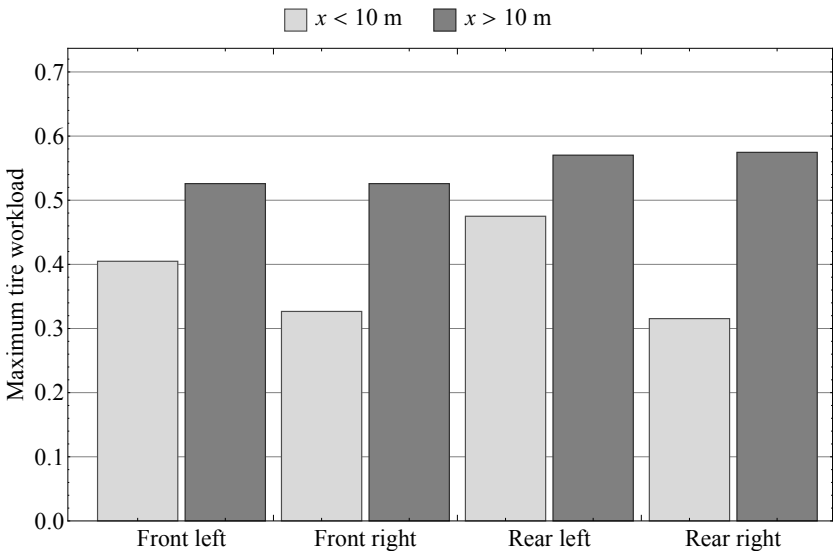

Figure 3.18: Maximum tire workloads before and after the change in x_f.

3.6 Conclusion

In this chapter, we investigated a collision avoidance system that combines the steering and braking inputs. Nondimensionalization and algebraic manipulations on simultaneous equations reduce the optimal control problem to an implicit equation in one unknown and two parameters. An improved tire force distributor that minimizes the maximum tire workload was used to distribute the longitudinal and lateral vehicle forces and total yaw moment to the tires. The simulation results suggest that a good tire force distributor enables point-mass-based optimal control for collision avoidance, instead of a higher-

degree-of-freedom-model-based optimal control, which simultaneously solves the collision avoidance and vehicle stabilization problems. A decision making diagram for the selection of the most effective maneuver among the steering with braking, steering, and braking maneuvers by comparing the dimensionless form of the vehicle force required to avoid a collision is presented. The region in which the steering with braking maneuver is superior to the other two maneuvers is identified. Moreover, we have proven that the shape of the vehicle position path depends only on the ratio of the final lateral distance to the final longitudinal distance. For the feedback control simulation, the path generated using a nonlinear vehicle model closely follows that of a point mass. This implies that the solution method using a point mass is applicable to a more realistic vehicle model. The minimax tire force distributor is more efficient than that based on the square sum because it provides a lower maximum tire workload among the four tires throughout the maneuver. Case studies on the lateral movement of the obstacle and the appearance of another obstacle between the vehicle and the first obstacle after the intervention has been initiated demonstrate the ability of the controller to adapt to situation changes. Although not shown in this chapter, depending on the friction and actuator limits, the controller can cope with disturbances such as crosswinds and lateral wind gusts.

Chapter 4

Minimum Jerk Trajectory for Obstacle Avoidance

4.1 Introduction

Autonomous vehicles have become one of the main areas of interest in the field of the intelligent transportation. Among the various autonomous functions, collision avoidance has been attracting a lot of interest [102, 100, 37]. Avoiding a collision includes recognition of obstacles and surroundings, decision-making regarding the selection of avoidance maneuver (e.g., stopping and lane change) and intervention timing, and generation and tracking control of the collision-free trajectory. This chapter focuses on trajectory generation and tracking control, as they are the essential aspects of collision avoidance technologies.

When an obstacle suddenly appears in the current lane, stopping or lane change maneuvers should be performed to avoid obstacles. In many situations, the obstacle can only be avoided by lane change maneuvers. Optimal control theory is among the most effective methods by which to solve the obstacle avoidance problem using a lane change maneuver and can be mathematically proven to yield the optimal trajectory with respect to an appropriate objective function, such as the avoidance distance. Shiller and Sundar [106] formulated an obstacle avoidance problem as an optimal control problem to find a path with minimum longitudinal avoidance distance. Using optimal control theory, Horiuchi *et al.* [52] solved an obstacle avoidance problem that finds the optimal steering and braking inputs such that the time integral of the weighted sum of the sum of the squared tire force usages and the squared steering rate is minimized. These studies established the last point to avoid a collision with the optimal combination of the steering and braking inputs. The optimal trajectories were generated using vehicle models that include a nonlinear tire model, and, therefore, the computation can be demanding.

The computational load can be reduced if a point mass model is used to represent the vehicle for the optimal control problem formulation. For the minimum longitudinal avoidance distance problem with the assumption of a point mass, a look-up table approach to represent the feedback controller based on the solutions obtained from optimal control theory was proposed by Hattori *et al.* [42]. In Chapter 2, we proved that the optimal state feedback control for the minimum avoidance distance problem can be found by implicitly solving a nondimensionalized equation in an unknown. Chapter 2 gives a more accurate solution than what can be expected from a look-up table. However, these studies did not consider reduction of jerk during the lane change maneuver. High jerk can cause discomfort and may be harmful to vehicle occupants and so is not desirable.

We formulate the obstacle avoidance problem as the minimization of the time integral of the squared resultant vehicle jerk. The solution to a minimum jerk problem is known to be obtained as quintic polynomials using variational methods. The minimum jerk formulation is known to explain the human reaching movements of the arms [34], as well as saccadic eye movements [50]. These facts would support the idea that the trajectory generated by minimizing jerk realizes a comfortable and less harmful collision avoidance maneuver. In addition, obtaining the lane change path using polynomials has been considered in numerous studies [23, 104, 90, 107, 103]. In this chapter, for the generation of a trajectory with minimum jerk and because of the popularity of using polynomials for obtaining the lane change maneuver, we select quintic polynomials to address the obstacle avoidance problem.

In an emergency situation, the computation of the reference trajectory must be fast enough for real-time implementation. In this chapter, trajectory generation requires knowledge of the initial longitudinal velocity, the desired final lateral position, and the tire-road friction coefficient. With nondimensionalization, these three input variables are grouped into a single dimensionless input variable referred to as the dimensionless initial longitudinal vehicle velocity. For the given dimensionless initial longitudinal velocity, the trajectory can be readily calculated once a nondimensionalized equation with respect to the lane change aspect ratio is solved numerically. The lane change aspect ratio is the ratio between the longitudinal avoidance distance and the desired final lateral position. A fast numerical solution is obtainable because a good initial guess for the numerical method can be obtained from a one-dimensional look-up table prepared using the offline solution.

Different strategies for tracking the desired path have been reported in the literature. In [10], the path tracking performance was compared among the following obstacle avoidance strategies: two-wheel steering (2WS), four-wheel steering (4WS), and steering by braking the front, rear, or both the front and rear wheels. Moreover, integration of the 2WS control and direct yaw-moment control (DYC) using different control strategies for path tracking has been proposed [126, 54]. These controllers minimize the tracking errors at the vehicle

center of gravity (CG). Kumamoto *et al.* [65] proposed a 4WS sliding mode controller based on centers of percussion (COPs) relative to the front and rear wheels. In [65], the front steering controller minimizes the course error of the COP relative to the rear wheels, and the rear steering controller minimizes the course error of the COP relative to the front wheels. Moreover, using COPs, Raksincharoensak *et al.* [99] developed a different path tracking controller and demonstrated that a 4WS path tracking controller based on COPs yields lower tracking errors as compared to a 2WS path tracking controller. These studies considered only the path tracking problem.

For certain maneuvers, the desired trajectory consisting of the path and velocity profile must be tracked for the realization of the maneuver. To track the velocity profile, the vehicle is accelerated or braked. Under acceleration or braking, the longitudinal tire forces should be distributed in a way such that tire force saturation is avoided so as to maintain stable vehicle motion. The yaw moment generated by the difference of the longitudinal tire forces between the left and right sides of the vehicle body, known as the direct yaw moment, can also contribute to the path tracking performance. The effectiveness of DYC implementation depends on the tire force distributor. The two tire force distributors considered in this chapter are the minimax optimization of the squared tire force usage and the minimization of the weighted sum of the squared tire force usages. The minimax optimization is a one-dimensional optimization problem [81], and square sum minimization has a closed-form solution [71].

In this chapter, integration of 4WS control and DYC for trajectory tracking is investigated. The steering controller based on COPs is designed using the sliding mode control approach. The approach considered in this chapter differs from that in [65], such that the control inputs are different. The lateral tire forces are treated as the control inputs instead of steering angles, as in [65]. The lateral tire forces are translated into steering angles using the brush tire model, which assumes nonlinear tire characteristics. The brush tire model requires the estimated value of the friction coefficient to be available once the estimation is performed for reference trajectory generation. The estimation methods reported in [96] are suitable for practical implementation and can be adopted here.

The remainder of this chapter is organized as follows. Section 4.2 formulates the obstacle avoidance problem as the minimum time integral of the squared resultant jerk problem and then derives the solution method. In Section 4.3, the decision-making diagrams based on the lane change aspect ratio and dimensionless time to collision are explained. Section 4.4 describes the design of the sliding mode controller for trajectory tracking. The tire force distribution methods are described in Section 4.5. Section 4.6 provides numerical examples. Finally, conclusions are presented in Section 4.7.

4.2 Trajectory Generation

4.2.1 Obstacle Avoidance Maneuver

An emergency lane change scenario is shown in Fig. 4.1, in which a vehicle moving at a longitudinal velocity v_{x0} encounters an obstacle in the current lane. The vehicle should execute a lane change maneuver to reach a desired final lateral position y_f. Note that y_f is the width of the lane. At the beginning of the maneuver ($t = 0$), the lateral velocity v_{y0} is assumed to be zero, and at the end of the maneuver ($t = t_f$), the lateral velocity v_{yf} is set to zero. The vehicle jerk during the lane change is reduced. The maximum resultant acceleration is set to the maximum available vehicle acceleration, which is given by the product of tire-road friction coefficient μ and gravitational acceleration g. This is done to achieve a shorter longitudinal avoidance distance x_f.

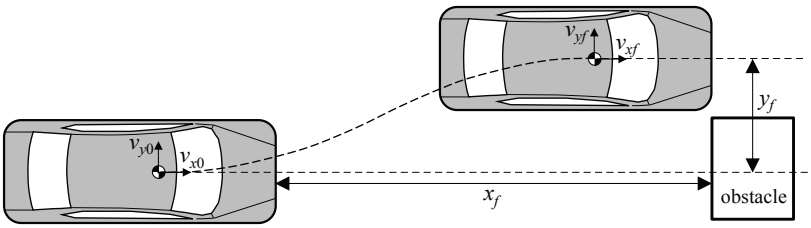

Figure 4.1: Lane change for obstacle avoidance.

4.2.2 Minimum Jerk Trajectory

A point mass model is assumed for the obstacle avoidance problem. The point mass has two degrees of freedom (2DOF), which are the motions in the x and y directions.

The obstacle avoidance problem can be formulated as a TPBVP. The objective function is the time integral of the squared resultant vehicle jerk

$$J = \int_0^{t_f} \dddot{x}^2 + \dddot{y}^2 \, dt \tag{4.1}$$

where x and y are the positions in the x and y directions, respectively, and the dot indicates the derivative with respect to time. For compactness, we define $L = \dddot{x}^2 + \dddot{y}^2$. The minimum jerk trajectory is obtained using calculus of variations, which gives the functions $x(t)$ and $y(t)$ that minimize the functional J. $x(t)$ and $y(t)$ are determined using the Euler-Lagrange equations, which are written as

$$\frac{\partial L}{\partial x} - \frac{d}{dt}\left(\frac{\partial L}{\partial \dot{x}}\right) + \frac{d^2}{dt^2}\left(\frac{\partial L}{\partial \ddot{x}}\right) - \frac{d^3}{dt^3}\left(\frac{\partial L}{\partial \dddot{x}}\right) = 0 \tag{4.2a}$$

$$\frac{\partial L}{\partial y} - \frac{d}{dt}\left(\frac{\partial L}{\partial \dot{y}}\right) + \frac{d^2}{dt^2}\left(\frac{\partial L}{\partial \ddot{y}}\right) - \frac{d^3}{dt^3}\left(\frac{\partial L}{\partial \dddot{y}}\right) = 0 \tag{4.2b}$$

The first three terms in the left-hand side of (4.2a) and (4.2b) are equal to zero because L depends only on the third derivatives of x and y. From (4.2a) and (4.2b), we obtain $x^{(6)} = 0$ and $y^{(6)} = 0$, respectively, where superscript (6) indicates the sixth derivative with respect to time. These differential equations are then solved to obtain the positions $x(t)$ and $y(t)$ that are quintic polynomials with respect to time

$$x(t) = a_5t^5 + a_4t^4 + a_3t^3 + a_2t^2 + a_1t + a_0 \tag{4.3a}$$

$$y(t) = b_5t^5 + b_4t^4 + b_3t^3 + b_2t^2 + b_1t + b_0 \tag{4.3b}$$

where a_i and b_i $(i = 0, ..., 5)$ are the coefficients of the polynomials. For a detailed explanation of the derivation of these polynomials, see [34].

The first, second, and third derivatives of (4.3a) give the velocity, acceleration, and jerk in the x direction, respectively

$$\dot{x}(t) = \frac{dx(t)}{dt} = 5a_5t^4 + 4a_4t^3 + 3a_3t^2 + 2a_2t + a_1 \tag{4.4a}$$

$$\ddot{x}(t) = \frac{d^2x(t)}{dt^2} = 20a_5t^3 + 12a_4t^2 + 6a_3t + 2a_2 \tag{4.4b}$$

$$\dddot{x}(t) = \frac{d^3x(t)}{dt^3} = 60a_5t^2 + 24a_4t + 6a_3 \tag{4.4c}$$

Similarly, the first, second, and third derivatives of (4.3b) give the velocity, acceleration, and jerk in the y direction, respectively

$$\dot{y}(t) = \frac{dy(t)}{dt} = 5b_5t^4 + 4b_4t^3 + 3b_3t^2 + 2b_2t + b_1 \tag{4.5a}$$

$$\ddot{y}(t) = \frac{d^2y(t)}{dt^2} = 20b_5t^3 + 12b_4t^2 + 6b_3t + 2b_2 \tag{4.5b}$$

$$\dddot{y}(t) = \frac{d^3y(t)}{dt^3} = 60b_5t^2 + 24b_4t + 6b_3 \tag{4.5c}$$

The initial conditions of the trajectory are

$$\begin{aligned} &x(0) = 0, \dot{x}(0) = v_{x0}, \ddot{x}(0) = 0, \\ &y(0) = 0, \dot{y}(0) = 0, \ddot{y}(0) = 0 \end{aligned} \tag{4.6}$$

and the final conditions of the trajectory are

$$\begin{aligned} &x(t_f) = x_f, \dot{x}(t_f) = v_{xf}, \ddot{x}(t_f) = 0, \\ &y(t_f) = y_f, \dot{y}(t_f) = 0, \ddot{y}(t_f) = 0 \end{aligned} \tag{4.7}$$

where t_f, x_f, and v_{xf} are free. Note that x_f is an important parameter to decide the last point at which to avoid the collision, and v_{xf} should be nonnegative, so that the vehicle is always moving in the forward direction.

Using the boundary conditions in (4.6) and (4.7), the polynomial coefficients in (4.3a)

are derived as

$$a_5 = \frac{6x_f - 3t_f\,(v_{x0} + v_{xf})}{t_f^5} \tag{4.8a}$$

$$a_4 = \frac{t_f\,(8v_{x0} + 7v_{xf}) - 15x_f}{t_f^4} \tag{4.8b}$$

$$a_3 = -\frac{2\,[t_f\,(3v_{x0} + 2v_{xf}) - 5x_f]}{t_f^3} \tag{4.8c}$$

$$a_2 = a_0 = 0 \tag{4.8d}$$

$$a_1 = v_{x0} \tag{4.8e}$$

The polynomial coefficients in (4.3b) are derived using the boundary conditions in (4.6) and (4.7).

$$b_5 = \frac{6y_f}{t_f^5}, b_4 = -\frac{15y_f}{t_f^4}, b_3 = \frac{10y_f}{t_f^3}, b_2 = b_1 = b_0 = 0 \tag{4.9}$$

Partial derivatives of (4.1) with respect to v_{xf} and t_f are

$$\frac{\partial J}{\partial v_{xf}} = \frac{24[t_f(7v_{x0} + 8v_{xf}) - 15x_f]}{t_f^4} \tag{4.10a}$$

$$\frac{\partial J}{\partial t_f} = -\frac{72[\omega t_f^2 - 20x_f t_f\,(v_{x0} + v_{xf}) + 25(x_f^2 + y_f^2)]}{t_f^6} \tag{4.10b}$$

where

$$\omega = 4v_{x0}^2 + 7v_{x0}v_{xf} + 4v_{xf}^2$$

By simultaneously solving the extremal equations $\partial J/\partial v_{xf} = 0$ and $\partial J/\partial t_f = 0$ with respect to v_{xf} and t_f, we have

$$\left.\begin{matrix} v_{xf1} \\ v_{xf2} \end{matrix}\right\} = \frac{v_{x0}(5x_f^2 - 112y_f^2) \pm 3x_f v_{x0}\sqrt{x_f^2 - 240y_f^2}}{8x_f^2 + 128y_f^2} \tag{4.11a}$$

$$\left.\begin{matrix} t_{f1} \\ t_{f2} \end{matrix}\right\} = \frac{4x_f \mp \sqrt{x_f^2 - 240y_f^2}}{3v_{x0}} \tag{4.11b}$$

Inspection reveals that the pair v_{xf1} and t_{f1} gives the lowest J. Therefore, we choose $v_{xf} = v_{xf1}$ and $t_f = t_{f1}$.

The lane change is performed using combined steering and velocity control by respecting the friction constraint given by the friction circle theory. The friction circle theory states that the vector sum of the longitudinal and lateral tire forces is limited by the product of the tire-road friction coefficient and the vertical tire load. This concept can be extended to a vehicle for which the vector sum of the total longitudinal force and total lateral force is bounded by the product of the friction coefficient and the vehicle weight.

Using the longitudinal vehicle acceleration a_x and the lateral vehicle acceleration a_y, this can be written as

$$a_x^2(t) + a_y^2(t) \leq \left(\frac{F_{\max}}{m_t}\right)^2 \tag{4.12}$$

where $F_{\max}$ is the maximum available vehicle force and m_t is the total vehicle mass. Fig. 4.2 shows a vehicle friction circle.

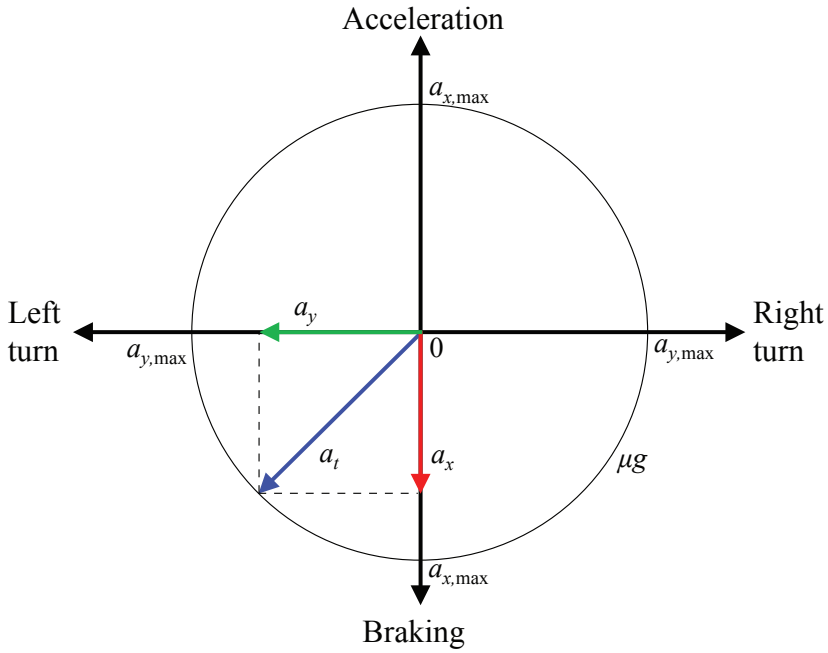

Figure 4.2: Coupling of the longitudinal and lateral vehicle accelerations. This is an example in which the resultant acceleration a_t is equal to the maximum available vehicle acceleration μg.

In order to ensure that the upper bound corresponding to the friction circle is not violated, the maximum resultant vehicle acceleration is set to be equal to the radius of the circle that corresponds to the maximum available vehicle acceleration. Let us find the time at which this maximum resultant acceleration occurs. To do this, we equate the first time derivative of the resultant acceleration to zero

$$\frac{d}{dt}(\ddot{x}^2(t) + \ddot{y}^2(t)) = 0 \tag{4.13}$$

After performing algebraic manipulations on (4.13), we arrive at

$$f_1(t) = c_3 t^3 + c_2 t^2 + c_1 t + c_0 = 0 \tag{4.14}$$

where

$$c_3 = 75\{[t_f(v_{x0} + v_{xf}) - 2x_f]^2 + 4y_f^2\} \tag{4.15a}$$

$$c_2 = -25t_f\{[t_f(5v_{x0} + 4v_{xf}) - 9x_f][t_f(v_{x0} + v_{xf}) - 2x_f] + 18y_f^2\} \tag{4.15b}$$

$$c_1 = t_f^2\{[t_f(21v_{x0} + 19v_{xf}) - 40x_f][t_f(3v_{x0} + 2v_{xf}) - 5x_f] + 200y_f^2\} \tag{4.15c}$$

$$c_0 = -t_f^3\{[t_f(3v_{x0} + 2v_{xf}) - 5x_f]^2 - 25y_f^2\} \tag{4.15d}$$

Let $d_2 = c_2/c_3$, $d_1 = c_1/c_3$, and $d_0 = c_0/c_3$. Then, the real roots of the cubic (4.14) can be found depending on the sign of the polynomial discriminant

$$D_3 = Q^3 + R^2 \tag{4.16}$$

where

$$Q = \frac{3d_1 - d_2^2}{9}, \quad R = \frac{9d_2d_1 - 27d_0 - 2d_2^3}{54}$$

If $D_3 > 0$, then there is only one real root, given by

$$t_{1a} = -\frac{d_2}{3} + (S + T) \tag{4.17}$$

where

$$\left.\begin{matrix} S \\ T \end{matrix}\right\} = \sqrt[3]{R \pm \sqrt{D_3}}$$

If $D_3 < 0$, then there are three distinct real roots, given by

$$t_{1b} = -\frac{d_2}{3} + 2\sqrt{-Q}\cos\left(\frac{\theta}{3}\right) \tag{4.18a}$$

$$t_{2b} = -\frac{d_2}{3} + 2\sqrt{-Q}\cos\left(\frac{\theta + 2\pi}{3}\right) \tag{4.18b}$$

$$t_{3b} = -\frac{d_2}{3} + 2\sqrt{-Q}\cos\left(\frac{\theta + 4\pi}{3}\right) \tag{4.18c}$$

where

$$\theta = \arccos\left(\frac{R}{\sqrt{-Q^3}}\right)$$

We found then that the time at which the maximum resultant acceleration occurs is $t_a = t_{1a}$ if $D_3 > 0$, and $t_a = t_{2b}$ if $D_3 < 0$. Recall that x_f is still an unknown. To find x_f, we need to solve the following equality with $t = t_a$:

$$\sqrt{\ddot{x}^2(t_a) + \ddot{y}^2(t_a)} = \frac{F_{\max}}{m_t} \tag{4.19}$$

Since x_f is to be solved using an iterative method, a good initial guess is preferred. The solution of x_f depends on the parameters v_{x0}, y_f, $F_{\max}$, and m_t. The last two parameters can be represented by $a_{\max} = F_{\max}/m_t$. Now, there are three parameters that determine x_f. A look-up table that is a numerical mapping from $\{v_{x0}, y_f, a_{\max}\}$ to x_f can be built to give the initial guess. However, such a table may require a large amount of data and is difficult to visualize. In order to overcome this problem, we can perform nondimensionalization to reduce the number of variables.

4.2.3 Nondimensionalization

The dimensionless variables are defined as

$$V_{x0} = \sqrt{\frac{m_t}{F_{\max} y_f}} v_{x0}, V_{xf} = \frac{v_{xf}}{v_{x0}}, A_r = \frac{x_f}{y_f}, \tau_f = \sqrt{\frac{F_{\max}}{m_t y_f}} t_f, \tau = \frac{t}{t_f}, \tau_a = \frac{t_a}{t_f} \tag{4.20}$$

In (4.20), V_{x0} is the dimensionless initial longitudinal velocity, V_{xf} is the final-to-initial longitudinal velocity ratio, A_r is the lane change aspect ratio, τ_f is the dimensionless final time, τ is the dimensionless time, and τ_a is the dimensionless time at which the maximum resultant acceleration occurs.

Using the dimensionless variables, the final-to-initial longitudinal velocity ratio is expressed as

$$V_{xf} = \frac{5A_r^2 + 3A_r\sqrt{A_r^2 - 240} - 112}{8(16 + A_r^2)} \tag{4.21}$$

and the dimensionless final time is written as

$$\tau_f = \frac{4A_r - \sqrt{A_r^2 - 240}}{3V_{x0}} \tag{4.22}$$

Now, (4.14) can be expressed in a dimensionless form

$$f_{1n}(t) = c_{3n}\tau^3 + c_{2n}\tau^2 + c_{1n}\tau + c_{0n} = 0 \tag{4.23}$$

where

$$c_{3n} = 75\{[V_{x0}\tau_f(1 + V_{xf}) - 2A_r]^2 + 4\} \tag{4.24a}$$

$$c_{2n} = -25\{[9A_r - V_{x0}\tau_f(5 + 4V_{xf})][2A_r - V_{x0}\tau_f(1 + V_{xf})] + 18\} \tag{4.24b}$$

$$c_{1n} = \{[40A_r - V_{x0}\tau_f(21 + 19V_{xf})][5A_r - V_{x0}\tau_f(3 + 2V_{xf})] + 200\} \tag{4.24c}$$

$$c_{0n} = -[V_{x0}\tau_f(3 + 2V_{xf}) - 5A_r]^2 - 25 \tag{4.24d}$$

Let $d_{2n} = c_{2n}/c_{3n}$, $d_{1n} = c_{1n}/c_{3n}$ and $d_{0n} = c_{0n}/c_{3n}$

$$D_{3n} = Q_n^3 + R_n^2 \tag{4.25}$$

where

$$Q_n = \frac{3d_{1n} - d_{2n}^2}{9}, \quad R_n = \frac{9d_{2n}d_{1n} - 27d_{0n} - 2d_{2n}^3}{54}$$

If $D_{3n} > 0$, then there is only one real root, given by

$$\tau_a = -\frac{d_{2n}}{3} + (S_n + T_n) \tag{4.26}$$

where

$$\left.\begin{matrix} S_n \\ T_n \end{matrix}\right\} = \sqrt[3]{R_n \pm \sqrt{D_{3n}}}$$

If $D_{3n} < 0$, then the root corresponding to (4.18b) is given by

$$\tau_a = -\frac{d_{2n}}{3} + 2\sqrt{-Q_n}\cos\left(\frac{\theta_n + 2\pi}{3}\right) \tag{4.27}$$

where

$$\theta_n = \arccos\left(\frac{R_n}{\sqrt{-Q_n^3}}\right)$$

The dimensionless resultant acceleration $\mathcal{A}$ is defined as

$$\mathcal{A} = \frac{m_t}{F_{\max}}\sqrt{\ddot{x}^2(t) + \ddot{y}^2(t)} \tag{4.28}$$

With the dimensionless variables given in (4.20), (4.28) is written as a function of τ

$$\mathcal{A}(\tau) = \frac{12\tau}{\tau_f^2}\sqrt{\nu_1} \tag{4.29}$$

where

$$\nu_1 = 25(1 + A_r^2)(1 - 3\tau + 2\tau^2)^2 + V_{x0}\tau_f\nu_2(\tau - 1)^2[10A_r(2\tau - 1) + V_{x0}\tau_f\nu_2]$$

with

$$\nu_2 = 3 + 2V_{xf} - 5\tau(1 + V_{xf})$$

Fig. 4.3 shows the dimensionless resultant acceleration for the lane change maneuver with different V_{x0}. The black points at $\tau_a = 0.298086, 0.248947, 0.226997, 0.215098, 0.212672$ corresponding to $V_{x0} = 7, 10, 15, 30, 50$, respectively, are where the maximum resultant acceleration occurs. Note that the points at $\tau_a = 0.215098, 0.212672$ are close and appear to overlap. This figure shows that the limit imposed by the friction circle is not violated. Verification, as in this figure, is made much clearer by the effect of nondimensionalization.

Here, A_r can be obtained by numerically solving the following equation with $\tau = \tau_a$:

$$f_2 = 1 - \frac{12\tau}{\tau_f^2}\sqrt{\nu_1} = 0 \tag{4.30}$$

4.3 Decision Making and Velocity Ratio

In this section, nondimensionalized indices for collision avoidance are explained. First, a dimensionless distance-based index referred to as the lane change aspect ratio is presented. This is followed by the dimensionless version of time to collision *ttc*. The definitions of these dimensionless indices are presented in a previous study [111]. These dimensionless indices are used to decide whether a collision is avoidable and whether a lane change or stopping maneuver is the most effective maneuver. The most effective maneuver refers to the maneuver that can avoid an obstacle at the last possible instant. The advantage of

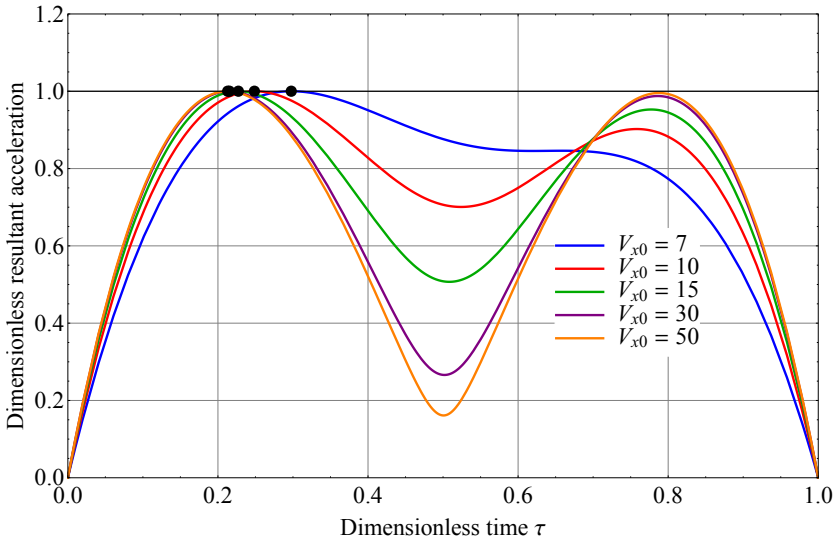

Figure 4.3: Dimensionless resultant acceleration as a function of dimensionless time with the points at which the maximum resultant acceleration occurs for different V_{x0}.

a nondimensionalized index as compared to an index with dimension is that the relation between the essential parameters and the avoidance distance or time to collision can be seen in a two-dimensional plot [111]. Finally, a plot of the ratio of the final-to-initial longitudinal vehicle velocity is provided.

4.3.1 Lane Change Aspect Ratio

The lane change aspect ratio A_r is the ratio of the longitudinal avoidance distance x_f to the desired final lateral position y_f. This ratio can be used to decide whether the lane change maneuver can avoid the collision. Fig. 4.4 shows a decision-making diagram based on the lane change aspect ratio. In this figure, the blue solid line represents the lane change aspect ratio obtained by solving (4.30) for A_r with $\tau = \tau_a$. For the purpose of comparison, we introduce a stopping maneuver. A stopping maneuver is a maneuver in which braking by fully using the maximum available vehicle force $m_t \mu g$ to stop the vehicle in the current lane with the front end of the vehicle just touching the rear end of the obstacle. The longitudinal distance x_s required to stop a vehicle with initial longitudinal velocity v_{x0} is as given in [42]

$$x_s = \frac{m_t v_{x0}^2}{2F_{\max}} \tag{4.31}$$

Dividing (4.31) by y_f and then substituting $v_{x0} = V_{x0}\sqrt{F_{\max} y_f}/\sqrt{m_t}$ from (4.20) into the resulting equation gives the aspect ratio for the stopping maneuver, which is obtained as $V_{x0}^2/2$. This expression is the same as that given in Chapter 2. This aspect ratio is represented by the red dashed line in Fig. 4.4.

Depending on the values of the ratio x/y_f and V_{x0} and the diagram in Fig. 4.4, whether a collision is avoidable and whether a lane change or stopping maneuver will be more effective can be decided. The most effective maneuver is the maneuver with the smallest aspect ratio. The blue solid line indicates the last point at which the collision can be avoided by a lane change maneuver, and the red dashed line indicates the last point at which the collision can be avoided by a stopping maneuver. The switching point between these maneuvers is at $V_{x0} = 5.614465$ and $A_r = 15.761107$. The region labeled as collision unavoidable is the region in which a collision cannot be avoided using the maneuvers considered in this chapter. However, depending on x/y_f and V_{x0}, there is a possibility that aggressive lane change maneuvers, such as those in Chapter 2, can avoid the collision. Otherwise, collision mitigation by full braking is the only option.

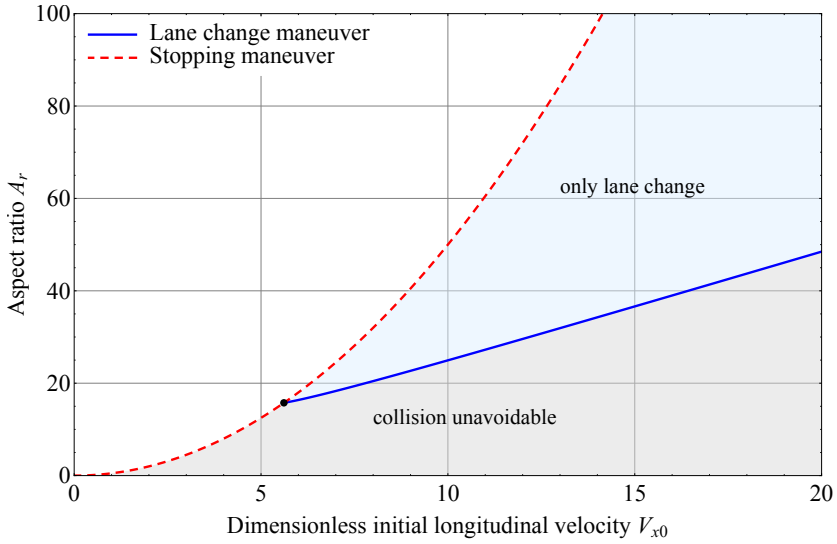

Figure 4.4: Decision-making diagram based on the lane change aspect ratio.

Note that $F_{\max}$ depends on the tire-road friction coefficient μ. Before initiating the avoidance maneuver, first, braking in the current lane can be performed to estimate μ using a real-time estimation method [96].

4.3.2 Dimensionless Time to Collision

An alternative criterion for deciding whether a collision is avoidable is the dimensionless time to collision TTC. The conventional time to collision ttc is defined as the ratio of the range to the range rate. Since the obstacle encountered in the current lane is static, ttc becomes the ratio of the longitudinal distance between the vehicle and the obstacle to the longitudinal velocity of the vehicle. Here, ttc is related to the dimensionless form TTC

using the following definition:

$$TTC = \sqrt{\frac{F_{\max}}{m_t y_f}} ttc \tag{4.32}$$

Using the definition in (4.32), TTC for the lane change maneuver is A_r/V_{x0} and TTC for the stopping maneuver is $V_{x0}/2$. By plotting the dimensionless TTC for the lane change and stopping maneuvers, we obtain another decision-making diagram, as shown in Fig. 4.5. Based on this diagram and the measured TTC and V_{x0}, whether a collision is avoidable and which is the best maneuver for collision avoidance can be decided. The blue solid line and the red dashed line indicate the last points at which a collision can be avoided using the lane change and stopping maneuvers, respectively. The switching point is at $V_{x0} = 5.614465$ and $TTC = 2.807232$.

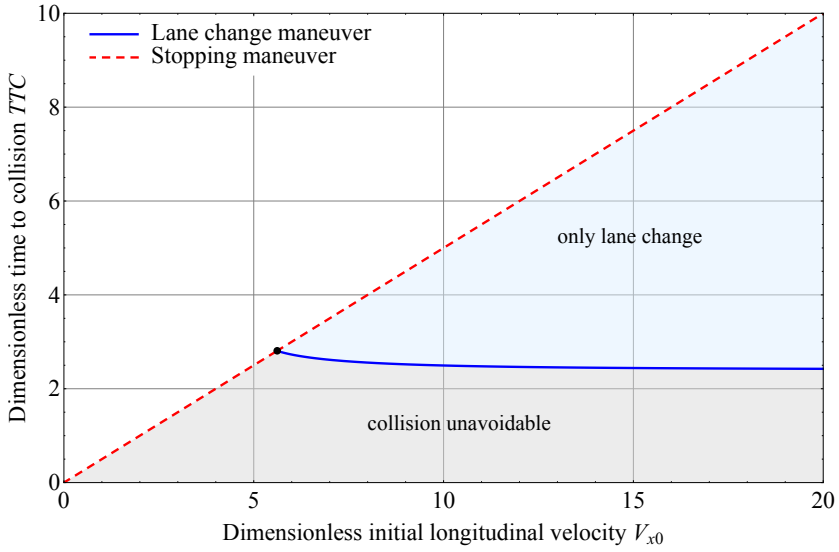

Figure 4.5: Decision-making diagram based on the dimensionless time to collision.

4.3.3 Final-to-Initial Longitudinal Velocity Ratio

For the lane change maneuver, the ratio of the final-to-initial longitudinal vehicle velocity is shown in Fig. 4.6. For the range of V_{x0} considered in this figure, the ratio is less than one, indicating that the final velocity is always lower than the initial velocity. For safety reasons, a lower final longitudinal velocity is desirable. As V_{x0} increases, the ratio increases.

4.4 Sliding Mode Controller Design

This section describes the controller design for tracking the desired trajectory consisting of the path and the velocity profile that are generated using the method explained in

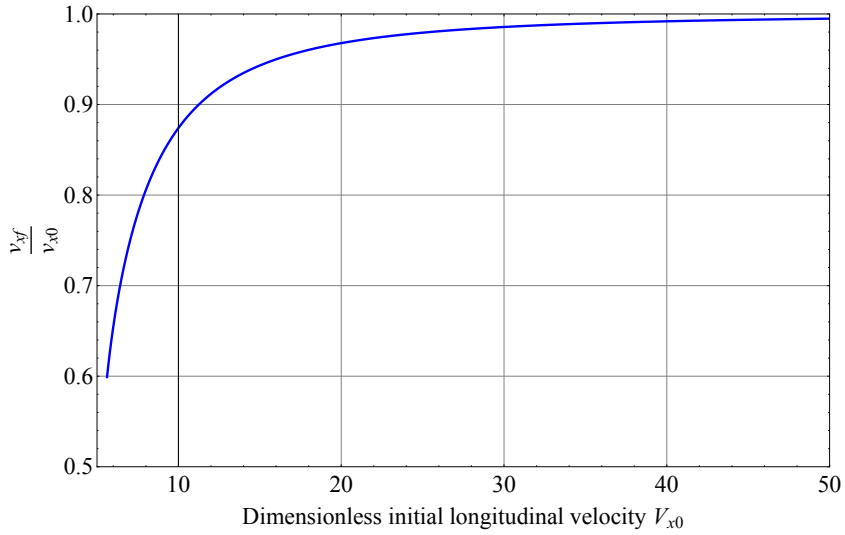

Figure 4.6: Final-to-initial longitudinal vehicle velocity ratio.

Section 4.2. A combination of 4WS control and DYC is used to track the desired trajectory. The 4WS controller design is described in this section, and the DYC method is described in the next section. The 4WS steering controller is designed to track the desired path based on two points that are equivalent to the COPs relative to the rear and front wheels. They are referred to as points P and Q, respectively. As shown in Fig. 4.7, point P is at a distance l_p from the vehicle CG, and point Q is at a distance l_q from the vehicle CG. These distances are given as

$$l_p = \frac{I_z}{m_t l_r} \tag{4.33a}$$

$$l_q = \frac{I_z}{m_t l_f} \tag{4.33b}$$

where I_z is the yaw moment of inertia, and l_f and l_r are the distances from the vehicle CG to the front and rear axles, respectively. The introduction of points P and Q as the COPs in this chapter essentially follows previous studies [65, 64].

In mechanics textbooks [120, 46, 39], the point at which the force is applied to a rigid body is called the COP relative to the point at which no effect on the acceleration is observed. If the initial state of the rigid body was stationary, then the translation and rotation cancel each other at that point. In the case of hitting a ball with a bat, the desirable hitting point is the COP relative to the batter's hand. In some cases, the observation point is termed the pivot.

From (4.33a) and (4.33b), it is easily seen that the pivot-COP pair is interchangeable. Specifically, when the lateral force acts at the rear axle, no effects on the lateral acceleration will be observed at point P. Actually, this relation is more essential for the introduction of points P and Q, because this realizes the decoupling; i.e., the lateral accelerations at

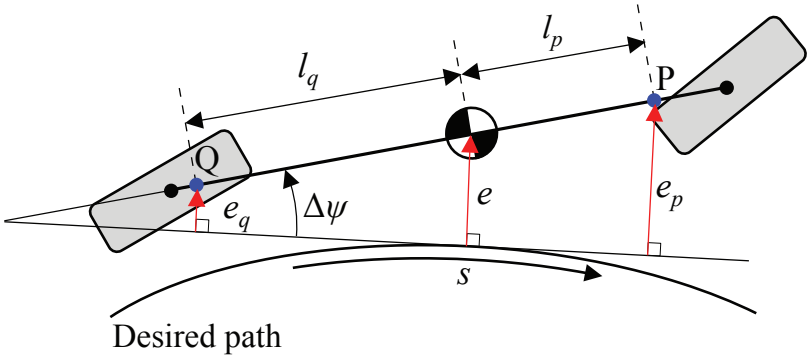

Figure 4.7: Path tracking variable definitions.

points P and Q are controllable by the lateral forces of the front and rear tires, respectively. Point P is actually the unique point such that the rear axle becomes the COP relative to this point.

4.4.1 Error Dynamics

Using the single-track vehicle model shown in Fig. 4.8 along with the assumptions that the longitudinal tire forces are zero and the front steering angle δ_f and rear steering angle δ_r are small, the lateral and yaw equations of motion are

$$F_{yf} + F_{yr} = m_t(\dot{u}_y + u_x\gamma) \tag{4.34a}$$

$$F_{yf}l_f - F_{yr}l_r = I_z\dot{\gamma} \tag{4.34b}$$

where F_{yf} and F_{yr} are the lateral tire forces at the front and rear axles, respectively, u_y and u_x are the lateral and longitudinal vehicle velocities, respectively, and γ is the vehicle yaw rate.

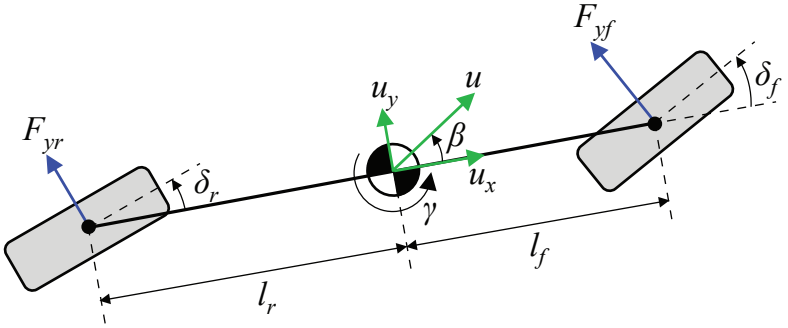

Figure 4.8: Single-track model for a 4WS vehicle.

Fig. 4.7 shows the heading error $\Delta\psi$, vehicle CG lateral error e, point P lateral error e_p, point Q lateral error e_q, and the distance along the path s. According to [64, 36], the

following equations can be derived from Fig. 4.7:

$$\Delta\psi = \psi - \psi_d \tag{4.35a}$$
$$e_p = e + l_p \sin(\Delta\psi) \tag{4.35b}$$
$$e_q = e - l_q \sin(\Delta\psi) \tag{4.35c}$$
$$\dot{e} = u_y \cos(\Delta\psi) + u_x \sin(\Delta\psi) \tag{4.35d}$$
$$\dot{s} = u_x \cos(\Delta\psi) - u_y \sin(\Delta\psi) \tag{4.35e}$$

where ψ is the yaw angle of the vehicle and ψ_d is the heading angle of the desired path. Assuming that $\Delta\psi$ is small, the first-order error derivatives are expressed as in [64, 36]

$$\Delta\dot{\psi} = \gamma - \kappa\dot{s} \tag{4.36a}$$
$$\dot{e}_p = \dot{e} + l_p\Delta\dot{\psi} \tag{4.36b}$$
$$\dot{e}_q = \dot{e} - l_q\Delta\dot{\psi} \tag{4.36c}$$

The path curvature κ is given by

$$\kappa = \frac{\dot{x}\ddot{y} - \ddot{x}\dot{y}}{v^3} \tag{4.37}$$

where $v = \sqrt{\dot{x}^2 + \dot{y}^2}$ is the tangential velocity along the desired path.

Assuming that $\dot{u}_x\Delta\psi \approx 0$, the second-order error derivatives are given as

$$\Delta\ddot{\psi} = \dot{\gamma} - \kappa\ddot{s} - \dot{\kappa}\dot{s} \tag{4.38a}$$
$$\ddot{e}_p = \dot{u}_y + u_x\gamma - u_x\kappa\dot{s} + l_p\dot{\gamma} - l_p(\kappa\ddot{s} + \dot{\kappa}\dot{s}) \tag{4.38b}$$
$$\ddot{e}_q = \dot{u}_y + u_x\gamma - u_x\kappa\dot{s} - l_q\dot{\gamma} + l_q(\kappa\ddot{s} + \dot{\kappa}\dot{s}) \tag{4.38c}$$

where the time derivative of the curvature $\dot{\kappa}$ is given as

$$\dot{\kappa} = \frac{(\dot{x}\dddot{y} - \dddot{x}\dot{y})v^2 + 3(\ddot{x}\dot{y} - \dot{x}\ddot{y})(\dot{x}\ddot{x} + \dot{y}\ddot{y})}{v^5} \tag{4.39}$$

Using (4.34a) and (4.34b), (4.38b) and (4.38c) are rewritten as

$$\ddot{e}_p = \frac{F_{yf} + F_{yr}}{m_t} - u_x\kappa\dot{s} + l_p\frac{F_{yf}l_f - F_{yr}l_r}{I_z} - l_p(\kappa\ddot{s} + \dot{\kappa}\dot{s}) \tag{4.40a}$$
$$\ddot{e}_q = \frac{F_{yf} + F_{yr}}{m_t} - u_x\kappa\dot{s} - l_q\frac{F_{yf}l_f - F_{yr}l_r}{I_z} + l_q(\kappa\ddot{s} + \dot{\kappa}\dot{s}) \tag{4.40b}$$

By substituting (4.33a) and (4.33b) into the third terms of (4.40a) and (4.40b), respectively, and simplifying, (4.40a) and (4.40b) are reduced to

$$\ddot{e}_p = \frac{l}{l_r}\frac{F_{yf}}{m_t} - u_x\kappa\dot{s} - l_p(\kappa\ddot{s} + \dot{\kappa}\dot{s}) \tag{4.41a}$$
$$\ddot{e}_q = \frac{l}{l_f}\frac{F_{yr}}{m_t} - u_x\kappa\dot{s} + l_q(\kappa\ddot{s} + \dot{\kappa}\dot{s}) \tag{4.41b}$$

Detailed explanation on the error dynamics can be found in [64, 36].

Eqs. (4.41a) and (4.41b) indicate that the error at point P depends only on the lateral force at the front axle, and, similarly, the error at point Q depends only on the lateral force at the rear axle. The lateral forces at the front and rear axles are controllable by the steering angle at the front and rear axles, respectively. The path tracking problem can be divided into two distinct problems: point P tracks the desired path using front-wheel steering, and point Q tracks the desired path using rear-wheel steering. Due to the characteristic of the COPs, these two problems are completely decoupled. The locations of points P and Q are determined so as to realize the decoupling.

4.4.2 Path Tracking

In this chapter, the sliding mode control technique is used to design the path tracking controller because this technique offers robustness with respect to parametric and modeling uncertainties [113]. In addition, sliding mode control has been successfully applied to various automotive related nonlinear systems including antilock braking system [108], engine control system [89], and vehicle stability control system [24].

The control objective is to track the desired path. In order to achieve this objective, the sliding surfaces are defined as

$$\sigma_p = \lambda_p e_p + \dot{e}_p \tag{4.42a}$$

$$\sigma_q = \lambda_q e_q + \dot{e}_q \tag{4.42b}$$

where λ_p and λ_q are sliding surface design parameters and are strictly positive constants. Differentiating (4.42a) and (4.42b) with respect to time, we have

$$\dot{\sigma}_p = \lambda_p \dot{e}_p + \ddot{e}_p \tag{4.43a}$$

$$\dot{\sigma}_q = \lambda_q \dot{e}_q + \ddot{e}_q \tag{4.43b}$$

Since the controller derivation for point Q is similar to that for point P, only the derivation for point P is shown here. Substituting (4.41a) into (4.43a) yields

$$\dot{\sigma}_p = \lambda_p \dot{e}_p + \frac{l}{l_r}\frac{F_{yf}}{m_t} - u_x \kappa \dot{s} - l_p(\kappa \ddot{s} + \dot{\kappa}\dot{s}) \tag{4.44}$$

The equivalent control front lateral force can be obtained by solving $\dot{\sigma}_p = 0$ for F_{yf}.

$$F_{yf,\mathrm{eq}} = \frac{m_t l_r}{l}[u_x \kappa \dot{s} + l_p(\kappa \ddot{s} + \dot{\kappa}\dot{s}) - \lambda_p \dot{e}_p] \tag{4.45}$$

The control input front lateral force can be written as

$$F_{yf,c} = F_{yf,\mathrm{eq}} - k_p \,\mathrm{sgn}(\sigma_p) \tag{4.46}$$

where k_p is the control gain and sgn is the sign function. The magnitude of k_p can be chosen using the Lyapunov method. Let us use the Lyapunov function candidate as

$$\mathcal{V}_p = \frac{1}{2}\sigma_p^2 \tag{4.47}$$

The time derivative of (4.47) is

$$\dot{\mathcal{V}}_p = \sigma_p \dot{\sigma}_p \tag{4.48}$$

The magnitude of k_p is chosen so that the following sliding condition is satisfied:

$$\dot{\mathcal{V}}_p = \sigma_p \dot{\sigma}_p \leq -\eta_p |\sigma_p| \tag{4.49}$$

where η_p is a strictly positive constant. Substituting (4.44) into (4.49) yields

$$\sigma_p \left[\lambda_p \dot{e}_p + \frac{l}{l_r} \frac{F_{yf}}{m} - u_x \kappa \dot{s} - l_p (\kappa \ddot{s} + \dot{\kappa} \dot{s}) \right] \leq -\eta_p |\sigma_p| \tag{4.50}$$

Using the control input (4.46), (4.50) can be expressed as

$$-\frac{k_p l \sigma_p \operatorname{sgn}(\sigma_p)}{m_t l_r} \leq -\eta_p |\sigma_p| \tag{4.51}$$

By solving the inequality (4.51) for k_p, we obtain

$$k_p \geq \frac{\eta_p m_t l_r}{l} \tag{4.52}$$

In order to reduce the chattering effects, the sign function is replaced with a saturation function [113]

$$\operatorname{sat}\left(\frac{\sigma_p}{\Phi_p}\right) = \begin{cases} \dfrac{\sigma_p}{\Phi_p}, & \text{if } \left|\dfrac{\sigma_p}{\Phi_p}\right| \leq 1 \\ \operatorname{sgn}(\sigma_p), & \text{otherwise.} \end{cases} \tag{4.53}$$

where Φ_p is the boundary layer thickness. Then, the control input front lateral force becomes

$$F_{yf,c} = \frac{m_t l_r}{l} [u_x \kappa \dot{s} + l_p (\kappa \ddot{s} + \dot{\kappa} \dot{s}) - \lambda_p \dot{e}_p] - k_p \operatorname{sat}\left(\frac{\sigma_p}{\Phi_p}\right) \tag{4.54}$$

Similarly, the control input rear lateral force is derived as

$$F_{yr,c} = \frac{m_t l_f}{l} [u_x \kappa \dot{s} - l_q (\kappa \ddot{s} + \dot{\kappa} \dot{s}) - \lambda_q \dot{e}_q] - k_q \operatorname{sat}\left(\frac{\sigma_q}{\Phi_q}\right) \tag{4.55}$$

where Φ_q is the boundary layer thickness. The value of k_q that satisfies the sliding condition is

$$k_q \geq \frac{\eta_q m_t l_f}{l} \tag{4.56}$$

One can easily obtain the sharpness ς of the path, which is defined as the rate of change of the curvature with respect to the distance along the path

$$\varsigma = \frac{\dot{\kappa}}{v} \tag{4.57}$$

Using $\dot{\kappa} = \varsigma v$ from (4.57), $\dot{s} = v$, and $\ddot{s} = \dot{v}$, the control laws (4.54) and (4.55) are rewritten as

$$F_{yf,c} = \frac{m_t l_r}{l} [u_x \kappa v + l_p (\kappa \dot{v} + \varsigma v^2) - \lambda_p \dot{e}_p] - k_p \operatorname{sat}\left(\frac{\sigma_p}{\Phi_p}\right) \tag{4.58}$$

$$F_{yr,c} = \frac{m_t l_f}{l}[u_x \kappa v - l_q(\kappa \dot{v} + \varsigma v^2) - \lambda_q \dot{e}_q] - k_q \,\mathrm{sat}\left(\frac{\sigma_q}{\Phi_q}\right) \tag{4.59}$$

Now, these control laws are given as functions of the path sharpness.

From (4.33a) and (4.33b) with $I_z \approx m_t l_f l_r$ [7], $l_p = l_f$ and $l_q = l_r$. The lateral accelerations at points P and Q, denoted as a_{yp} and a_{yq}, respectively, are given as

$$a_{yp} = \frac{l}{m_t l_r} F_{yf,c} \tag{4.60a}$$

$$a_{yq} = \frac{l}{m_t l_f} F_{yr,c} \tag{4.60b}$$

The lateral force f_{ty} of a tire is given by the pure lateral slip brush tire model, as in [61]

$$f_{ty} = \begin{cases} -C_\alpha z + \dfrac{C_\alpha^2}{3\mu F_z}|z|z - \dfrac{C_\alpha^3}{27\mu^2 F_z^2} z^3, & \text{if } |\alpha| \le \alpha_{sl} \\ -\mu F_z \,\mathrm{sgn}(\alpha), & \text{otherwise.} \end{cases} \tag{4.61}$$

where C_α is the tire cornering stiffness, α is the tire slip angle, F_z is the vertical tire load, $z = \tan\alpha$, and $\alpha_{sl} = \arctan(3\mu F_z / C_\alpha)$. The angle α_{sl} is the angle at which sliding begins. Brush tire model is a nonlinear tire model that is commonly used for controllers that are designed for different purposes [47, 61, 87]. Compared to the Magic Formula tire model which is an empirical tire model, brush tire model is an analytical tire model and it requires fewer parameters.

The tire model (4.61) can be used to generate the sum of the lateral tire forces at each axle. Accordingly, the cornering stiffness C_α in (4.61) becomes the sum of the cornering stiffnesses at each axle, and the vertical tire load F_z in (4.61) becomes the vertical load at each axle. The vertical load at the front axle F_{zf} and the vertical load at the rear axle F_{zr} are given as

$$F_{zf} = \frac{m_s g l_r}{l} + m_{fs} g - \frac{m_t a_x h_s}{l} \tag{4.62a}$$

$$F_{zr} = \frac{m_s g l_f}{l} + m_{rs} g + \frac{m_t a_x h_s}{l} \tag{4.62b}$$

where m_s is the sprung mass, m_{fs} and m_{rs} are the unsprung masses at the front and rear axles, respectively, a_x is the longitudinal acceleration, and h_s is the height of sprung mass CG.

The desired tire slip angle can be obtained by taking the inverse function of (4.61), which is denoted as f_{ty}^{-1}. This inverse function is obtained by solving (4.61) with respect to α [61]. The front steering angle command δ_f and rear steering angle command δ_r are expressed as functions of the lateral forces $F_{yf,c}$ and $F_{yr,c}$, respectively,

$$\delta_f = \beta + \frac{l_f \gamma}{u_x} - f_{ty}^{-1}(F_{yf,c}) \tag{4.63a}$$

$$\delta_r = \beta - \frac{l_r \gamma}{u_x} - f_{ty}^{-1}(F_{yr,c}) \tag{4.63b}$$

where β is the vehicle sideslip angle.

In a previous study [65], a path tracking sliding mode controller for 4WS based on COPs was developed. In this previous study, the errors for the COPs were defined as the difference between the radius of the desired path and the radius of the actual path. The disadvantage of using the radius for error definition is that there may be situations in which the radius becomes infinite. Furthermore, the steering angles were treated as control inputs with the assumption of a linear lateral tire force model. In this chapter, motivated by [64, 36], the lateral forces at the front and rear axles are treated as the control inputs and are then converted into the respective steering angles using (4.63a) and (4.63b). Fig. 4.9 is a comparison plot of lateral tire force generated using a linear model and a brush model. From this figure, the increase in the deviation of the lateral tire force for a linear model from that of the brush model as the slip angle increases can be clearly seen, especially at a low friction coefficient. Therefore, a linear tire model gives a less accurate representation of the lateral force.

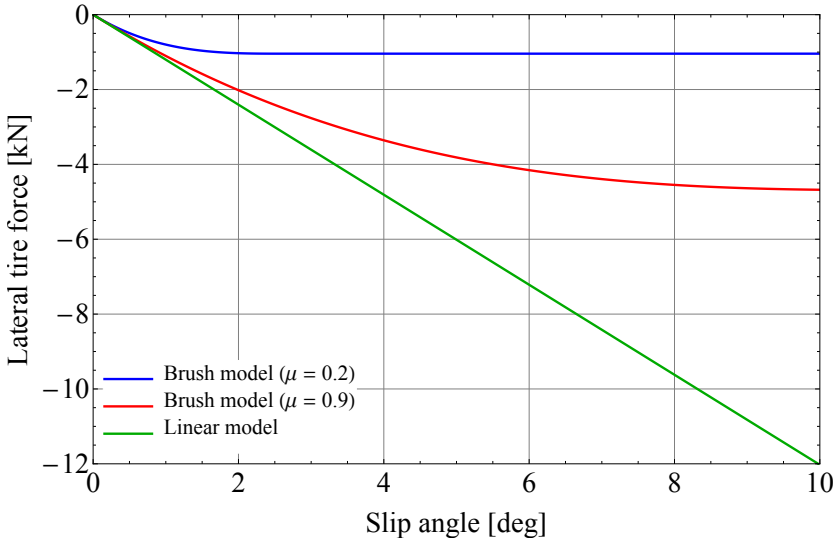

Figure 4.9: Lateral tire force as a function of tire slip angle with $C_\alpha = 68.91$ kN/rad and $F_z = 5.211$ kN.

4.4.3 Velocity Profile Tracking

In order to track the desired velocity, the sliding surface is defined as the difference between the actual velocity $\dot{s}$ and the desired velocity v

$$\sigma_x = \dot{s} - v = u_x \cos(\Delta\psi) - u_y \sin(\Delta\psi) - v \tag{4.64}$$

Assuming a small angle for $\Delta\psi$, (4.64) is rewritten as

$$\sigma_x = u_x - u_y \Delta\psi - v \tag{4.65}$$

Differentiating (4.64) with respect to time, we have

$$\dot{\sigma}_x = \dot{u}_x - \dot{u}_y \Delta\psi - u_y \Delta\dot{\psi} - \dot{v} \tag{4.66}$$

With the assumption $\dot{u}_y \Delta\psi \approx 0$, and using $\Delta\dot{\psi} = \gamma - \kappa\dot{s}$ from (4.36a) and $\dot{s} = v$, (4.66) becomes

$$\dot{\sigma}_x = \dot{u}_x - u_y\gamma + u_y\kappa v - \dot{v} \tag{4.67}$$

The longitudinal dynamics is expressed as

$$X_t = m_t(\dot{u}_x - u_y\gamma) \tag{4.68}$$

where X_t is the total longitudinal force. Solving (4.68) with respect to $\dot{u}_x$ and substituting the resulting equation into (4.69) gives

$$\dot{\sigma}_x = \frac{X_t}{m_t} + u_y\kappa v - \dot{v} \tag{4.69}$$

Solving $\dot{\sigma}_x = 0$ with respect to X_t gives the equivalent control input

$$X_{t,eq} = m_t(\dot{v} - u_y\kappa v) \tag{4.70}$$

The control input total longitudinal force $X_{t,c}$ is expressed as

$$X_{t,c} = X_{t,eq} - k_x \operatorname{sgn}(\sigma_x) \tag{4.71}$$

Consider a Lyapunov function candidate

$$\mathcal{V}_x = \frac{1}{2}\sigma_x^2 \tag{4.72}$$

The time derivative of the Lyapunov function candidate is

$$\dot{\mathcal{V}}_x = \sigma_x\dot{\sigma}_x \leq -\eta_x|\sigma_x| \tag{4.73}$$

Substituting (4.69) into (4.73) gives

$$\dot{\mathcal{V}}_x = \sigma_x\Big(\frac{X_t}{m_t} + u_y\kappa v - \dot{v}\Big) \leq -\eta_x|\sigma_x| \tag{4.74}$$

Next, substituting (4.71) into (4.74) and then solving the resulting inequality with respect to k_x yields

$$k_x \geq \eta_x m_t \tag{4.75}$$

By replacing the sign function in (4.71) with the saturation function, we have

$$X_{t,c} = m_t(\dot{v} - u_y\kappa v) - k_x \operatorname{sat}\left(\frac{\sigma_x}{\Phi_x}\right) \tag{4.76}$$

where Φ_x is the boundary layer thickness.

4.5 Direct Yaw-moment Control

In this section, how the longitudinal tire forces should be distributed so that the vehicle remains stable throughout the avoidance maneuver is described. These longitudinal forces are determined according to the total longitudinal force $X_{t,c}$ and the lateral accelerations of the COPs a_{yp} and a_{yq}. Fig. 4.10 shows a two-track vehicle model that is assumed for the direct yaw-moment control. The vehicle is assumed to perform translational and yaw motions on a horizontal plane.

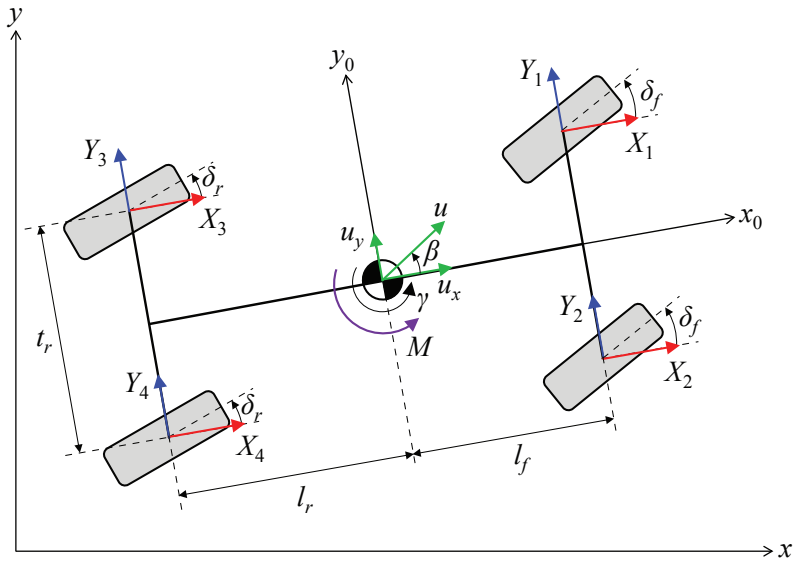

Figure 4.10: Two-track model for a 4WS vehicle.

One of the most commonly used performance indices for the tire force distributors is the tire force usage [87, 115, 67]. Tire force usage is defined as the ratio of the resultant tire force to the maximum available tire force

$$\eta_i = \frac{\sqrt{X_i^2 + Y_i^2}}{\mu_i Z_i} \tag{4.77}$$

where X_i, Y_i, and Z_i are the longitudinal and lateral forces, and the vertical tire load, respectively. The subscript $i \in \{1, 2, 3, 4\}$ denotes the front left, front right, rear left, and rear right tires, respectively. Note that X_i and Y_i are reference forces, and Z_i is the estimated load. If η_i is greater than 1, then the reference tire force will not be realized owing to saturation, and the required $X_{t,c}$, a_{yp}, and a_{yq} will not be realized, which will result in unstable vehicle motion.

The evaluation of tire force usage requires the longitudinal and lateral forces, and the vertical tire loads. Since the wheels on the same axle are assumed to have the same

steering angle, the lateral tire force of each tire is given as in [81]

$$Y_1 = \frac{Z_1}{Z_1 + Z_2} \frac{m_t a_{yp} l_r - M}{l} \tag{4.78a}$$

$$Y_2 = \frac{Z_2}{Z_1 + Z_2} \frac{m_t a_{yp} l_r - M}{l} \tag{4.78b}$$

$$Y_3 = \frac{Z_3}{Z_3 + Z_4} \frac{m_t a_{yq} l_f + M}{l} \tag{4.78c}$$

$$Y_4 = \frac{Z_4}{Z_3 + Z_4} \frac{m_t a_{yq} l_f + M}{l} \tag{4.78d}$$

where M is the direct yaw moment. The vertical tire loads are expressed as follows:

$$Z_1 = \frac{1}{2}\frac{m_s g l_r}{l} + \frac{m_{fs} g}{2} - \frac{1}{2}\frac{m_t a_x h_s}{l} - \frac{m_t a_y h_s}{t_r}\frac{k_{\phi f}}{k_{\phi f} + k_{\phi r}} \tag{4.79a}$$

$$Z_2 = \frac{1}{2}\frac{m_s g l_r}{l} + \frac{m_{fs} g}{2} - \frac{1}{2}\frac{m_t a_x h_s}{l} + \frac{m_t a_y h_s}{t_r}\frac{k_{\phi f}}{k_{\phi f} + k_{\phi r}} \tag{4.79b}$$

$$Z_3 = \frac{1}{2}\frac{m_s g l_f}{l} + \frac{m_{rs} g}{2} + \frac{1}{2}\frac{m_t a_x h_s}{l} - \frac{m_t a_y h_s}{t_r}\frac{k_{\phi r}}{k_{\phi f} + k_{\phi r}} \tag{4.79c}$$

$$Z_4 = \frac{1}{2}\frac{m_s g l_f}{l} + \frac{m_{rs} g}{2} + \frac{1}{2}\frac{m_t a_x h_s}{l} + \frac{m_t a_y h_s}{t_r}\frac{k_{\phi r}}{k_{\phi f} + k_{\phi r}} \tag{4.79d}$$

where t_r is the track width, and $k_{\phi f}$ and $k_{\phi r}$ denote the roll stiffnesses at the front and rear axles, respectively. In the right-hand side of (4.79), the first and second terms correspond to the static vertical tire loads, the third term corresponds to the longitudinal load transfer, and the fourth term corresponds to the lateral load transfer [9].

The following equations are treated as the constraints that must be satisfied by the longitudinal tire forces [81]:

$$X_1 + X_2 + X_3 + X_4 = X_{t,c} \tag{4.80a}$$

$$\frac{t_r}{2}(X_2 - X_1 + X_4 - X_3) = M \tag{4.80b}$$

For simplicity, let $X_L = X_1 + X_3$ and $X_R = X_2 + X_4$, where X_L is the sum of the longitudinal forces of the left-side tires, and X_R is the sum of the longitudinal forces of the right-side tires. Here, X_L and X_R are obtained as the solution to the simultaneous equations (4.80a) and (4.80b), as given in [81]

$$\left.\begin{matrix} X_L \\ X_R \end{matrix}\right\} = \frac{X_{t,c}}{2} \mp \frac{M}{t_r} \tag{4.81}$$

4.5.1 Minimax Optimization of Squared Tire Force Usage

In this subsection, we formulate the problem as minimizing the maximum tire force usage. In a previous paper [48], a tire force distribution method that minimizes the maximum tire workload for given direct yaw moment was proposed. Later, the convexity of the

objective function with respect to the direct yaw moment was proved [81], and the golden section search method was used to find the optimum direct yaw moment M_{opt}. Once M_{opt} is calculated, the tire force distribution can be readily determined. However, the tire workload does not consider the individual tire-road friction coefficient.

In this chapter, we use the following objective function, which is the maximum value of the squared tire force usage:

$$J_\infty = \max_i \eta_i^2 = \max_i \frac{X_i^2 + Y_i^2}{F_i^2} \tag{4.82}$$

where $F_i = \mu_i Z_i$ is introduced for simplicity. The evaluation of the objective function (4.82) requires knowledge of the friction coefficient, and estimation methods are available [85, 82].

The solution method for the minimax optimization of the squared tire force usage is essentially given in [81]. That method is explained here, with minor modifications. In [81], the objective function was originally defined based on the tire workloads.

The objective function (4.82) is rewritten as

$$J_\infty = \max(J_L, J_R) \tag{4.83}$$

where J_L and J_R are the maximum squared tire force usage on the left and right halves of the vehicle body, respectively [81].

$$J_L = \max\left(\eta_1^2, \eta_3^2\right) = \max\left(\frac{X_1^2 + Y_1^2}{F_1^2}, \frac{(X_L - X_1)^2 + Y_3^2}{F_3^2}\right) \tag{4.84a}$$

$$J_R = \max\left(\eta_2^2, \eta_4^2\right) = \max\left(\frac{X_2^2 + Y_2^2}{F_2^2}, \frac{(X_R - X_2)^2 + Y_4^2}{F_4^2}\right) \tag{4.84b}$$

Let us consider the left half of the vehicle body for the derivation of the longitudinal tire forces. The difference in the squared tire force usage between the front and rear wheels is expressed as a function of X_1

$$f_L(X_1) = \eta_1^2 - \eta_3^2 = a_L X_1^2 + b_L X_1 + c_L \tag{4.85}$$

where

$$a_L = \frac{1}{F_1^2} - \frac{1}{F_3^2}, b_L = \frac{2X_L}{F_3^2}, c_L = \frac{Y_1^2}{F_1^2} - \frac{Y_3^2 + X_L^2}{F_3^2}$$

Three modes are identified using (4.85): mode F, mode R, and mode C [81]. For mode F, $X_1 = X_L$ and $X_3 = 0$. The activation condition for this mode is

$$f_L(X_L) \leq 0 \tag{4.86}$$

For mode R, $X_1 = 0$, $X_3 = X_L$, and the activation condition is

$$f_L(0) \geq 0 \tag{4.87}$$

For mode C, $X_1 = X_c$ and $X_3 = X_L - X_c$. This mode is active when neither (4.86) nor (4.87) holds. The solution to $f_L(X_1) = 0$ is obtained based on the stable formula for the solution of a quadratic equation given in [95]

$$X_c = \frac{\left(X_L^2 + Y_3^2\right) F_1^2 - Y_1^2 F_3^2}{F_1^2 \left(X_L + \dfrac{F_3}{F_1} \operatorname{sgn}(X_L) \sqrt{A}\right)} \tag{4.88}$$

where

$$A = X_L^2 + \left(1 - \frac{F_3^2}{F_1^2}\right) Y_1^2 + \left(1 - \frac{F_1^2}{F_3^2}\right) Y_3^2$$

Moreover, M_{opt} is determined using the golden section search method with the lower bound M_l and the upper bound M_u, given as

$$M_l = \max(M_{ll}, M_{rl}) \tag{4.89a}$$

$$M_u = \min(M_{lu}, M_{ru}) \tag{4.89b}$$

where

$$\left.\begin{matrix} M_{ll} \\ M_{lu} \end{matrix}\right\} = \frac{t_r}{2}[(X_{t,c} \mp 2(F_1 + F_3)]$$

$$\left.\begin{matrix} M_{rl} \\ M_{ru} \end{matrix}\right\} = \frac{t_r}{2}[-X_{t,c} \mp 2(F_2 + F_4)]$$

These bounds are modified from those in [81] for the different definition of the objective function.

4.5.2 Minimization of Weighted Sum of Squared Tire Force Usages

In a previous study [71], the weighted sum of the squared tire workloads was considered as the objective function of the optimization problem for the tire force distribution. Here, we consider the minimization of the weighted sum of the squared tire force usages. The objective function is given as

$$J_2 = \sum_{i=1}^{4} w_i \eta_i^2 = \sum_{i=1}^{4} w_i \frac{X_i^2 + Y_i^2}{\mu_i^2 Z_i^2} \tag{4.90}$$

where η_i^2 is the objective function of tire i and w_i is the weight of η_i^2. In order to treat all objective functions equally, set the weight $w_i = 1$ $(i = 1, 2, 3, 4)$. The derivation given here is based on the research in [79] on the minimization of the sum of the squared tire workloads.

Next, we substitute (4.78), $X_3 = X_L - X_1$, and $X_4 = X_R - X_2$ into (4.90), and then substitute (4.81) into the resulting equation. Solving the optimality condition $\partial J_2/\partial X_1 = 0$ with respect to X_1 gives

$$X_1 = \frac{w_3\mu_1^2 Z_1^2(X_{t,c}t_r - 2M)}{2t_r(w_3\mu_1^2 Z_1^2 + w_1\mu_3^2 Z_3^2)} \tag{4.91}$$

and solving another optimality condition $\partial J_2/\partial X_2 = 0$ with respect to X_2 gives

$$X_2 = \frac{w_4\mu_2^2 Z_2^2(X_{t,c}t_r + 2M)}{2t_r(w_4\mu_2^2 Z_2^2 + w_2\mu_4^2 Z_4^2)} \tag{4.92}$$

Using $X_3 = X_L - X_1$, $X_4 = X_R - X_2$, (4.91), (4.92), (4.78), and (4.81), the objective function (4.90) is expressed as a function of M, which is an essential decision variable. Here, X_i and Y_i are determined by the optimum direct yaw moment M_{opt}, which is obtained by setting the partial derivative of the objective function (4.90) with respect to M to zero

$$\frac{\partial J_2}{\partial M} = 0 \tag{4.93}$$

and then solving (4.93) for M

$$M_{\mathrm{opt}} = \frac{M_n}{M_d} \tag{4.94}$$

where

$$M_n = \frac{a_{yp}l_r m_t(w_2\mu_1^2 + w_1\mu_2^2)}{(Z_1+Z_2)^2\mu_1^2\mu_2^2} - \frac{a_{yq}l_f m_t(w_4\mu_3^2 + w_3\mu_4^2)}{(Z_3+Z_4)^2\mu_3^2\mu_4^2} + \frac{A_1 X_{t,c}}{2}$$
$$M_d = \frac{w_2\mu_1^2 + w_1\mu_2^2}{(Z_1+Z_2)^2\mu_1^2\mu_2^2} + \frac{w_4\mu_3^2 + w_3\mu_4^2}{(Z_3+Z_4)^2\mu_3^2\mu_4^2} + \frac{A_2}{t_r}$$

with

$$\left.\begin{matrix} A_1 \\ A_2 \end{matrix}\right\} = \frac{l^2}{t_r}\left(\frac{w_1 w_3}{w_3\mu_1^2 Z_1^2 + w_1\mu_3^2 Z_3^2} \mp \frac{w_2 w_4}{w_4\mu_2^2 Z_2^2 + w_2\mu_4^2 Z_4^2}\right)$$

4.5.3 Wheel Torque Command

The driving/braking torque command T_i is given as

$$T_i = r_{wi}X_i \tag{4.95}$$

where r_{wi} is the radius of wheel i.

4.6 Numerical Examples

4.6.1 Longitudinal Avoidance Distance and Maximum Jerk

In this chapter, jerk is minimized, which would generally yield a longer longitudinal avoidance distance. In [58], a maximum jerk of 30 m/s^3 was considered for collision avoidance. For automated lane change maneuver, a jerk of 1 m/s^3 was considered for human comfort [23]. Since in this dissertation, the focus is given to collision avoidance, a maximum jerk of 30 m/s^3 is considered as a reference value.

It is important to compare the avoidance distance given by the minimum jerk trajectory to that obtained using other methods. Here, we consider three more methods: sigmoid, clothoid, and minimum longitudinal avoidance distance-based optimal control. The optimal control assumes that the vehicle is, at all times, operated at the boundary of the vehicle friction circle. For sigmoid and clothoid control, the trajectories are generated by taking into account the initial longitudinal velocity, the desired final lateral position, the maximum lateral acceleration, and the maximum lateral jerk [58]. For the minimum jerk and optimal control, the trajectory is generated based on the initial longitudinal velocity, the desired final lateral position, and the maximum available vehicle force. The avoidance distance comparison is made using the collision avoidance scenarios reported by Isermann *et al.* [58]. In order to reduce the vehicle resultant jerk, in a previous study, we considered another objective function, which is the time average of the time integral of the squared vehicle resultant jerk [112]

$$J = \frac{1}{t_f}\int_0^{t_f} \dddot{x}^2 + \dddot{y}^2\, dt \tag{4.96}$$

Tables 4.1 and 4.2 list the longitudinal avoidance distances and maximum jerks for five avoidance methods. Note that Quintic 1 and Quintic 2 refer to the avoidance maneuvers using (4.1) and (4.96), respectively. As indicated in these tables, the optimal control yields the shortest avoidance distances but the highest maximum jerks. Compared to Quintic 2, Quintic 1 yields higher jerks but shorter longitudinal avoidance distances.

Table 4.1: Longitudinal Avoidance Distances and Maximum Jerks for $v_{x0} = 36$ m/s, $a_{\max} = 5$ m/s^2, and $y_f = 3$ m

Quintic 1	Quintic 2 [112]	Optimal	Sigmoid [58]	Clothoid [58]
Longitudinal avoidance distance [m]				
70.04	73.13	54.48	70.42	78.85
Maximum jerk [m/s^3]				
21.37	18.89	55.82	30.00	30.00

Table 4.2: Longitudinal Avoidance Distances and Maximum Jerks for $v_{x0} = 36$ m/s, $a_{\max} = 5$ m/s^2, and $y_f = 2$ m

Quintic 1	Quintic 2 [112]	Optimal	Sigmoid [58]	Clothoid [58]
Longitudinal avoidance distance [m]				
56.29	57.84	44.80	53.39	64.30
Maximum jerk [m/s^3]				
28.66	26.46	87.12	30.00	30.00

4.6.2 Simulations

In this subsection, numerical simulations are performed to evaluate the tracking performance provided by the integration of 4WS sliding mode control and DYC. A 14-degree-of-freedom (14DOF) vehicle model with a combined slip nonlinear tire model and parameters corresponding to the E-segment sedan are used for the numerical simulations. The important vehicle parameters are given in Table 4.3. The simulations are performed in the Matlab/SIMULINK environment. A tire-road friction coefficient μ of 0.5, corresponding to a wet road surface condition, is assumed. The desired final lateral position y_f is set to 3.5 m, which corresponds to the lane width. Three cases, in which the initial longitudinal vehicle velocities v_{x0} are 35 m/s, 30 m/s, and 25 m/s, are investigated. For each case, the two tire force distributors described in Section 4.5 are tested. The weights of the weighted sum of the squared tire force usages are set to one. Then, the weighted square sum minimization becomes square sum minimization.

Instead of using $\mu = 0.5$, a lower friction coefficient can be used for the trajectory generation in order to avoid the vehicle operating at its friction limit. Since a point mass model is assumed for the trajectory generation, the maximum resultant acceleration μg serves as a theoretical lower bound. Therefore, using $\mu = 0.45$, $y_f = 3.5$ m, and $v_{x0} =$ 35 m/s, 30 m/s, and 25 m/s, the trajectories consisting of the paths and velocity profiles are generated using the method described in Section 4.2. As μ is reduced from 0.5 to 0.45, the longitudinal avoidance distances for $v_{x0} = 35$ m/s, 30 m/s, and 25 m/s increase from 75.08 m, 65.89 m, and 57.52 m to 78.66 m, 68.82 m, and 59.64 m, respectively. The dimensionless initial velocities V_{x0} corresponding to $v_{x0} = 35$ m/s, 30 m/s, and 25 m/s are 8.451543, 7.24418, and 6.036816, respectively. Referring to Fig. 4.4, at these V_{x0}, stopping in the current lane would require a larger aspect ratio (longer avoidance distance for given y_f) than the lane change maneuvers.

Fig. 4.11 shows the vehicle CG paths obtained by integrated control of 4WS and two different tire force distribution methods for $v_{x0} = 35$ m/s, 30 m/s, and 25 m/s. Although both tire force distributors can track the desired path, the minimax optimization yields better path tracking performance compared to the square sum minimization. The path

Table 4.3: Vehicle Parameters

Parameter	Symbol	Value	Units
Total vehicle mass	m_t	1830	kg
Sprung mass	m_s	1650	kg
Yaw moment of inertia	I_z	3234	kgm^2
Front axle distance from vehicle CG	l_f	1.40	m
Rear axle distance from vehicle CG	l_r	1.65	m
Track width	t_r	1.60	m
Height of sprung mass CG	h_s	0.53	m
Front suspension roll stiffness	$k_{\phi f}$	1144	Nm/deg
Rear suspension roll stiffness	$k_{\phi r}$	1372	Nm/deg
Front axle unsprung mass	m_{fs}	90	kg
Rear axle unsprung mass	m_{rs}	90	kg
Wheel radius	r_w	0.353	m
Front axle cornering stiffness	$C_{\alpha f}$	115	kN/rad
Rear axle cornering stiffness	$C_{\alpha r}$	109	kN/rad

tracking performance is measured in terms of the lateral errors of the COPs. The COPs lateral errors are shown in Fig. 4.12. With square sum minimization, the maximum lateral errors of point P are larger compared to the errors of point Q, whereas with minimax optimization, the maximum lateral errors of points P and Q are approximately the same. As shown in Fig. 4.12, the maximum error of point P with minimax optimization is significantly smaller than that with square sum minimization.

The reasonably small values of the lateral errors for the COPs demonstrates the robustness of the path tracking controller despite the use of relatively simple single-track vehicle model and the lumped lateral tire force assumption for the controller design.

The velocity profiles and simulated vehicle velocities for the three different initial velocities are shown in Fig. 4.13. For each initial vehicle velocity, the vehicle velocity with minimax optimization matches the velocity profile very well, while the vehicle velocity with square sum minimization has a noticeable deviation from the velocity profile. The path and velocity profile tracking results suggest that the avoidance maneuver can be realized using the integration of the 4WS sliding mode control and an effective optimization scheme for the tire force distributor, e.g., minimax optimization.

Fig. 4.14 shows the steering wheel angle, wheel torque, and maximum tire force usage of each tire for $v_{x0} = 25$ m/s. The case in which $v_{x0} = 25$ m/s is chosen here because it has the largest lateral error of point P among the three different initial velocities. As shown in Fig. 4.14a, for each tire force distributor, the maximum front steering angle is

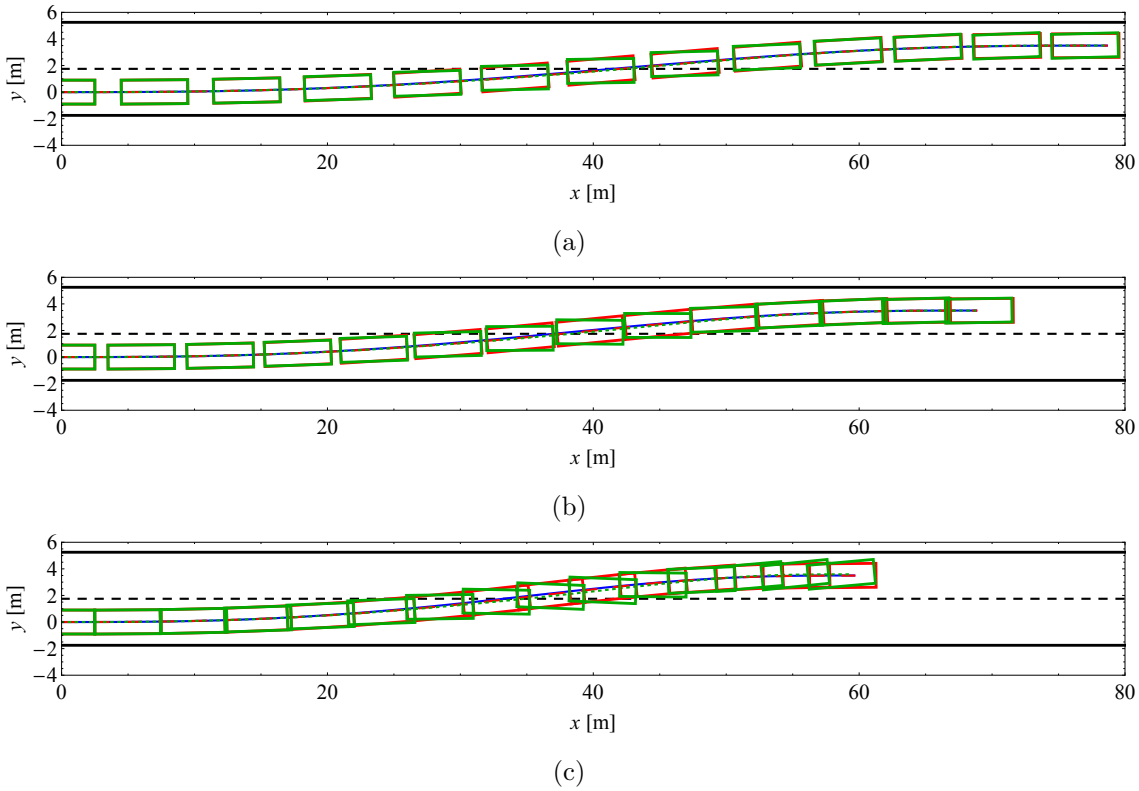

Figure 4.11: Vehicle CG paths for (a) $v_{x0} = 35$ m/s, (b) $v_{x0} = 30$ m/s, and (c) $v_{x0} = 25$ m/s. (Blue solid line) Desired path. (Red dashed line) With minimax optimization. (Green dotted line) With square sum minimization. The red rectangle indicates the vehicle with minimax optimization, and the green rectangle indicates the vehicle with square sum minimization. The first rectangle in each plot is drawn at $t = 0$ s, and the remaining rectangles are drawn at increments of 0.2 s.

larger than that of the rear steering angle. Fig. 4.14a also shows that the vehicle with minimax optimization requires a smaller maximum front steering angle than that with square sum minimization. The maximum front steering rate of the vehicle with square sum minimization is higher than that with minimax optimization. A slower maximum steering rate is desirable.

The wheel torques for all wheels are shown in Fig. 4.14b. Note that negative torque indicates braking torque. For both tire force distributors, the braking torques of the front wheels are larger than those of the rear wheels. The maximum braking torque required for minimax optimization is smaller than that required for square sum minimization.

The maximum tire force usages for both tire distributors are shown in Fig. 4.14c. The maximum force usage here refers to the peak value of the tire force usage throughout the lane change maneuver. Note that the tire force usage in Fig. 4.14c is evaluated based on the longitudinal and lateral tire forces and vertical tire load obtained as the simulation results using the 14DOF vehicle model. As shown in Fig. 4.14c, the front left tire for

the vehicle with square sum minimization reaches its limit of 1, indicating that tire force saturation occurs. None of the tires for the vehicle with minimax optimization reaches their tire force saturation limit, and there is a reasonable margin to the limit. For the point mass, the ratio of the maximum resultant acceleration to the maximum available vehicle acceleration is

$$\frac{\sqrt{\ddot{x}^2(t_a) + \ddot{y}^2(t_a)}}{\mu g} = \frac{0.45g}{0.5g} = 0.9 \tag{4.97}$$

For minimax optimization, among the four tires, the rear left tire experiences the highest tire usage, which is equal to 0.933. Compared to the value given in (4.97), the highest tire force usage with minimax optimization is 3.67% larger. This value is small and indicates that the minimax optimization is quite effective in reducing the maximum tire force usage.

4.7 Conclusion

Lane change maneuvers with minimum jerk for obstacle avoidance were investigated. The generation of the desired trajectory takes into account the constraint imposed by the tire-road friction coefficient. This trajectory can be generated by a numerical solution to a nondimensionalized equation with one unknown and one input. Therefore, fast computation of the trajectory can be expected. The longitudinal avoidance distance is reasonably short, and the maximum jerk is lower compared to other trajectory generation methods. The integration of the 4WS sliding mode control and DYC is effective for realizing the obstacle avoidance maneuver and avoiding high tire force usage. Simulation results also proved that the minimax optimization achieves a lower maximum tire force usage compared to that of minimization of the sum of the squared tire force usages.

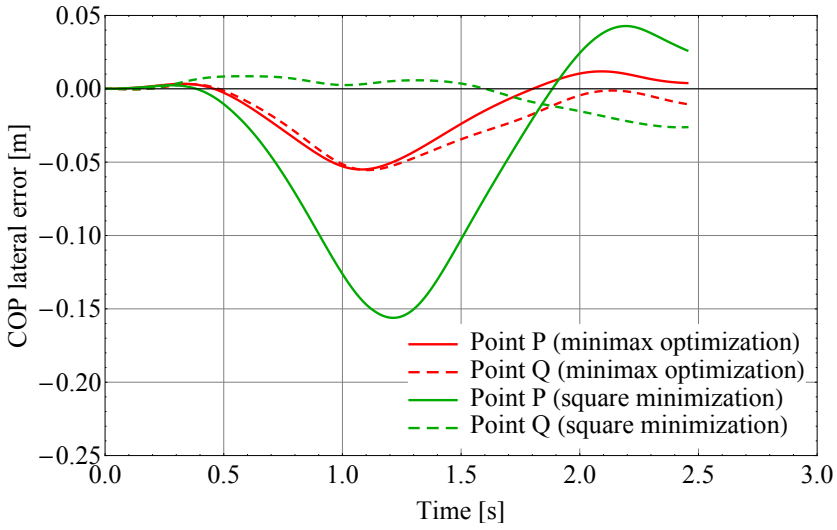

(a)

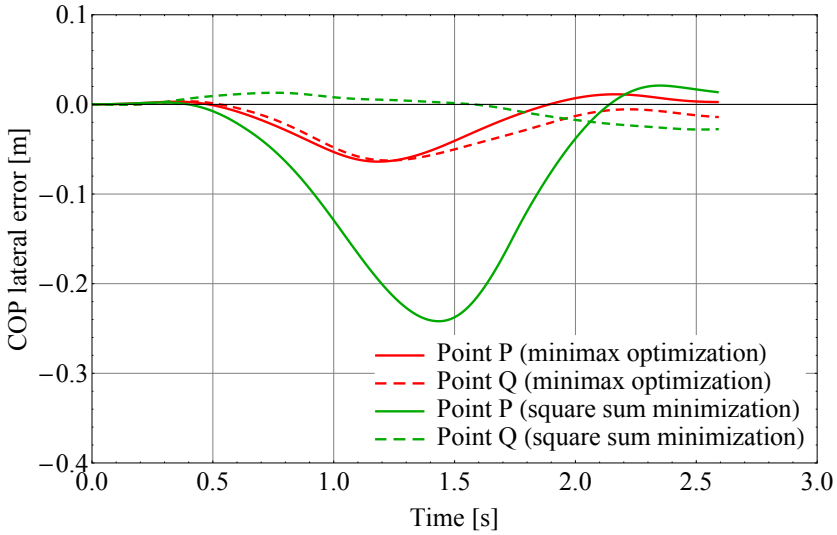

(b)

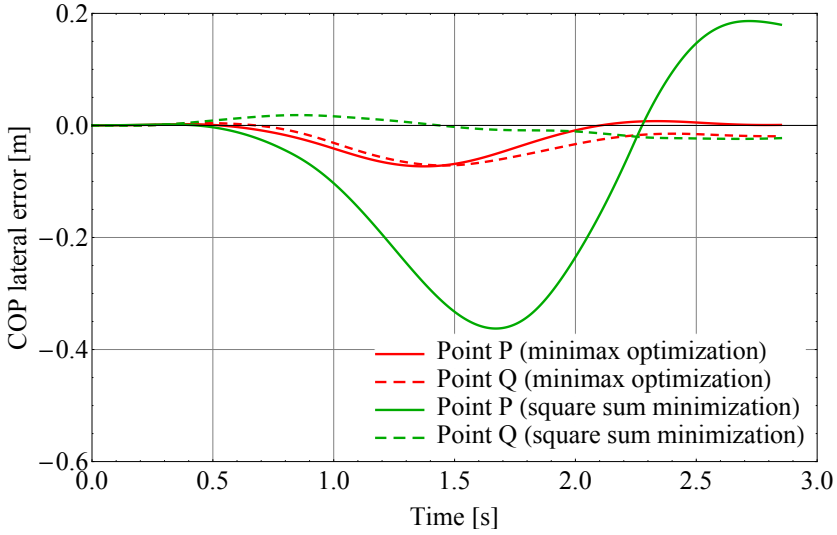

(c)

Figure 4.12: COP lateral errors for (a) $v_{x0} = 35$ m/s, (b) $v_{x0} = 30$ m/s, and (c) $v_{x0} = 25$ m/s.

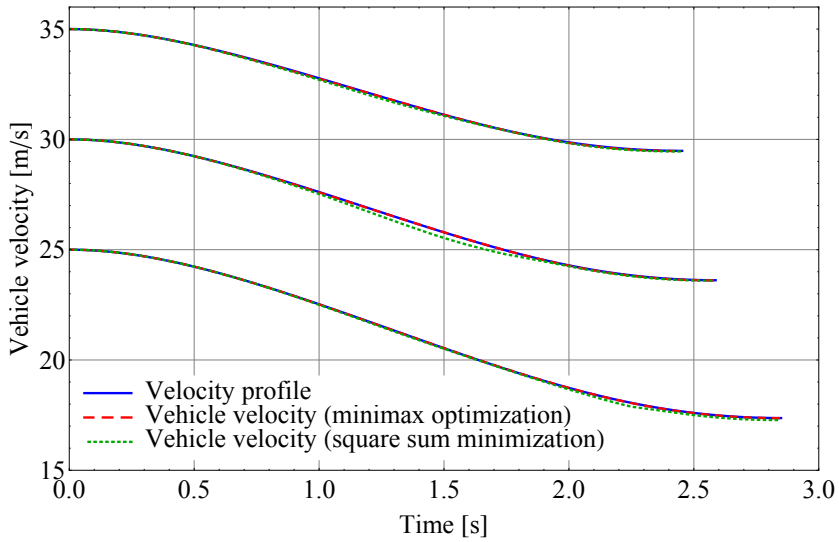

Figure 4.13: Velocity profiles and vehicle velocities.

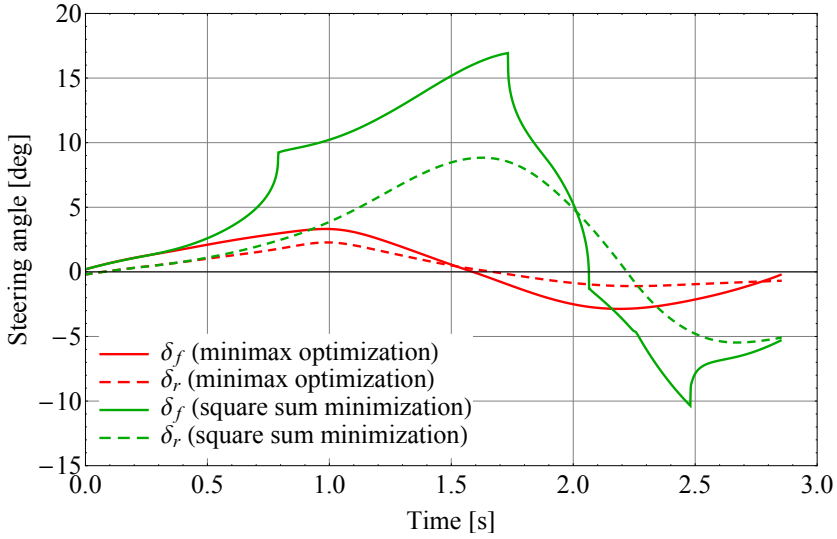

(a)

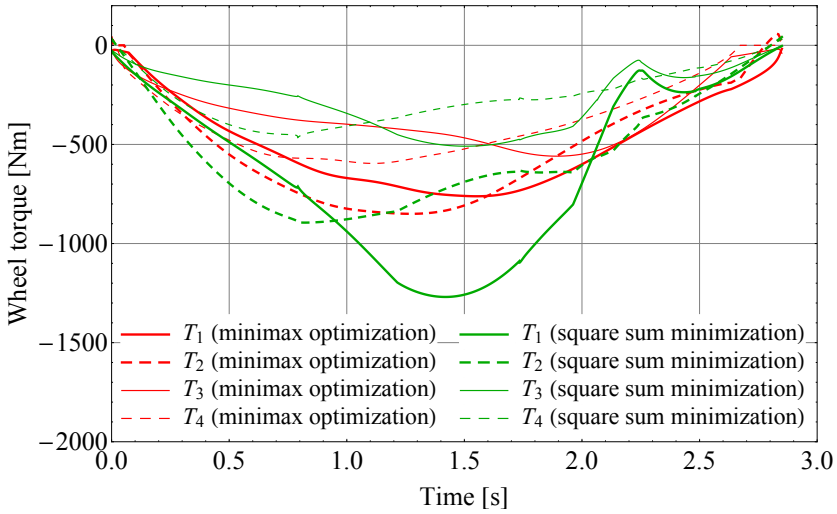

(b)

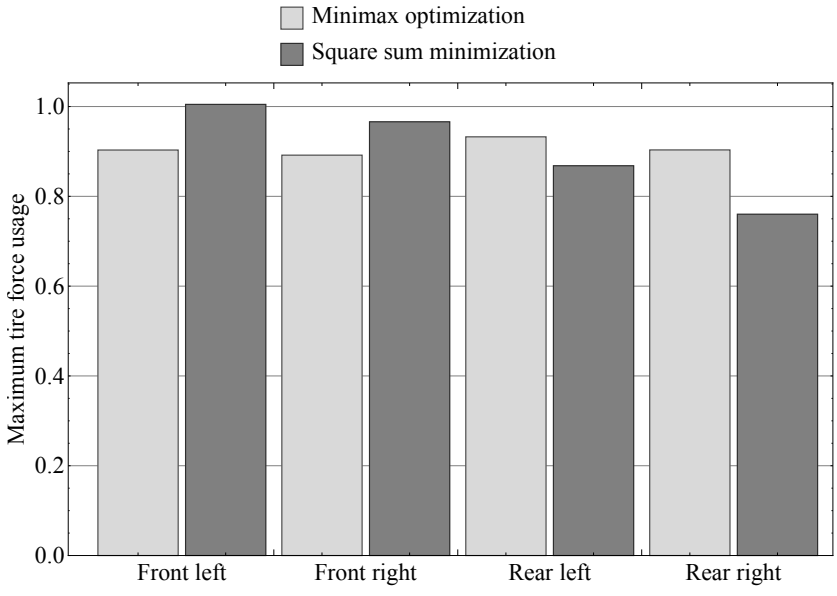

(c)

Figure 4.14: Simulation results for $v_{x0} = 25$ m/s. (a) Steering angles. (b) Wheel torques. (c) Maximum tire force usage.

Chapter 5

Optimal Tire Force Allocation with Workload Equalization

5.1 Introduction

Maneuverability of a vehicle can be greatly improved by the introduction of the electric drive system [51, 74, 127, 35, 75]. In addition to the environmental benefits, in-wheel motors enable individual wheel torque control that enhances the vehicle dynamics performance. Researchers in the field of vehicle dynamics and control have proposed various direct yaw-moment control (DYC) strategies to achieve better vehicle stability and trajectory tracking performances. In general, DYC generates the yaw moment to the vehicle body using the difference in the left and right longitudinal tire forces [105]. The DYC system can be integrated with the active steering control or it can be used as a skid steering [72].

Considerable efforts have been made to develop the longitudinal tire force allocation for an improved vehicle dynamics performance [93, 25, 67]. In [119], the authors used longitudinal tire forces to control vehicle body roll through the suspension mechanism and have shown that the integration of the roll control and tire force allocation control achieves better vehicle stability compared to that of the stand-alone roll control system. In [122], the optimal braking force distribution to minimize the vehicle pitch angle is studied. In order to further improve the vehicle dynamics performance, there have been attempts to optimize the vertical tire forces in addition to optimizing the longitudinal and lateral tire forces, where the vertical tire forces are controlled through the roll stiffness distribution [86] or by active suspension [68]. The study in [32] has demonstrated that the coordination of the vertical and longitudinal tire forces contributes to shorter braking distance.

The integration of DYC and steering control yields better maneuverability. The effects

of this integration can be studied using optimal tire force allocation. The optimal tire force allocation is an integrated chassis control method that optimally allocates the total longitudinal force, the total lateral force, and the total yaw moment to the longitudinal and lateral tire forces in such a way that tire force saturation is avoided. A tire saturates if there are no available longitudinal and lateral tire forces, and this may lead to unstable vehicle motion. A reasonable index to measure how near the tire is to saturation is the tire force usage. Tire force usage is defined as the ratio of the resultant of the longitudinal and lateral tire forces to the product of the vertical tire force and tire-road friction coefficient [9, 131]. Tire force saturation occurs when the tire force usage reaches unity, and, therefore, the tire force usage should be kept as low as possible. If the friction coefficient at all four tires is assumed to be the same, the tire workload, which is defined as the ratio of the resultant of the longitudinal and lateral tire forces to the vertical tire force, is a reasonable index to be minimized [32]. If the value of the tire workload reaches the value of the tire-road friction coefficient, then tire force saturation occurs. In some studies, the tire grip margin, which is defined as the residual tire force divided by the product of the vertical tire force and friction coefficient, is used to measure how near the tire is to force saturation [132]. Instead of using tire force based index to detect tire force saturation, a combined tire slip based approach was proposed in [60].

The total longitudinal force, the total lateral force, and the total yaw moment, which are the inputs to the tire force allocator, are the desired values that are computed by controllers that were designed for different purposes. These controllers include vehicle dynamics, trajectory tracking, and collision avoidance controllers. In a vehicle dynamics controller [125, 115, 71], the forces and moment are determined in order to achieve the desired vehicle motion based on the driver's inputs to the steering wheel and accelerator/brake pedals. The trajectory tracking controller [91] calculates the forces and moment required to track the desired trajectory including the path and speed profile. The collision avoidance controllers determine the forces and moment required to avoid an obstacle by performing a lane change maneuver [41] or to control the post-impact vehicle path to avoid a secondary collision [129]. The desired values of the total longitudinal force, total lateral force, and total yaw moment are achievable using an effective optimal tire force allocation method that minimizes the worst tire force usage among the four tires.

In order to prevent a tire that is under the worst tire force usage condition from reaching force saturation, various optimal tire force allocation methods have been proposed for various integrated chassis control strategies having different objective functions. The optimal tire force allocation is studied for integrated chassis control methods, such as a four-wheel independent driving/braking force distribution and either two-wheel steering (2WS), four-wheel steering (4WS), or four-wheel independent steering (4WIS). Mokhiamar and Abe proposed minimization of the sum of the squared tire workloads [70] and

minimization of the weighted sum of the squared tire workloads [71] for 4WIS and a four-wheel independent driving/braking force distribution. Ono *et al.* [87] proposed an optimal tire force allocation scheme for a vehicle with 4WIS and a four-wheel independent driving/braking force distribution system that achieves the minimum common tire force usage among the four tires. Nishihara and Higashino [81] studied minimax optimization, or more specifically minimization of the maximum squared tire workload for the combinations of 4WS or 4WIS and a four-wheel independent driving/braking force distribution. A comparison study [79] based on the envelopes on the longitudinal-lateral acceleration plane that represent the limit performance of the vehicle for the assumed total yaw moment demonstrated that the minimax optimization achieves a better limit performance of the vehicle compared to that obtained using the minimization of the sum of the squared tire workloads. The considerable improvements of the limit performance by minimax optimization comes from the direct formulation of the problem, whereas the square sum minimization depends on the indirect effect through the minimization of the averaged workload [79].

In addition to the work of Ono *et al.* [87], a number of studies have formulated the optimal tire force allocation problem by keeping the tire force usage of the four tires close to each other in order to prevent the situation in which one tire is under a higher force usage condition as compared to the other tires. Peng *et al.* [94] minimized the difference in the normalized tire force reserves. In order to reduce both the difference in tire force usage among the tires and the tire force usage of each tire, Dai *et al.* [27] considered minimization of the weighted sum of the variance and mean value of the tire force usage. Park and Gerdes [91, 92] proposed an optimization problem that gives the tire force allocation with equal tire force usage by considering the limitations of the steering and braking actuators. The optimal tire force allocation problems in [27, 91, 92] are solved using numerical methods for which reasonably accurate initial guesses are required in order to ensure fast convergence to the optimal solution.

In this chapter, the tire force allocation by equalizing the tire workloads of the four tires for a vehicle with 4WS and a four-wheel independent driving/braking force distribution system is studied and an algebraic solution is derived. The purpose of this chapter is to clarify the limit performance of the vehicle with the tire force allocation that gives the minimum common tire workload and the feasibility of the proposed method. The contributions of this chapter are the derivation of the simple algebraic solution method for this problem, and the investigation of their effectiveness and feasibility. The problem is reduced to finding solutions of the two quadratic equations with respect to the direct yaw moment. The solution of the quadratic equations that gives the minimum common tire workload is taken. The advantage of algebraic solution over the solution provided by numerical methods is that there is no need for an initial guess for the design variable. The

limit performance of the vehicle is evaluated using contour plots of the tire workloads on the acceleration plane. Then, the feasibility of the tire force allocation is investigated and studied. It was found that there are cases in which the workload equalization problem is not feasible. Therefore, this chapter does not propose a practicable tire force allocator.

The remainder of this chapter is organized as follows. The vehicle model used for the analysis is explained in Section 5.2. Section 5.3 develops the solution method to the tire force allocation with an equalized tire workload among the four tires for 4WS and a four-wheel independent driving/braking force distribution. In Section 5.4, the limit performance of the vehicle is first discussed based on tire workload contour plots, and the feasibility of the proposed allocation is then discussed. The conclusions are presented in Section 5.5.

5.2 Vehicle Model

This section describes the vehicle model used for the derivation of the solution method for the optimal tire force allocation problem.

In this chapter, a three-degree-of-freedom (3DOF) vehicle model, as shown in Fig. 5.1, is considered in order to develop the optimal tire force allocation method. As shown in Fig. 5.1, only longitudinal, lateral, and yaw motions that are the motions on a horizontal plane are performed by the vehicle. Both wheels on the same axle are assumed to have the same steering angle. The front and rear wheel steering angles are denoted as δ_f and δ_r, respectively. The tire forces X_i and Y_i are expressed as functions of F_{xi} and F_{yi}, where F_{xi} and F_{yi} are the longitudinal and lateral tire forces, respectively.

$$X_i = F_{xi}\cos\delta_f - F_{yi}\sin\delta_f, \qquad i = 1,2 \tag{5.1a}$$

$$X_i = F_{xi}\cos\delta_r - F_{yi}\sin\delta_r, \qquad i = 3,4 \tag{5.1b}$$

$$Y_i = F_{xi}\sin\delta_f + F_{yi}\cos\delta_f, \qquad i = 1,2 \tag{5.1c}$$

$$Y_i = F_{xi}\sin\delta_r + F_{yi}\cos\delta_r, \qquad i = 3,4 \tag{5.1d}$$

The suffix i has values of 1, 2, 3, and 4, which indicate the front left, front right, rear left, and rear right tires, respectively. For simplicity, the steering angles are assumed to be small, such that the longitudinal and lateral tire forces can be represented by X_i and Y_i, respectively.

The sum of the longitudinal tire forces is given by

$$X_1 + X_2 + X_3 + X_4 = X_t \tag{5.2}$$

where X_t is the total longitudinal force. Similarly, the sum of the lateral tire forces is

$$Y_1 + Y_2 + Y_3 + Y_4 = Y_t \tag{5.3}$$

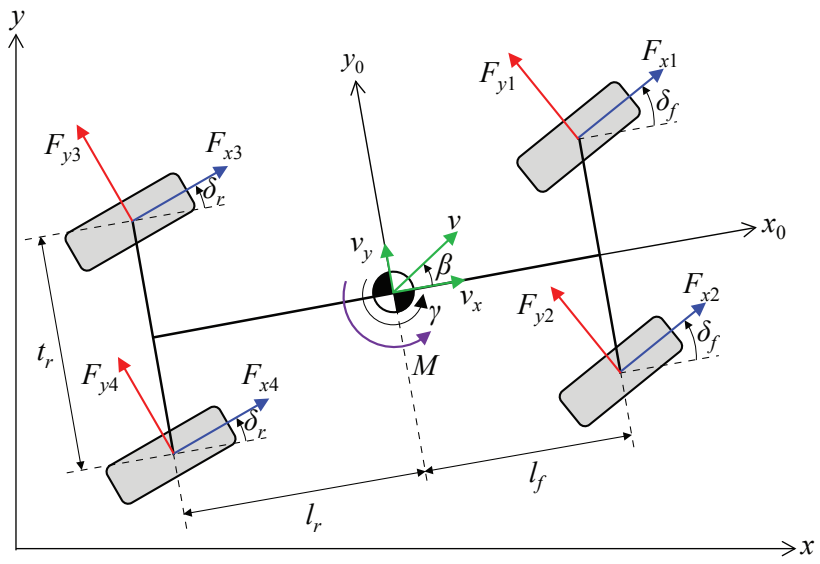

Figure 5.1: Two-track vehicle model.

where Y_t is the total lateral force. The sum of the yaw moments generated by the longitudinal and lateral tire forces is given by

$$l_f(Y_1 + Y_2) - l_r(Y_3 + Y_4) + M = M_t \tag{5.4}$$

where M_t is the total yaw moment, l_f and l_r are the distances of the front and rear axles from the vehicle center of gravity (CG), respectively, and M is the direct yaw moment. The direct yaw moment is defined as the moment generated by the difference in the longitudinal tire forces of the left and right tires

$$M = \frac{t_r}{2}(X_2 - X_1 + X_4 - X_3) \tag{5.5}$$

where t_r is the track width.

The values of X_t, Y_t, and M_t are the desired values of the forces and moment given by a high-level controller and should be allocated to the longitudinal and lateral tire forces such that the situation in which one tire is under a higher workload condition compared to the other tires is avoided. In Section 5.3, an optimal tire force allocation that achieves the minimum equalized tire workload among the four tires is presented.

5.3 Optimal Tire Force Allocation With Workload Equalization

In this section, the derivation of the optimal direct yaw moment and the determination of the optimal tire force allocation for a vehicle with 4WS and a four-wheel independent driving/braking force distribution system are presented.

5.3.1 Lateral Tire Forces

The sum of the lateral tire forces at the front axle can be expressed in terms of the lateral acceleration, a_p, at the center of percussion (COP) relative to the rear axle [81, 48]

$$Y_f = Y_1 + Y_2 = \frac{m_t a_p l_r - M}{l} \tag{5.6}$$

Similarly, the sum of the lateral tire forces at the rear axle is expressed in terms of the lateral acceleration, a_q, at the COP relative to the front axle

$$Y_r = Y_3 + Y_4 = \frac{m_t a_q l_f + M}{l} \tag{5.7}$$

In (5.6) and (5.7), m_t is the total vehicle mass, and $l = l_f + l_r$ is the wheelbase. The lateral accelerations a_p and a_q are given as functions of Y_t and M_t, as in [81]

$$a_p = \frac{Y_t}{m_t} + \frac{M_t}{m_t l_r} \tag{5.8a}$$

$$a_q = \frac{Y_t}{m_t} - \frac{M_t}{m_t l_f} \tag{5.8b}$$

The COPs relative to the rear and front axles are located at a distance l_p in front of the vehicle CG and a distance l_q behind the vehicle CG, respectively. These distances are given as

$$l_p = \frac{I_z}{m_t l_r} \tag{5.9a}$$

$$l_q = \frac{I_z}{m_t l_f} \tag{5.9b}$$

where I_z is the yaw moment of inertia.

Since the steering angles of the wheels for the same axle are assumed to be the same, the lateral tire forces are expressed as in [81]

$$Y_1 = \frac{Z_1}{Z_1 + Z_2} \frac{m_t a_p l_r - M}{l} \tag{5.10a}$$

$$Y_2 = \frac{Z_2}{Z_1 + Z_2} \frac{m_t a_p l_r - M}{l} \tag{5.10b}$$

$$Y_3 = \frac{Z_3}{Z_3 + Z_4} \frac{m_t a_q l_f + M}{l} \tag{5.10c}$$

$$Y_4 = \frac{Z_4}{Z_3 + Z_4} \frac{m_t a_q l_f + M}{l} \tag{5.10d}$$

where Z_i is the vertical force of tire i.

5.3.2 Vertical Tire Forces

The vertical tire forces are required for the determination of the optimal tire force allocation and are estimated by the following equations:

$$Z_1 = \frac{1}{2}\frac{m_s g l_r}{l} + \frac{m_{uf} g}{2} - \frac{1}{2}\frac{m_t a_x h_s}{l} - \frac{m_s a_y h_{sr}}{t_r}\frac{k_{\phi f}}{k_{\phi f}+k_{\phi r}} - \frac{m_s a_y h_f l_r}{t_r l} - \frac{m_{uf} a_y h_{uf}}{t_r} \tag{5.11a}$$

$$Z_2 = \frac{1}{2}\frac{m_s g l_r}{l} + \frac{m_{uf} g}{2} - \frac{1}{2}\frac{m_t a_x h_s}{l} + \frac{m_s a_y h_{sr}}{t_r}\frac{k_{\phi f}}{k_{\phi f}+k_{\phi r}} + \frac{m_s a_y h_f l_r}{t_r l} + \frac{m_{uf} a_y h_{uf}}{t_r} \tag{5.11b}$$

$$Z_3 = \frac{1}{2}\frac{m_s g l_f}{l} + \frac{m_{ur} g}{2} + \frac{1}{2}\frac{m_t a_x h_s}{l} - \frac{m_s a_y h_{sr}}{t_r}\frac{k_{\phi r}}{k_{\phi f}+k_{\phi r}} - \frac{m_s a_y h_r l_f}{t_r l} - \frac{m_{ur} a_y h_{ur}}{t_r} \tag{5.11c}$$

$$Z_4 = \frac{1}{2}\frac{m_s g l_f}{l} + \frac{m_{ur} g}{2} + \frac{1}{2}\frac{m_t a_x h_s}{l} + \frac{m_s a_y h_{sr}}{t_r}\frac{k_{\phi r}}{k_{\phi f}+k_{\phi r}} + \frac{m_s a_y h_r l_f}{t_r l} + \frac{m_{ur} a_y h_{ur}}{t_r} \tag{5.11d}$$

The detailed derivation of (5.11) can be found in [114]. In (5.11), m_s is the sprung mass, m_{uf} and m_{ur} are the front and rear unsprung masses, respectively, g is gravitational acceleration, and a_x and a_y are the vehicle CG longitudinal and lateral accelerations, respectively. The constants $k_{\phi f}$ and $k_{\phi r}$ represent the front and rear roll stiffnesses, respectively. The heights h_s, h_{sr}, h_f, h_r, h_{uf}, and h_{ur} refer to the height of the sprung mass CG from the ground, the height of the sprung mass CG above the roll axis, the height of the front roll center, the height of the rear roll center, the height of the front unsprung mass CG, and the height of the rear unsprung mass CG, respectively. The height h_{sr} is expressed as

$$h_{sr} = h_s - h_{rc} \tag{5.12}$$

where h_{rc} is the height of the sprung mass roll center from the ground and is given as in [8]

$$h_{rc} = \frac{l_r h_f + l_f h_r}{l} \tag{5.13}$$

The first, second, and third terms on the right-hand side of (5.11) are the static load due to the sprung mass, the weight of the unsprung mass, and the load transfer due to the longitudinal acceleration, respectively. The remaining terms express the load transfer due to the lateral acceleration [108].

The effect of the roll angle on the vertical tire forces can be included for more detailed numerical simulation or practical implementation, and knowledge of the roll angle can be made available using an appropriate estimation method [97]. Note that the effects of the pitch and roll motions on the vehicle CG position are not included.

5.3.3 Longitudinal Tire Forces

Let the sum of the longitudinal tire forces on the left side of the vehicle body be represented by $X_L = X_1 + X_3$, and let the sum of the longitudinal tire forces on the right side of the vehicle body be represented by $X_R = X_2 + X_4$. Then, (5.2) and (5.5) can be rewritten as

$$X_L + X_R = X_t \tag{5.14}$$

$$\frac{t_r}{2}(X_R - X_L) = M \tag{5.15}$$

By solving the simultaneous equations (5.14) and (5.15), X_L and X_R are obtained as in [81]

$$\left.\begin{matrix} X_L \\ X_R \end{matrix}\right\} = \frac{X_t}{2} \mp \frac{M}{t_r} \tag{5.16}$$

Equation (5.16) gives the allocation of the direct yaw moment to the left and right tires.

Once X_1, X_2, and M are determined, the rear left and rear right longitudinal tire forces, which are denoted as X_3 and X_4, respectively, are computed as $X_L - X_1$ and $X_R - X_2$, respectively. The determination of X_1, X_2, and M is described later herein, where we show that the problem of finding the optimal tire force allocation is reduced to finding the direct yaw moment M that gives the minimum common tire workload among the four tires.

5.3.4 Performance Index

The tire workload W_i is defined as the ratio of the resultant tire force to the vertical tire force Z_i

$$W_i = \frac{\sqrt{X_i^2 + Y_i^2}}{Z_i}, \qquad i = 1, ..., 4 \tag{5.17}$$

The tire friction circle theory states the resultant tire force at any time is limited by the product of the tire-road friction coefficient and the vertical tire force. Based on this theory, we can derive the following inequality:

$$W_i \leq \mu, \qquad i = 1, ..., 4 \tag{5.18}$$

where μ is the tire-road friction coefficient. All tires should satisfy (5.18) during vehicle motion in order to avoid unstable vehicle behavior. Therefore, tire workload is a reasonable performance index to be minimized.

If the tire workload reaches the value of the tire-road friction coefficient, then there is no available tire force for stabilizing the vehicle motion. If the tire workloads of the four tires are equalized and the equalized value is minimized, then a situation in which a tire is under a higher workload condition can be avoided.

5.3.5 Finding the Optimal Direct Yaw Moment

In this subsection, we derive the solution method for the direct yaw moment that results in the minimum equalized tire workload among the four tires. The resulting direct yaw moment is the optimal direct yaw moment. Once the optimal direct yaw moment has been determined, the desired values for the longitudinal and lateral tire forces can be readily computed.

The squared tire workload of each tire is expressed as follows:

$$W_i^2 = \frac{X_i^2 + Y_i^2}{Z_i^2}, \qquad i = 1, ..., 4 \tag{5.19}$$

Let us define the difference in the squared tire workloads between the front left and front right tires as

$$f_{12} = W_1^2 - W_2^2 \tag{5.20}$$

Using the definition of the squared tire workload in (5.19), along with (5.10a) and (5.10b), and by setting $f_{12} = 0$, we obtain

$$X_1^2 Z_2^2 - X_2^2 Z_1^2 = 0 \tag{5.21}$$

Solving (5.21) with respect to X_1 gives two roots

$$\left.\begin{matrix} X_{1a} \\ X_{1b} \end{matrix}\right\} = \pm \frac{Z_1}{Z_2} X_2 \tag{5.22}$$

Note that (5.22) has an intuitive interpretation. Here, X_{1a} indicates that X_1 is equal to the product of X_2 and the ratio between Z_1 and Z_2, and both X_1 and X_2 are in the same direction. In addition, X_{1b} indicates that X_1 has a magnitude equal to the product of X_2 and the ratio between Z_1 and Z_2, and X_1 and X_2 are in the opposite direction.

We choose $X_1 = X_{1a}$ because both longitudinal tire forces are in the same direction. Then, the difference between the rear left and rear right squared tire workloads are given as

$$f_{34}(X_2) = W_3^2 - W_4^2 = \frac{(2t_r X_2 Z_1 + 2M Z_2 - t_r X_t Z_2)^2}{4t_r^2 Z_2^2 Z_3^2} - \frac{[2M + t_r(X_t - 2X_2)]^2}{4t_r^2 Z_4^2} \tag{5.23}$$

Equation (5.23) is identified as a quadratic function with respect to X_2. Solving $f_{34}(X_2) = 0$ with respect to X_2 gives

$$X_{2a} = \frac{Z_2[t_r X_t (Z_3 - Z_4) + 2M(Z_3 + Z_4)]}{2t_r(Z_2 Z_3 - Z_1 Z_4)} \tag{5.24}$$

$$X_{2b} = \frac{Z_2[2M(Z_3 - Z_4) + t_r X_t (Z_3 + Z_4)]}{2t_r(Z_2 Z_3 + Z_1 Z_4)} \tag{5.25}$$

To avoid numerical instabilities when $Z_2 Z_3 - Z_1 Z_4 = 0$ in the denominator of (5.24), it can be assumed that $|Z_2 Z_3 - Z_1 Z_4| > \varepsilon$ where ε is a small positive constant.

Using (5.24), the difference between the front left and rear left tire squared workloads can be written as a quadratic function with respect to the direct yaw moment M

$$f_{13a}(M) = W_1^2 - W_3^2 = a_2 M^2 + a_1 M + a_0 \tag{5.26}$$

where a_2, a_1, and a_0 are the coefficients of the quadratic function (5.26) and are written as

$$a_2 = \frac{1}{l^2(Z_1+Z_2)^2} - \frac{1}{l^2(Z_3+Z_4)^2} - \frac{(Z_1+Z_2-Z_3-Z_4)(Z_1+Z_2+Z_3+Z_4)}{t_r^2(Z_2Z_3-Z_1Z_4)^2} \tag{5.27a}$$

$$a_1 = -\frac{2a_p l_r m_t}{l^2(Z_1+Z_2)^2} - \frac{2a_q l_f m_t}{l^2(Z_3+Z_4)^2} + \frac{X_t(Z_2^2+Z_3^2-Z_1^2-Z_4^2)}{t_r(Z_2Z_3-Z_1Z_4)^2} \tag{5.27b}$$

$$a_0 = \frac{a_p^2 l_r^2 m_t^2}{l^2(Z_1+Z_2)^2} - \frac{a_q^2 l_f^2 m_t^2}{l^2(Z_3+Z_4)^2} - \frac{X_t^2(Z_1+Z_3-Z_2-Z_4)(Z_1+Z_4-Z_2-Z_3)}{4(Z_2Z_3-Z_1Z_4)^2} \tag{5.27c}$$

Then, $f_{13a}(M) = 0$ is a quadratic equation with respect to M for which the roots M_1 and M_2 can be expressed as functions of the coefficients a_2, a_1, and a_0 based on the formula given in [95]

$$M_1 = \frac{q_{Ma}}{a_2} \tag{5.28}$$

$$M_2 = \frac{a_0}{q_{Ma}} \tag{5.29}$$

where

$$q_{Ma} = -\frac{1}{2}\left[a_1 + \operatorname{sgn}(a_1)\sqrt{a_1^2 - 4a_2a_0}\right] \tag{5.30}$$

Now, using (5.25), the difference between the squared workloads of the front left and rear left tires becomes

$$f_{13b}(M) = W_1^2 - W_3^2 = b_2 M^2 + b_1 M + b_0 \tag{5.31}$$

where the coefficients b_2, b_1, and b_0 are

$$b_2 = \frac{1}{l^2(Z_1+Z_2)^2} - \frac{1}{l^2(Z_3+Z_4)^2} - \frac{(Z_1+Z_2+Z_3-Z_4)(Z_1+Z_2-Z_3+Z_4)}{t_r^2(Z_2Z_3+Z_1Z_4)^2} \tag{5.32a}$$

$$b_1 = -\frac{2a_p l_r m_t}{l^2(Z_1+Z_2)^2} - \frac{2a_q l_f m_t}{l^2(Z_3+Z_4)^2} + \frac{X_t(Z_2^2+Z_3^2-Z_1^2-Z_4^2)}{t_r(Z_2Z_3+Z_1Z_4)^2} \tag{5.32b}$$

$$b_0 = \frac{a_p^2 l_r^2 m_t^2}{l^2(Z_1+Z_2)^2} - \frac{a_q^2 l_f^2 m_t^2}{l^2(Z_3+Z_4)^2} + \frac{X_t^2[(Z_3+Z_4)^2 - (Z_1-Z_2)^2]}{4(Z_2Z_3+Z_1Z_4)^2} \tag{5.32c}$$

By solving $f_{13b}(M) = 0$ with respect to M, we obtain

$$M_3 = \frac{q_{Mb}}{b_2} \tag{5.33}$$

$$M_4 = \frac{b_0}{q_{Mb}} \tag{5.34}$$

where

$$q_{Mb} = -\frac{1}{2}\left[b_1 + \text{sgn}\,(b_1)\sqrt{b_1^2 - 4b_2b_0}\right] \tag{5.35}$$

From the four roots given in (5.28), (5.29), (5.33), and (5.34), the root that gives the minimum common tire workload among the four tires is the optimal direct yaw moment M_{opt}. In order to find M_{opt}, the front right tire workload W_2 is evaluated using M_1, M_2, M_3, and M_4. For M_1 and M_2, the front right tire workload is evaluated as

$$W_2(M) = \frac{\sqrt{X_{2a}^2 + Y_2^2}}{Z_2} \tag{5.36}$$

and for M_3 and M_4, the front right tire workload is evaluated as

$$W_2(M) = \frac{\sqrt{X_{2b}^2 + Y_2^2}}{Z_2} \tag{5.37}$$

Let $W_2(M_1)$, $W_2(M_2)$, $W_2(M_3)$, and $W_2(M_4)$ be the front right tire workloads evaluated at M_1, M_2, M_3, and M_4, respectively. The optimal direct yaw moment M_{opt} corresponds to the direct yaw moment that gives $\min[W_2(M_1), W_2(M_2), W_2(M_3), W_2(M_4)]$.

5.3.6 Optimization Procedures

The optimal longitudinal and lateral tire forces are determined according to the procedures summarized as follows:

1. Calculate the vertical tire forces using the longitudinal and lateral accelerations according to (5.11).

2. Compute M_1, M_2, M_3, and M_4 using (5.28), (5.29), (5.33), and (5.34), respectively.

3. Evaluate the front right tire workload W_2 using M_1, M_2, M_3, and M_4. Find the optimal direct yaw moment M_{opt} among M_1, M_2, M_3, and M_4 that gives $\min[W_2(M_1), W_2(M_2), W_2(M_3), W_2(M_4)]$.

4. Setting $M = M_{\text{opt}}$, compute the lateral tire forces $Y_1, ..., Y_4$ using (5.10).

5. The front right longitudinal tire force X_2 is given by either (5.24) or (5.25), depending on which equation corresponds to the minimum common workload among the four tires. Next, compute the front left longitudinal tire force as $X_1 = (Z_1/Z_2)X_2$. With $M = M_{\text{opt}}$, compute X_L and X_R using (5.16). Then, X_3 and X_4 are obtained as $X_L - X_1$ and $X_R - X_2$, respectively.

5.3.7 Driving/Braking Torque and Steering Angle Commands

The driving/braking torque command of each wheel is simply a linear function of the longitudinal tire force

$$T_i = r_i X_i, \qquad i = 1, ..., 4 \tag{5.38}$$

where r_i is the radius of wheel i.

The steering angle commands for the front and rear wheels are denoted as δ_f and δ_r, respectively, and are given as functions of the lateral accelerations a_p and a_q and the optimal direct yaw moment M_{opt} as in [81]

$$\delta_f = \frac{m_t a_p l_r - M_{\text{opt}}}{l(C_{\alpha 1} + C_{\alpha 2})} + \beta + \frac{l_f \gamma}{v} \tag{5.39a}$$

$$\delta_r = \frac{m_t a_q l_f + M_{\text{opt}}}{l(C_{\alpha 3} + C_{\alpha 4})} + \beta - \frac{l_r \gamma}{v} \tag{5.39b}$$

where $C_{\alpha i} (i = 1, ..., 4)$ is the cornering stiffness of tire i, β is the vehicle sideslip angle, v is the vehicle velocity, and γ is the vehicle yaw rate.

5.4 Numerical Examples

This section presents the evaluation of the limit performance of the vehicle and clarifies the feasibility of the optimal tire force allocation with workload equalization. Table 5.1 shows the vehicle parameters for an E-class sedan obtained from CarSim that are used for numerical examples.

Table 5.1: Vehicle Parameters of an E-Class Sedan

Parameter	Symbol	Value & Units
Total vehicle mass	m_t	1830 kg
Sprung mass	m_s	1650 kg
Distance from vehicle CG to front/rear axle	l_f/l_r	1.40/1.65 m
Track width	t_r	1.60 m
Height of sprung mass CG	h_s	0.53 m
Front suspension roll stiffness	$k_{\phi f}$	1144 Nm/deg
Rear suspension roll stiffness	$k_{\phi r}$	1372 Nm/deg
Height of front/rear roll center	h_f/h_r	0.062/0.405 m
Front unsprung mass	m_{uf}	90 kg
Rear unsprung mass	m_{ur}	90 kg
Height of front unsprung mass CG	h_{uf}	0.32 m
Height of rear unsprung mass CG	h_{ur}	0.30 m

5.4.1 Limit Performance Evaluation

Fig. 5.2 shows a plot of the tire workload as a function of the direct yaw moment for $X_t = -5.49$ kN, $Y_t = 7.32$ kN, and $M_t = 0$ Nm. In order to obtain this plot, the workload of each tire is evaluated using the lateral and vertical tire forces given in subsections 5.3.1 and 5.3.2, respectively. In order to evaluate the tire workloads, the longitudinal tire forces are computed by equalizing the workloads of the tires on each side of the vehicle body as described in [81]. The case in which $X_t = -5.49$ kN, $Y_t = 7.32$ kN, and $M_t = 0$ Nm corresponds to a vehicle performing a left turn with a lateral acceleration of $a_y = 4$ m/s^2 while decelerating ($a_x = -3$ m/s^2). For the given X_t, Y_t, and M_t, the optimal direct yaw moment M_{opt} is equal to -1143.41 Nm, and the minimum common tire workload W_{min} is equal to 0.5102. With zero direct yaw moment, the left tires have a higher common workload with a value of 0.5786, as compared to the right tires, for which the common workload is 0.4859. With tire workload equalization, the maximum workload decreases by 0.0684, which an indication of the effect of keeping the workloads of the four tires at the same value on achieving a lower maximum tire workload during simultaneous turning and deceleration.

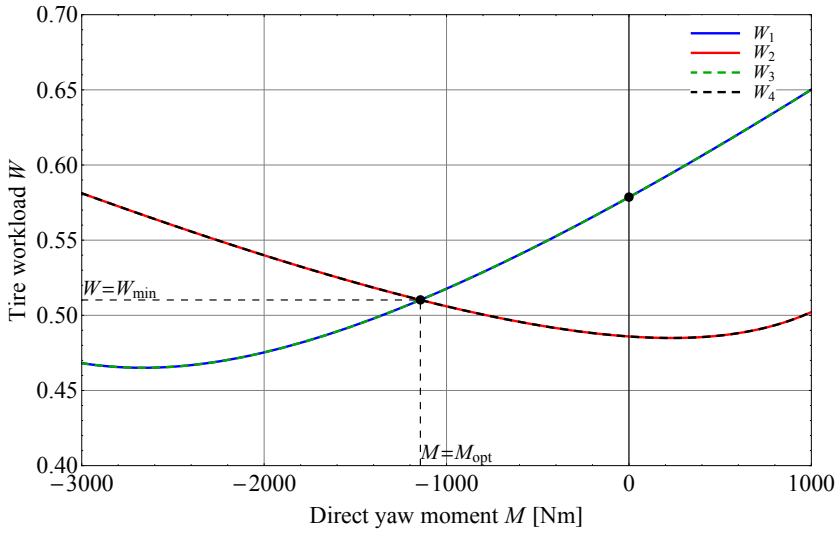

Figure 5.2: Graphical solution to the optimal tire force allocation with workload equalization for $X_t = -5.49$ kN, $Y_t = 7.32$ kN, and $M_t = 0$ Nm.

A plot of the tire workload as a function of the direct yaw moment for $X_t = 5.49$ kN, $Y_t = 7.32$ kN, and $M_t = 0$ Nm is shown in Fig. 5.3. In this case, the vehicle turns with a lateral acceleration of $a_y = 4$ m/s^2 and a longitudinal acceleration of $a_x = 3$ m/s^2. As shown in the previous plot, the tires on each side of the vehicle body have an identical workload. In this case, the optimal direct yaw moment M_{opt} is 1145.98 Nm and the workload at M_{opt} is 0.5103, which is the minimum common tire workload W_{min}. When $M = 0$ Nm, the left tires experience the same workload of 0.5878, which is higher than the

common workload value of 0.4818 for the right tires. Compared to the case in which $M = 0$ Nm, the maximum workload is decreased by 0.0775 through the workload equalization, demonstrating the effect of the optimization of the direct yaw moment in achieving a lower maximum workload during simultaneous turning and acceleration.

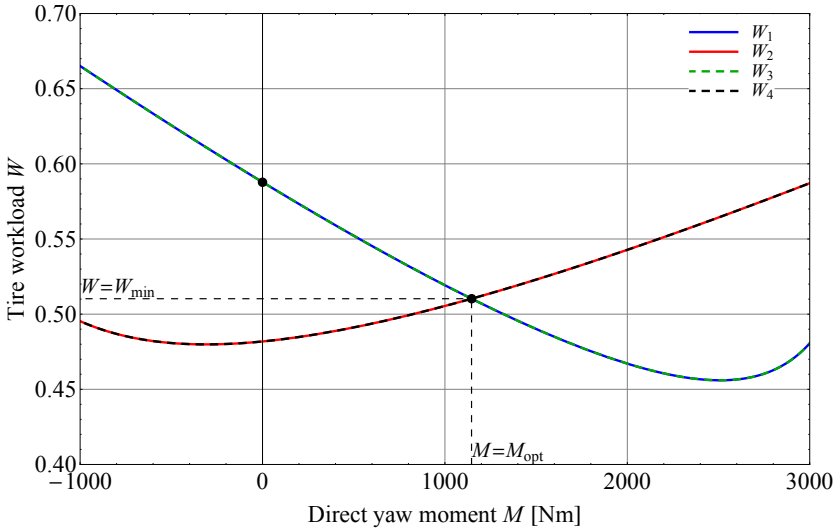

Figure 5.3: Graphical solution to the optimal tire force allocation with workload equalization for $X_t = 5.49$ kN, $Y_t = 7.32$ kN, and $M_t = 0$ Nm.

Fig. 5.4 shows the resultant tire force vector and the friction circle of each tire for $X_t = -5.49$ kN, $Y_t = 7.32$ kN, and $M_t = 0$ Nm. The resultant tire force vector is indicated by the blue arrow, and the friction circle for an assumed tire-road friction coefficient of 0.6 is indicated by the red dashed circle. The radius of the friction circle is given by the product of the tire-road friction coefficient and the vertical tire force. A blue circle with a radius equal to the magnitude of the resultant tire force vector is added in order to better visualize the available force of each tire. With $M = M_{\text{opt}}$, the resultant tire force vectors are far from the corresponding friction circles compared to the case in which $M = 0$ Nm (see Fig. 5.4b). For the $M = 0$ Nm case, as shown in Fig. 5.4b, the resultant force vectors of the left tires are near the corresponding friction circles, and the resultant force vectors of the right tires are far from the corresponding friction circles. The resultant tire force vectors and the friction circles for $X_t = 5.49$ kN, $Y_t = 7.32$ kN, and $M_t = 0$ Nm for a tire-road friction coefficient of 0.6 are shown in Fig. 5.5. When $M = M_{\text{opt}}$, none of the resultant tire force vectors are near the corresponding friction circles and when $M = 0$ Nm, the left tires resultant force vectors are near the corresponding friction circles. These examples demonstrate the effectiveness of the optimization of the direct yaw moment with workload equalization in preventing the tire forces from saturating.

Fig. 5.6 shows a contour plot of the minimum common tire workload for $M_t = 0$ Nm. In this figure, the horizontal and vertical axes represent the longitudinal and lateral ac-

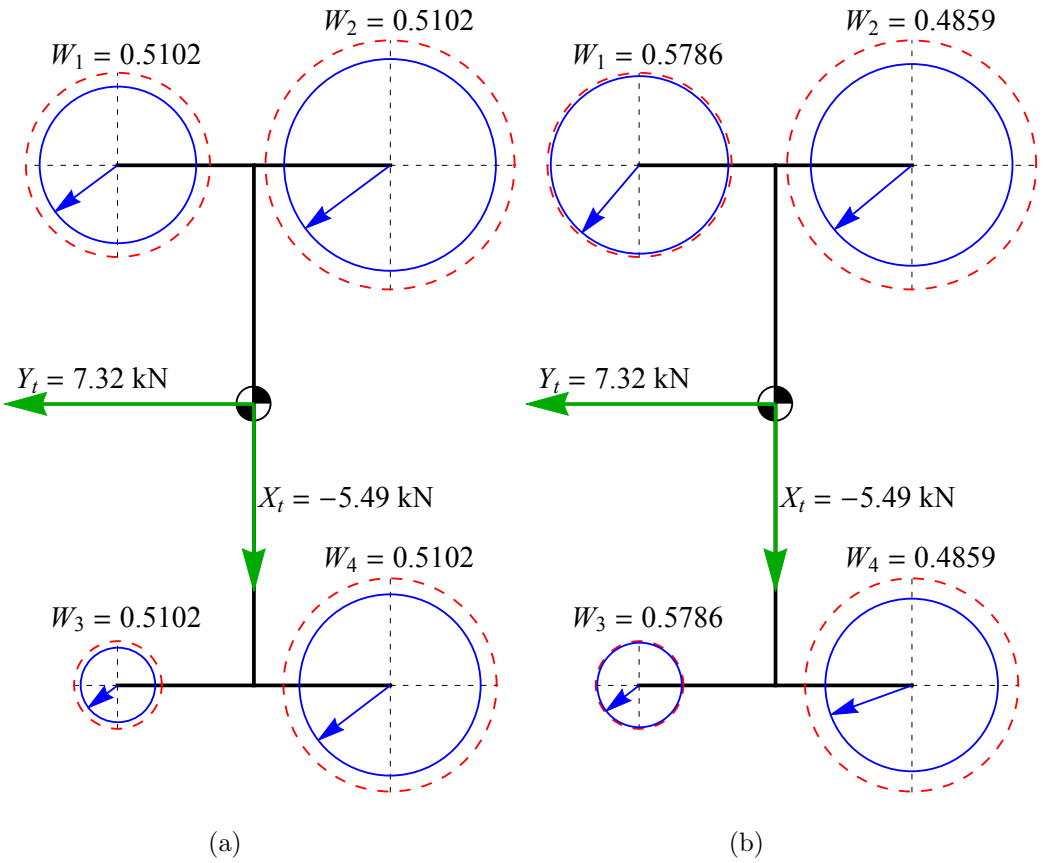

Figure 5.4: Tire force allocation for $X_t = -5.49$ kN, $Y_t = 7.32$ kN, and $M_t = 0$ Nm when (a) $M = M_{\text{opt}}$ and (b) $M = 0$ Nm.

celerations, respectively. These accelerations are X_t/m_t and Y_t/m_t, respectively. Five minimum common tire workload contour lines from 0.1 to 0.5, with an increment of 0.1, are shown in Fig. 5.6. The shapes of the contour lines are approximately concentric circles centered at $(a_x, a_y) = (0, 0)$. The radius of the circle obtained from each contour line with a value μ is similar to the radius of the friction circle, which is equal to μg. This indicates that the theoretical bound imposed by the friction circle can almost be achieved by the corresponding minimum common tire workload. The shape and size of the contour lines are similar to those obtained by minimax optimization [81]. In minimax optimization, the objective function to be minimized is the maximum value of the squared tire workload among the four tires [81]

$$J_\infty = \max_i W_i^2 = \max_i \frac{X_i^2 + Y_i^2}{Z_i^2}, \qquad i = 1, ..., 4 \tag{5.40}$$

The contour plot of the optimal direct yaw moment M_{opt} for $M_t = 0$ Nm is shown in Fig. 5.7. A positive direct yaw moment corresponds to the yaw moment in the counterclockwise direction, and vice versa. As shown in Fig. 5.7, the absolute value of M_{opt} is large when the vehicle is turning with high lateral acceleration and high longitudinal acceleration/deceleration. The top left, top right, bottom left, and bottom right regions

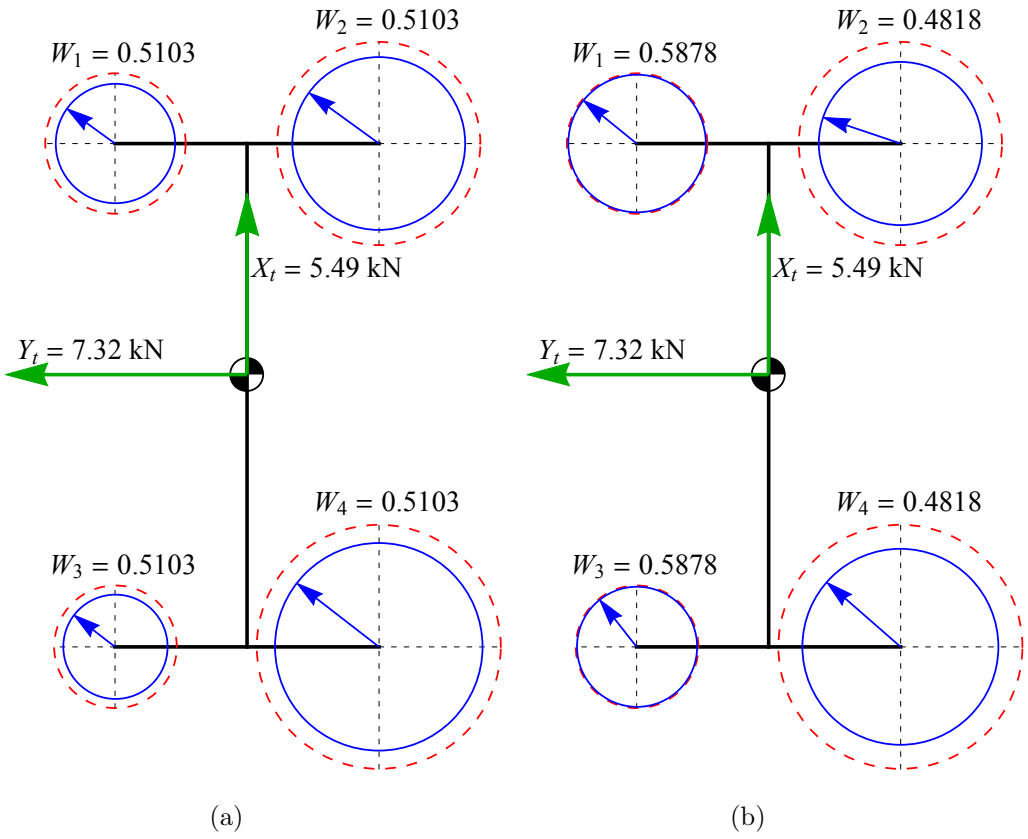

Figure 5.5: Tire force allocation for $X_t = 5.49$ kN, $Y_t = 7.32$ kN, and $M_t = 0$ Nm when (a) $M = M_{\text{opt}}$ and (b) $M = 0$ Nm.

are the regions with the largest absolute M_{opt}. When the lateral acceleration is equal to zero, M_{opt} is zero, irrespective of the value of the longitudinal acceleration/deceleration.

5.4.2 Feasibility of Optimal Tire Force Allocation with Workload Equalization

The examples considered thus far assume $M_t = 0$ Nm. Through inspection, we found that there are possibilities that the quadratic equations $f_{13a}(M) = 0$ and $f_{13b}(M) = 0$ have pairs of complex roots when $M_t \neq 0$. This indicates that there are combinations of X_t, Y_t, and M_t for which there are no feasible tire force allocations with an equalized tire workload among the four tires.

Note the advantage of the algebraic solutions of $f_{13a}(M) = 0$ and $f_{13b}(M) = 0$ as given in (5.28), (5.29), (5.33), and (5.34) for the analysis performed in this subsection. The radicands in (5.30) and (5.35) facilitate checking for the existence of real roots for M. The radicands in (5.30) and (5.35), which are the discriminants of the quadratics (5.26)

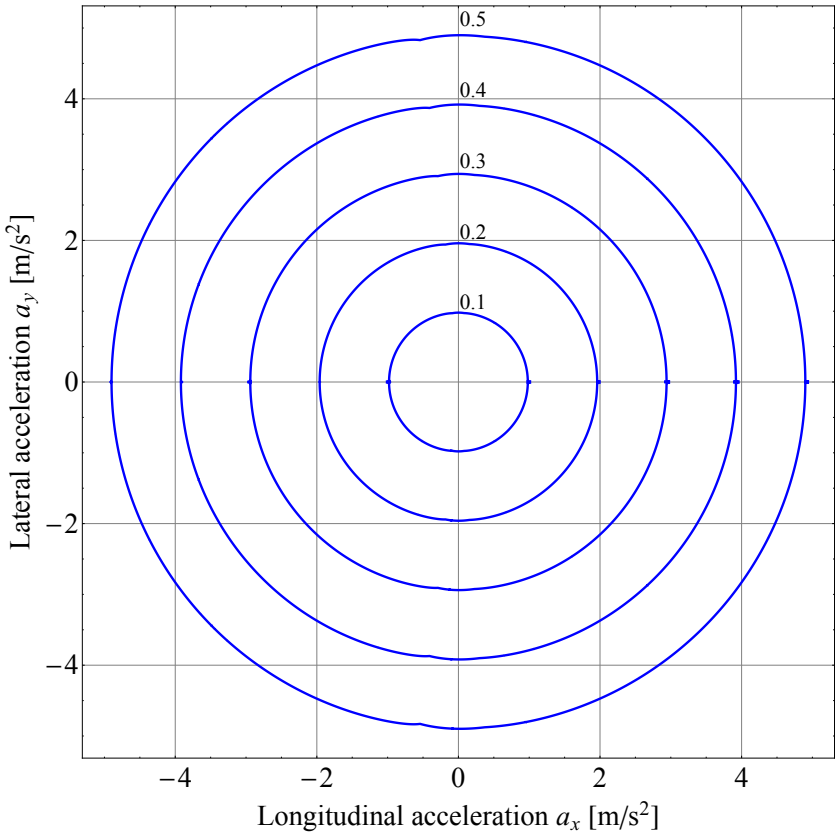

Figure 5.6: Minimum common tire workload contour plot for $M_t = 0$ Nm.

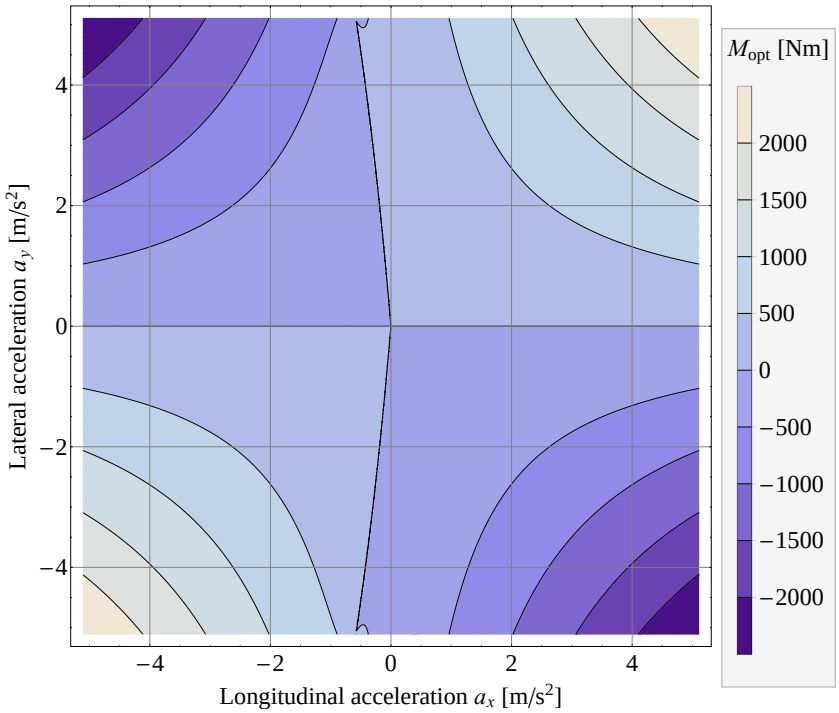

Figure 5.7: Optimal direct yaw moment contour plot for $M_t = 0$ Nm.

and (5.31), respectively, are denoted as $g_1(X_t, Y_t, M_t)$ and $g_2(X_t, Y_t, M_t)$ and are given by

$$g_1(X_t, Y_t, M_t) = a_1^2 - 4a_2a_0 \tag{5.41}$$

$$g_2(X_t, Y_t, M_t) = b_1^2 - 4b_2b_0 \tag{5.42}$$

where a_2, a_1, and a_0 are the coefficients of the quadratic function (5.26) and are given in (5.27a), (5.27b), and (5.27c), respectively. The coefficients b_2, b_1, and b_0 of the quadratic function (5.31) are given in (5.32a), (5.32b), and (5.32c), respectively.

The nature of the roots of the quadratic equations $f_{13a}(M) = 0$ and $f_{13b}(M) = 0$ depends on the sign of the discriminants. Let us consider the discriminant $g_1(X_t, Y_t, M_t)$. If $g_1(X_t, Y_t, M_t) > 0$, then $f_{13a}(M) = 0$ has two distinct real roots. If $g_1(X_t, Y_t, M_t) = 0$, then $f_{13a}(M) = 0$ has a repeated real root. If $g_1(X_t, Y_t, M_t) < 0$, then $f_{13a}(M) = 0$ has no real roots. The discriminant $g_2(X_t, Y_t, M_t)$ can be explained in a similar manner. Therefore, the conditions for no real roots of the equations $f_{13a}(M) = 0$ and $f_{13b}(M) = 0$ are $g_1(X_t, Y_t, M_t) < 0$ and $g_2(X_t, Y_t, M_t) < 0$, respectively.

Fig. 5.8 shows a contour plot of the minimum common tire workload for $M_t = 1000$ Nm. The blue solid lines represent the contour lines that are labeled with the corresponding minimum common tire workload value. The green region corresponds to $g_1(X_t, Y_t, M_t) < 0$, and the red region corresponds to $g_2(X_t, Y_t, M_t) < 0$. There are no real roots for both $f_{13a}(M) = 0$ and $f_{13b}(M) = 0$ in the region produced by the intersection of the regions corresponding to $g_1(X_t, Y_t, M_t) < 0$ and $g_2(X_t, Y_t, M_t) < 0$. This implies that in the intersection region, there is no value of M that will yield tire force allocation with a minimum common value of the tire workload.

For the case in which $M_t = 3000$ Nm, the contour plot of the minimum common tire workload is shown in Fig. 5.9. The green and red regions correspond to $g_1(X_t, Y_t, M_t) < 0$ and $g_2(X_t, Y_t, M_t) < 0$, respectively. As in the previous case, the intersection region is the region in which there are no real roots for both $f_{13a}(M) = 0$ and $f_{13b}(M) = 0$. Compared to the case in which $M_t = 1000$ Nm, this case has a larger region for no real roots for M.

Fig. 5.10 shows the regions in the longitudinal-lateral acceleration plane in which M_1, M_2, M_3, and M_4 become the optimal direct yaw moment M_{opt} for $M_t = 0$ Nm. The blue, green, red, and yellow regions correspond to the regions in which M_{opt} is given by M_1, M_2, M_3, and M_4, respectively. This plot clarifies that the optimal tire force allocation with workload equalization is always possible for $M_t = 0$ Nm as there is always an appropriate real root for M. For positive longitudinal acceleration, in most cases, the optimal direct yaw moment is given by M_2, and for negative longitudinal acceleration, the optimal direct yaw moment is given by M_1, M_2, M_3, or M_4 depending on the values of the pair (a_x, a_y). The regions in which M_1, M_2, M_3, and M_4 are the optimal direct yaw moments for $M_t = 1000$ Nm and $M_t = 3000$ Nm are shown in Figs. 5.11 and 5.12, respectively. In

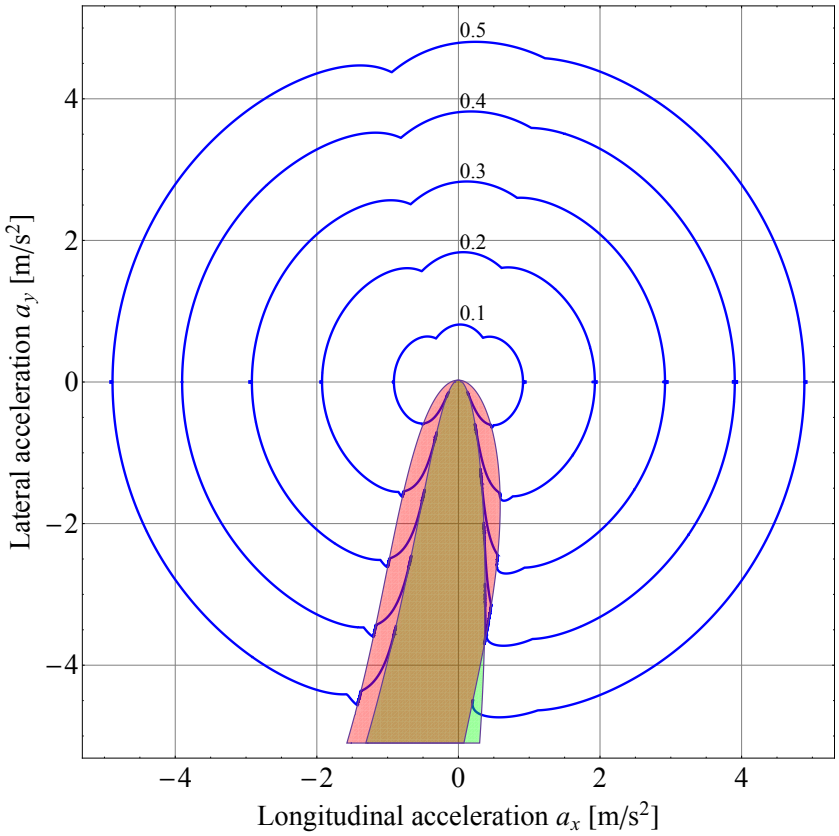

Figure 5.8: Minimum common tire workload contour plot for $M_t = 1000$ Nm. (Green region) $g_1(X_t, Y_t, M_t) < 0$. (Red region) $g_2(X_t, Y_t, M_t) < 0$. (Brown region) Region produced by the intersection of the regions in which $g_1(X_t, Y_t, M_t) < 0$ and $g_2(X_t, Y_t, M_t) < 0$.

Figs. 5.11 and 5.12, the cyan regions are the regions produced by the intersection of the regions corresponding to $g_1(X_t, Y_t, M_t) < 0$ and $g_2(X_t, Y_t, M_t) < 0$. In the cyan region, there are no real roots for M, as already explained.

It should be noted that the discussion on the infeasible regions is based on the assumption that the front left and front right longitudinal tire forces are in the same direction. More specifically, the root $X_1 = X_{1a}$ was chosen among the two roots in (5.22).

5.4.3 Discussion

There is a possibility that the constraint due to the workload equalization may be relaxed by some appropriate approach that keeps the workloads of the four tires close to each other [27]. In this chapter, we did not consider the relaxation problem as we focused on the workload equalization in order to gain insight into the optimal tire force allocation. The previous subsection clarified the limitation of the optimal tire force allocation with workload equalization among the four tires for 4WS and a four-wheel independent driv-

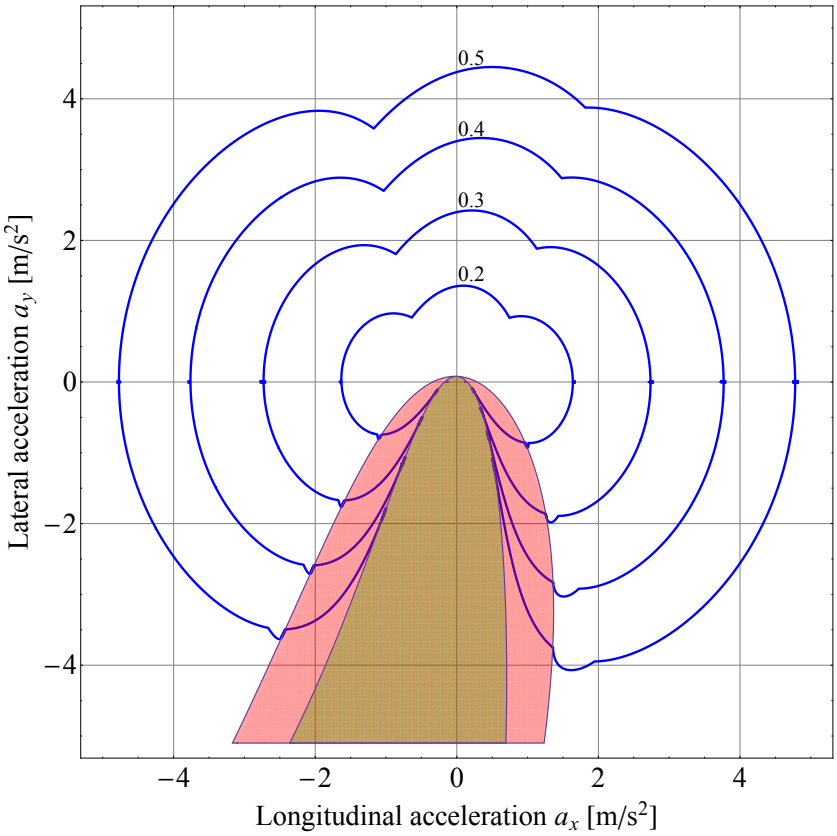

Figure 5.9: Minimum common tire workload contour plot for $M_t = 3000$ Nm. (Red region) $g_2(X_t, Y_t, M_t) < 0$. (Brown region) Region produced by the intersection of the regions in which $g_1(X_t, Y_t, M_t) < 0$ and $g_2(X_t, Y_t, M_t) < 0$.

ing/braking force distribution system. Due to the strict equality constraint on the tire workload, the tire force allocation with common tire workload is not always achievable. However, the solution for the case in which $M_t = 0$ Nm is useful for lane change maneuvers for emergency obstacle avoidance [41, 42, 84].

Note that for a vehicle with 4WS and a four-wheel independent driving/braking force distribution system, one of the most promising optimal tire force allocation methods is minimax optimization. The objective function for minimax optimization is given in (5.40). The minimax optimization problem is reduced to a one-dimensional optimization problem with the direct yaw moment as the design variable [80, 81]. Nishihara and Higashino [80, 81] proposed the use of the golden section search method to solve the minimax optimization problem. The golden section search method realizes a reasonably fast and precise optimization.

As already explained based on the contour plot for $M_t = 0$ Nm in Fig. 5.6, the optimal tire force allocation with minimum common tire workload achieves the limit performance of the vehicle as given by minimax optimization. The workload equalization problem

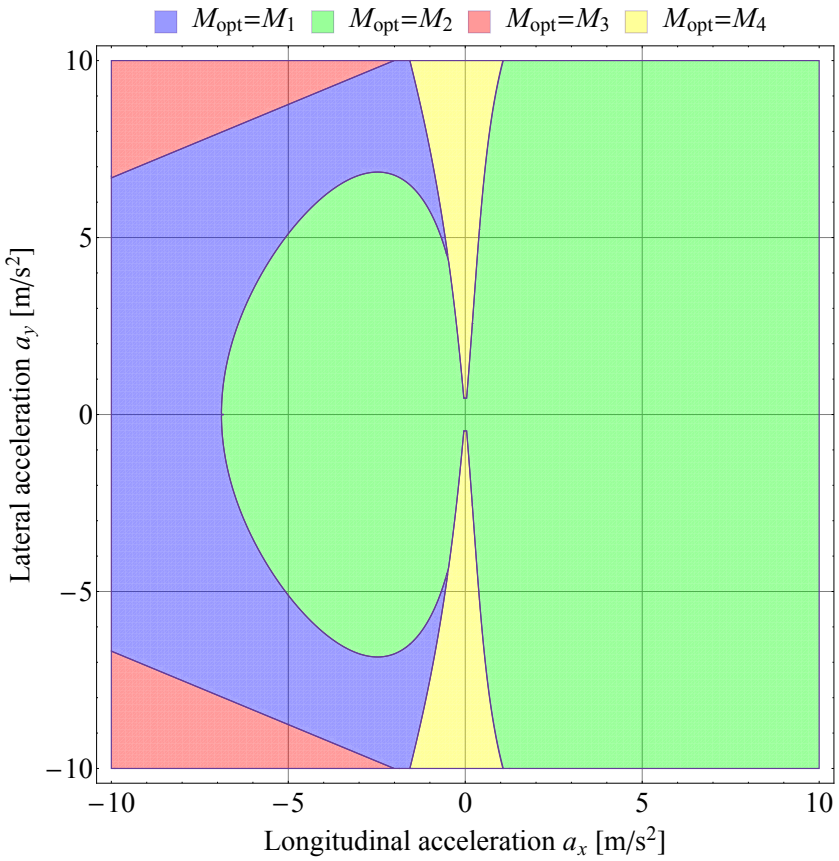

Figure 5.10: Regions in which M_1, M_2, M_3, and M_4 become the optimal direct yaw moment for $M_t = 0$ Nm.

requires lower computational effort compared to that of minimax optimization as there is a simple algebraic solution for the equalization problem. However, for the cases in which there are feasible solutions when $M_t \neq 0$, the limit performance of the vehicle obtained using workload equalization is not always as good as that of minimax optimization.

Another optimization scheme for the tire force allocation that can be found in previous studies is the square sum minimization, in which the objective function to be minimized is the square sum of the tire workloads, as given in [70]

$$J_{ss} = \sum_{i=1}^{4} W_i^2 = \sum_{i=1}^{4} \frac{X_i^2 + Y_i^2}{Z_i^2} \tag{5.43}$$

For 4WS and a four-wheel independent driving/braking force distribution, the square sum minimization has an algebraic solution, and therefore fast computation is expected, but the limit performance is lower than that of minimax optimization [79]. The minimax optimization based tire force allocation is the best for the workload minimization because it directly considers the objective function, and the exact optimal solutions are given in all cases.

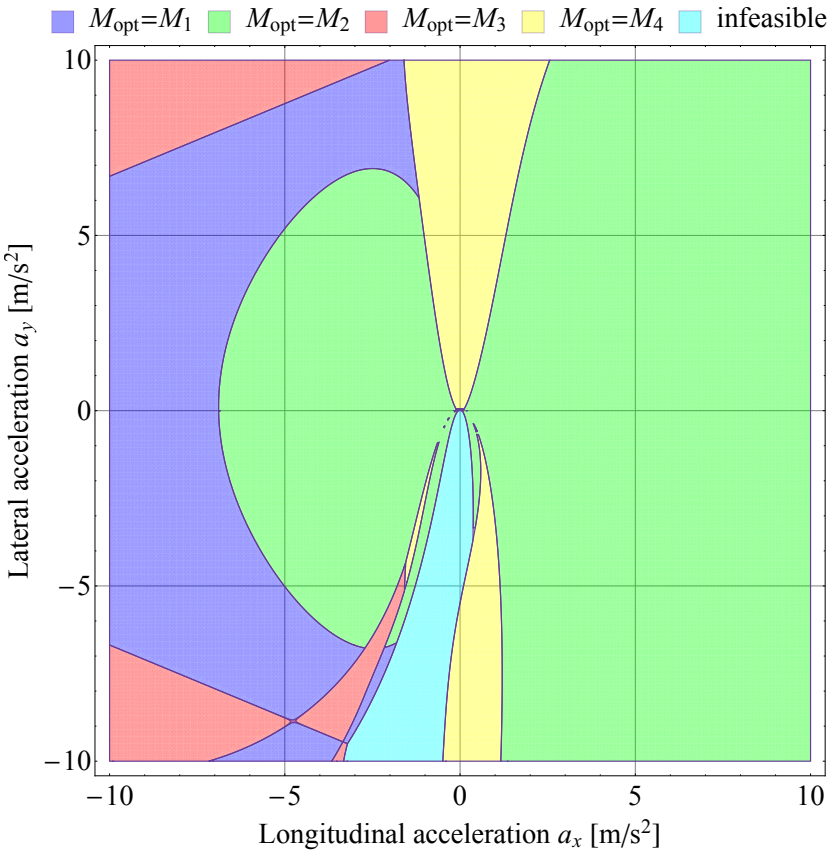

Figure 5.11: Regions in which M_1, M_2, M_3, and M_4 become the optimal direct yaw moment for $M_t = 1000$ Nm.

5.5 Conclusion

In this chapter, we have derived and investigated the algebraic solution to the tire force allocation for the minimum common tire workload among the four tires for a vehicle with 4WS and a four-wheel independent driving/braking force distribution system. The direct yaw moment as the solution of two quadratic equations that gives the minimum common tire workload was taken. The theoretical limit performance of the vehicle with the tire force allocation was evaluated, and the limitation of this allocation was clarified. Using the discriminants of the quadratic equations, the regions in which there are no feasible solutions to the workload equalization were identified. Numerical examples demonstrated that, for the case in which the total yaw moment is zero, the tire force allocation with a minimum common tire workload among the four tires is always achievable.

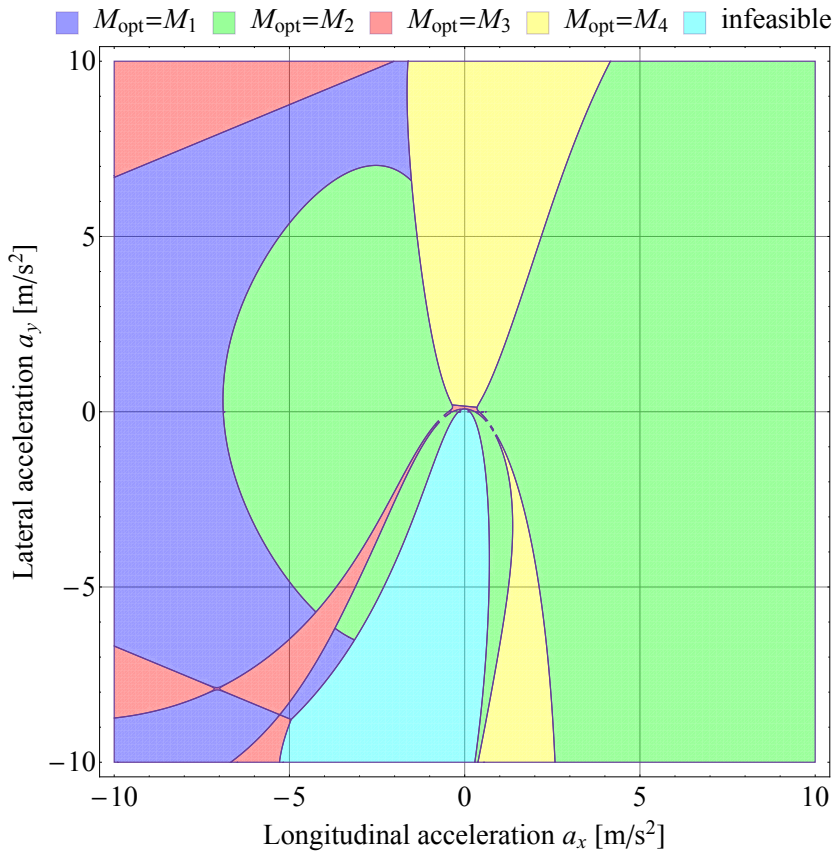

Figure 5.12: Regions in which M_1, M_2, M_3, and M_4 become the optimal direct yaw moment for $M_t = 3000$ Nm.

Chapter 6

Conclusion and Future Work

6.1 Conclusion

This dissertation presented autonomous lane change maneuvers for emergency obstacle avoidance. Two approaches were considered: optimal state feedback control and trajectory generation and tracking control. Chapters 2 and 3 developed the optimal state feedback controls for the minimum longitudinal avoidance distance and minimum resultant vehicle force, respectively. The minimum jerk trajectory generation and tracking control methods were developed in Chapter 4. Both approaches required an effective optimal tire force allocation method for the realization of the avoidance maneuver. Chapter 5 derived an algebraic solution to the optimal tire force allocation with a workload equalization for a vehicle with four-wheel steering (4WS) and four-wheel independent driving/braking distribution systems.

In Chapter 2, the lane change maneuver with the shortest longitudinal traveling distance was considered. First, the shortest longitudinal avoidance distances for three avoidance maneuvers, namely, the braking, steering, and steering with braking maneuvers, were derived. Next, the aspect ratio of the lane change, defined as the ratio of the longitudinal avoidance distance to the final lateral position, was introduced, and the effectiveness of the three avoidance maneuvers were discussed based on the aspect ratio of the lane change. Then, the optimal state feedback control problem for the shortest longitudinal avoidance distance with combined steering and braking was studied. The outputs of the state feedback controller were the total longitudinal and total lateral vehicle forces, assuming a point mass model of the vehicle. The problem was reduced to a fully nondimensionalized equation in a single control parameter that could be determined by using the bisection method. The effectiveness of the proposed method was demonstrated through numerical examples. The vehicle path and velocity obtained using the optimal state feedback control agreed well with those of an open-loop optimal control.

A lane change maneuver for obstacle avoidance with a minimum resultant vehicle force was discussed in Chapter 3. The shape of the lane change path was proven to be dependent only on the aspect ratio of lane change. An optimal state feedback control that minimized the resultant vehicle force was developed. The optimal control was determined by the solution of a fully nondimensionalized equation in a control parameter. The bisection method, which is a robust root-finding method, was used to solve this equation. A comparative study of two different objective functions for the optimal tire force allocation demonstrated that the minimax optimization of the tire workload gave a lower maximum tire workload during the obstacle avoidance maneuver compared to the minimization of the squared sum of the workload of each tire. The integration of the optimal control and the minimax optimization-based optimal tire force allocation was shown to be effective in avoiding a collision, even in those cases where there was a lateral movement of the obstacle or the appearance of another obstacle after the intervention was initiated.

Chapter 4 presented the minimum jerk lane change trajectory and integrated chassis control for obstacle avoidance. A fast computation of the trajectory was expected as only one nondimensionalized equation in the aspect ratio of the lane change had to be solved using an iterative method. A comparative study with other trajectory generation methods such as the sigmoid, clothoid, and optimal control approach, as presented in Chapter 2 indicated that the lane change maneuver with minimum jerk required a reasonably short longitudinal traveling distance and the lowest jerk during the obstacle avoidance maneuver. To track the desired trajectory, an integrated 4WS sliding mode control and DYC was used. This integration achieved a good trajectory tracking and vehicle stabilization performance.

Chapter 5 focused on the optimal tire force allocation by keeping the workloads of the four tires at the same value for the 4WS and four-wheel independent driving/braking distribution. An algebraic solution was derived for the tire force allocation problem. For the case in which the total yaw moment was zero, the contour plot of the minimum common tire workload was similar to concentric circles with the radius of the contour being almost the same as the radius of the friction circle, which was given by the product of the friction coefficient (the value of the friction coefficient was the same as that of the workload) and the gravitational acceleration. This demonstrated that the theoretical limit imposed by the friction circle could almost be reached. For those cases in which the total yaw moment was not zero, the optimal tire force allocation with the workload equalization could not always be achieved. The region where the tire force allocation with the workload equalization was not feasible could be easily identified by using the discriminants of two quadratics.

6.2 Future Work

The obstacle avoidance problem and integrated chassis control can be further studied in several ways.

6.2.1 Estimation of Friction Coefficient

The friction coefficient is an important parameter for both the trajectory generation and optimal tire force allocation. Before the lane change trajectory to avoid the obstacle can be generated, the friction coefficient information is needed as the maximum available vehicle acceleration depends on the friction coefficient. The optimal tire force allocation that uses the tire force as a performance index requires the estimated value of the friction coefficient for the evaluation of the objective function. In this thesis, the friction coefficient was assumed to be known. Under the assumption that the vehicle is traveling on a straight road, the estimation of the friction coefficient can be done in real-time by braking in the current lane prior to the obstacle avoidance maneuver. Future work could focus on the collision avoidance system together with an accurate friction coefficient estimation method so that the maximum available vehicle force and the maximum available tire force can be accurately estimated.

6.2.2 Integration of Four-Wheel Independent Steering and Four-Wheel Independent Driving/Braking Distribution Systems

In vehicles equipped with in-wheel motors, the longitudinal tire forces can be independently controlled, while with a steering actuator at each wheel, the lateral tire forces can be independently controlled. In vehicles with a 4WIS and four-wheel independent driving/braking distribution systems, the longitudinal and lateral tire forces of each tire can be independently controlled to achieve better limit performance. The distribution of the longitudinal and lateral tire forces with an effective optimization scheme, such as the minimax optimization of the tire force usage [79] would lower the maximum tire force usage during the obstacle avoidance maneuver compared to that obtained with a 4WS and four-wheel independent driving/braking distribution.

6.2.3 Optimization of the Longitudinal, Lateral, and Vertical Tire Forces

In addition to the optimization of the longitudinal and lateral tire force distribution, the vertical tire forces can be optimized for improved limit performance. The vertical tire forces can be controlled through the roll stiffness distribution [86] and by using an active suspension [68]. With the optimization of the three forces of each tire, a further reduction in the maximum tire force usage or maximum tire workload during the obstacle avoidance

maneuver can be expected, with a better limit performance by the active suspension compared to the roll stiffness distribution.

6.2.4 Avoidance of Collision with Oncoming Vehicle in Overtaking Maneuver

In this dissertation, single-lane change maneuvers for the avoidance of obstacles were studied. However, the situation where there is an oncoming vehicle in the adjacent lane was not considered. The possibility of a collision with the oncoming vehicle exists. With the Vehicle-to-X communication, the presence of an oncoming vehicle can be detected. Fig. 6.1 shows an ego vehicle (Vehicle A) autonomously performing an overtaking maneuver to avoid a static obstacle (Vehicle B) with an oncoming vehicle (Vehicle C) in the adjacent lane. To reduce the risk of collision between the ego and oncoming vehicles, the distance margin d_{AC}, which is defined as the longitudinal distance between them at the end of the maneuver should be maximized [12].

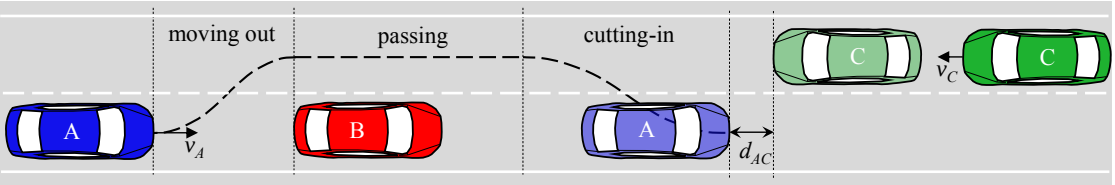

Figure 6.1: Three phases of an overtaking maneuver in the presence of an oncoming vehicle. (Vehicle A) Ego vehicle. (Vehicle B) Static obstacle. (Vehicle C) Oncoming vehicle.

In [12], the overtaking maneuver with the presence of an oncoming vehicle is formulated as an optimal control problem with a point mass representation of the vehicle, and it is solved using PROPT, which is an optimal control software. In [12], the overtaking maneuver is treated as a single optimal control problem. By dividing the overtaking maneuver into three phases (moving out, passing, and cutting-in), and defining an optimal control problem for each of these three phases, some simple solutions can be expected. The approach that is used in Chapters 2 and 3 can be explored to derive simple solution method for the overtaking maneuver with the presence of an oncoming vehicle. Another interesting work would be to investigate the benefit of integrating the 4WS/4WIS and four-wheel independent driving/braking distribution systems for the maximum achievable d_{AC}.

Bibliography

[1] *Dymore User's Manual: Chebyshev polynomials.*

[2] Seeking even greater traffic accident reductions through vehicle advancements (promotion of ASV in order to realize automated driving). http://www.mlit.go.jp/jidosha/anzen/01asv/resourse/data/asv6pamphlet-e.pdf.

[3] *Automotive Technology Handbook: Test & Evaluation (Vehicles)*, volume 9. JSAE, 2016. (in Japanese).

[4] D. A. Abbink, M. Mulder, and E. R. Boer. Haptic shared control: smoothly shifting control authority? *Cognit., Technol., Work*, 14(1):19–28, 2012.

[5] M. Abe. Vehicle dynamics and control for improving handling and active safety: From four-wheel steering to direct yaw moment control. *Proc. Inst. Mech. Eng. K, J. Multi-Body Dyn.*, 213(2):87–101, 1999.

[6] M. Abe. *Vehicle Handling Dynamics: Theory and Application.* Butterworth-Heinemann, Oxford, 2nd ed. edition, 2015.

[7] J. Ackermann and W. Sienel. Robust yaw damping of cars with front and rear wheel steering. *IEEE Trans. Control Syst. Technol.*, 1(1):15–20, 1993.

[8] G. Adireddy, T. Shim, D. Rhode, and J. Asgari. Combined wheel torque and steering control based on model predictive controller using a simplified tyre model. *Int. J. Veh. Design*, 65(1):31–51, 2014.

[9] A. Alleyne. A comparison of alternative intervention strategies for unintended roadway departure (URD) control. *Veh. Syst. Dyn.*, 27(3):157–186, 1997.

[10] A. Alleyne. A comparison of alternative obstacle avoidance strategies for vehicle control. *Veh. Syst. Dyn.*, 27(5-6):371–392, 1997.

[11] A. Arikere, D. Yang, and M. Klomp. Optimal motion control for collision avoidance at left turn across path/opposite direction intersection scenarios using electric propulsion. *Veh. Syst. Dyn.*, 2018.

[12] A. Arikere, D. Yang, M. Klomp, and M. Lidberg. Integrated evasive manoeuvre assist for collision mitigation with oncoming vehicles. *Veh. Syst. Dyn.*, 56(10):1577–1603, 2018.

[13] T. Asami, O. Nishihara, and A. Baz. Analytical solutions to H_∞ and H_2 optimization of dynamic vibration absorbers attached to damped linear systems. *Trans. ASME J. Vib. Acoust.*, 124(2):284–295, 2002.

[14] A. Balachandran, M. Brown, S. M. Erlien, and J. C. Gerdes. Predictive haptic feedback for obstacle avoidance based on model predictive control. *IEEE Trans. Autom. Sci. Eng.*, 13(1):26–31, 2016.

[15] BASt. Traffic and accident data. Summary statistics, Federal Highway Research Institute, 2017.

[16] N. K. Basu. On double Chebyshev series approximation. *SIAM J. Numer. Anal.*, 10(3):496–505, 1973.

[17] M. Best. Optimisation of high-speed crash avoidance in autonomous vehicles. *Int. J. Veh. Auton. Syst.*, 10(4):337–354, 2012.

[18] D. M. Bevly, J. Ryu, and J. C. Gerdes. Integrating INS sensors with GPS measurements for continuous estimation of vehicle sideslip, roll, and tire cornering stiffness. *IEEE Trans. Intell. Transp. Syst.*, 7(4):483–493, 2006.

[19] G. Birkhoff and S. Mac Lane. *A survey of modern algebra*. A.K. Peters, Wellesley, Massachusetts, 1997.

[20] M. Blank and D. L. Margolis. Minimizing the path radius of curvature for collision avoidance. *Veh. Syst. Dyn.*, 33(3):183–201, 2000.

[21] A. Bryson. *Dynamic Optimization*. Addison Wesley Longman, Menlo Park, CA, 1999.

[22] A. E. Bryson and Y. C. Ho. *Applied Optimal Control: Optimization, Estimation and Control*. Taylor & Francis, New York, 1975.

[23] W. Chee and M. Tomizuka. Lane change maneuver for AHS applications. In *Proc. AVEC*, pages 420–425, 1994.

[24] W. Cho, J. Choi, C. Kim, S. Choi, and K. Yi. Unified chassis control for the improvement of agility, maneuverability, and lateral stability. *IEEE Trans. Veh. Technol.*, 61(3):1008–1020, 2012.

[25] W. Cho, J. Yoon, J. Kim, J. Hur, and K. Yi. An investigation into unified chassis control scheme for optimised vehicle stability and manoeuvrability. *Veh. Syst. Dyn.*, 46(sup1):87–105, 2008.

[26] D. A. Cox, J. Little, and D. O'Shea. *Using Algebraic Geometry.* Springer, New York, 2005.

[27] Y. Dai, Y. Luo, W. Chu, and K. Li. Optimum tyre force distribution for four-wheel-independent drive electric vehicle with active front steering. *Int. J. Veh. Design*, 65(4):336–359, 2014.

[28] P. Dingle and L. Guzzella. Optimal emergency maneuvers on highways for passenger vehicles with two- and four-wheel active steering. In *Proc. Amer. Control Conf.*, pages 5374–5381, 2010.

[29] M. Dowell and P. Jarratt. A modified regula falsi method for computing the root of an equation. *BIT*, 11(2):168–174, 1971.

[30] M. Dowell and P. Jarratt. The "Pegasus" method for computing the root of an equation. *BIT*, 12(4):503–508, 1972.

[31] A. Eckert, B. Hartmann, M. Sevenich, and P. E. Rieth. Emergency steer & brake assist: a systematic approach for system integration of two complementary driver assistance systems. In *Proc. ESV*, 2011.

[32] J. Edrén, M. Jonasson, J. Jerrelind, A. S. Trigell, and L. Drugge. Utilisation of optimisation solutions to control active suspension for decreased braking distance. *Veh. Syst. Dyn.*, 53(2):256–273, 2015.

[33] S. M. Erlien, S. Fujita, and J. C. Gerdes. Shared steering control using safe envelopes for obstacle avoidance and vehicle stability. *IEEE Trans. Intell. Transp. Syst.*, 17(2):441–451, 2016.

[34] T. Flash and N. Hogan. The coordination of arm movements: an experimentally confirmed mathematical model. *J. Neurosci.*, 5(7):1688–1703, 1985.

[35] H. Fujimoto and S. Harada. Model-based range extension control system for electric vehicles with front and rear driving-braking force distributions. *IEEE Trans. Ind. Electron.*, 62(5):3245–3254, 2015.

[36] J. Funke. *Collision avoidance up to the handling limits for autonomous vehicles.* PhD thesis, Stanford University, 2015.

[37] J. Funke, M. Brown, S. M. Erlien, and J. C. Gerdes. Collision avoidance and stabilization for autonomous vehicles in emergency scenarios. *IEEE Trans. Control Syst. Technol.*, 25(4):1204–1216, 2017.

[38] J. Funke and J. C. Gerdes. Simple clothoid lane change trajectories for automated vehicles incorporating friction constraints. *Trans. ASME J. Dyn. Syst. Meas. Control*, 138(2):021002–021002–9, 2016.

[39] D. T. Greenwood. *Advanced Dynamics*. Cambridge University Press, 2003.

[40] Y. Hattori and A. Ohmuro. Optimum vehicle trajectory control for obstacle avoidance - feedback controllers for various objective functions. In *Proc. AVEC*, pages 267–272, 2010.

[41] Y. Hattori, E. Ono, and S. Hosoe. Optimum vehicle trajectory control for obstacle avoidance problem. *IEEE/ASME Trans. Mechatronics*, 11(5):507–512, 2006.

[42] Y. Hattori, E. Ono, and S. Hosoe. An optimum vehicle trajectory control for obstacle avoidance with the shortest longitudinal traveling distance. *Trans. SICE*, 43(11):1047–1054, 2007. (in Japanese).

[43] R. Hayashi, S. Fujimori, H. Iwata, and M. Nagai. The autonomous frontal obstacle avoidance system with trajectory updating function. *Mech. Eng. J.*, 4(1):16–00306, 2017.

[44] R. Hayashi, J. Isogai, P. Raksincharoensak, and M. Nagai. Autonomous collision avoidance system by combined control of steering and braking using geometrically optimised vehicular trajectory. *Veh. Syst. Dyn.*, 50(sup1):151–168, 2012.

[45] M. T. Heath. *Scientific Computing: An Introductory Survey*. McGraw-Hill, New York, 2nd ed. edition, 2002.

[46] R. C. Hibbeler. *Engineering Mechanics: Dynamics*. Prentice Hall, 2010.

[47] R. Hindiyeh and J. Gerdes. A controller framework for autonomous drifting: Design, stability, and experimental validation. *Trans. ASME J. Dyn. Syst. Meas. Control*, 136(5):051015–051015–9, 2014.

[48] T. Hiraoka, O. Nishihara, and H. Kumamoto. Driving/braking force distribution by minimax optimization of tire workload (case of active four-wheel steering for zero-sideslip control). *Trans. JSME, Ser. C*, 71(4):1238–1246, 2005. (in Japanese).

[49] T. Hiraoka, O. Nishihara, and H. Kumamoto. Automatic path-tracking controller of a four-wheel steering vehicle. *Veh. Syst. Dyn.*, 47(10):1205–1227, 2009.

[50] N. Hogan. An organizing principle for a class of voluntary movements. *J Neurosci.*, 4(11):2745–2754, 1984.

[51] Y. Hori. Future vehicle driven by electricity and control-research on four-wheel-motored "UOT Electric March II". *IEEE Trans. Ind. Electron.*, 51(5):954–962, 2004.

[52] S. Horiuchi, R. Hirao, K. Okada, and S. Nohtomi. Optimal steering and braking control in emergency obstacle avoidance. *Trans. JSME, Ser. C*, 72(722):3250–3255, 2006. (in Japanese).

[53] S. Horiuchi, K. Okada, and S. Nohtomi. Numerical analysis of optimal vehicle trajectories for emergency obstacle avoidance. *JSAE Rev.*, 22(4):495 – 502, 2001.

[54] C. Hu, R. Wang, and F. Yan. Integral sliding mode-based composite nonlinear feedback control for path following of four-wheel independently actuated autonomous vehicles. *IEEE Trans. Transport. Electrific.*, 2(2):221–230, 2016.

[55] W. Hucho and G. Sovran. Aerodynamics of road vehicles. *Annu. Rev. Fluid Mech.*, 25(1):485–537, 1993.

[56] D. G. Hull. *Optimal Control Theory for Applications*. Springer, New York, 2003.

[57] S. Inoue, H. Inoue, T. Ozawa, P. Raksincharoensak, and M. Nagai. Enhancing path tracking performance by using haptic shared steering control combined with DYC. In *Proc. AVEC*, pages 49–54, 2016.

[58] R. Isermann, M. Schorn, and U. Stählin. Anticollision system PRORETA with automatic braking and steering. *Veh. Syst. Dyn.*, 46(sup1):683–694, 2008.

[59] J. Ji, A. Khajepour, W. W. Melek, and Y. Huang. Path planning and tracking for vehicle collision avoidance based on model predictive control with multiconstraints. *IEEE Trans. Veh. Technol.*, 66(2):952–964, 2017.

[60] E. Joa, K. Park, Y. Koh, K. Yi, and K. Kim. A tyre slip-based integrated chassis control of front/rear traction distribution and four-wheel independent brake from moderate driving to limit handling. *Veh. Syst. Dyn.*, 56(4):579–603, 2018.

[61] N. Kapania, J. Subosits, and J. Gerdes. A sequential two-step algorithm for fast generation of vehicle racing trajectories. *Trans. ASME J. Dyn. Syst. Meas. Control*, 138(9):091005–091005–10, 2016.

[62] J. Kiusalaas. *Numerical Methods in Engineering with MATLAB*. Cambridge University Press, New York, 2009.

[63] M. Klomp, M. Lidberg, and T. J. Gordon. On optimal recovery from terminal understeer. *Proc. IMechE Part D, J. Automobile Eng.*, 228(4):412–425, 2014.

[64] K. Kritayakirana and J. C. Gerdes. Using the centre of percussion to design a steering controller for an autonomous race car. *Veh. Syst. Dyn.*, 50(sup1):33–51, 2012.

[65] H. Kumamoto, O. Nishihara, K. Tenmoku, H. Shimoura, K. Katou, and H. Higashimura. Automated, sliding mode, 4WS control based on centers of percussion of front and rear wheels. In *Proc. IEEE Veh. Technol. Conf.*, pages 2293–2297, 1999.

[66] F. L. Lewis, D. L. Vrabie, and V. L. Syrmos. *Optimal Control*. Wiley, New York, 2012.

[67] B. Li, A. Goodarzi, A. Khajepour, S.-K. Chen, and B. Litkouhi. An optimal torque distribution control strategy for four-independent wheel drive electric vehicles. *Veh. Syst. Dyn.*, 53(8):1172–1189, 2015.

[68] Y. Luo, K. Cao, Y. Xiang, and K. Li. Vehicle stability and attitude improvement through the coordinated control of longitudinal, lateral and vertical tyre forces for electric vehicles. *Int. J. Veh. Design*, 69(1-4):25–49, 2015.

[69] C. March and T. Shim. Integrated control of suspension and front steering to enhance vehicle handling. *Proc. IMechE Part D, J. Automobile Eng.*, 221(4):377–391, 2007.

[70] O. Mokhiamar and M. Abe. Effects of an optimum cooperative chassis control from the view points of tire workload. In *Proc. of JSAE Spring Conv.*, pages 15–20, 2003.

[71] O. Mokhiamar and M. Abe. Simultaneous optimal distribution of lateral and longitudinal tire forces for the model following control. *Trans. ASME J. Dyn. Syst. Meas. Control*, 126(4):753–763, 2004.

[72] O. Mokhiamar and S. Amine. Lateral motion control of skid steering vehicles using full drive-by-wire system. *Alexandria Eng. J.*, 56(4):383 – 394, 2017.

[73] C. Moler. *Numerical Computing with Matlab, Revised Reprint.* Society for Industrial and Applied Mathematics, 2004.

[74] S. Murata. Innovation by in-wheel-motor drive unit. *Veh. Syst. Dyn.*, 50(6):807–830, 2012.

[75] N. Mutoh. Driving and braking torque distribution methods for front- and rear-wheel-independent drive-type electric vehicles on roads with low friction coefficient. *IEEE Trans. Ind. Electron.*, 59(10):3919–3933, 2012.

[76] M. Nagai, Y. Hirano, and S. Yamanaka. Integrated control of active rear wheel steering and direct yaw moment control. *Veh. Syst. Dyn.*, 27(5-6):357–370, 1997.

[77] NHTSA. Traffic safety facts: Summary of motor vehicle crashes. 2016 Data HS 812 580, US Department of Transportation, 2018.

[78] J. Nilsson, A. C. E. Ödblom, and J. Fredriksson. Worst-case analysis of automotive collision avoidance systems. *IEEE Trans. Veh. Technol.*, 65(4):1899–1911, 2016.

[79] O. Nishihara. Comparison of optimization schemes for tire force distribution in integrated chassis control. In *Proc. AVEC*, pages 409–414, 2014.

[80] O. Nishihara and S. Higashino. Exact solution to four-wheel independent driving/braking force distribution and direct yaw-moment optimization with minimax criterion of tire workload. In *Proc. AVEC*, 2012.

[81] O. Nishihara and S. Higashino. Exact optimization of four-wheel steering and four-wheel independent driving/braking force distribution with minimax criterion of tire workload. *Trans. JSME, Ser. C*, 79(799):629–644, 2013. (in Japanese).

[82] O. Nishihara and M. Kurishige. Estimation of road friction coefficient based on the brush model. *Trans. ASME J. Dyn. Syst. Meas. Control*, 133(4):041006–041006–9, 2011.

[83] O. Nishihara and K. Sono. Reduction of tire workload with distribution of normal loads on wheels. In *Proc. Mech. Eng. Congr. Japan*, page G1000502, 2015. (in Japanese).

[84] A. Ohmuro and Y. Hattori. Optimum vehicle trajectory control for obstacle avoidance (a minimax problem of resultant vehicle force). *Trans. JSME, Ser. C*, 76(772):3587–3594, 2010. (in Japanese).

[85] E. Ono, K. Asano, and K. Koibuchi. Estimation of tire grip margin using electric power steering system. In *Proc. IAVSD Symp.*, 2003.

[86] E. Ono, Y. Hattori, and S. Monzaki. Improvement in critical performance of vehicle dynamics integrated control by optimal distribution of four wheel tire forces. *Trans. JSAE*, 39(2):33–38, 2008. (in Japanese).

[87] E. Ono, Y. Hattori, Y. Muragishi, and K. Koibuchi. Vehicle dynamics integrated control for four-wheel-distributed steering and four-wheel-distributed traction/braking systems. *Veh. Syst. Dyn.*, 44(2):139–151, 2006.

[88] B. Paláncz, J. L. Awange, P. Zaletnyik, and R. H. Lewis. Linear homotopy solution of nonlinear systems of equations in geodesy. *J. Geodesy*, 84(1):79–95, 2010.

[89] S. Pan and J. Hedrick. Tracking controller design for mimo nonlinear systems with application to automotive cold start emission reduction. *Journal of Dynamic Systems, Measurement and Control, Transactions of the ASME*, 137(10):101013–101013–12, 2015.

[90] I. Papadimitriou and M. Tomizuka. Fast lane changing computations using polynomials. In *Proc. Amer. Control Conf.*, volume 1, pages 48–53, 2003.

[91] H. Park and J. C. Gerdes. Optimal tire force allocation for trajectory tracking with an over-actuated vehicle. In *Proc. IEEE Intell. Vehicles Symp.*, pages 1032–1037, 2015.

[92] H. Park and J. C. Gerdes. Analysis of feasible tire force regions for optimal tire force allocation with limited actuation. *IEEE Intell. Transp. Syst. Mag.*, 9(3):75–87, 2017.

[93] H. Peng and J.-S. Hu. Traction/braking force distribution for optimal longitudinal motion during curve following. *Veh. Syst. Dyn.*, 26(4):301–320, 1996.

[94] H. Peng, R. Sabahi, S.-K. Chen, and N. Moshchuk. Integrated vehicle control based on tire force reserve optimization concept. In *Proc. ASME Int. Mech. Eng. Congr. and Expo.*, pages 327–335, 2011.

[95] W. H. Press, S. A. Teukolsky, W. T. Vetterling, and B. P. Flannery. *Numerical Recipes in C: The Art of Scientific Computing.* Cambridge University Press, New York, 1992.

[96] R. Rajamani, G. Phanomchoeng, D. Piyabongkarn, and J. Y. Lew. Algorithms for real-time estimation of individual wheel tire-road friction coefficients. *IEEE/ASME Trans. Mechatronics*, 17(6):1183–1195, 2012.

[97] R. Rajamani, D. Piyabongkarn, V. Tsourapas, and J. Y. Lew. Parameter and state estimation in vehicle roll dynamics. *IEEE Trans. Intell. Transp. Syst.*, 12(4):1558–1567, 2011.

[98] R. Rajamani, H.-S. Tan, B. K. Law, and W.-B. Zhang. Demonstration of integrated longitudinal and lateral control for the operation of automated vehicles in platoons. *IEEE Trans. Control Syst. Technol.*, 8(4):695–708, 2000.

[99] P. Raksincharoensak, M. Nagai, and H. Mouri. Investigation of automatic path tracking control using four-wheel steering vehicle. In *Proc. IEEE Veh. Electron. Conf.*, pages 73–77, 2001.

[100] U. Rosolia, S. De Bruyne, and A. G. Alleyne. Autonomous vehicle control: A nonconvex approach for obstacle avoidance. *IEEE Trans. Control Syst. Technol.*, 25(2):469–484, 2017.

[101] SAE. Taxonomy and definitions for terms related to on-road motor vehicle automated driving systems. Technical report, 2016.

[102] A. Schaub, D. Baumgartner, and D. Burschka. Reactive obstacle avoidance for highly maneuverable vehicles based on a two-stage optical flow clustering. *IEEE Trans. Intell. Transp. Syst.*, 18(8):2137–2152, 2017.

[103] J. Shah, M. Best, A. Benmimoun, and M. L. Ayat. Autonomous rear-end collision avoidance using an electric power steering system. *Proc. IMechE Part D, J. Automobile Eng.*, 229(12):1638–1655, 2015.

[104] T. Shamir. How should an autonomous vehicle overtake a slower moving vehicle: design and analysis of an optimal trajectory. *IEEE Trans. Autom. Control*, 49(4):607–610, 2004.

[105] Y. Shibahata, K. Shimada, and T. Tomari. Improvement of vehicle maneuverability by direct yaw moment control. *Veh. Syst. Dyn.*, 22(5-6):465–481, 1993.

[106] Z. Shiller and S. Sundar. Emergency lane-change maneuvers of autonomous vehicles. *Trans. ASME J. Dyn. Syst. Meas. Control*, 120(1):37–44, 1998.

[107] T. Shim, G. Adireddy, and H. Yuan. Autonomous vehicle collision avoidance system using path planning and model-predictive-control-based active front steering and wheel torque control. *Proc. IMechE Part D, J. Automobile Eng.*, 226(6):767–778, 2012.

[108] T. Shim, S. Chang, and S. Lee. Investigation of sliding-surface design on the performance of sliding mode controller in antilock braking systems. *IEEE Trans. Veh. Technol.*, 57(2):747–759, 2008.

[109] S. Shmakov. A universal method of solving quartic equations. *Int. J. Pure Appl. Math.*, 71(2):251–259, 2011.

[110] Y. Shtessel, C. Edwards, L. Fridman, and A. Levant. *Sliding Mode Control and Observation*. Birkhäuser Basel, 2015.

[111] A. S. P. Singh and O. Nishihara. Obstacle avoidance by steering and braking with minimum total vehicle force. In *IFAC HMS*, pages 486 – 493, 2016.

[112] A. S. P. Singh and O. Nishihara. Trajectory generation and tracking using integrated control of 4WS and DYC for minimum jerk obstacle avoidance. In *Proc. FAST-zero*, 2017.

[113] J. E. Slotine and W. Li. *Applied Nonlinear Control*. Prentice-Hall, Englewood Cliffs, NJ, 1991.

[114] J. Song. Performance evaluation of a hybrid electric brake system with a sliding mode controller. *Mechatronics*, 15(3):339 – 358, 2005.

[115] P. Song, M. Tomizuka, and C. Zong. A novel integrated chassis controller for full drive-by-wire vehicles. *Veh. Syst. Dyn.*, 53(2):215–236, 2015.

[116] D. Soudbakhsh, A. Eskandarian, and D. Chichka. Vehicle collision avoidance maneuvers with limited lateral acceleration using optimal trajectory control. *Trans. ASME J. Dyn. Syst. Meas. Control*, 135(4):041006–041006–12, 2013.

[117] R. F. Stengel. *Optimal Control and Estimation*. Dover Publications, New York, 1994.

[118] J.-L. Su and A. W. Ordys. Collision avoidance manoeuvre for a vehicle: a practical approach. *Proc. IMechE Part D, J. Automobile Eng.*, 224(3):299–312, 2010.

[119] Y. Suzuki, Y. Kano, M. Abe, T. Sugai, K. Mogi, J. Hirata, and N. Suzuki. Roll control using tire longitudinal forces integrated with tire force distribution of full drive-by-wire electric vehicle. In *Proc. AVEC*, pages 415–420, 2014.

[120] K. R. Symon. *Mechanics*. Addison-Wesley Publishing Company, 1971.

[121] T. Szirtes and P. Rózsa. *Applied Dimensional Analysis and Modeling*. Butterworth-Heinemann, Burlington, 2007.

[122] D. Tavernini, E. Velenis, and S. Longo. Feedback brake distribution control for minimum pitch. *Veh. Syst. Dyn.*, 55(6):902–923, 2017.

[123] M. Trott. *The Mathematica Guidebook for Symbolics*. Springer-Verlag, New York, 2006.

[124] A. Vahidi and A. Eskandarian. Research advances in intelligent collision avoidance and adaptive cruise control. *IEEE Trans. Intell. Transp. Syst.*, 4(3):143–153, 2003.

[125] J. Wang and R. G. Longoria. Coordinated and reconfigurable vehicle dynamics control. *IEEE Trans. Control Syst. Technol.*, 17(3):723–732, 2009.

[126] R. Wang, C. Hu, F. Yan, and M. Chadli. Composite nonlinear feedback control for path following of four-wheel independently actuated autonomous ground vehicles. *IEEE Trans. Intell. Transp. Syst.*, 17(7):2063–2074, 2016.

[127] Y. Wang, H. Fujimoto, and S. Hara. Driving force distribution and control for EV with four in-wheel motors: A case study of acceleration on split-friction surfaces. *IEEE Trans. Ind. Electron.*, 64(4):3380–3388, 2017.

[128] J. Y. Wong. *Theory of Ground Vehicles*. Wiley, New York, 2001.

[129] D. Yang, T. J. Gordon, B. Jacobson, and M. Jonasson. Quasi-linear optimal path controller applied to post impact vehicle dynamics. *IEEE Trans. Intell. Transp. Syst.*, 13(4):1586–1598, 2012.

[130] H. Yoshida, S. Shinohara, and M. Nagai. Lane change steering manoeuvre using model predictive control theory. *Veh. Syst. Dyn.*, 46(sup1):669–681, 2008.

[131] L. Zhang, L. Yu, Z. Wang, L. Zuo, and J. Song. All-wheel braking force allocation during a braking-in-turn maneuver for vehicles with the brake-by-wire system considering braking efficiency and stability. *IEEE Trans. Veh. Technol.*, 65(6):4752–4767, 2016.

[132] X. Zhang, D. Göhlich, and W. Zheng. Karush–Kuhn–Tuckert based global optimization algorithm design for solving stability torque allocation of distributed drive electric vehicles. *J. Franklin Institute*, 354(18):8134 – 8155, 2017.

Appendix A: List of Author's Work

Journal Papers

1. A. S. P. Singh, O. Nishihara. Nondimensionalized univariate equation characterizing optimal state feedback control for collision avoidance. *IEEE Trans. Intell. Transp. Syst.*, 19(10): 3344-3359, 2019.
2. A. S. P. Singh, O. Nishihara. Minimum resultant vehicle force optimal state feedback control for obstacle avoidance. *IEEE Trans. Control Syst. Technol.*, (under revision).
3. A. S. P. Singh, O. Nishihara. Trajectory tracking and integrated chassis control for obstacle avoidance with minimum jerk. *IEEE Trans. Intell. Transp. Syst.*, (under revision).

Conference Proceedings

1. A. S. P. Singh, O. Nishihara. Obstacle avoidance by steering and braking with minimum total vehicle force. In *Proc. IFAC HMS*, pages 486–493, 2016.
2. A. S. P. Singh, O. Nishihara. Nondimensionalized indices for collision avoidance based on optimal control theory. In *Proc. FISITA*, 2016.
3. A. S. P. Singh, O. Nishihara. Trajectory generation and tracking using integrated control of 4WS and DYC for minimum jerk obstacle avoidance. In *Proc. FAST-zero*, 2017.